The dynamics of circumbinary discs and embedded planets

Dissertation

der Mathematisch-Naturwissenschaftlichen Fakultät
der Eberhard Karls Universität Tübingen
zur Erlangung des Grades eines
Doktors der Naturwissenschaften
(Dr. rer. nat.)

vorgelegt von
Dipl.-Phys. Daniel Gerd Thun
aus Reutlingen

Tübingen
2018

Gedruckt mit Genehmigung der Mathematisch-Naturwissenschaftlichen Fakultät der Eberhard Karls Universität Tübingen.

Tag der mündlichen Qualifikation:	13.02.2019
Dekan:	Prof. Dr. Wolfgang Rosenstiel
1. Berichterstatter:	Prof. Dr. Wilhelm Kley
2. Berichterstatter:	Prof. Dr. Klaus Werner

Zusammenfassung

Seit der ersten Entdeckung eines zirkumbinären Planeten mit dem Kepler Weltraumteleskop im Jahr 2011 wurden neun weitere Planeten entdeckt, die um einen Binärstern kreisen. All diese zirkumbinären Kepler Systeme haben folgende Gemeinsamkeiten: Sie sind planar, das heißt die Umlaufbahn des Planeten liegt in derselben Ebene wie die Umlaufbahn des Binärsterns, was auf eine Entstehung der Planeten in einer Akkretionsscheibe, die beide Komponenten des Binärsterns umgab, hindeutet. Des Weiteren liegt die Umlaufbahn all dieser Planeten sehr nahe am berechneten Stabilitätslimit. Für die Entstehung von zirkumbinären Planeten gibt es grundsätzlich zwei Erklärungsmöglichkeiten: Eine Entstehung direkt am Ort der heutigen Beobachtung oder eine Entstehung in den äußeren Bereichen der Scheibe, gefolgt von einer Migration zur beobachteten Position. Wie Simulationen gezeigt haben, ist eine Entstehung am Ort der Beobachtung unwahrscheinlich, da Planetesimale auf Umlaufbahnen in der Nähe des Binärsterns destruktiv kollidieren. Das zweite Szenario führt direkt zur Frage, wie die Migration der Planeten an der beobachteten Stelle gestoppt werden kann. In dieser Arbeit wird das zweite Szenario mit Hilfe von numerischen Simulationen untersucht.

Die gravitative Interaktion zwischen Binärstern und Akkretionsscheibe führt zur Bildung einer zentralen, exzentrischen Lücke, die langsam prograd um den Binärstern präzediert. Diese innere Lücke formt eine Barriere für den migrierenden Planeten. Daher untersucht der erste Teil dieser Arbeit wie Parameter des Binärsterns (Exzentrizität, Massenverhältnis) und Parameter der Scheibe (Druck, Viskosität) die Größe, Exzentrizität und Präzessionsperiode der Lücke beeinflussen. Dabei stellt sich die Exzentrizität des Binärsterns (e_{bin}) als ein wichtiger Parameter heraus. So zeigt sich, wenn man die Präzession der Lücke gegen ihre Größe darstellt, eine Bifurkation bei Variation von e_{bin}. Erhöht man, von null ausgehend, die Exzentrizität des Binärsterns, so sinken zunächst die Präzessionsperiode und die Größe der Lücke. Dieses Verhalten ändert sich mit Erreichen einer kritischen Exzentrizität von $e_{\mathrm{bin}} = 0.18$, ab der Präzessionsperiode und Größe der Lücke wieder zunehmen. Das Massenverhältnis des Binärsterns hat lediglich Auswirkung auf die Präzessionsperiode, die mit steigendem Massenverhältnis sinkt, die Größe der Lücke bleibt konstant. Bei der Variation des Druckes und der Viskosität erhält man das erwartete Ergebnis, dass sich mit steigendem Druck und Viskosität die Größe der Lücke verringert.

Im zweiten Teil dieser Arbeit wird der Migrationsprozess von Planeten in zirkumbinären Scheiben untersucht. Dazu wurde anhand von fünf Kepler Systemen (Kepler-16, -34, -35, -38 und -413) simuliert wie die finalen Bahnparameter vom Verhältnis der Planeten- und Scheibenmasse abhängen, und wie die Planeten die Struktur der Scheibe verändern. Wie erwartet migrieren die Planeten in allen Fällen bis zur Lücke. In Abhängigkeit der Planetenmasse zeigen sich zwei verschiedene Migrationsszenarien: Schwere Planeten dominieren die Scheibe, verringern die Größe der inneren Lücke und formen sie kreisförmiger. Leichte Planeten werden hingegen von der Scheibe dominiert. Sie richten ihren Orbit an der präzedierenden Lücke in der Scheibe aus und ihre Exzentrizität wird angeregt. Im Allgemeinen sind die simulierten finalen Bahnparameter, im Vergleich zu den Beobachtungen, zu groß. Zirkumbinäre Planeten um Systeme, welche sehr exzentrische Lücke erzeugen (Kepler-34 und -413) haben auch die höchsten simulierten Exzentrizitäten im Einklang mit den Beobachtungen.

Abstract

Since the first detection of a circumbinary planet with the Kepler space telescope in 2011 nine more circumbinary planets have been discovered. All these circumbinary Kepler systems have two things in common: First they are very flat, meaning that the orbit of the binary and the planet are in one plane, suggesting that they formed in an accretion disc surrounding both binary components. Second, the orbits of the planets are very close to the calculated stability limit. To explain the formation of these planets two scenarios are possible: An in situ formation at the observed location or a formation further outside in the disc followed by radial migration to the current observed position. Simulations have shown that an in situ formation is unlikely, due to destructive collisions of planetesimals on orbits close to the binary. The second scenario leads to the question of how the migrating planets can be stopped at the observed location. In this thesis the second scenario is examined through numerical simulations.

The gravitational interaction between the binary and the disc leads to the formation of an eccentric inner gap, which precesses slowly in a prograde manner around the binary. This inner gap constitutes a barrier for a migrating planet. Therefore, the first part of this thesis investigates how binary parameters (eccentricity, mass ratio) as well as disc parameters (pressure, viscosity) influence the size, eccentricity, and precession period of the gap. The binary eccentricity (e_{bin}) is identified as an important parameter. In the precession period – gap-size diagram a bifurcation occurs for varying e_{bin}. Increasing the binary eccentricity from zero, precession period and gap-size decrease until a critical eccentricity of $e_{\mathrm{bin}} = 0.18$ is reached. From this point onward, precession period and gap-size increase again for increasing binary eccentricities. The binary mass ratio changes only the precession period, which decreases with increasing mass ratios, while the gap-size remains constant. For increasing viscosity and pressure in the disc the expected behaviour is observed: precession period and gap-size decrease.

The second part of this thesis investigates the migration of planets in circumbinary discs. For five Kepler systems (Kepler-16, -34, -35, -38, -413) the dependence of the final orbital parameters on the planet-to-disc mass ratio is examined as well as the change in the disc structure due to the presence of the planet. The planets migrate in all cases to the edge of the gap, as expected. Depending on the planet mass, two migration scenarios are observed. Massive planets dominate the disc by shrinking and circularising the inner gap, whereas light planets are influenced by the disc. They align their orbits to the precessing disc and their eccentricity is excited. In general the final simulated orbital parameters are too large compared to the observations. Circumbinary planets around systems which create large, eccentric gaps (Kepler-34 and -413) also have the highest simulated eccentricities in agreement with the observations.

Contents

1 Introduction

This chapter outlines the general context of this thesis. It starts with a brief historic overview of the understanding of the Solar System, followed by an overview of the theory of planet formation. Focus is then put on extrasolar planets, especially the for this thesis important circumbinary planets and the theory of planet migration, a possible way to explain the observed population of circumbinary planets. The last sections introduce the numerical method and the computer code used in this thesis to simulate circumbinary planets embedded in a disc, with a special focus on GPU computing.

1.1 The Solar System

The night sky always had a special attraction to mankind during all epochs. So from early on, humans observed and studied the Solar System. First known observations go back to Babylonian astronomers who were able to observe the planets Mercury, Venus, Mars, Jupiter, and Saturn due to their visibility by eye in the second millennium BCE (Sachs, 1974). The modern scientific view of the Solar System begun with the ancient Greeks. In fact the word planet goes back to the Greek word for "wandering star", because of their movement relative to the background of the fixed stars. First models of the Solar System assumed a stationary Earth with the planets and the Sun on circular orbits around it. Although this geocentric model was challenged by observations, like the retrograde movement of the planets, it was the dominant model in the West until the Copernican Revolution in 1543. The dominance of the geocentric model was mainly due to Claudius Ptolemy's main work, the "Almagest" (150 CE) in which he formalized the concept of epicycles introduced by Apollonius of Perga and Hipparchus of Rhodes to explain the retrograde movement of the planets as well as their variation in brightness.

In his principal work "De Revolutionibus Orbium Coelestium" Nicolaus Copernicus introduced 1543 the heliocentric model[1]. This model, where the Earth and all other known planets move around the Sun on circular orbits, could easily explain the retrograde movements and even predict an ordering of the planets. Although, due to the assumption that the planets move on circular orbits, epicycles were still needed and the predictions of planet positions did not improve compared to the Ptolemaic model.

One year after the invention of the telescope in 1609, Galileo Galilei observed the phases of the Venus and discovered the four largest moons of Jupiter[2], today known as the Galilean moons, with his own constructed telescope. Both observations strongly support the heliocentric model of Copernicus in favour of a geocentric model.

Between 1609 and 1619 Johannes Kepler published his famous three laws of planetary motion based on detailed observations by Tycho Brahe. Kepler had to introduce elliptical orbits with the Sun located in one focal point of the ellipse to explain the orbit of Mars. As

[1] A heliocentric model was already developed by Aristarchus of Samos, but it could not prevail against the geocentric model.

[2] Io, Europa, Ganymede, and Callisto.

a lucky incident of history, Kepler tried to calculate the orbit of Mars, which has a relative high eccentricity of 0.0934. It was due to this high eccentricity that no circular solution fit to Kepler's satisfaction and therefore he at last used elliptical orbits.

In 1687 Isaac Newton published his three books "Principia" containing Newton's laws of motion and Newton's law of universal gravitation. With both laws he was able to derive Kepler's laws of planetary motion, the field of celestial mechanics was born. In 1781 William Herschel discovered the planet Uranus and first thought of it as a comet. Calculations by Anders Johan Lexell showed that the orbit of Uranus is almost circular, suggesting that the discovered object is a planet and not a comet.

The dwarf planet Ceres, located in the Asteroid Belt, which separates the inner from the outer planets, was anticipated by the Titius-Bode law, a simple numerical relation between the distance of a planet from the Sun and the number of planetary sequence[3]. In 1801 Ceres was discovered by Giuseppe Piazzi, who was able to follow the orbit of Ceres for one month before loosing sight again. Carl Friedrich Gauss developed a method (including his famous least squares method) to calculate the orbit of an object out of at least three angular observations (Gronchi, 2004). It was due to this method that Ceres could be rediscovered at the predicted position only one year after its initial discovery.

The planet Neptune was predicted independently by John Couch Adamas and Urbain Le Verrier to explain irregularities in the orbit of Uranus which could not solely be explained by the gravitational pull of Jupiter and Saturn. In 1846 Johann Galle discovered Neptune within one degree of Le Verrier's prediction. This discovery was a great success and validation for the theory of celestial mechanics.

In 1930 the then ninth planet of the Solar System, Pluto, was discovered by Clyde Tombaugh. The discovery of Eris a trans-Neptunian object with a larger mass than Pluto by a team led by Mike Brown (Brown et al., 2005) in 2005 started a discussion about a strict definition of a planet. In 2006 the International Astronomical Union passed the following scientific definition of a Solar System planet: "A planet is a celestial body that: (a) is in orbit around the Sun, (b) has sufficient mass for its self-gravity to overcome rigid body forces so that it assumes a hydrostatic equilibrium (nearly round) shape, and (c) has cleared the neighbourhood around its orbit"[4]. This definition demoted Pluto to a dwarf planet[5] leaving the Solar System with eight Planets and five dwarf planets (Ceres, Pluto, Haumea, Makemake, and Eris).

Recently it was proposed by Batygin and Brown (2016) that the orbital elements of trans-Neptunian objects could be explained by a massive planet in the outer Solar System. As of today the hunt for the so called Planet Nine is still ongoing and Planet Nine could be the second, only after Neptune, discovery of a planet predicted by irregularities in orbits of already known objects.

The Solar System consists of the four terrestrial planets, Mercury, Venus, Earth, and Mars mainly made of rocky material (silicates and metals) and located from 0.39 au[6] to 1.53 au. The inner planets are separated by the Asteroid Belt from the four outer planets. The Asteroid Belt spans from 2.0 au to 3.25 au and hosts the orbit of the dwarf planet Ceres. The outer planets are the two gas giants Jupiter and Saturn and the two ice giants Uranus and Neptune, ranging from 5.0 au to 30.0 au. Behind Neptune is the area of trans-Neptunian objects, further

[3] Nowadays it is thought that the Titius-Bode law is not based on any basic physical principles.

[4] IAU Resolution B5, `https://www.iau.org/static/resolutions/Resolution_GA26-5-6.pdf`, accessed 19 November 2018.

[5] Dwarf planets fulfil point (a) and (b) of the planet definition but have not cleared their orbit.

[6] Astronomical Unit, roughly the distance between the Earth and the Sun. Defined as 1.0 au = 149 597 870 700 m.

divided by the Kuiper Belt (origin of the short range comets), the scattered disc and the theoretical Oort cloud (origin of the long range comets). The dwarf planets Pluto, Haumea, Makemake, and Eris lay all beyond the orbit of Neptun in the Kuiper Belt and the scattered disc and are all considered trans-Neptunian objects.

Before the detection of extrasolar planets, the Solar System was the only known planetary system. Any theory of planetary formation had to explain the quirks of the Solar System

- The nearly circular, prograde orbits of the planets with almost no inclination.
- The mass and angular momentum distribution: 99% of the mass is present in the Sun, while 99% of the angular momentum is present in the orbits of the planets.
- The distribution of the planets. Terrestrial planets close to the Sun separated from the gas giants further out.

The next section will give a brief overview of the general theory of planet formation, developed to explain the structure of the Solar System.

1.2 Planet formation

The theory of planet formation developed from early ideas by Kant (1755) and Laplace (1796) of a collapsing molecular cloud made of dust and gas. Because of the initial rotation of this cloud and the conservation of angular momentum a flat disc around the protostar develops. This so called protoplanetary or accretion disc can extend up to a few hundred astronomical units with typical masses between $10^{-4}\,\mathrm{M}_\odot$[7]and $10^{-1}\,\mathrm{M}_\odot$ (Andrews and Williams, 2007), and lifetimes of a few million years (Haisch et al., 2001). The protoplanetary disc is made of 99% gas (hydrogen, helium) and 1% dust (silicates, metals). The typical size of the dust agglomerates is of the order of micrometres (Mathis et al., 1977). The protostar can accrete matter from the disc while angular momentum is transported outward. Calculations show that the molecular viscosity is far too weak to drive this process. A possible mechanism to create an effective viscosity is turbulence in the disc (Shakura and Sunyaev, 1973). It is therefore assumed that various instabilities, for example the magnetorotational instability (Balbus and Hawley, 1991) or the vertical-shear instability (Nelson et al., 2013; Stoll and Kley, 2014) lead to turbulence yielding the high effective viscosity necessary to explain the observed mass flux in the disc.

The formation of the terrestrial planets in the inner Solar System and the gas giants in the outer Solar System is still under heavy investigation. While the general process seems identified, formation by core accretion, many details are still unexplained. The idea of the core accretion scenario is, that the terrestrial planets and the cores of the giant planets formed by growing smaller particles into larger ones through millions and millions of collisions. This bottom-up process is broken further down into substeps. First the formation of planetesimals with sizes of 10 to 100 kilometres out of submicron dust particles. Then the formation of planetary cores by the gravitational interaction of these planetesimals. Finally the terrestrial planets are formed by collisions of these cores, whereas the cores in the outer Solar System are massive enough to accrete gas from the surrounding protoplanetary disc and can therefore grow further into gas giants.

[7]Mass of the Sun, $\mathrm{M}_\odot = 1.989\,11 \cdot 10^{30}\,\mathrm{kg}$.

Inside the disc the small submicron to micron sized dust particles are well coupled to the gas and can easily stick together, due to the small relative velocities induced by Brownian motion (Kempf et al., 1999), and form fluffy dust agglomerates after collisions. When these dust particles reach sizes in the order of centimetres they decouple from the gas. Since the gas is supported by pressure and therefore moves with sub-Keplerian velocity the dust particles, which move with Keplerian velocity, feel an aerodynamic drag. This drag has the following effects: First it leads to the settlement of the particles in the disc's midplane. Second the dust particles begin to migrate inwards and the relative velocity between the different sized particles is increased (Weidenschilling, 1977). These high relative velocities lead to bouncing or even fragmentation of colliding grains. To grow planetesimals these destructive collisions and the fast radial inward migration of the dust grains are serious problems. To overcome the drift-barrier a fast mechanism to produce planetesimals is needed. A possible mechanism could be the streaming instability (Youdin and Goodman, 2005). For this instability an aerodynamically coupled dust and gas mixture, with a dust-to-gas ratio of approximately one, is needed. Such a high dust-to-gas ratio can be reached in the midplane of the disc due to the settling of the dust. In the vortices the radial drift of the dust grains is stopped and the relative velocities are low enough to grow further. In addition it is possible to form planetesimals in these vortices through the direct gravitational collapse of the mm – cm sized dust particles into planetesimals (Carrera et al., 2015).

For planetesimals with the size of 10 up to 100 kilometres gravitational effects become more important than the aerodynamic drag. Especially gravitational focusing, which increases the collision cross section of two planetesimals, induces further growth. As shown by Greenberg et al. (1978), the time it takes for a planetesimals to double its mass is shortest for the largest planetesimals, leading to a runaway growth (see also Wetherill and Stewart (1989) and Kokubo and Ida (1996)). Typically, one planetesimal sweeps up the smaller bodies in its feeding zone, which has an radial extend up to a few Hill radii[8] of the forming embryo. The growth stops when the core has depleted its feeding zone and reached its isolation mass. This isolation mass depends on the location in the disc. Usually it is $M_{\mathrm{iso}} = 0.05\,\mathrm{M}_{\oplus}$[9] in the inner part of the disc. Whereas in the outer parts isolation masses of $M_{\mathrm{iso}} = 5 - 9\,\mathrm{M}_{\oplus}$ can be reached due to the higher abundance of solids. Typically, a four times higher abundance of solids can be reached through the condensation of additional molecules, especially water (H_2O), methane (CH_4), and ammonia (NH_3), behind the snowline. The snowline lies for solar type star at around 4 au, explaining the separation of the terrestrial planets from the gas giants.

Since the runaway growth of a planetary core is restricted to its feeding zone it is a local effect and more than one embryo can grow in the protoplanetary disc. These embryos tend to grow in an orderly manner. Larger cores increase the velocity of planetesimals close to them, which decrease their own collision cross section and therefore the smaller cores can grow faster than the larger ones. This phase was coined oligarchic growth by Kokubo and Ida (1998). At the end of this phase around 40 planetary embryos, with masses between the Moon and the Mars, and radial separations of approximately ten Hill radii, have grown (Kokubo and Ida, 1998). The terrestrial planets finally form through the interaction (collision, scattering) between these cores on very long timescales of more than ten million years. The necessary perturbation of the cores, to achieve crossing orbits, comes from secular resonances and the influence of the giant planets (Chambers and Wetherill, 1998).

[8] The gravitational sphere of influence of a body with mass m on an orbit with semi-major axis a around a star with mass M is given by the Hill radius $R_{\mathrm{H}} = \left(\frac{m}{3M}\right)^{1/3} a$.

[9] Mass of the Earth, $\mathrm{M}_{\oplus} = 5.9736 \cdot 10^{24}\,\mathrm{kg}$.

The heavy cores in the outer part of the disc are able to accrete gas and form an envelope (Pollack et al., 1996). At first the envelope is in hydrostatic equilibrium and the mass is roughly accreted with a constant rate until a critical mass of about $20 - 30\,M_\oplus$ is reached. Reaching the critical mass, the envelope cannot maintain hydrostatic equilibrium any more and collapses, triggering a runaway phase during which hundreds of Earth masses can be accreted in a very short period of time (Mizuno, 1980). This process explains the solid cores of the gas giants but it also needs to form the cores fast before the dispersal of the gas disc. To overcome the long timescales necessary to form the cores additional mechanisms like planet-disc interaction via gravity are discussed. This interaction leads in general to an inward migration of the forming planet. Through this migration a depletion of the feeding-zone can be prevented, leading to cores above the critical mass on timescale of around one million years (Alibert et al., 2005). Migration is discussed in more detail in Sec. 1.4. Another possible way to form giant planets was suggest by Boss (2003), the formation by gravitational instability. This formation process is similar to the formation of the protosun, where a lump of gas becomes massive enough to trigger a collapse, directly forming a planet. This top-down mechanism has the advantage of a short timescale but needs a high disc mass and low temperatures, generally only fulfilled in the very outer parts of the disc. Furthermore, it does not explain the solid cores of the gas giants.

The theory of planet formation, discussed in the previous paragraphs can explain in general the structure of the Solar System, although many details are still poorly understood and under active investigation. The discovery of extrasolar planets added a large diversity of planetary systems which challenge the theory of planet formation.

1.3 Extrasolar planets

Since the first detection of an extrasolar planet around a main sequence star, (51 Pegasi b) in 1995 (Mayor and Queloz, 1995), 3815[10] extrasolar planets have been discovered, revealing a wide range of different planet types and orbital configurations. Fig. 1.1 gives an impression of the mass and orbital parameters of selected extrasolar planets. Amongst the so far detected planets are two types of planet classes not present in our Solar System. First the so called hot Jupiters (upper left corner of the left panel of Fig. 1.1), giant planets on orbits close to their host star. Second super-Earths terrestrial planets with masses greater than $10\,M_\oplus$. The right panel of Fig. 1.1 shows that a high fraction of extrasolar planets posses an orbit with significant eccentricity, making the low eccentric orbits of the Solar System planets special. Through the detections made so far it became clear that extrasolar planets are quite common and therefore the planet formation process has to be very robust. It is believed that on average every star in the Milky Way is at least host to one planet (Cassan et al., 2012).

1.3.1 Planet detection methods

Most of the planets detected so far were discovered with indirect techniques, namely the radial-velocity method and the transit method. The radial-velocity method is based on the fact that the planet and the star orbit around a common barycentre. This leads to small velocities of the star, for example the Sun moves with a speed of $13\,\mathrm{m/s}$ due to the gravitational pull of Jupiter. If the system can be observed edge on, the star moves periodically towards and away from the observer. This movement is observable with the help of the stellar spectrum. If

[10] Data from `https://exoplanetarchive.ipac.caltech.edu/`, accessed 19 November 2018.
[11] See footnote 10.

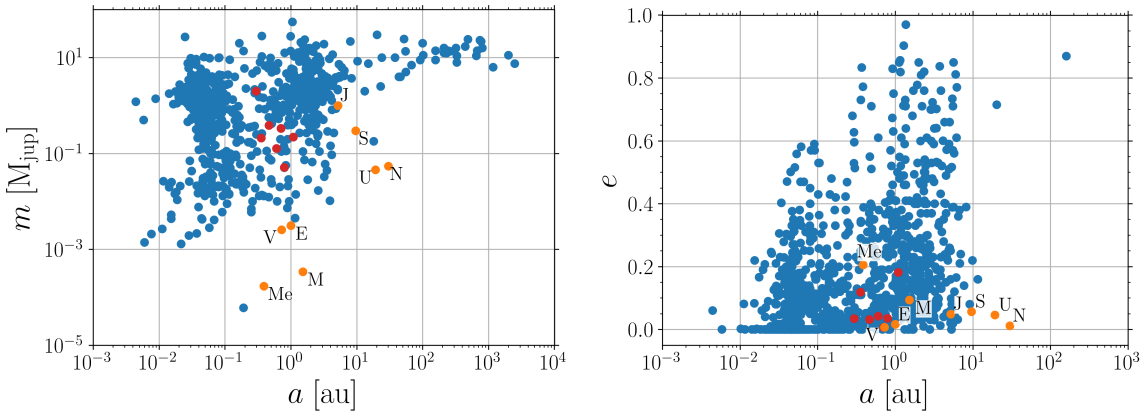

Figure 1.1: Planet mass (left) and eccentricity (right) plotted against the semi-major axis. Orange dots mark the Solar System planets and red dots mark circumbinary planets detected by the Kepler space telescope. Data taken from the NASA Exoplanet Archive[11]. The mass of Jupiter is $M_{jup} = 1898.6 \cdot 10^{24}$ kg

.

the star moves away form the observer the spectrum is redshifted and if it moves toward the observer it is blueshifted. Careful measurements of these shifts allow for the calculation of the orbital period and a lower limit of the planet mass (since the inclination of the planet is typically unknown).

Monitoring the stellar flux for periodic dips, caused by a transiting planet which dims the light received from the star, is the idea of the transit method. Jupiter mass planets typically reduce the stellar flux by 1% and Earth mass rocky planets by a fraction of 0.0001 (Armitage, 2010). From these periodic drops in the light curve it is possible to calculate the period of the orbit as well as the radius of the planet, if the star's radius is known.

The detection of circumbinary planets with the transit method is more difficult, since the dips, caused by the transiting planet, are neither periodic nor of equal duration. The variation of the transit period is known as transit-timing variation and is also used for single-star systems to hunt for additional planets. The variation occurs because the primary and secondary orbit around their common barycentre and therefore the transit can occur before or after stellar conjunction. While in single-star systems the period between transits can vary up to a few hours, for binary systems this can be days. The second effect which is present in binary systems is the variation of the length of transits, called transit-duration variation. Since the primary and secondary orbit around their common barycentre it is possible that the primary moves with the planet during its transit, leading to longer transits, or moving against the planet, shortening the transit (Welsh et al., 2014).

Besides these two detection methods, which both favour heavy planets on close orbits, explaining the missing planets in the lower right corner of the left panel of Fig 1.1, a variety of other detection methods exist. For a discussion of these methods, like direct imaging or gravitational microlensing, I refer to the literature (Armitage, 2010).

1.3.2 Kepler circumbinary planets

On 7 March 2009 the Kepler space telescope was launched to observe approximately 150 000 main sequence stars in order to look for extrasolar planets around these stars. During its

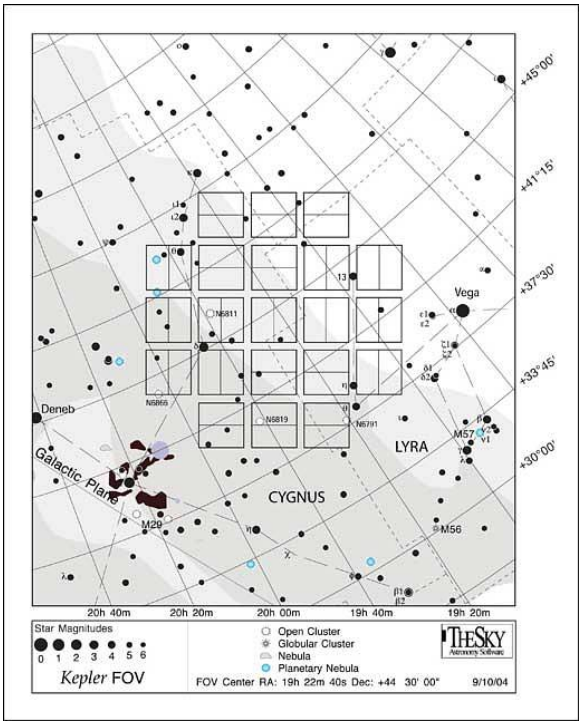

Figure 1.2: Kepler's field of view. (Source: NASA)

primary mission the Kepler space telescope pointed at a field close to the galactic plane and close to the northern constellations Cygnus, Lyra and Draco (see Fig. 1.2). At the time of this writing[12] the Kepler mission has detected 2327[13] confirmed extrasolar planets. In 2011 the first circumbinary planet in a P-type orbit, Kepler-16b, was detected (Doyle et al., 2011). A planet is in a P-type orbit when it orbits both binary components, contrary to a S-type orbit where only one star of the binary is orbited by the planet. The host stars of Kepler-16b are a K-type main-sequence star with mass $M_\mathrm{A} = 0.69\,\mathrm{M}_\odot$ and a M-type red dwarf with mass $M_\mathrm{B} = 0.203\,\mathrm{M}_\odot$. The binary has a semi-major axis of $a_\mathrm{bin} = 0.224\,\mathrm{au}$ and an eccentricity of $e_\mathrm{bin} = 0.159$. Kepler-16b has a semi-major axis of $a_\mathrm{p} = 0.705\,\mathrm{au}$ and an eccentricity of $e_\mathrm{bin} = 0.007$.

Since the detection of Kepler-16b, the Kepler telescope has detected nine more circumbinary planets in a P-type orbit[14]. These detection gave a wide range of binary parameters. The Kepler circumbinary systems range from mass ratios between $q_\mathrm{bin} = 0.207$ (Kepler-453) up to $q_\mathrm{bin} = 0.974$ (Kepler-34) and eccentricities from almost circular $e_\mathrm{bin} = 0.023$ (Kepler-47) up to very eccentric binaries with $e_\mathrm{bin} = 0.521$ (Kepler-34). All these binary system are very close with semi-major axis ranging from $a_\mathrm{bin} = 0.083\,\mathrm{au}$ (Kepler-47) up to $a_\mathrm{bin} = 0.229\,\mathrm{au}$ (Kepler-34) and orbital periods from $T_\mathrm{bin} = 7.4\,\mathrm{d}$ (Kepler-47) up to $T_\mathrm{bin} = 41.1\,\mathrm{d}$ (Kepler-16). These detection suggest that no special binary configuration is needed to host circumbinary planets.

[12] 17 October 2018, `www.nasa.gov/kepler/discoveries`.

[13] Not included are detections from the K2 mission, which was started after reaction wheels failed and Kepler was not able to continue its primary mission.

[14] Kepler-34 and -35 (Welsh et al., 2012), Kepler-38 (Orosz et al., 2012a), Kepler-47 (Orosz et al., 2012b), Kepler-64 (Schwamb et al., 2013), Kepler-413 (Kostov et al., 2014), Kepler-453 (Welsh et al., 2015), and Kepler-1647 (Kostov et al., 2016).

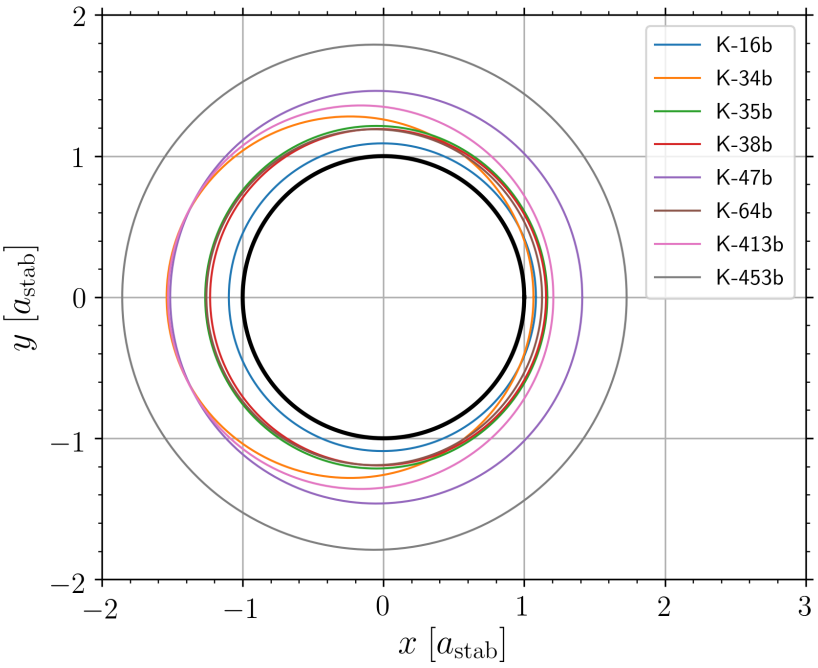

Figure 1.3: Orbits of various circumbinary Kepler planets normalized to the stability radius (1.1) of their binary system. Kepler-47c and Kepler-1647b are not shown since they are not close to the stability limit.

The planets in these systems have masses comparable or slightly below Saturn with orbital periods ranging from 50 to 300 days. Pierens and Nelson (2008) showed that Saturn mass circumbinary planets are more likely than Jovian-type planets, since these heavy planets tend to get captured in a 4:1 mean-motion resonance with the binary, leading to close encounters (due to the increased eccentricity of the planet) with the secondary star. Table 1.1 summarises the orbital parameters of the Kepler systems with a circumbinary planet.

Besides all these differences there are two properties all systems have in common. First, they are very flat (Kepler-413 is slightly misaligned), meaning the planet orbits in the same plane as the binary. Second, the inner most planet of these systems is very close to the stability limit. From direct N-body simulations Holman and Wiegert (1999) derived the following approximation for the critical radius around a binary below which orbits are unstable:

$$a_{\mathrm{stab}} = \left(1.6 + 5.1e_{\mathrm{bin}} + 4.12\mu - 2.22e_{\mathrm{bin}}^2 - 4.27e_{\mathrm{bin}}\mu - 5.09\mu^2 + 4.61e_{\mathrm{bin}}^2\mu^2\right) a_{\mathrm{bin}}\,. \tag{1.1}$$

The mass ratio is given by $\mu = M_B/(M_A+M_B)$, where M_A is the mass of the primary and M_B is the mass of the secondary. Fig. 1.3 shows the orbits of various Kepler circumbinary planets normalized to the stability radius of their binary system. The flatness of the circumbinary systems suggest that the planets formed in an accretion disc surrounding both stars, hence a circumbinary disc. These accretion disc around binaries have been observed indirectly (Jensen and Mathieu, 1997) and directly (Dutrey et al., 1994). It is reasonably to assume that the planet formation process in circumbinary discs follows the same path as in discs around single stars, through collisional growth. Although, it is not clear where in the disc the planets have formed. The planets could have formed in situ at their observed location, or they could have formed in the outer parts of the disc and migrated to their current location. In this thesis the

System	M_A [$M_\odot$]	M_B [$M_\odot$]	q_{bin}	a_{bin} [au]	e_{bin}	T_{bin} [d]	m_p [M_{jup}]	a_p [au]	e_p
K-16	0.690	0.203	0.294	0.224	0.159	41.079	0.333	0.705	0.007
K-34	1.048	1.021	0.974	0.229	0.521	27.796	0.220	1.090	0.182
K-35	0.888	0.809	0.912	0.176	0.142	20.734	0.127	0.603	0.042
K-38	0.949	0.249	0.262	0.147	0.103	18.795	<0.384	0.464	<0.032
K-47	1.043	0.362	0.347	0.084	0.023	7.448	<2.000	0.296	<0.035
K-64	1.384	0.386	0.279	0.174	0.212	20.000	<0.542	0.634	0.054
K-413	0.820	0.542	0.661	0.101	0.037	10.116	0.211	0.355	0.118
K-453	0.944	0.195	0.207	0.128	0.052	27.322	<0.051	0.790	0.036

Table 1.1: Kepler circumbinary systems. The mass ratio is defined as $q_{bin} = M_B/M_A$. Kepler-47c and Kepler-1647b are not shown since they are not close to the stability limit. References: Kepler-16 (Doyle et al., 2011), Kepler-34 and -35 (Welsh et al., 2012), Kepler-38 (Orosz et al., 2012a), Kepler-47 (Orosz et al., 2012b), Kepler-64 (Schwamb et al., 2013), Kepler-413 (Kostov et al., 2014), Kepler-453 (Welsh et al., 2015).

second scenario will be investigated therefore the next section gives a brief overview of the migration mechanism through planet-disc interaction.

1.4 Planet-disc interaction

Observations of hot Jupiters (Mayor and Queloz, 1995), resonant systems (Gillon et al., 2017) or circumbinary planets close to the stability limit (Doyle et al., 2011) challenge the theory of planet formation discussed in Sec. 1.2 and are hard to explain by in situ planet formation. A mechanism to explain these observations is the gravitational interaction between a planet and the gaseous disc, which changes the orbital elements (semi-major axis, eccentricity and inclination) of the planet. For example if a torque Γ, arising from an azimuthal asymmetry in the disc, is applied to a planet of mass m_p, on a circular orbit with radius a_p around a star of mass M_*, its semi-major axis changes according to

$$\frac{da_p}{dt} = 2\frac{\Gamma}{m_p}\sqrt{\frac{a_p}{GM_*}}, \tag{1.2}$$

with the gravitational constant $G = 6.672 \cdot 10^{-11}\,m^3\,kg^{-1}\,s^{-2}$. This follows directly from $\dot{J}_p = \Gamma$, where J_p is the angular momentum component of the planet perpendicular to the plane of motion. This change in the semi-major axis is called planet migration. Depending on the planet's mass and how the planet is able to influence the gaseous disc different migration regimes are defined. Low mass planets, typically up to a few Earth masses, which do not alter the disc structure are subject to type I migration (see upper panel of Fig. 1.4). High mass planets, typically with masses greater than one Jupiter mass, which are able to open

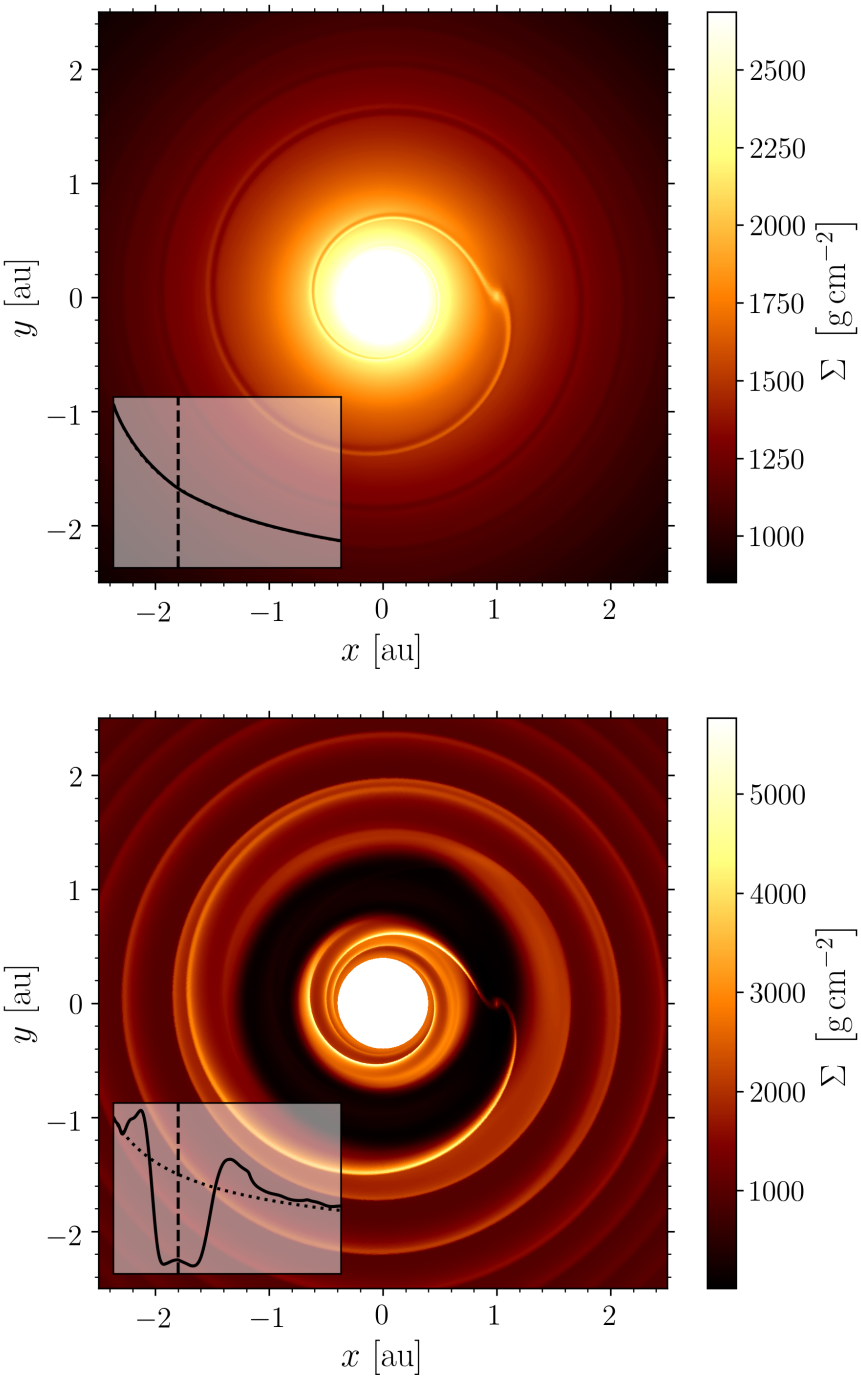

Figure 1.4: The upper panel shows an Earth mass planet subject to type I migration and the lower panel a two Jupiter masses planet subject to type II migration. Both snapshots show the surface density after 100 planet orbits. The inlet shows the azimuthally averaged surface density, the dashed line marks the fixed location of the planet and the doted line shows the initial surface density.

a gap in the disc, are subject to type II migration (see lower panel of Fig. 1.4). There also exists an intermediate regime (type III migration) where a fast runaway migration due to the coupling of the torque with the migration rate of the planet can occur. Although, planets can migrate inwards as well as outwards, the typical migration direction is inward with a timescale of the order of 10^5 yr which, is far shorter than the expected lifetime of the disc. Therefore migration, while being a solution for the formation of hot Jupiters or close by circumbinary planets, also challenges the theory of planet formation since the process is too fast. In the following, I will briefly discuss the key concepts and results for type I and II migration an refer to the literature for type III migration (Masset and Papaloizou, 2003).

1.4.1 Type I migration

Type I migration denotes the regime in which planets are not massive enough to alter the disc structure significantly. For typical disc models these planets have masses up to a few Earth masses. The presence of the planet alters the fluid flow and creates asymmetric features in the disc. The torques created by these asymmetries can be divided into two parts. The first part, the wave torque, arises from density waves excited by the planet, which are sheared out by the differentially rotating disc into a one armed spiral wave (see upper panel of Fig. 1.4). The spiral waves are regions with increased density and their back reaction onto the planet creates a torque. The gravitational pull of the inner spiral arm on the planet creates a positive torque which leads to an outward migration of the planet according to equation (1.2). Similar the gravitational pull of the outer spiral creates a negative torque, leading to inward migration. In general the spiral waves are not symmetric with respect to the planet, leading to a net wave torque, which is usually negative. The second part, the corotation torque, arises from a region close to the planet, where fluid elements are on horseshoe orbits, in the frame of the planet. The interaction between the planet and these fluid elements leads to a positive torque on the planet.

To quantitatively calculate the torques acting on a planet in the type I regime a linear analysis is suitable, since the perturbations introduced by the planet are small (Goldreich and Tremaine, 1979). In a first step the potential of the planet is decomposed in Fourier modes and then the effect of these modes onto the linearised hydrodynamical equations is studied. This analysis shows that a strong disc response is triggered where the pattern frequency of the modes matches a characteristic frequency of the gaseous disc.

The wave torque arises from locations, so called Lindblad resonances, where the pattern speed of the mode, as seen in the local frame of the fluid element, matches the epicyclic frequency κ_0 of the fluid element

$$m(\Omega - \Omega_\mathrm{p}) = \pm\kappa_0\,, \tag{1.3}$$

with the orbital frequency of the planet Ω_p and an integer m. The epicyclic frequency is the frequency with which a radial displaced fluid element oscillates. It is equal to the Keplerian frequency $\Omega(R) = \sqrt{GM_*/R^3}$ in a Keplerian rotating disc. In this case the locations of the Lindblad resonances are given by

$$R_\mathrm{L} = \left(1 \pm \frac{1}{m}\right)^{2/3} R_\mathrm{p}\,, \tag{1.4}$$

with the orbital radius of the planet R_p. Since the forcing frequency matches a natural frequency of the gas, the disc feedback is strong at the Lindblad resonances and density waves

are excited. Waves excited at the inner Lindblad resonances (minus sign in eq. 1.4) carry negative angular momentum away from the planet, while waves excited at the outer Lindblad resonances (plus sign in eq. 1.4) carry positive angular momentum. As the waves damp, they deposit their angular momentum in the disc, causing fluid elements in the inner and outer part of the disc to move away from the planet. The superposition of all these waves, launched at the various Lindblad resonances, form the one-armed spiral structure seen in the upper panel of Fig. 1.4 (Ogilvie and Lubow, 2002). For a detailed calculation of the torques at the resonances I refer to Goldreich and Tremaine (1979) and Meyer-Vernet and Sicardy (1987).

Another natural frequency of the gaseous disc is the corotation frequency, where the angular frequency Ω of the gas matches the angular frequency of the planet Ω_p, giving rise to the corotation torque. As pointed out by Paardekooper and Papaloizou (2008), this corotation torque is non-linear and cannot be treated in a linear analysis. An alternative view of the corotation torque was developed by Ward (1991) by considering the interaction between the planet and fluid elements on horseshoe orbits close to the planet. This corotation torque or horseshoe drag[15] depends on the vortensity gradient (vorticity divided by surface density) (Ward, 1991)[16] and the entropy gradient (Paardekooper and Mellema, 2006; Baruteau and Masset, 2008). In the reference frame corotating with the planet fluid elements on an orbit larger than the planet approach it from the front since their rotational frequency is lower than the planet's rotational frequency. Through the interaction with the planet the orbit of these approaching fluid elements is changed to an orbit interior of the planet with a higher rotational frequency. Therefore they perform a U-turn in front of the planet (similar they also perform a U-turn behind the planet). Since the entropy is conserved on streamlines in an adiabatic disc (a similar argument holds for isothermal, inviscid discs, where the vortensity is conserved on streamlines) a cold fluid element approaching the planet from the front ends up after the U-turn in a region where, assuming a negative entropy gradient, the gas is hotter. To maintain the local pressure equilibrium and conserve entropy the density of the fluid element has to increase. Therefore a region of higher density builds up in front of the planet. Similar a region of low density is created behind the planet. The asymmetry of these high and low density regions before and behind the planet gives rise to a strong positive corotation torque, capable of counteracting the Lindblad torque.

Although the corotation torque can, under the right conditions, counteract the Lindblad torque and drive an outward migration of the planet, in general planets tend to migrate inwards. Furthermore, different libration times, the time to execute one horseshoe orbit, of fluid elements on different orbits introduce a mixing effect which flattens the vortensity and entropy gradient, eventually leading to a saturation of the corotation torque. Viscosity in the case of vortensity and thermal diffusion in the case of the entropy can maintain the gradients. Viscosity supplies "new" angular momentum to the corotation region which then can interact with the planet.

Since in this work two-dimensional simulations in polar coordinates (R, φ) are conducted, the following discussion will be restricted to this special case. Three-dimensional variables, like the gas density ϱ or pressure p, are averaged over the z direction to obtain two-dimensional variables, like the surface density Σ or the vertical integrated pressure P. Power law scalings are assumed for the surface density $\Sigma(R) \propto R^{-\alpha}$ and the midplane temperature $T(R) \propto R^{-\beta}$. The disc is further characterized by the pressure scale height $H = c_s/\Omega$ with the sound speed c_s and the Keplerian frequency Ω. The aspect ratio is defined as $h = H/R$. The torque on a

[15] To distinguish it from the linear corotation torque.

[16] This scaling with vortensity was already derived through linear analysis by Goldreich and Tremaine (1979).

planet with mass m_p, on an orbit with radius R_p around a central star of mass M_*, scales with the factor

$$\Gamma_0 = \left(\frac{m_\mathrm{p}}{M_*}\right)^2 \left(\frac{H}{R_\mathrm{p}}\right)^{-2} \Sigma_\mathrm{p} R_\mathrm{p}^4 \Omega_\mathrm{p}^2 \,, \tag{1.5}$$

where a subscript p refers to the planet's location, and Σ_p is the unperturbed surface density at the planet's location. The torque scales with the planet's mass squared, one factor coming from the density perturbation in the disc through the planet and the other one from the back reaction of the spiral wave onto the planet. The opening angle of the spiral arm is directly proportional to the temperature in the disc, with lower temperatures leading to a tighter spiral and vice versa. Since for a lower opening angle the overdensities in the spiral arms are closer to the planet, the torque on the planet is stronger. The temperature is proportional to h^2 and therefore the torque scales with $\Gamma_0 \propto 1/T \propto h^{-2}$.

A first semi-analytical expression for the strength of the torques on the planet in an isothermal disc was given by Tanaka et al. (2002). D'Angelo and Lubow (2010) simulated a planet in a three-dimensional locally isothermal disc ($T \propto R^{-\beta}$) and calculated the torques acting on the planet. Paardekooper et al. (2010) calculated the torque for non-isothermal planetary migration in a two-dimensional disc. In the locally isothermal limit they find a total torque of

$$\Gamma/\Gamma_0 = -(2.5 - 0.5\beta - 0.1\alpha)\left(\frac{0.4}{\varepsilon}\right)^{0.71} - 1.4\beta\left(\frac{0.4}{\varepsilon}\right)^{1.26} + 1.1\left(\frac{3}{2} - \alpha\right)\left(\frac{0.4}{\varepsilon}\right) \,, \tag{1.6}$$

where the first term is the Lindblad torque, the second term is due to the entropy related corotation torque and the third term is due to the vortensity related corotation torque. The factors $(0.4/\varepsilon)$ account for the smoothing of the planet's potential, necessary for the correct treatment of a vertically extended three-dimensional disc in a two-dimensional approximation (Müller et al., 2012). The smoothed potential is given by

$$\Phi_\mathrm{p}(\mathbf{R}) = -\frac{G m_\mathrm{p}}{\sqrt{(\mathbf{R} - \mathbf{R}_\mathrm{p})^2 + (\varepsilon H)^2}} \,, \tag{1.7}$$

with a value ε typically between 0.4 and 0.6.

1.4.2 Type II migration

When the planet is massive enough, typically more than one Jupiter mass, the planet can significantly alter the disc structure. The now non-linear response of the disc forms shocks, which can deposit their angular momentum flux locally in the disc. This means that gas just outside of the planet gains angular momentum and is therefore pushed outwards. Similarly, gas close to the planet, on orbits interior to the planet, loses angular momentum and is pushed inwards. Since gas is pushed away from the planet on both sides a gap in the disc forms around the planet. In order to open a gap in the disc the torque from the planet onto the disc has to overcome the viscous torque and pressure effects, both tending to close the gap. Taking both effects into account, Crida et al. (2006) derived the following gap open criteria

$$\frac{3}{4}\frac{H}{R_\mathrm{H}} + \frac{50\nu}{q a_\mathrm{p}^2 \Omega_\mathrm{p}} \leq 1 \,, \tag{1.8}$$

with the Hill radius R_H, the planet-to-star mass ratio q, and the dynamical viscosity coefficient ν.

If a planet has opened a gap in the disc the corotation and Lindblad torques are strongly reduced due to the reduced disc mass around the planet. In this case the migrating planet is coupled to the disc, since the one-sided Lindblad torques will push the planet back to the centre of the gap if the planet migrates too close to either of the gap edges. Due to the viscosity the gap slowly migrates inward on the viscous timescale, dragging the planet with it (Lin and Papaloizou, 1986). This picture assumes that there is no mass flow across the gap. Simulations show that this is not true (see lower panel of Fig 1.4). Recently, Dürmann and Kley (2015) showed that the migration rate can be faster or slower than the viscous rate, depending on the local disc mass, when the planet is able to accrete gas.

1.5 Numerics and GPU computing

The migration process of circumbinary planets, embedded in an accretion disc, is studied via hydrodynamical simulations. To simulate the circumbinary disc, the Navier-Stokes equations are solved. This set of equations, describing viscous fluid flow, is given in conservation form by

$$\frac{\partial}{\partial t}\begin{pmatrix}\varrho\\ \varrho\mathbf{v}\\ \varrho e\end{pmatrix}+\boldsymbol{\nabla}\cdot\begin{pmatrix}\varrho\mathbf{v}\\ \varrho\mathbf{v}\otimes\mathbf{v}-\boldsymbol{\Pi}+\mathbf{I}p\\ (\varrho e+p)\,\mathbf{v}-\boldsymbol{\Pi}\cdot\mathbf{v}\end{pmatrix}=\begin{pmatrix}0\\ \varrho\mathbf{g}\\ \varrho\mathbf{v}\cdot\mathbf{g}\end{pmatrix}. \tag{1.9}$$

The first row describes the conservation of mass, the second the conservation of linear momentum and the third the conservation of energy. The derivation of this set of equations can be found in standard textbooks, for example Landau and Lifshitz (1959). The gas density is given by ϱ, the pressure by p and the velocity by $\mathbf{v}$. Furthermore, the specific total energy is given by $e=\frac{1}{2}\mathbf{v}^2+\varepsilon$ consisting of the kinetic energy term and the specific internal energy ε. The external force on the gas, for example the gravitation from the binary and the planet, is given by $\mathbf{g}$. The symbol $\mathbf{I}$ denotes the identity matrix and the viscous stress tensor $\boldsymbol{\Pi}$ is given by

$$\boldsymbol{\Pi}_{ij}=2\eta\left[\frac{1}{2}\left(v_{j;i}+v_{i;j}\right)-\frac{1}{3}\delta_{ij}(\boldsymbol{\nabla}\cdot\mathbf{v})\right]+\zeta\left(\boldsymbol{\nabla}\cdot\mathbf{v}\right)\delta_{ij}\,, \tag{1.10}$$

with the coefficient of dynamical viscosity η and the coefficient of bulk viscosity ζ. All simulations in this work use a zero bulk viscosity. To close the system, the ideal gas law is applied, which models the gas molecules as point masses that interact only through perfectly elastic collisions. This approximation, which neglects short range intermolecular forces and the volume of the individual molecules, is applicable in most astrophysical scenarios, where one typically deals with rarefied gases. The equation of state for the ideal gas reads

$$p=\frac{k_\mathrm{B}}{\mu m_\mathrm{H}}\varrho T\,, \tag{1.11}$$

with the temperature T, the Boltzmann constant $k_\mathrm{B}=1.380\,648\cdot10^{-23}\,\mathrm{J\,K^{-1}}$, the mass of the hydrogen atom $m_\mathrm{H}=1.661\cdot10^{-27}\,\mathrm{kg}$ and the mean molecular mass of the gas μ. For an ideal gas the temperature is connected to the specific internal energy by

$$\varepsilon=c_v T\,, \tag{1.12}$$

with the specific heat capacity at constant volume c_v.

1.5.1 Disc model

All simulations presented in this thesis use cylindrical coordinates (R, φ, z), centred at the centre of mass of the binary. This is a natural choice for modelling accretion discs, since the cylindrical geometry is adapted to the problem and conservation of angular momentum is easily achieved. This choice of coordinate system comes with the drawback of an inner hole in the computational domain, due to the coordinate singularity at the origin. In this thesis the optimal location of this inner radius and the correct choice of boundary conditions are studied in great detail. To simplify the simulations the following assumptions are made:

1. The height H of the disc is small compared to the radial extend of the disc $H/R \ll 1$ and the vertical velocity v_z is zero. These two assumptions are justified by the flatness of the Kepler circumbinary systems and allow the reduction of the problem from three to two dimensions. This reduction is done by averaging relevant quantities vertically:

$$Q(R, \varphi) = \int_{-\infty}^{-\infty} q(R, \varphi, z) \, \mathrm{d}z \, . \tag{1.13}$$

   This process is sketched in Fig. 1.5. In two dimensions the important variables are: the surface density Σ, the two-dimensional velocity vector $(v_R, v_\varphi)^{\mathrm{T}}$, the vertically integrated pressure P and the midplane temperature T.

2. The disc can efficiently radiate away any heat created through viscous friction. This assumption justifies the use of a locally isothermal equation of state, which means that the temperature does not evolve in time and is a function of radius only $T = T(R)$. This assumptions simplifies the calculation enormously since the energy equation in (1.9) can be replaced by the simple relation $P = c_\mathrm{s}(R)^2 \Sigma$, with the sound speed $c_\mathrm{s}(R)$.

3. An unspecified turbulence mechanism exists in the disc to create an effective viscosity. This effective viscosity is modelled by the α-viscosity ansatz by Shakura and Sunyaev (1973), where the kinematic viscosity is given by $\nu = \alpha c_\mathrm{s} H$ with $\alpha < 1$. This basically states that the turbulent eddies in the disc cannot be larger than the disc's height and are subsonic (supersonic eddies would be damped fast through shock dissipation).

4. Self-gravity of the disc is not considered important. For typically disc masses in this work of $M_\mathrm{disc} = 0.01 \, M_\mathrm{bin}$ the Toomre parameter (Toomre, 1964)

$$Q = \frac{c_\mathrm{s} \Omega}{\pi G \Sigma} \, , \tag{1.14}$$

   measuring strength of gravity against thermal pressure, is always greater than one. A Toomre parameter greater than one indicates that the disc is stable against self-gravity.

A detailed description of the physical and numerical model used for the simulations in this thesis can be found in Thun et al. (2017) and Thun and Kley (2018).

1.5.2 The PLUTO code

Most of the simulations in this work were conducted with a modified version of the open source code Pluto (Mignone et al., 2007)[17] which is able to run on graphics processing

[17] The modified version is based on the Pluto 4.2 version. The actual version of Pluto can be downloaded at `http://plutocode.ph.unito.it/`, accessed 26 November 2018.

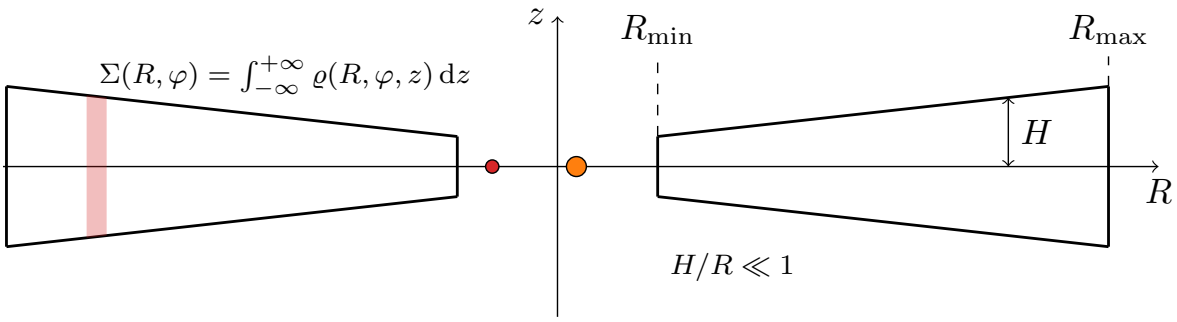

Figure 1.5: Sketch of the disc model with the averaging process indicated for the three-dimensional density ϱ. The orange circle marks the primary and the red circle the secondary star of the Kepler-38 system, the sizes are proportional to the stellar masses. The origin of the coordinate system lies at the centre of mass of the binary. The radial extend of the computational domain is marked by R_{min} and R_{max}. Typically the binary is not part of the computational domain.

units (GPUs). Pluto is based on a shock-capturing Godunov scheme. In addition two other hydrodynamical codes, namely Rh2d (Kley, 1989, 1999) and Fargo/Fargo3D (Masset, 2000; Benítez-Llambay and Masset, 2016), which both are based on a finite difference scheme, were used. This approach strengthens the results and identifies possible numerical artefacts. Since in the framework of this thesis the hydrodynamical module of Pluto was adapted to run on GPUs, to significantly speed up the calculations, the rest of this subsection will briefly discuss the numerical method behind Pluto.

The code Pluto solves a system of partial differential equations in conservation form

$$\frac{\partial}{\partial t}\mathbf{U} + \boldsymbol{\nabla}\cdot\mathbf{T}(\mathbf{U}) = \mathbf{S}(\mathbf{U})\,, \tag{1.15}$$

where $\mathbf{U}$ is the vector of conservative variables, $\mathbf{T}(\mathbf{U})$ is a rank 2 tensor, containing the fluxes and $\mathbf{S}(\mathbf{U})$ is a vector containing source terms like an external gravitational field or additional terms from curvilinear coordinates. In the case of this work, the hydrodynamical module of Pluto was used to numerically solve the Navier-Stokes equations (1.9).

To solve these equations, Pluto uses the finite volume method, where cell averages are evolved in time. First the computational domain is covered by a grid and in each cell the continuous quantities of the gas are averaged (see upper panel of Fig 1.6). This discrete average, defined at the cell centre can only change, according to eq (1.15), through a flux of the appropriate quantity in or out of the cell. The numerically difficult part is to calculate the fluxes through the cell interfaces. To do so, first the cell averages are interpolated to the cell interfaces (second panel of Fig. 1.6). This interpolation yields a discontinuity on the left and right side of each interface. Such an initial value problem is known as the Riemann problem and a semi-analytical solution is possible which involves a combination of different waves (shocks, rarefaction waves and contact discontinuities, see third panel of Fig 1.6). The flux through the interface can be calculated with the help of the Riemann problem's solution. Typically not all information gained from a full solution of the Riemann problem are needed, therefore often an approximate solution to the Riemann problem is calculated to speed up the computation. For a detailed discussion of exact and approximate Riemann solvers see the

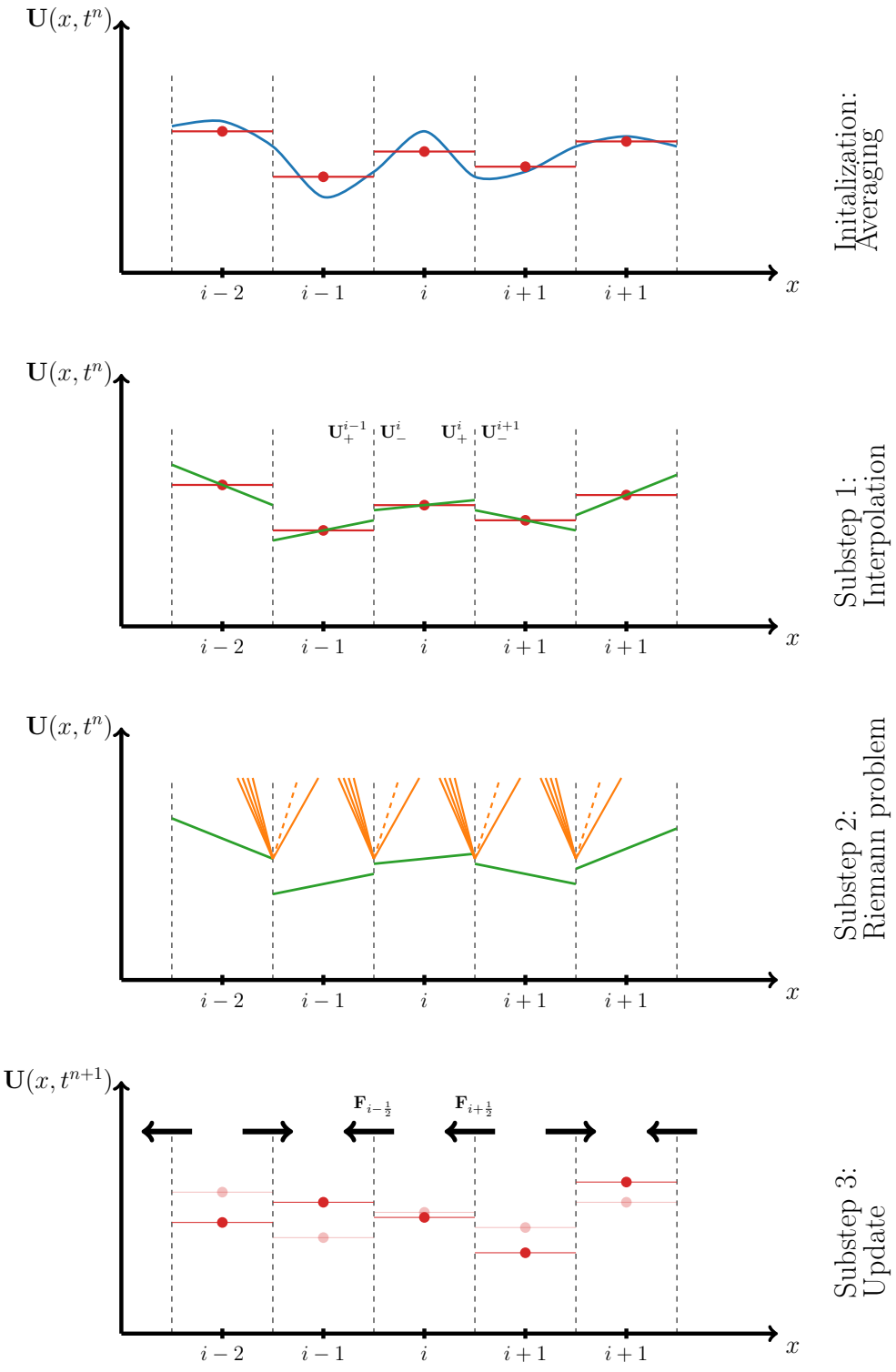

Figure 1.6: Sketch of the numerical strategy of Pluto. The upper panel shows the initial discretization of the gas quantities through averaging over the cells. The second panel shows the interpolation substep, where the cell averages are interpolated (here linear) to the cell interfaces. The third panel shows the solution of the Riemann problem at each interface. Finally in the last panel the discrete quantities are updated with the interface fluxes.

book by Toro (2009). Finally the cell averages are updated with the help of the interface fluxes calculated in the previous step (see last panel of Fig. 1.6). For a more in depth description of the numerical method see Mignone et al. (2007) and the PLUTO User's Guide[18].

1.5.3 GPU architecture

A recent development in high performance computing is to exploit the power of GPUs for scientific applications. GPUs were originally designed for efficient image and computer graphics processing, where the manipulation of large data chunks is needed. For example the rotation of a computer graphic scene requires to perform the same transformation to millions of vertices. Therefore GPUs are optimized for data parallel tasks. Contrary, CPUs are designed to complete different tasks as fast as possible. CPUs are low latency[19], low throughput[20] processors. Whereas GPUs are high latency, high throughput processors. CPUs achieve their low latency with a sophisticated flow control and the help of caches (fast, on-chip memory) to hide the limited memory bandwidth. GPUs achieve their high throughput by dedicating most of their transistors to data processing, rather than caching and flow control. Since on all data elements the same set of instructions is performed no sophisticated flow control is needed. Furthermore, no large caches are needed since the memory latency can be hidden by switching to another group of threads whose data is already available. This architecture is called single instruction multiple data (SIMD). Not just graphic processing problems are prone to this architecture. Solving the hydrodynamical equations on a grid is a perfect example of how the SIMD architecture can be utilized for non graphical problems. To advance the solution by one time step, the operations for the three substeps (discussed in Sec. 1.5.2, single set of instructions) have to be performed on each grid cell (multiple data).

The most advanced interface for general purpose GPU programming is CUDA[21] from Nvidia. The CUDA toolkit provides compiler, development tools, GPU-accelerated libraries and the CUDA runtime to harness the power of GPUs. Functions which are executed on the GPU have to be written in a special language called CUDA-C, an extension to the C programming language. The drawback, is of course, that programs written with the CUDA framework are restricted to Nvidia GPUs. Nvidia GPUs consist of a global memory (comparable to the RAM in a CPU server) and an array of Streaming Multiprocessors (SMs). For example the Nvidia Tesla K40, used for most of the simulations in this work, has a global memory of 12 Gbyte and 13 SMs. A Streaming Multiprocessor consists of thousand of registers, a fast on-chip memory (called shared memory), and so called CUDA cores, which perform the actual calculation. In case of the K40 one SM has 192 CUDA cores each with a clock rate of 824 MHz.

The CPU, called host, controls the GPU, called device. The CPU is responsible for the overall program flow, like copying data to and from the global GPU memory or the launching of GPU functions called kernels. Kernels are executed in parallel on the GPU by a given number of threads. When the CPU launches a kernel on the GPU the number of threads can be specified, which then are grouped into blocks. Each block is then executed independently from the other blocks on a SM. The number of blocks which can be executed at the same time on one SM depends on the resources (registers and shared memory) that the kernel needs. This gives the opportunity for some problem dependent optimizations and Nvidia provides tools to find the optimal number of threads inside a block for a special kernel. This division in

[18] `http://plutocode.ph.unito.it/userguide.pdf`, accessed 26 November 2018.
[19] Latency is the time between initiating something and seeing a result.
[20] Throughput is the number of completed tasks per unit time.
[21] CUDA was an acronym for Compute Unified Device Architecture.

independent blocks allows an automatic scalability, since GPUs with more SMs can execute more blocks at the same time, thus reducing the overall execution time of the program.

Threads within a block can cooperate via the on-chip shard memory. To avoid race conditions, threads within a block can be synchronized. The use of shared memory also minimizes the access to the global memory, reducing the memory latency. Threads inside a block are grouped into warps, 32 threads are one warp. Switching between different warps causes no overhead. Therefore memory latency can be hidden by switching to another warp, whose data is already available. Threads within a warp are always at the same instruction address, this has the consequence that different execution paths inside a warp are serialized. Therefore branching of threads inside a warp should be avoided. To fully use the potential of the GPU the programmer should use the on-chip shared memory and keep in mind the grouping of threads into warps. A detailed description of the GPU architecture and the CUDA C programming model can be found in the Nvidia CUDA Toolkit Documentation[22].

1.5.4 The GPU version of PLUTO

In the framework of this thesis the hydrodynamical module of the Pluto code was ported to run on Nvidia GPUs to speed up the various simulations. Analysing the performance of the CPU version revealed, not surprisingly, that most of the time (roughly 78%) is spend in the three substep routines. It is therefore advisable to perform the whole calculation on the GPU. This has in addition the advantage that data transfer between the CPU and the GPU, the strongest bottleneck in GPU computing, is limited to when data output is required. A drawback of this approach is that every function involved in the calculation has to be ported to CUDA-C. Furthermore, two versions of every function, a CPU version and a GPU version, have to be maintained. Fargo3D (Benítez-Llambay and Masset, 2016) follows another approach to avoid these two drawbacks by making use of a special scripting language to translate C to CUDA-C. The disadvantage here is the loss of transparency, since all control over the code is given to the translation script. At the end of the day, the preferred approach is a decision of personal taste.

The CUDA-C implementation of all three substeps follows one general approach, which will be sketched in the following. As an example the (linear) interpolation step in the x-direction is presented. The example computational domain has two ghost cells on each side (this is determined by the used interpolation) and a size of 17×13 cells (see upper panel of Fig. 1.7). First the active computational domain is identified, which, in the example case, is given by the dashed blue rectangle in the upper panel of Fig. 1.7. The tuple `(domBeg.x, domBeg.y, domBeg.z)` marks the indices of the lower left cell of the active computational domain, here (1,2,0), and the tuple `(domEnd.x, domEnd.y, domEnd.z)` marks the upper right cell, here (15,10,0). Inside all cells of the marked region the cell centred value has to be interpolated to the x-interfaces. When the CPU calls the interpolation kernel, first the active computational domain is divided into blocks of threads (red squares in the lower panel of Fig. 1.7, blocks of 4×4 threads are used to cover the active domain). The number of blocks is chosen in a way that all cells in the active computational domain are covered by one thread. Most of the time this leads to an overlap, threads not assigned to a cell of the active domain stay inactive for the rest of the calculation. Each thread inside a block has an unique identification number which can be accessed through the tuple `(threadIdx.x, threadIdx.y, threadIdx.z)` provided by the CUDA runtime. Each thread knows in addition the unique identification number

[22] `https://docs.nvidia.com/cuda/index.html`, accessed 22 November 2018.

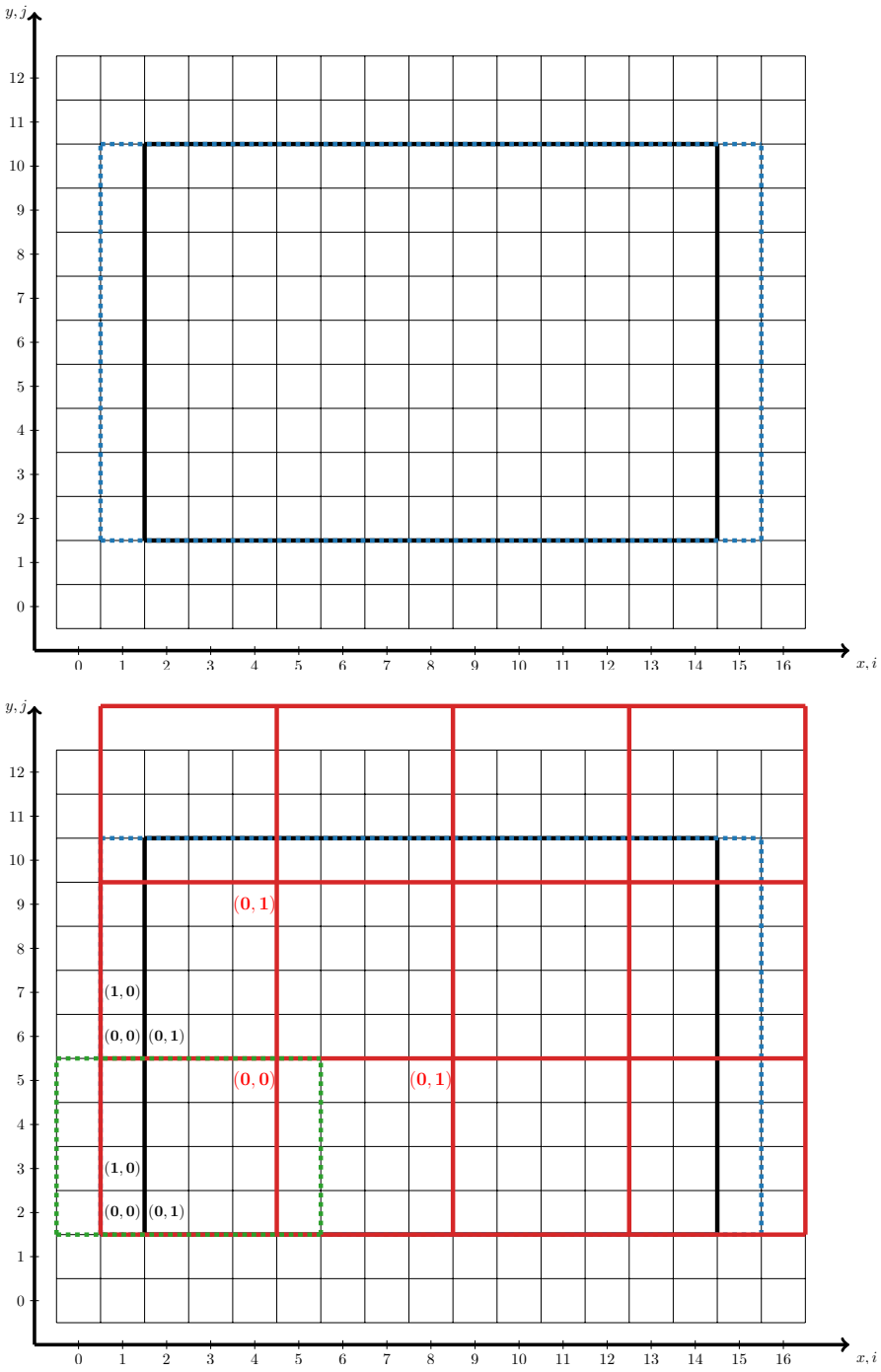

Figure 1.7: *Top panel:* The two-dimensional computational domain with two ghost cells at each side. The bold rectangle marks the part of the computational domain where the hydro quantities are evolved in time. The dashed blue rectangle shows the active computational domain. Within each cell of the active computational domain a linear interpolation to the x-interfaces has to be calculated. *Bottom panel:* Shown is how two-dimensional CUDA blocks cover the active computational domain (red squares). Furthermore, for some blocks the internal numbering as well as the numbering of single threads inside a block are displayed. The green dashed rectangle shows which cells of the global grid are loaded into the shared memory of block $(0, 0)$.

of its block `(blockIdx.x, blockIdx.y, blockIdx.z)` as well as the dimensions of its block `(blockDim.x, blockDim.y, blockDim.z)`. This unique thread identification number is used to calculate the cell in the global grid, which is assigned to the thread. Looking at the lower panel of Fig. 1.7 thread (0,0) of block (0,0) is assigned to cell (1,2) of the global grid. Given the lower left edge of the active domain each thread can calculate the indices (i, j, k) of its cell, for example `i = threadIdx.x + blockIdx.x * blockDim.x + domBeg.x`.

To calculate the interface values through a linear interpolation, each thread needs, besides the data of its own cell, also the data from the cells adjacent to the left and right. To minimize data reads from global memory each thread first loads the data from its cell to the assigned shared memory part of its block (threads at a block boundary also load an additional left or right value to the shared memory). The dashed green rectangle in the bottom panel of Fig. 1.7 marks the cells of the global grid which are loaded into the shared memory of block $(0, 0)$. After the data loading process the actual calculation begins. It is important to assure that all threads loaded their data to the shared memory before the calculation starts to avoid race conditions. Finally each thread writes its results back to the global memory, so that they can be used in the next step.

In summary a typically PLUTO kernel consists of the following steps:

1. Identification of the active computational domain (described by the index of the lower left corner and the upper right corner).
2. Calculation of the required blocks to cover the active computational domain by threads. Threads not assigned to a cell are inactive.
3. Each thread calculates the cell indices of its assigned cell with the help of its unique identification number.
4. Each thread loads data from its cell to the shared memory of its block to minimize access to the global memory.
5. Synchronization between the threads of one block, to avoid race conditions.
6. Performing the actual calculation.
7. Writing the results back to global memory of the GPU.

1.5.5 Validation and performance of the GPU version of PLUTO

The GPU implementation was extensively tested against the CPU version using well known test problems. A common test for hydrodynamical codes are fluid instabilities, like the Kelvin-Helmholtz instability, a shear instability which arises at the interface between two streams of different densities and velocities. Fig. 1.8 shows the comparison of the CPU and GPU versions for the Kelvin-Helmholtz test problems. The problem was setup according to Springel (2010, Sec. 8.7) with an initial vertical velocity perturbation to trigger a main mode of the instability. The results of the codes are in very good agreement. The relative error between the CPU and GPU version of the code is of the order of 10^{-12}. Fig. 1.9 shows the strong scaling in case of the two-dimensional Kelvin-Helmholtz test problem with a high resolution of 4096×4096 grid cells. The strong scaling measures how the execution time decreases when more cores or GPUs are involved in the calculation of a problem with fixed size. Since for all simulations presented in this thesis a fixed grid resolution was used, the strong scaling is the preferred

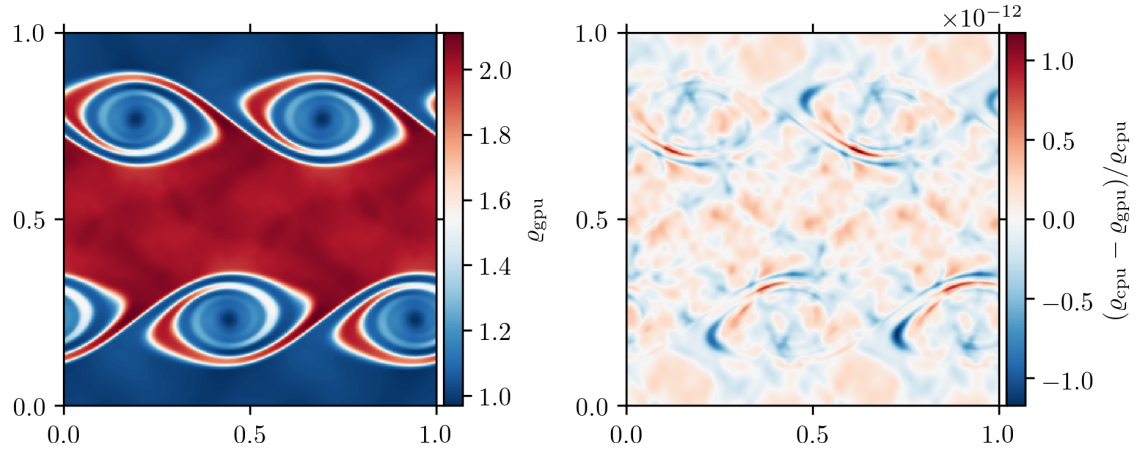

Figure 1.8: Comparison of CPU and GPU version of Pluto for the Kelvin-Helmholtz test problem on a grid with 500×500 cells. The left panel shows the density distribution of the GPU version after two time units. The right panel shows the relative error in density between the two code versions also after two time units.

metric to measure the speed-up of the GPU version of Pluto compared to the CPU version. The scaling was done on a cluster with two Nvidia K80 GPUs per node. One K80 consists of two Nvidia GK210 chips (basically, a K80 consists of two glued together K40), which can be used separately. This means one GPU node has access to four GPUs. The scaling for the CPU version was calculated on nodes consisting of 28 Intel Xeon E5-2690 (2.40 GHz) processors, divided onto 2 sockets. As one can see the scaling is almost linear up to four GPUs (speed-up factor 3.69) but drops significantly as soon as inter-node communication is required. In comparison to the CPU version of the code, four GPUs already outperform 112 CPU cores (four CPU nodes). Extrapolating the average time per step for one core (assuming a perfect linear scaling) and comparing this value with the average time per step of one GPU, a speed-up of 47 is achieved. Fig. 1.10 presents the scaling of different Nvidia GPU generations for a simulation of the Kelvin-Helmholtz instability. Shown is the average time per step plotted against increasing number of grid cells. As discussed above, at the beginning of each GPU calculation the computational domain is divided into blocks which need to run independently. Each block is then assigned to a Streaming Multiprocessor (SM), the building blocks of a GPU. This architecture guarantees scalability since more blocks can be executed simultaneously on GPUs with more SMs. This automatic scalability can be seen in Fig. 1.10 where, as expected, the modern GPUs easily outperform older models without any changes to the code. The legend in Fig. 1.10 shows the GPUs ordered according to their power in decreasing order. Nvidia has two GPU lines: Consumer cards, designed mainly for video games, and professional cards for the high performance sector. The professional cards use error-correcting code (ECC) memory. This feature can be turned on and off and has a small influence on the performance (compare the orange and the blue curve in Fig. 1.10).

The Sedov blast problem, the propagation of a strong shock due to an explosion, is another standard hydrodynamical test problem. The initial density was set to one in the whole computational domain and the initial pressure to 10^{-5}. At time zero an energy of unity was inserted around the origin. The adiabatic index γ was set to 1.4 throughout the calculation. The left panel of Fig. 1.11 shows a radial cut through the two-dimensional computational domain along the x-axis after 0.5 time units. The results of both code versions as well as the

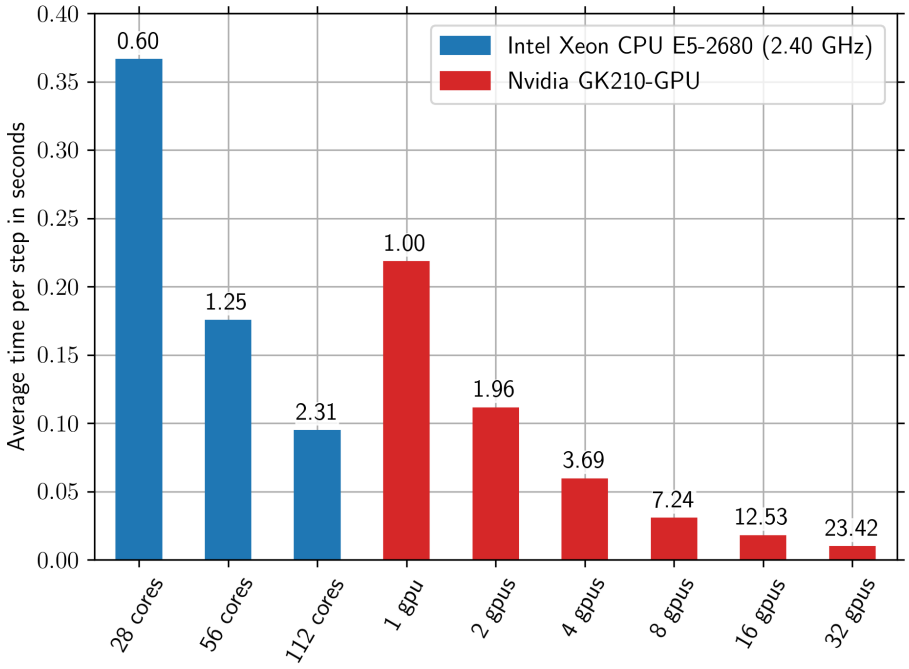

Figure 1.9: Strong scaling of the two-dimensional Kelvin-Helmholtz test problem, on a grid with 4096×4096 cells. The speed-up factor, shown above each column, is calculated relative to the speed of one GPU.

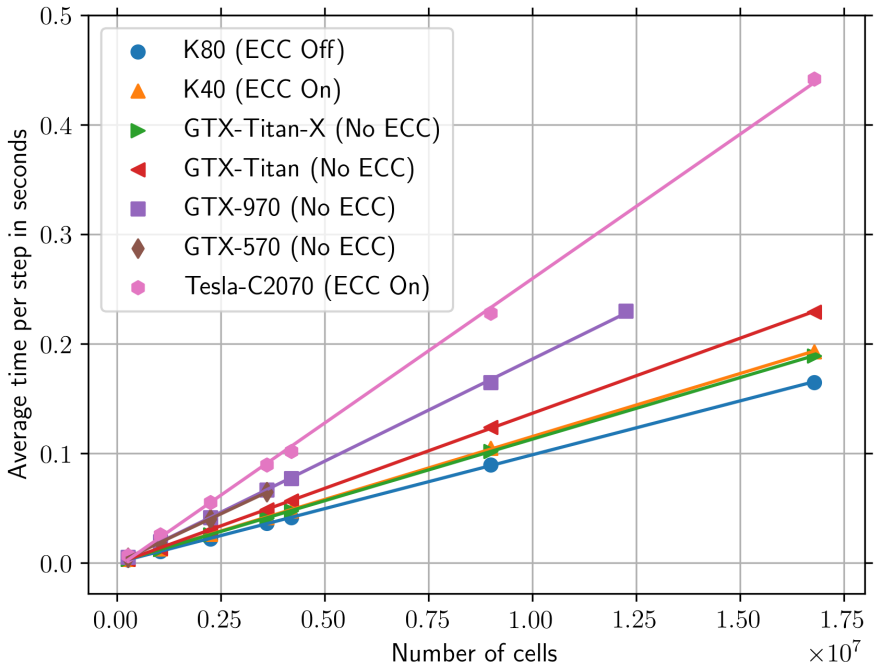

Figure 1.10: Scaling of different Nvidia GPU generations for the two-dimensional Kelvin-Helmholtz test problem. Since the memory is limit on some GPUs not all grid sizes could be calculated on each GPU. The GPUs are ordered according to their power in decreasing order.

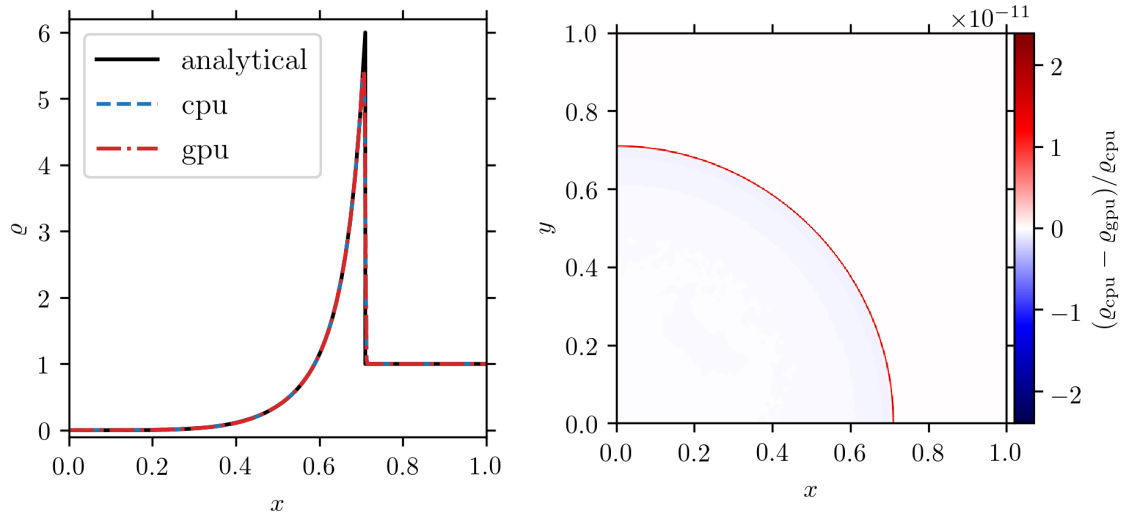

Figure 1.11: Comparison of CPU and GPU version of Pluto for the Sedov test problem on a grid with 500 × 500 cells. The left panel shows a radial cut through the two-dimensional computational domain along the x-axis after 0.5 time units. The right panel shows the relative error in density between the two code versions after 0.5 time units.

analytical solution is shown, which are all in very good agreement. For a discussion of the analytical solution see Landau and Lifshitz (1959). The right panel of Fig. 1.11 displays the relative error in density between the CPU and GPU version after 0.5 time units. Both codes differ only by a factor of 10^{-11} along the shock front. The strong scaling of the Sedov blast test problem in two and three dimensions is presented in Fig. 1.12. The two-dimensional problem uses a grid of 4096×4096 cells and the three-dimensional problem uses a grid of $250 \times 250 \times 250$ cells. Extrapolating again the average time per step for one core and comparing this value with the average time per step of one GPU, one arrives at a speed-up of 53 for the two-dimensional problem and a speed-up of 42 for the three-dimensional problem. The numbers in parenthesis indicate in which dimension the domain decompositions was done. In case of two-dimensional simulations the domain decompositions does not play an important role. This changes in three-dimensional simulations (see lower panel in Fig. 1.12). It is better to decompose the computational domain only in the X2 and X3 direction, since the performance of the code drastically drops when also the first dimension (X1) is divided. As soon as more than one GPU is used for the calculation, the GPUs have to communicate the boundary values of their subdomains. To do so they have to copy this data back to their controlling CPUs, which then exchange the data and copy it back to the GPUs. In general it is favourable to copy large chunks of data. To understand the performance drop, one has to look at how the boundary values are stored in memory. Fig. 1.13 shows this for a two-dimensional example. Pluto stores more dimensional grids line by line in memory. This means that the boundaries of the second dimension are stored consecutive in memory (orange shading in Fig. 1.13), whereas the boundary values of the first dimension are scattered in small parts throughout the memory (blue shading in Fig. 1.13). To exchange the boundary values the orange parts can be copied as one chunk to the CPU whereas many little copy operations have to be done for the blue parts. In three dimensions the most scattered boundary is again the first dimension, explaining the large performance drop when these values have to been exchanged.

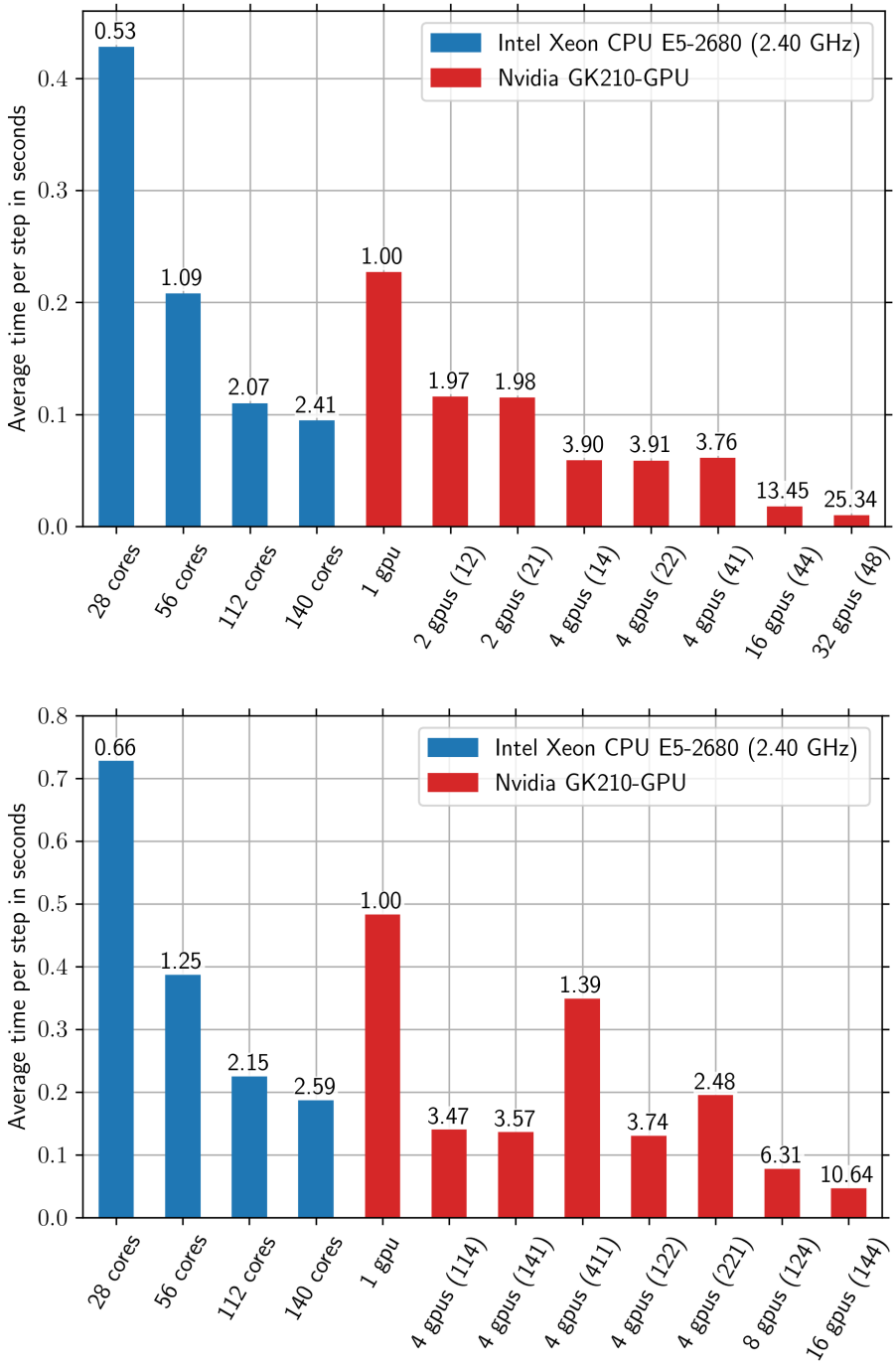

Figure 1.12: Strong scaling of the two-dimensional (upper panel) and three-dimensional (lower panel) Sedov blast test problem. The numbers in parentheses indicate the domain decompositions, for example (21) means that the decomposition was only done in the first dimension, whereas for (22) the domain was decompositions into 4 equal parts. The speed-up factor, shown above each column, is calculated relative to the speed of one GPU.

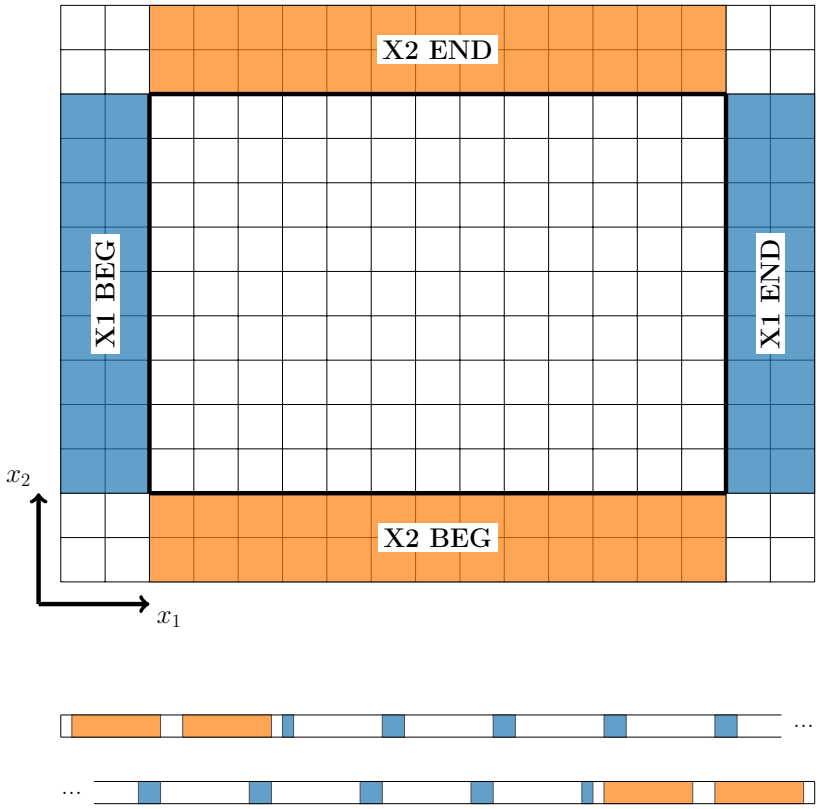

Figure 1.13: Two-dimensional grid and linear memory layout. PLUTO stores more dimensional problems line by line in memory. This leads to the shown linear memory layout. The blue and orange shaded regions show the ghost cells in the first (blue) and second (orange) dimension. The value in these ghost cells are exchanged between GPUs in each iteration. While the orange shaded ghost cells can be copied in one large chunk the blue ones, which are scattered throughout the memory, need a lot of copy operations, slowing down the exchange.

So far the discussed test problems only tested the code for the pure hydrodynamical equations (no source terms or additional physics) on a Cartesian grid. PLUTO offers additional geometries (polar, spherical) as well as additional physics (external forces, viscosity). For brevity not all test problems for these modules will be discussed. Fig. 1.14 gives an impression of the various additional test problems. Panel A shows a high resolution calculation of the Rayleigh-Taylor instability (Springel, 2010, Sec. 8.8). Panel B shows the two-dimensional supersonic flow around a sphere in spherical coordinates. This simulation was compared to a laboratory experiment in Thun et al. (2016). Panel C compares the simulation of a viscous spreading ring to the analytical solution (Speith and Riffert, 1999; Speith and Kley, 2003). Panels D shows the classical Sod shock tube problem, the solution of a Riemann problem with a shock, a rarefaction wave and contact discontinuity (Sod, 1978). Panel E shows the interaction of two shock waves (Woodward and Colella, 1984). Panel F shows the simulation of a strong rarefaction wave (Einfeldt et al., 1991). The reflection of a Mach 10 shock from a wall is seen in Panel G (Woodward and Colella, 1984). Finally panel H shows the simulation of a Kármán vortex street in polar coordinates.

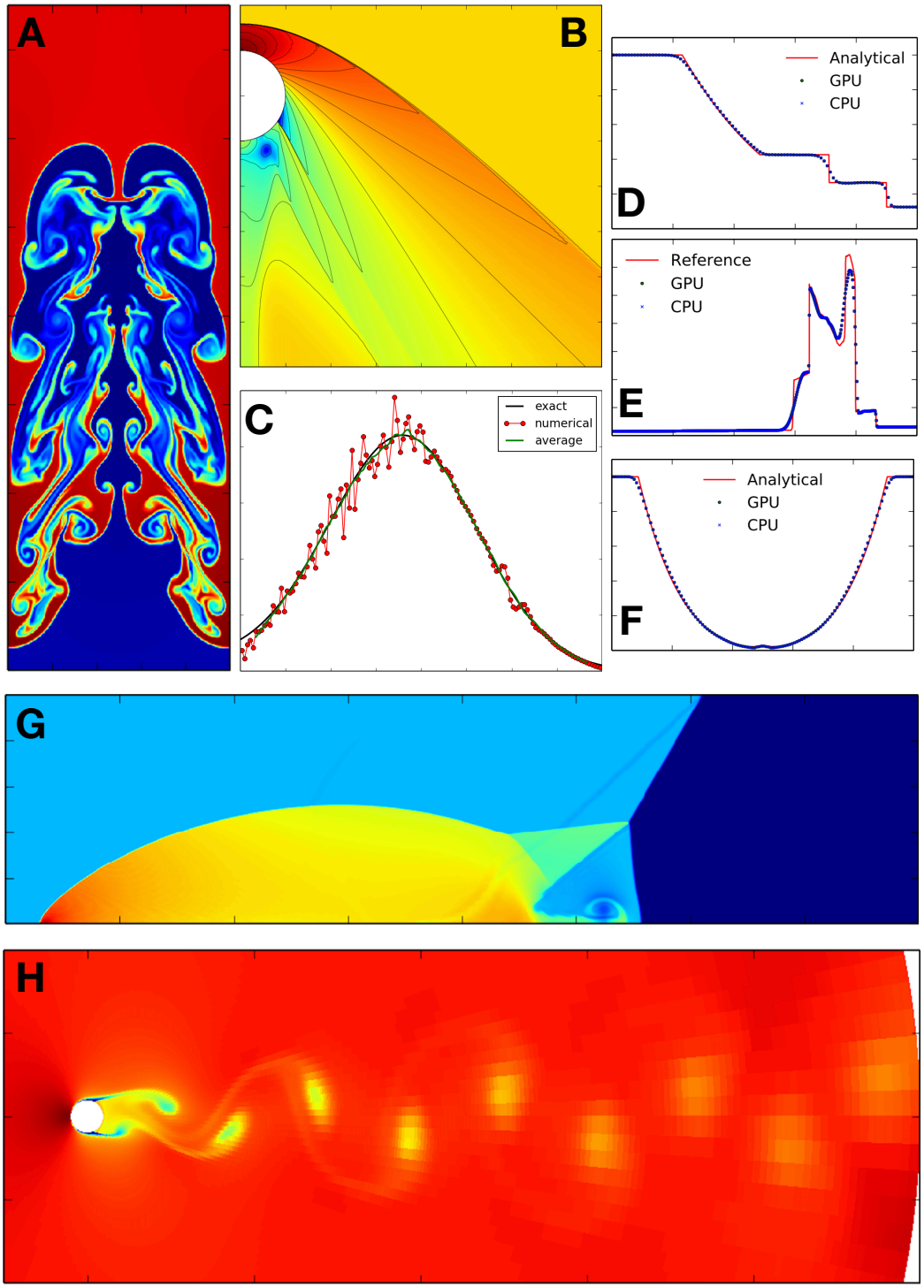

Figure 1.14: Collage of various test problems: (A) Rayleigh-Taylor instability, (B) Supersonic flow past sphere, (C) Viscous spreading ring, (D) Shock tube, (E) Strong interacting shock waves, (F) Strong rarefaction wave, (D) Reflection of a strong shock, (H) Kármán vortex street. For a short discussion and references see the text.

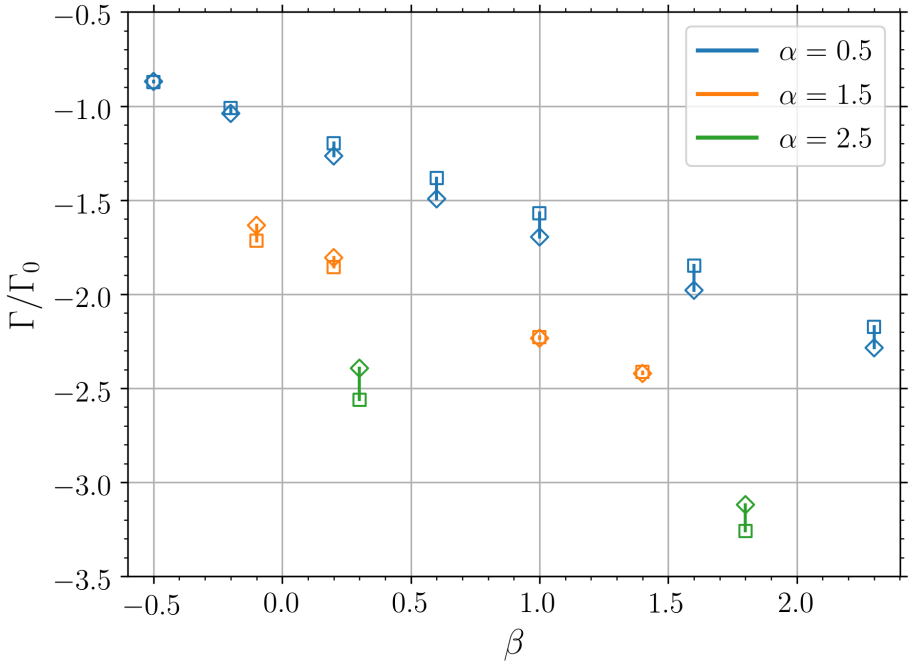

Figure 1.15: Comparison of numerical calculated torques onto a planet on a fixed circular orbit around a Solar mass star with mass ratio $q = 5.0 \cdot 10^{-6}$ to the theoretical torque (eq. 1.6). The numerical results are denoted by diamonds and the theoretical by squares. The surface density slope is given by $-\alpha$ and the midplane temperature slope is given by $-\beta$.

To test the interaction of a planet with a gaseous disc I simulated a planet on a fixed circular orbit around a Solar mass star with mass ratio $q = 5.0 \cdot 10^{-6}$. For a detailed numerical setup see Paardekooper et al. (2010). Fig. 1.15 compares the numerically calculated torque by summing the individual torques exerted by each cell onto the planet, and the torque calculated using equation (1.6). Diamonds represent the numerical results and squares the theoretical values, corresponding values are connected by a line. For the numerical result 500 planet orbits were simulated and the torque was calculated as the average over the last 200 orbits. Numerical and theoretical results are in good agreement over the whole range of simulated surface density and temperature profiles.

Numerical performance can be strongly problem dependent. Therefore Fig. 1.16 shows the strong scaling in case of a circumbinary disc simulation. The setup is discussed in detail in Thun and Kley (2018) and has a resolution of 684×584 cells. Compared to the Kelvin-Helmholtz and Sedov test problem, this test is far more sophisticated. While the previous two test problems only used the ideal hydrodynamical equations, here additional modules, like viscosity and external gravity are used. Furthermore, the geometry is not Cartesian, a polar grid is used and additional source terms, accounting for the curvilinear coordinates, have to be considered.

First, one notices that the multi-GPU scaling is not linear. The speed-up one gets by using 4 GPUs instead of one is roughly a factor of 2.9. Then, there is the question of how to compare the speed-up between the two code versions. Using the data from Fig. 1.16 to extrapolate the time one single CPU core would need and comparing this time to the single GPU time, one would arrive at a speed-up of roughly 37-39. Another metric is to compare the code

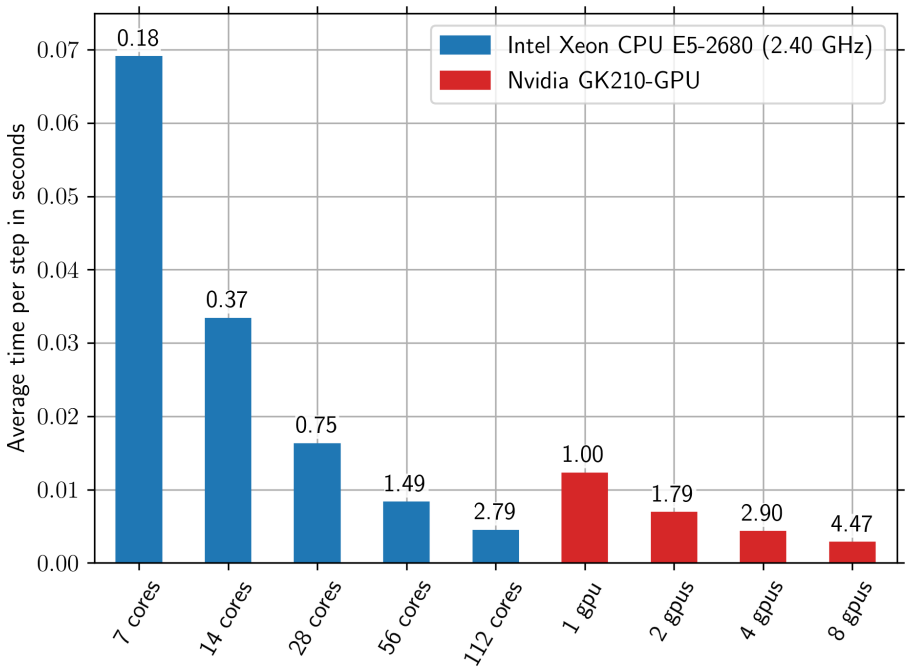

Figure 1.16: Strong scaling of an isothermal circumbinary disc around the Kepler-38 system. The speed-up factor, shown above each column, is normalized to the speed of one GPU.

performance on one compute node. The cluster on which most of the simulations in this thesis were performed, the BinAC cluster in Tübingen, offers nodes with 28 cores or 4 GPUs. Comparing the speed of 4 GPUs to 28 cores one arrives at a speed-up of approximately 3.9. This means that the GPU version of the code allows to run four times more models than the CPU version.

2 Aims

All so far detected circumbinary systems have two things in common: First, the orbit of the planet is in the same plane as the orbit of the binary and second, the planet is very close to the stability limit (see Sec. 1.3.2). The flatness of the system suggests that the planets formed in a circumbinary disc. The location of the planets close to the stability limit raises the question if the planets could have formed in situ at their observed position, since collisional growth close to the binary is complicated by its strong gravitational influence. The non-axisymmetric interaction between the binary and planetesimals leads to eccentric, precessing planetesimal orbits, which lead to high relative velocities between different mass planetesimals, resulting in destructive collisions (Scholl et al., 2007; Marzari et al., 2008). These reasons render the scenario of in situ formation highly unlikely.

A more likely scenario is the formation through collisional growth in the outer parts of the disc, far from the perturbing influence of the binary, followed by an inward migration phase to the observed location. The challenge in this scenario is how to stop the migration process at the observed position. Artymowicz and Lubow (1994) showed that through the gravitational interaction between the binary and the disc an eccentric inner gap is formed, which precesses slowly in a prograde manner around the binary. The structure of this gap (semi-major axis, eccentricity and precession period) depends on binary parameters (eccentricity and mass ratio) as well as on disc parameters (viscosity and pressure). As shown by Masset et al. (2006) and recently confirmed in three-dimensional simulations by Romanova et al. (2018), a strong density gradient can increase the corotation torque to a level where it can counteract the Lindblad torque responsible for inward migration. Therefore, the inner gap created by the binary can act like a planet trap, stopping the inward migration.

Since the inner gap in the circumbinary disc is a natural barrier for migrating planets, the first aim of this thesis is to examine the dynamical aspects of the disc under the influence of the binary through two-dimensional, locally isothermal, viscous hydrodynamical simulations. The goal of these simulations is to understand how binary and disc parameters have to be varied, to create a gap which is able to trap a planet at the observed location. Typically these kind of simulations are performed on a polar grid, with an inner hole in the computational domain. Since there is no common agreement about the location and the type of boundary condition applied at this inner boundary, the first part of this thesis also addresses the numerical conditions at the inner boundary.

The second aim is to examine the evolution of embedded planets in circumbinary discs. In detailed simulations with embedded planets the influence of the planet's mass onto the disc structure and the migration process is investigated. Of special interest are the final orbital parameters of simulated planets and their agreement with the observations and if therefore the migration scenario can be a vital scenario to explain the observed distribution of circumbinary planets.

3 Publications

This chapter presents the following publications written in the context of this thesis:

1. Thun, D., Kley, W., Picogna, G.: Circumbinary discs: Numerical and physical behaviour. Astronomy & Astrophysics 604, A102 (2017)

2. Thun, D. & Kley, W.: Migration of planets in circumbinary discs. Astronomy & Astrophysics 616, A47 (2018)

In Thun et al. (2017) the dynamical structure of circumbinary disc under the influence of a binary is studied in detail. First, numerical issues at the inner boundary (location, type of boundary condition) are examined. Second, the results of a large set of parameter studies are presented to understand the influence of binary and disc parameters onto the structure and behaviour of the gap.

This paper was written in collaboration with Prof Dr Wilhelm Kley and Dr Giovanni Picogna. All simulations were conducted by myself, expect the Rh2d simulations which were conducted by Prof Dr Wilhelm Kley and the Fargo simulations which were conducted by Dr Giovanni Picogna. The analysis of all simulations data was done by myself. Most parts of the manuscript were written by myself. Prof Dr Wilhelm Kley contributed to all parts of the publication, especially in the introduction, and the summary and discussion section. The section about the code Rh2d and Appendix B was written by him. Dr Giovanni Picogna wrote the section about the Fargo code.

Thun and Kley (2018) revisits the influence of binary parameters (eccentricity and mass ratio) onto the structure of the inner gap. An improved disc model and a larger parameter space lead to the discovery of additional features in the bifurcation diagram. In the second part the evolution of embedded planets in circumbinary disc around five Kepler systems (Kepler-16, -34, 38, 64, 413) is studied. Especially the influence of the planet-to-disc mass ratio is examined in detail. For each system the final simulated orbital parameters are compared to the observations.

This paper was written in collaboration with Prof Dr Wilhelm Kley. All simulations were conducted and analysed by myself. The publications was written mostly by myself with helpful intakes by Prof Dr Wilhelm Key, especially in the introduction, the discussion, and the summary sections.

A&A 604, A102 (2017)
DOI: 10.1051/0004-6361/201730666

Astronomy & Astrophysics

Circumbinary discs: Numerical and physical behaviour⋆

Daniel Thun[1], Wilhelm Kley[1], and Giovanni Picogna[2]

[1] Institut für Astronomie und Astrophysik, Universität Tübingen, Auf der Morgenstelle 10, 72076 Tübingen, Germany
e-mail: [daniel.thun;wilhelm.kley]@uni-tuebingen.de
[2] Universitäts-Sternwarte, Ludwig-Maximilians-Universität München, Scheinerstr. 1, 81679 München, Germany
e-mail: picogna@usm.lmu.de

Received 21 February 2017 / Accepted 26 April 2017

ABSTRACT

Aims. Discs around a central binary system play an important role in star and planet formation and in the evolution of galactic discs. These circumbinary discs are strongly disturbed by the time varying potential of the binary system and display a complex dynamical evolution that is not well understood. Our goal is to investigate the impact of disc and binary parameters on the dynamical aspects of the disc.
Methods. We study the evolution of circumbinary discs under the gravitational influence of the binary using two-dimensional hydrodynamical simulations. To distinguish between physical and numerical effects we apply three hydrodynamical codes. First we analyse in detail numerical issues concerning the conditions at the boundaries and grid resolution. We then perform a series of simulations with different binary parameters (eccentricity, mass ratio) and disc parameters (viscosity, aspect ratio) starting from a reference model with Kepler-16 parameters.
Results. Concerning the numerical aspects we find that the length of the inner grid radius and the binary semi-major axis must be comparable, with free outflow conditions applied such that mass can flow onto the central binary. A closed inner boundary leads to unstable evolutions.
We find that the inner disc turns eccentric and precesses for all investigated physical parameters. The precession rate is slow with periods ($T_{\rm prec}$) starting at around 500 binary orbits ($T_{\rm bin}$) for high viscosity and a high aspect ratio H/R where the inner hole is smaller and more circular. Reducing α and H/R increases the gap size and $T_{\rm prec}$ reaches 2500 $T_{\rm bin}$. For varying binary mass ratios $q_{\rm bin}$ the gap size remains constant, whereas $T_{\rm prec}$ decreases with increasing $q_{\rm bin}$.
For varying binary eccentricities $e_{\rm bin}$ we find two separate branches in the gap size and eccentricity diagram. The bifurcation occurs at around $e_{\rm crit} \approx 0.18$ where the gap is smallest with the shortest $T_{\rm prec}$. For $e_{\rm bin}$ lower and higher than $e_{\rm crit}$, the gap size and $T_{\rm prec}$ increase. Circular binaries create the most eccentric discs.

Key words. hydrodynamics – methods: numerical – planets and satellites: formation – protoplanetary disks – binaries: close

1. Introduction

Circumbinary discs are accretion discs that orbit a binary system that consists for example of a binary star or a binary black hole system. A very prominent example of a circumbinary disc orbiting two stars is the system GG Tau. Due to the large star separation, the whole system (stars and disc) can be directly imaged by interferometric methods (Guilloteau et al. 1999). Later data yielded constraints on the size of the dust in the system and have indicated that the central binary may consist of multiple stellar systems (see Andrews et al. 2014; Di Folco et al. 2014, and references therein). More recent observations have pointed to possible planet formation (Dutrey et al. 2014) and streamers from the disc onto the stars (Yang et al. 2017). A summary of the properties of the GG Tau system is given in Dutrey et al. (2016).

An additional important clue for the existence and importance of circumbinary discs is given by the observed circumbinary planets. These are planetary systems where the planets do not orbit one star, but instead orbit a binary star system. These systems have been detected in recent years by the *Kepler* Space Mission and have inspired an intense research activity. The first such circumbinary planet, Kepler-16b, orbits its host system consisting of a K-type main-sequence star and an M-type red dwarf, in what is known as a P-type orbit with a semi-major axis of 0.7048 au and a period of 228.7 days (Doyle et al. 2011). Presently there are ten Kepler circumbinary planets known and a summary of the properties of the first five systems discovered is given in Welsh et al. (2014)[1]. The observations have shown that in these systems the stars are mutually eclipsing each other, as well as the planets. The simultaneous eclipses of several objects is a clear indication of the flatness of the system because the orbital plane of the binary star has to coincide nearly exactly with the orbital plane of the planet. In this respect these systems are flatter than our own solar system. Because planets form in discs, the original protoplanetary disc in these systems had to orbit around both stars, hence it must have been a circumbinary disc that was also coplanar with respect to the orbital plane of the central binary.

⋆ Movies associated to Figs. 1 and 8 are available at http://www.aanda.org

[1] Additional known main-sequence binaries with circumbinary planets besides Kepler-16 are Kepler-34 and -35 (Welsh et al. 2012), Kepler-38 (Orosz et al. 2012a), Kepler-47 (Orosz et al. 2012b), Kepler-64 (Schwamb et al. 2013), Kepler-413 (Kostov et al. 2014), Kepler-453 (Welsh et al. 2015), and Kepler-1647 (Kostov et al. 2016).

In addition to their occurrence around younger stars, circumbinary discs are believed to orbit supermassive black hole binaries in the centres of galaxies (Begelman et al. 1980), where they may play an important role in the evolution of the host galaxies (Armitage & Natarajan 2002). In the early phase of the Universe there were many more close encounters between the young galaxies that already had black holes in their centres. The gravitational tidal forces between them often resulted in new merged objects that consisted of a central black hole binary surrounded by a large circumbinary disc (see e.g. Cuadra et al. 2009; Lodato et al. 2009, and references therein). The dynamical behaviour of such a system is very similar to the one described above, where we have two stars instead of black holes.

To understand the dynamics of discs around young binary stars such as GG Tau or the planet formation process in circumbinary discs or the dynamical evolution of a central black hole binary in a galaxy, it is important to understand in detail the behaviour of a disc orbiting a central binary. The strong gravitational perturbation by the binary generates spiral waves in the disc; these waves transport energy and angular momentum from the binary to the disc (Pringle 1991) and subseqently alter the evolution of the binary (Artymowicz et al. 1991). The most important impact of the angular momentum transfer to the disc is the formation of an inner cavity in the disc with a very low density whose size depends on disc parameters (such as viscosity or scale height) and on the binary properties (mass ratio, eccentricity) (Artymowicz & Lubow 1994).

The numerical simulation of these circumbinary discs is not trivial and over the years several attempts have been made. The first simulations of circumbinary discs used the smoothed particle hydrodynamics (SPH) method, a Lagrangian method where the fluid is modelled as individual particles (Artymowicz & Lubow 1996). On the one hand, this method has the advantage that the whole system can be included in the computational domain and hence the accretion onto the single binary components can be studied. On the other hand, because of the finite mass of the SPH-particles, the maximum density contrast that can be resolved is limited.

Later Rozyczka & Laughlin (1997) simulated circumbinary discs with the help of a finite difference method on a polar grid. The grid allowed for a much larger range in mass resolution than the SPH codes used to date. A polar grid is well suited for the outer parts of a disc, but suffers from the fact that there will always be an inner hole in the computational domain since the minimum radius $R_{\rm min}$ cannot be made arbitrarily small. Decreasing the minimum radius will also strongly reduce the required numerical time step, rendering long simulations unfeasible. But since circumbinary disc simulations have to be simulated for tens of thousands of binary orbits to reach a quasi-steady state, the minimum radius is often chosen such that the motion of the central stars is not covered by the computational domain, and the mass transfer from the disc to the binary cannot be studied.

Günther & Kley (2002) used a special dual-grid technique to use the best of the two worlds, the high resolution of the grid codes and the coverage of the whole domain of the particle codes. For the outer disc they used a polar grid and they overlaid the central hole with a Cartesian grid. In this way it was possible to study the complex interaction between the binary and the disc in greater detail. All these simulations indicated that despite the formation of an inner gap, material can enter the inner regions around the stars crossing the gap through stream like features to eventually become accreted onto the stars and influence their evolution (Bate et al. 2002).

Another interesting feature of circumbinary discs concerns their eccentricity. As shown in hydrodynamical simulations for planetary mass companions, discs develop a global eccentric mode even for circular binaries (Papaloizou et al. 2001). The eccentricity is confined to the inner disc region and shows a very slow precession (Kley & Dirksen 2006). These results were confirmed for equal mass binaries on circular orbits (MacFadyen & Milosavljević 2008). The disc eccentricity is excited by the 3:1 outer eccentric Lindblad resonance (Lubow 1991; Papaloizou et al. 2001), which is operative for a sufficiently cleared out gap. For circular binaries a transition, in the disc structure from more circular to eccentric is thought to occur for a mass ratio of secondary to primary above 1/25 (D'Orazio et al. 2016). However, this appears to contradict the mentioned results by Papaloizou et al. (2001) and Kley & Dirksen (2006) who show that this transition already occurs for a secondary in the planet mass regime with details depending on disc parameters such as pressure and viscosity.

Driven by the observation of planets orbiting eccentric binary stars and the possibility of studying eccentric binary black holes, a large number of numerical simulations have been performed over the last few years dealing with discs around eccentric central binaries (e.g. Pierens & Nelson 2013; Kley & Haghighipour 2014; Dunhill et al. 2015). The recent simulations of circumbinary discs by Pierens & Nelson (2013), Kley & Haghighipour (2014) and Lines et al. (2015) used grid-based numerical methods on a polar grid with an inner hole. This raises questions about the location and imposed boundary conditions at the innermost grid radius $R_{\rm min}$. In particular, the value of $R_{\rm min}$ must be small enough to capture the development of the disc eccentricity through gravitational interaction between the binary and the disc, especially through the 3:1 Lindblad resonance (Pierens & Nelson 2013). Therefore $R_{\rm min}$ has to be chosen in a way that all important resonances lie inside the computational domain.

In addition to the position of the inner boundary, there is no common agreement on which numerical boundary condition better describes the disc. In simulations concerning circumbinary planets mainly two types of boundary conditions are used: closed inner boundaries (Pierens & Nelson 2013; Lines et al. 2015) that do not allow for mass flow onto the central binary, and outflow boundaries (Kley & Haghighipour 2014, 2015) that do allow for accretion onto the binary. While Lines et al. (2015) do not find a significant difference between these two cases, Kley & Haghighipour (2014) see a clear impact on the surface density profile, and they were also able to construct discs with (on average) constant mass flow through the disc, which is not possible for closed boundaries. Driven by these discussions in the literature we decided to perform dedicated numerical studies to test the impact of the location of $R_{\rm min}$, the chosen boundary condition, and other numerical aspects in more detail. During our work we became aware of other simulations that were tackling similar problems. In October 2016 alone three publications appeared on `astro-ph` that described numerical simulations of circumbinary discs (Fleming & Quinn 2017; Miranda et al. 2017; Mutter et al. 2017). While the first paper considered SPH-simulations, in the latter two papers grid-codes were used and in both the boundary condition at $R_{\rm min}$ is discussed.

In our paper we start out with numerical considerations and investigate the necessary conditions at the inner boundary in detail, and we discuss aspects of the other recent results in the presentation of our findings below. Additionally, we present a detailed parameter study of the dynamical behaviour of circumbinary discs as a function of binary and disc properties.

Table 1. Orbital parameters of the Kepler-16 system.

M_A [$M_\odot$]	M_B [$M_\odot$]	q_{bin}	a_{bin} [au]	e_{bin}	T_{bin} [d]
0.69	0.20	0.29	0.22	0.16	41.08

Notes. Values taken from Doyle et al. (2011) (rounded to two decimals). The mass ratio is defined as $q_{bin} = M_B/M_A$.

We organised this paper in the following way. In Sect. 2 we describe the numerical and physical setup of our circumbinary simulations. In Sect. 3 we briefly describe the numerical methods of the different codes we used for our simulations. In Sect. 4 we examine the disc structure by varying the inner boundary condition and its location. The influence of different binary parameters are examined in Sect. 5. Different disc parameters and their influence are studied in Sect. 6. Finally we summarise and discuss our results in Sect. 7.

2. Model setup

To study the evolution of circumbinary discs we perform locally isothermal hydrodynamical simulations. As a reference system we consider a binary star having the properties of Kepler-16, whose dynamical parameters are presented in Table 1. This system has a typical mass ratio and a moderate eccentricity of the orbit, and it has been studied frequently in the literature. In our parameter study we start from this reference system and vary the different aspects systematically.

2.1. Physics and equations

Inspired by the flatness of the observed circumbinary planetary systems, for example in the Kepler-16 system the motion takes place in single plane to within 0.5° (Doyle et al. 2011), we make the following two assumptions:

1. the vertical thickness H of the disc is small compared to the distance from the centre R;
2. there is no vertical motion.

It is therefore acceptable to reduce the problem to two dimensions by vertically averaging the hydrodynamical equations. In this case it is meaningful to work in cylindrical coordinates (R, φ, z)[2] and the averaging process is done in the z-direction. Furthermore, we choose the centre of mass of the binary as the origin of our coordinate system with the vertical axis aligned with the rotation axis of the binary. The averaged hydrodynamical equations are then given by

$$\frac{\partial}{\partial t}\Sigma + \boldsymbol{\nabla}\cdot(\Sigma\boldsymbol{u}) = 0, \tag{1}$$

$$\frac{\partial}{\partial t}(\Sigma\boldsymbol{u}) + \boldsymbol{\nabla}\cdot(\Sigma\boldsymbol{u}\otimes\boldsymbol{u} - \boldsymbol{\Pi}) = -\boldsymbol{\nabla}P - \Sigma\boldsymbol{\nabla}\Phi, \tag{2}$$

where $\Sigma = \int_{-\infty}^{\infty}\varrho\,\mathrm{d}z$ is the surface density, $P = \int_{-\infty}^{\infty}p\,\mathrm{d}z$ the vertically integrated pressure, and $\boldsymbol{u} = (u_R, u_\varphi)^{\mathrm{T}}$ the two-dimensional velocity vector. We close this system of equations with a locally isothermal equation of state

$$P = c_s^2(R)\Sigma, \tag{3}$$

with the local sound speed $c_s(R)$.

[2] With $\boldsymbol{r}$ we denote the three-dimensional positional vector $\boldsymbol{r} = R\hat{\boldsymbol{e}}_R + z\hat{\boldsymbol{e}}_z$ and with $\boldsymbol{R}$ the two-dimensional positional vector in the $R-\varphi$-plane $\boldsymbol{R} = R\hat{\boldsymbol{e}}_R$.

The gravitational potential Φ of both stars is given by

$$\Phi = -\sum_{k=1}^{2}\frac{GM_k}{\left[(\boldsymbol{R}-\boldsymbol{R}_k)^2 + (\varepsilon H)^2\right]^{1/2}}. \tag{4}$$

Here M_k denotes the mass of the kth star, G is the gravitational constant, and $\boldsymbol{R} - \boldsymbol{R}_k$ a vector from a point in the disc to the primary or secondary star. From a numerical point of view, the smoothing factor εH is not necessary if the orbit of the binary is not inside the computational domain. We use this smoothing factor to account for the vertically extended three-dimensional disc in our two-dimensional case (Müller et al. 2012). For all simulations we use a value of $\varepsilon = 0.6$.

In our simulations with no bulk viscosity the viscous stress tensor $\boldsymbol{\Pi}$ is given in tensor notation by

$$\boldsymbol{\Pi}_{ij} = 2\eta\left[\frac{1}{2}\left(u_{j;i} + u_{i;j}\right) - \frac{1}{3}\delta_{ij}(\boldsymbol{\nabla}\cdot\boldsymbol{u})\right], \tag{5}$$

where $\eta = \Sigma\nu$ is the vertically integrated dynamical viscosity coefficient. To model the viscosity in the disc we use the α-disc model by Shakura & Sunyaev (1973), where the kinematic viscosity is given by $\nu = \alpha c_s H$. The parameter α is less than one, and for our reference model we use $\alpha = 0.01$.

To calculate the aspect ratio $h = {}^{H}/_{R}$ we assume a vertical hydrostatic equilibrium

$$\frac{1}{\varrho}\frac{\partial p}{\partial z} = -\frac{\partial\Phi}{\partial z}, \tag{6}$$

with the density ϱ and pressure p. To solve this equation we use the full three-dimensional potential of the binary $\Phi = -\sum_k \frac{GM_k}{|\boldsymbol{r}-\boldsymbol{r}_k|}$ and the isothermal equation of state $p = c_s^2(R)\varrho$ (we also assume an isothermal disc in the z-direction). Integration over z yields

$$\varrho = \varrho_0\exp\left\{-\frac{1}{2}\frac{z^2}{H^2}\right\}, \tag{7}$$

with the disc scale height (Günther & Kley 2002)

$$H = \left[\sum_k \frac{1}{c_s^2}\frac{GM_k}{|\boldsymbol{R}-\boldsymbol{R}_k|^3}\right]^{-\frac{1}{2}} \tag{8}$$

and the midplane density

$$\varrho_0 = \frac{\Sigma}{\sqrt{2\pi}H}, \tag{9}$$

which can be calculated by using the definition of the surface density.

If we concentrate the mass of the binary $M_{bin} = M_A + M_B$ in its centre of mass ($\boldsymbol{R}_k \to 0$), this reduces to

$$H = \frac{c_s}{u_K}R, \tag{10}$$

with the Keplerian velocity $u_K = \sqrt{GM_{bin}/R}$. Test calculations with the simpler disc height (10) showed no significant difference compared to calculations with the more sophisticated disc height (8). Therefore, we use the simpler disc height in all our calculation to save some computation costs.

For our locally isothermal simulations we use a temperature profile of $T \propto R^{-1}$, which corresponds to a disc with constant aspect ratio. The local sound speed is then given by $c_s(R) = hu_K \propto R^{-1/2}$. If not stated otherwise we use a disc aspect ratio of $h = 0.05$.

Table 2. Setup for our reference model.

Numerical parameters	
$R_{\rm min}$	0.25 au
$R_{\rm max}$	15.4 au
Resolution	762×582
Inner boundary	Outflow
Binary parameters	
$a_{\rm bin}$	0.22 au
$e_{\rm bin}$	0.16
$q_{\rm bin}$	0.29
Disc parameters	
h	0.05
α	0.01

2.2. Initial disc parameters

For the initial disc setup we follow Lines et al. (2015). The initial surface density in all our models is given by

$$\Sigma(t=0) = f_{\rm gap}\Sigma_{\rm ref}R^{-\alpha_\Sigma}, \tag{11}$$

with the reference surface density $\Sigma_{\rm ref} = 10^{-4}\,M_\odot\,{\rm au}^{-2}$. The initial slope is $\alpha_\Sigma = 1.5$ and the gap function, which models the expected cavity created by the binary-disc interaction, is given by

$$f_{\rm gap} = \left[1 + \exp\left(-\frac{R - R_{\rm gap}}{\Delta R}\right)\right]^{-1} \tag{12}$$

(Günther & Kley 2002), with the transition width $\Delta R = 0.1\,R_{\rm gap}$ and the estimated size of the gap $R_{\rm gap} = 2.5\,a_{\rm bin}$ (Artymowicz & Lubow 1994). The initial radial velocity is set to zero $u_R(t=0) = 0$, and for the initial azimuthal velocity we choose the local Keplerian velocity $u_\varphi(t=0) = u_{\rm K}$.

2.3. Initial binary parameters

For models run with PLUTO or FARGO we start the binary at periastron at time $t = 0$ (upper signs in Eqs. (13) and (14)). Models carried out with RH2D start the binary at apastron (lower signs in Eqs. (13) and (14));

$$\boldsymbol{R}_{\rm A} = \begin{pmatrix} K_1 a_{\rm bin}(1 \mp e_{\rm bin}) \\ 0 \end{pmatrix}, \qquad \boldsymbol{v}_{\rm A} = \begin{pmatrix} 0 \\ K_1 \frac{2\pi}{T_{\rm bin}} a_{\rm bin} \sqrt{\frac{1 \pm e_{\rm bin}}{1 \mp e_{\rm bin}}} \end{pmatrix}, \tag{13}$$

$$\boldsymbol{R}_{\rm B} = \begin{pmatrix} -K_2 a_{\rm bin}(1 \mp e_{\rm bin}) \\ 0 \end{pmatrix}, \qquad \boldsymbol{v}_{\rm B} = \begin{pmatrix} 0 \\ -K_2 \frac{2\pi}{T_{\rm bin}} a_{\rm bin} \sqrt{\frac{1 \pm e_{\rm bin}}{1 \mp e_{\rm bin}}} \end{pmatrix}, \tag{14}$$

with $K_1 = M_{\rm B}/M_{\rm bin}$, $K_2 = M_{\rm A}/M_{\rm bin}$, and the period of the binary $T_{\rm bin} = 2\pi\left[a_{\rm bin}^3/(GM_{\rm bin})\right]^{1/2}$.

2.4. Numerics

In our simulations we use a logarithmically increasing grid in the R-direction and a uniform grid in the φ-direction. The physical and numerical parameter for our reference system used in our extensive parameter studies in Sect. 5 and Sect. 6 are quoted in Table 2. In the radial direction the computational domain ranges from $R_{\rm min} = 0.25$ au to $R_{\rm max} = 15.4$ au and in the azimuthal direction from 0 to 2π, with a resolution of 762×582 grid cells. For our numerical studies we also use also different configurations as explained below.

Because of the development of an inner cavity where the surface density drops significantly, we use a density floor $\Sigma_{\rm floor} = 10^{-9}$ (in code units) to avoid numerical difficulties with too low densities. Test simulations using lower floor densities did not show any differences.

At the outer radial boundary we implement a closed boundary condition where the azimuthal velocity is set to the local Keplerian velocity. At the inner radial boundary the standard condition is the zero-gradient outflow condition as in Kley & Haghighipour (2014) or Miranda et al. (2017), but we also test different possibilities such as closed boundaries or the viscous outflow condition (Kley & Nelson 2008; Mutter et al. 2017).

The open boundary is implemented in such a way that gas can leave the computational domain but cannot reenter it. This is done by using zero-gradient boundary conditions ($\partial/\partial R = 0$) for Σ and negative u_R. For positive u_R we use a reflecting boundary to prevent mass in-flow. Since there is no well-defined Keplerian velocity at the inner boundary, due to the strong binary-disc interaction, we also use a zero-gradient boundary condition for the angular velocity $\Omega_\varphi = u_\varphi/R$. By using the zero-gradient condition for the angular velocity instead of the azimuthal velocity we ensure a zero-torque boundary. In the φ-direction we use periodic boundary conditions.

In all our simulations we use dimensionless units. The unit of length is $R_0 = 1$ au, the unit of mass is the sum of the primary and secondary mass $M_0 = M_{\rm A} + M_{\rm B}$ and the unit of time is $t_0 = \sqrt{R_0^3/(GM_0)}$ so that the gravitational constant G is equal to one. The unit density is then given by $\Sigma_0 = M_0/R_0^2$.

2.5. Monitored parameters

Since our goal is to study the evolution of the disc under the influence of the binary we calculated the disc eccentricity $e_{\rm disc}$ and the argument of the disc periastron $\varpi_{\rm disc}$ ten times per binary orbit. To calculate these quantities we treat each cell as a particle with the cells mass and velocity on an orbit around the centre of mass of the binary. Thus, the eccentricity vector of a cell is given by

$$\boldsymbol{e}_{\rm cell} = \frac{\boldsymbol{u} \times \boldsymbol{j}}{GM_{\rm bin}} - \frac{\boldsymbol{R}}{|\boldsymbol{R}|} \tag{15}$$

with the specific angular momentum $\boldsymbol{j} = \boldsymbol{R} \times \boldsymbol{u}$ of that cell. We have a flat system, thus the angular momentum vector only has a z-component. The eccentricity $e_{\rm cell}$ and longitude of periastron $\varpi_{\rm cell}$ of the cell's orbit are therefore given by

$$e_{\rm cell} = |\boldsymbol{e}_{\rm cell}|, \tag{16}$$

$$\varpi_{\rm cell} = {\rm atan2}(e_y, e_x). \tag{17}$$

The global disc values are then calculated through a mass-weighted average of each cell's eccentricity and longitude of periastron (Kley & Dirksen 2006)

$$e_{\rm disc} = \left[\int_{R_1}^{R_2}\int_0^{2\pi} \Sigma e_{\rm cell} R\,{\rm d}\varphi\,{\rm d}R\right] \Big/ \left[\int_{R_1}^{R_2}\int_0^{2\pi} \Sigma R\,{\rm d}\varphi\,{\rm d}R\right], \tag{18}$$

$$\varpi_{\rm disc} = \left[\int_{R_1}^{R_2}\int_0^{2\pi} \Sigma \varpi_{\rm cell} R\,{\rm d}\varphi\,{\rm d}R\right] \Big/ \left[\int_{R_1}^{R_2}\int_0^{2\pi} \Sigma R\,{\rm d}\varphi\,{\rm d}R\right]. \tag{19}$$

The integrals are simply evaluated by summing over all grid cells. The lower bound is always $R_1 = R_{\rm min}$. For the disc eccentricity we integrate over the whole disc ($R_2 = R_{\rm max}$) if not stated

otherwise, whereas for the disc's longitude of periastron it is suitable to integrate only over the inner disc ($R_2 = 1.0$ au) to obtain a well-defined value of $\varpi_{\rm disc}$ since animations clearly show a precession of the inner disc (see e.g. Kley & Haghighipour 2015). The radial eccentricity distribution of the disc is given by

$$e_{\rm ring}(R) = \left[\int_R^{R+{\rm d}R}\int_0^{2\pi} \Sigma e_{\rm cell} R'\,{\rm d}\varphi\,{\rm d}R'\right] \Big/ \left[\int_R^{R+{\rm d}R}\int_0^{2\pi} \Sigma R'\,{\rm d}\varphi\,{\rm d}R'\right]. \quad (20)$$

3. Hydrodynamic codes

Since the system under analysis is, in particular near the central binary, very dynamical we decided to compare the results from three different hydrodynamic codes to make sure that the observed features are physical and not numerical artefacts. We use codes with very different numerical approaches. PLUTO solves the hydrodynamical equations in conservation form with a Godunov-type shock-capturing scheme, whereas RH2D and FARGO are second-order upwind methods on a staggered mesh. In the following sections we describe each code and its features briefly.

3.1. PLUTO

We use an in-house developed GPU version of the PLUTO 4.2 code (Mignone et al. 2007). PLUTO solves the hydrodynamic equations using the finite-volume method which evolves volume averages in time. To evolve the solution by one time step, three substeps are required. First, the cell averages are interpolated to the cell interfaces, and then in the second step a Riemann problem is solved at each interface. In the last step the averages are evolved in time using the interface fluxes.

For all three substeps PLUTO offers many different numerical options. We found that the circumbinary disc model is very sensitive to the combination of these options. Third-order interpolation and time evolution methods lead very quickly to a negative density from which the code cannot recover, even though we set a density floor. We therefore use a second-order reconstruction of states and a second-order Runge-Kutta scheme for the time evolution. Another important parameter is the limiter, which is used during the reconstruction step to avoid strong oscillations. For the most diffusive limiter, the minmod limiter, no convergence is reached for higher grid resolutions. For the least diffusive limiter, the mc limiter, the code again produces negative densities and aborts the calculation. Thus, we use the van Leer limiter which, in kind of diffusion, lies between the minmod and the mc limiter.

For the binary position we solve Kepler's equation using the Newton–Raphson method at each Runge-Kutta substep.

3.2. Rh2d

The RH2D code is a two-dimensional radiation hydrodynamics code originally designed to study boundary layers in accretion discs (Kley 1989), but later extended to perform flat disc simulations with embedded objects (Kley 1999). It is based on the second-order upwind method described in Hawley et al. (1984) and Rozyczka (1985). It uses a staggered grid with second-order spatial derivatives and through operator-splitting the time integration is semi-second order. Viscosity can be treated explicitly or implicitly, artificial viscosity can be applied, and the Fargo algorithm has also been added. The motion of the binary stars is integrated using a fourth-order Runge-Kutta algorithm.

3.3. Fargo

We adopted the ADSG version of FARGO (Masset 2000; Baruteau & Masset 2008) updated by Müller & Kley (2012). This code uses a staggered mesh finite difference method to solve the hydrodynamic equations. Conceptually, the FARGO code uses the same methods as RH2D or the ZEUS code, but employs the special Fargo algorithm that avoids the time step limitations that are due to the rotating shear flow (Masset 2000). In our situation the application of the Fargo algorithm is not always beneficial because of the larger deviations from pure Keplerian flow near the binary. The position of the binary stars is calculated by a fifth-order Runge-Kutta algorithm.

4. Numerical considerations

Before describing our results on the disc dynamics, we present two important numerical issues that can have a dramatic influence on the outcome of the simulations: the inner boundary condition (open or closed) and the location of the inner radius of the disc. We show that "unfortunate" choices can lead to incorrect results. In this section we use a numerical setup different from that in Table 2. Specifically, the base model has a radial extent from $R_{\rm min} = 0.25$ au to $R_{\rm max} = 4.0$ au, which is covered with 448×512 gridcells for simulations with RH2D and FARGO, and 512×580 with PLUTO (see Appendix A for an explanation of why we use different resolutions for different codes). For simulations with varying inner radii, the number of gridcells in the radial direction is adjusted to always give the same resolution in the overlapping domain.

4.1. Inner boundary condition

All simulations using a polar-coordinate grid expericence the same problem: there is a hole in the computational domain because $R_{\rm min}$ cannot be zero. Usually this hole exceeds the binary orbit. Therefore, the area where gas flows from the disc onto the binary and where circumstellar discs around the binary components form is not part of the simulation. This complex gas flow around the binary has been shown by e.g. Günther & Kley (2002) with a special dual-grid technique that covers the whole inner cavity. Their code is no longer in use and modern efficient codes (FARGO and PLUTO) that run in parallel do not have the option of a dual-grid.

To reproduce nevertheless some results of Günther & Kley (2002), we carried out a simulation on a polar grid with an inner radius of $R_{\rm min} = 0.02$ au so that both orbits of the primary and secondary lie well inside the computational domain. A snapshot of this simulation is plotted in Fig. 1. The logarithm of the surface density is colour-coded, while the orbits of the primary and secondary stars are shown in white and green. The red cross marks the centre of mass of the binary, which lies outside the computational domain. Figure 1 shows circumstellar discs around the binary components, as well as a complex gas flow through the gap onto the binary. Although including the binary orbit inside the computational would be desirable, it is at the moment not feasible for long-term simulations because of the strong time step restriction resulting from the small cell size at the inner boundary. This means that for simulations where the binary

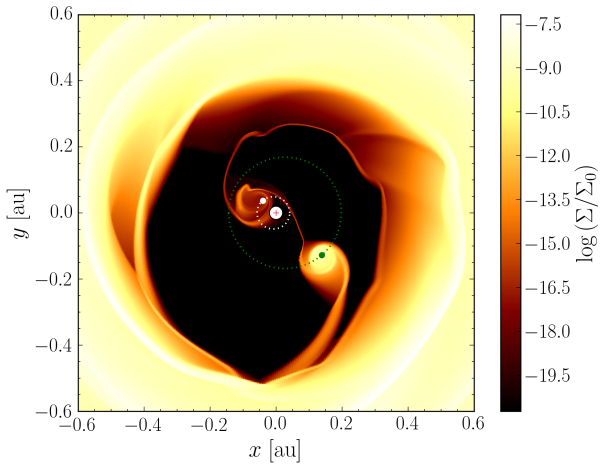

Fig. 1. Two-dimensional plot of the inner disc of one of our locally isothermal Kepler-16 simulations where both orbits of the binary lie inside the computational domain. The logarithm of the surface density is colour-coded. The orbits of the primary and secondary are shown in white and green. The white inner region lies outside the computational domain; the red cross marks the centre of mass of the binary. A video of the simulation can be found online.

orbit is not included in the computational domain, the boundary condition at the inner radius has to allow for flow into the inner cavity, at least approximately. Two boundary conditions are usually used in circumbinary disc simulations: closed boundaries (Lines et al. 2015; Pierens & Nelson 2013) and outflow boundaries (Kley & Haghighipour 2014, 2015; Miranda et al. 2017).

Given the importance of the boundary condition at $R_{\rm min}$, we carried out dedicated simulations for a model adapted from Lines et al. (2015) and used an inner radius of $R_{\rm min} = 0.345$ au, but otherwise it was identical to our standard model. We applied closed boundaries and open ones in order to examine their influence on the disc structure. We also varied different numerical parameters (resolution, radial grid spacing, integrator) for this simulation series.

The top panel of Fig. 2 shows the azimuthally averaged density profiles for different grid resolutions and spacings after 16 000 binary orbits. All these simulations were performed with PLUTO and a closed inner boundary. The strong dependence of the density distribution and inner gap size on the numerical setup stands out. This dependence on numerics is very surprising and not at all expected since the physical setup was identical in all these simulations and therefore the density profiles should all be similar and converge upon increasing resolution. Not only does the gap size show this strong dependence, but also the radial eccentricity distribution (bottom panel of Fig. 2). To examine this dependence further, which could in principle be the result of a bug in our code, we reran the identical physical setup with a different code, RH2D. The results of these RH2D simulations show the same strong numerical dependence as the PLUTO results. In Fig. 3 the total disc eccentricity time evolution for the RH2D simulations is plotted. Again, one would expect that different numerical parameters should produce approximately the same disc eccentricity, but our simulations show a radical change in the disc eccentricity if the numerical methods are slightly different.

We note that using a viscous outflow condition where the radial velocity at $R_{\rm min}$ is fixed to $-\beta 3\nu/(2R)$ with $\beta = 5$ (as suggested by Mutter et al. 2017) resulted in the same dynamical behaviour as the closed boundary condition. The reason for this lies

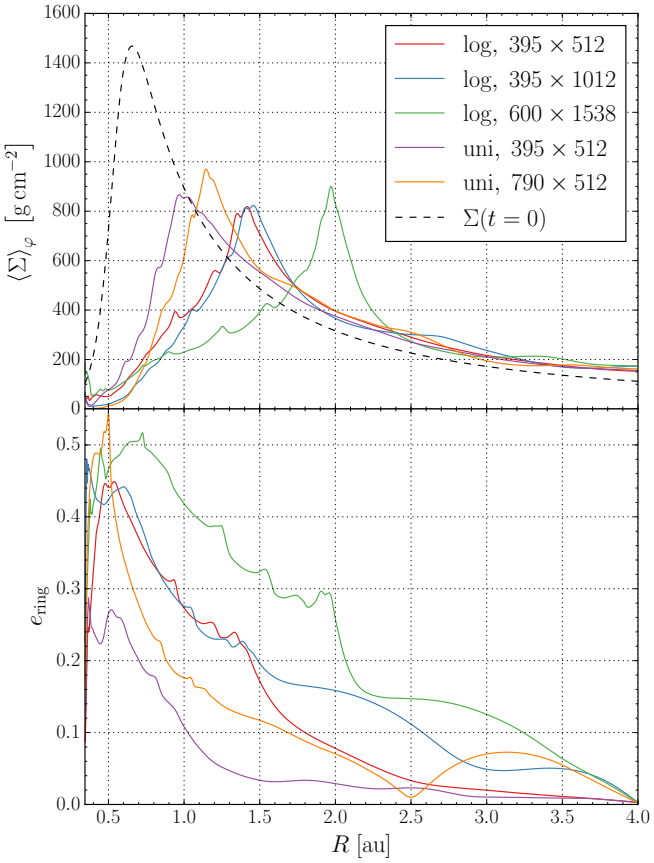

Fig. 2. Azimuthally averaged surface density profiles (*top*) and radial disc eccentricity (*bottom*) for our Kepler-16 reference setup (using $R_{\rm min} = 0.345$ au) with a closed inner boundary condition at $t = 16\,000\,T_{\rm bin}$. Coloured solid lines show the results from simulations with different resolutions or different grid-spacing in the R-direction (logarithmic and uniform spacing). The initial density profile is also shown as a dashed black line. All simulations were performed with PLUTO.

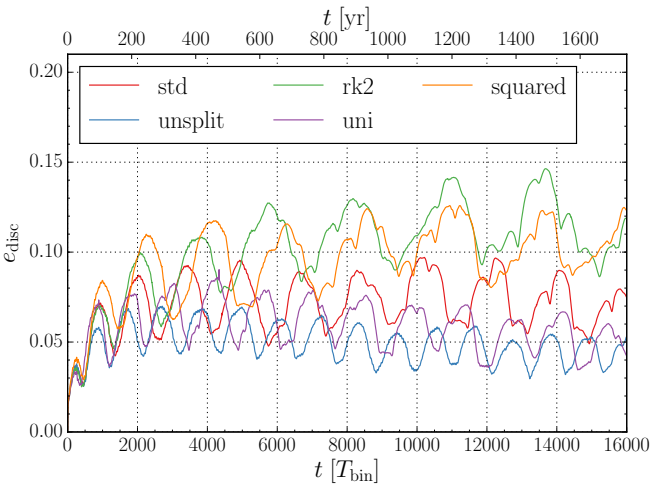

Fig. 3. Time evolution of the total disc eccentricity for simulations of the standard model with closed inner boundary and $R_{\rm min} = 0.345$ au. Different numerical parameters such as grid spacing, time integrator, and operator splitting have been used. The legend refers to: STD standard integrator (operator and directional splitting), UNSPLIT no directional splitting, RK2 second-order RK time integrator, UNI uniform grid, SQUARED squared grid cells. All simulations were performed with RH2D.

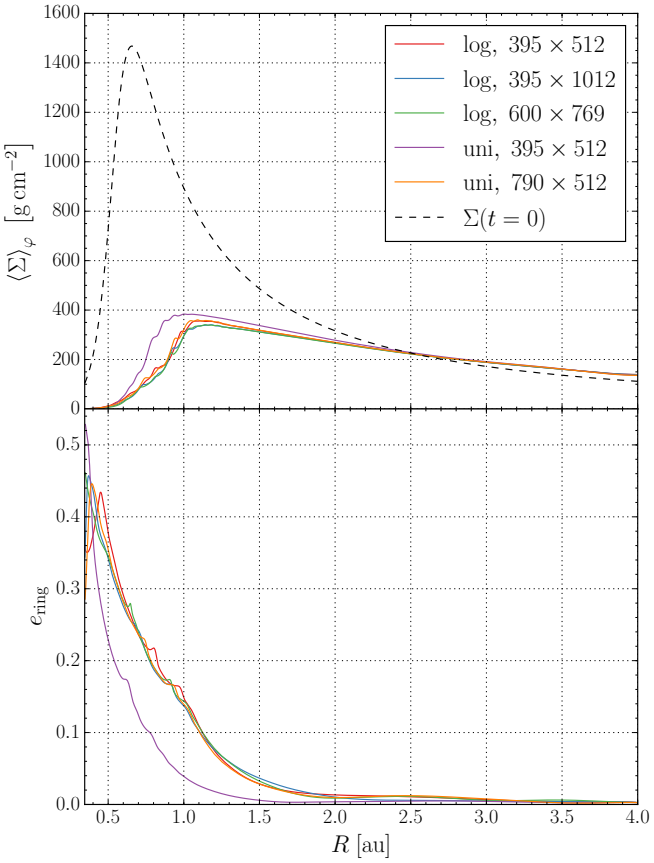

Fig. 4. Azimuthally averaged surface density profiles (*top*) and radial disc eccentricity (*bottom*) for our reference setup ($R_{\rm min}$ = 0.345 au) with a zero-gradient outflow inner boundary condition after 16 000 binary orbits. Coloured solid lines show results from simulations with different resolutions or different grid-spacing in the R-direction (logarithmic and uniform spacing). The initial density profile is also shown as a dashed black line. All simulations were performed with PLUTO.

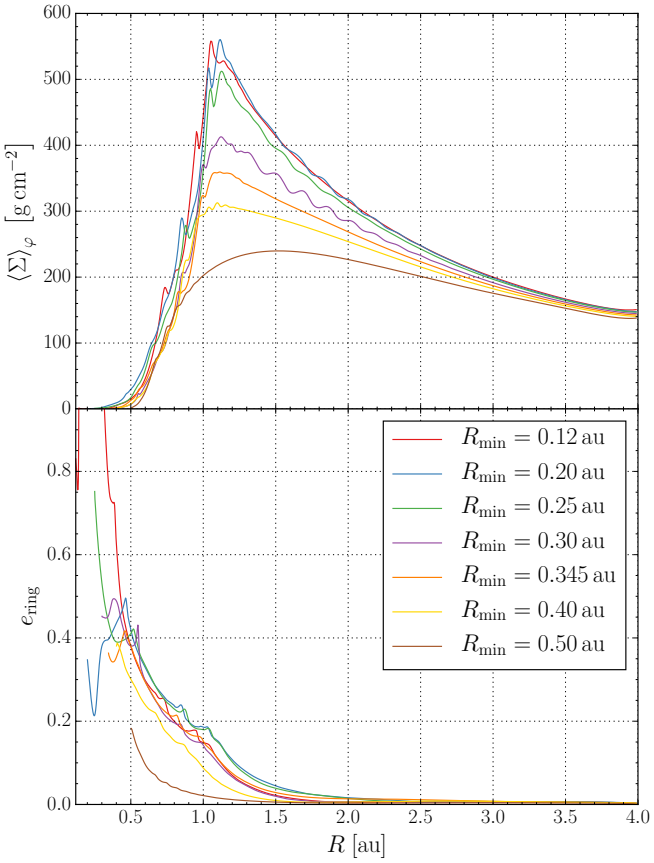

Fig. 5. Influence of different inner radii on the disc structure for simulations with a zero-gradient outflow inner boundary condition. *Top*: azimuthally averaged surface density profiles after 16 000 binary orbits. *Bottom*: radial disc eccentricity distribution at the same time.

in the fact that the viscous speed is very low in comparison to the radial velocity induced by the perturbations of the central binary and hence there is little difference between a closed and a viscous boundary.

In contrast to the closed inner boundary simulations, simulations with a zero-gradient outflow inner boundary reach a quasi-steady state. For the open boundaries PLUTO simulations with different numerical parameters produce very similar surface density and radial disc eccentricity profiles (Fig. 4) for different resolutions and grid spacings. Only the values for the uniform radial grid with a resolution of 395×512 (purple line in Fig. 4) deviate. Here the resolution in the inner computational domain is not high enough, because a simulation with a higher resolution uniform grid (790 × 512, orange line in Fig. 4) produces approximately the same results as the simulations with a logarithmic radial grid spacing.

We do not have a full explanation for this strong variability and non-convergence of the flow when using the closed inner boundary, but this result seems to imply that this problem is ill-posed. A closed inner boundary creates a closed cavity, which apparently implies in this case that the details of the flow depend sensitively on numerical diffusion as introduced by different spatial resolutions, time integrators, or codes. As a consequence, for circumbinary disc simulations a closed inner boundary is not recommended for two reasons. Firstly, it produces the described numerical instabilities and secondly, for physical reasons the inner boundary should be open because otherwise no material can flow into the inner region and be accreted by the stars. This is also indicated in Fig. 1 which shows mass flow through the inner gap, which cannot be modelled with a closed inner boundary.

4.2. Location of the inner radius

After determining that a zero gradient outflow condition is necessary, we use it now in all the following simulations and investigate in a second step the optimal location of $R_{\rm min}$. It should be placed in such a way that it simultaneously insures reliable results and computational efficiency. For the excitation of the disc eccentricity through the binary-disc interaction, nonlinear mode coupling, and the 3:1 Lindblad resonance are important (Pierens & Nelson 2013). Therefore, the location of the inner boundary is an important parameter and $R_{\rm min}$ should be chosen such that all major mean-motion resonances between the disc and the binary lie inside the computational domain. To investigate the influence of the inner boundary position, we set up simulations with an inner radius from $R_{\rm min}$ = 0.12 au to $R_{\rm min}$ = 0.5 au for the standard system parameter as noted in Table 2. Figure 5 shows the results of these simulations. Displayed are the azimuthally averaged surface density and the radial disc eccentricity distribution after 16 000 binary orbits. In agreement with Kley & Haghighipour (2014), we find that the radial disc

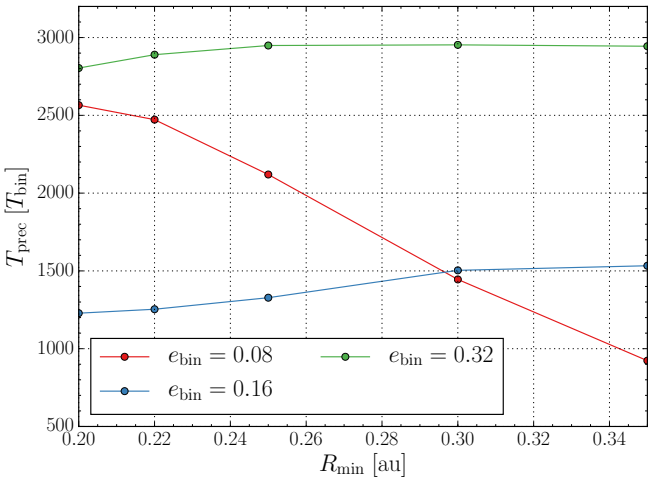

Fig. 6. Variation of precession period of the inner gap of the disc for varying inner radii, $R_{\rm min}$, and different binary eccentricities, $e_{\rm bin}$.

eccentricity does not depend much on the location of the inner radius and remains low in the outer disc ($R > 2$ au). Only for a large inner radius of $R_{\rm min} = 0.5$ au do we observe almost no disc eccentricity growth (brown line in Fig. 5). In this case the 3:1 Lindblad resonance ($R_{3:1} = 0.46$ au) lies outside the computational domain, confirming the conclusion from Pierens & Nelson (2013) about the importance of the 3:1 Lindblad resonance for the disc eccentricity growth. The variation of the radial disc eccentricity for inner radii smaller than 0.3 au occurs because the precessing discs are in different phases after 16 000 binary orbits. Contrary to the eccentricity distribution, the azimuthally averaged surface density shows a stronger dependence on the inner radius. As seen in the top panel of Fig. 5, the maximum of the surface density increases monotonically as the location of the inner boundary decreases because a smaller inner radius means also that the "area" where material can leave the computational domain decreases. For inner radii smaller than $R_{\rm min} \leq 0.25$ au the change in the maximum surface density becomes very low upon further reduction of $R_{\rm min}$. This implies that for too large $R_{\rm min}$ there is too much mass leaving the domain and it has to chosen small enough to capture all dynamics. Although the maximum value of the surface density increases, the position of the maximum does not depend on the inner radius and remains at approximately $R = 1.1$ au as long as the 3:1 Lindblad resonance lies inside the computational domain. Furthermore, we find that the slope of the surface density profile at the gap's edge does not depend on the location of the inner boundary. These results are in contrast to Mutter et al. (2017) who find a stronger dependence of the density profile on the location of the inner radius. However, their results may be a consequence of the viscous outflow condition used.

As is discussed below, the disc becomes eccentric with a slow precession that depends on the binary eccentricity, $e_{\rm bin}$. To explore how the location of the inner radius affects the disc dynamics, we ran additional simulations with varying $R_{\rm min}$ for different $e_{\rm bin}$. We chose $e_{\rm bin} = 0.08$ and $e_{\rm bin} = 0.32$ in addition to the Kepler-16 value of $e_{\rm bin} = 0.16$, which lies near the bifurcation point, $e_{\rm crit}$. Figure 6 shows the precession period of the inner gap for varying inner radii and three different binary eccentricities, where the blue curve refers to the model shown above with $e_{\rm bin} = 0.16$. For a higher binary eccentricity of $e_{\rm bin} = 0.32$ (green curve in Fig. 6 and on the upper branch of the bifurcation diagram) the disc dynamics seems to be captured well even for higher values of $R_{\rm min}$. Only for values lower than $R_{\rm min} = 0.22$ au are deviations seen. The simulation with $R_{\rm min} = 0.20$ au was more unstable, probably because the secondary moved in and out of the computational domain on its orbit. On the lower branch of the bifurcation diagram the convergence with decreasing $R_{\rm min}$ is slower as indicated by the case $e_{\rm bin} = 0.08$ (red curve in Fig. 6). Here, an inner radius of $R_{\rm bin} = a_{\rm bin}$ or even slightly lower may be needed. One explanation for this behaviour is that on the lower branch (for low $e_{\rm bin}$) the inner gap is smaller but nevertheless quite eccentric such that the disc is influenced more by the location of the inner boundary. The convergence of the results for smaller inner radii is also visible in the azimuthally averaged surface density and radial eccentricity profiles for $e_{\rm bin} = 0.08$ and $e_{\rm bin} = 0.32$ displayed in Fig. 7.

In summary, from the results shown in Figs. 5–7 we can conclude that to model the circumbinary disc properly, the inner radius should correspond to $R_{\rm min} \approx a_{\rm bin}$. This should be used in combination with a zero-gradient outflow (hereafter just outflow) condition. Since a smaller inner boundary increases the number of radial cells and imposes a stricter condition on the time step, long-term simulations with a small inner radius are very expensive. As a compromise to make long-term simulations possible, we have chosen in all simulations below an inner radius of $R_{\rm min} = 0.25$ au.

4.3. Location of the outer radius

While investigating the numerical conditions at the inner radius, we used an outer radius of $R_{\rm max} = 4.0$ au and assumed that this value is high enough, so that the outer boundary would not interfere with the dynamical behaviour of the inner disc. During our study of different binary and disc parameters, we found that in some cases this assumption is not true. Especially for binary eccentricities greater than 0.32, reflections from the outer boundary interfered with the complex inner disc structure. Therefore, we increased the outer radius of all the following simulations to $R_{\rm max} = 15.4$ au $= 70\,a_{\rm bin}$, a value used by Miranda et al. (2017). In order to keep the same spatial resolution as before we also increased the resolution to 762×582 cells. This ensures that in the radial direction we still have 512 grid cells between 0.25 au and 4.0 au. To save computational time it is also possible to use a smaller outer radius ($R_{\rm max} \approx 40\,a_{\rm bin}$) with a damping zone where the density and radial velocity are relaxed to their initial value. A detailed description of the implementation of such a damping zone can be found in de Val-Borro et al. (2006).

Hence, for our subsequent simulations we use from now on the numerical setup quoted in Table 2, unless otherwise stated. To study the dependence on different physical parameter we start from the standard values of the Kepler-16 system in Table 2 and vary individual parameter separately.

5. Variation of binary parameters

In this section we study the influence of the central binary parameter specifically its orbital eccentricity and mass ratio on the disc structure. Throughout this section we use a disc aspect ratio of $h = 0.05$ and a viscosity $\alpha = 0.01$. For the inner radius and the inner boundary condition we use the results from the previous section and apply the outflow condition at $R_{\rm min}$ (see also Table 2). All the results in this section were obtained with PLUTO, but comparison simulations using RH2D show very similar behaviour (see Fig. A.4).

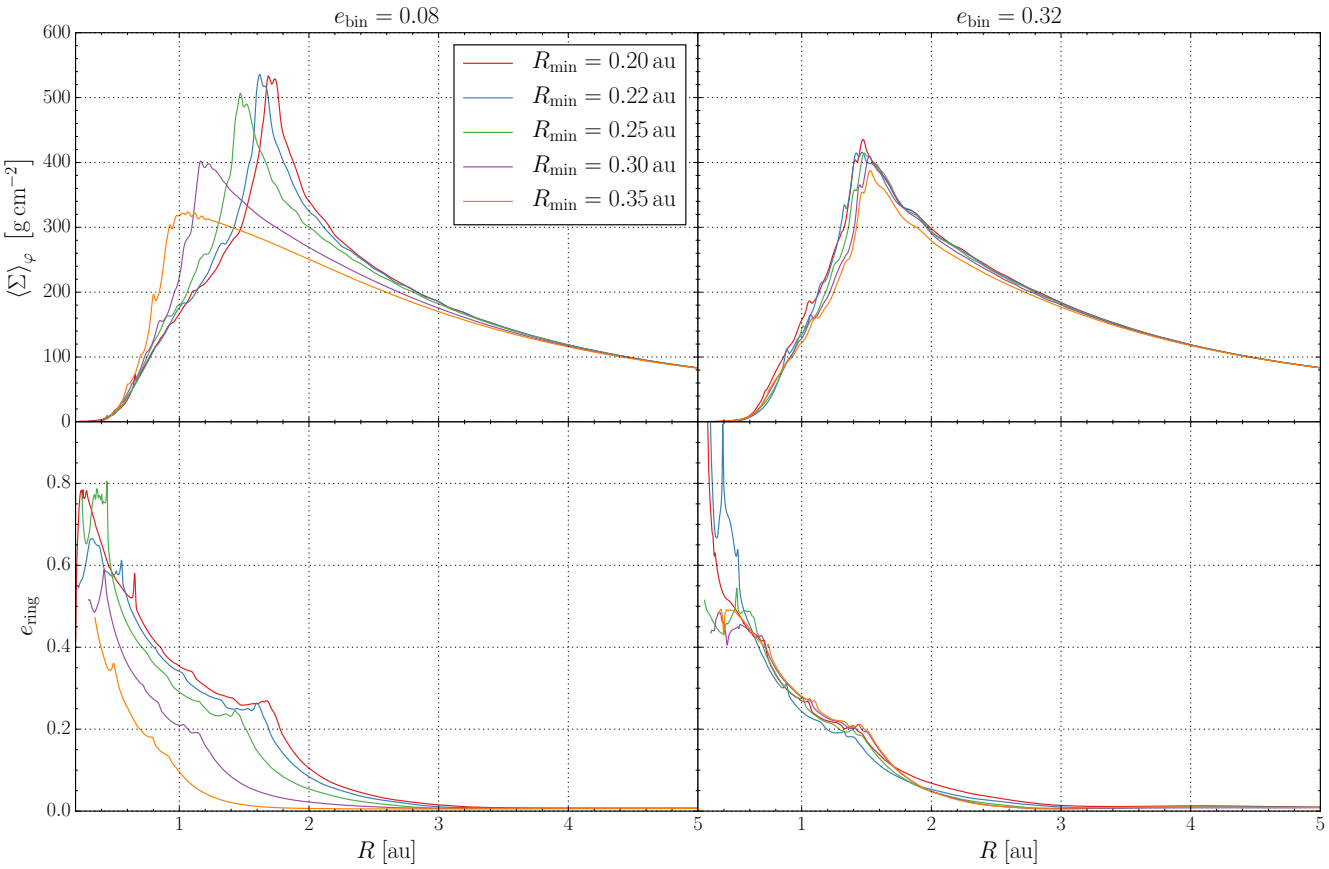

Fig. 7. Influence of different inner radii and binary eccentricities on the disc structure for simulations with a zero-gradient outflow inner boundary condition. *Top*: azimuthally averaged surface density profiles after 16 000 binary orbits. *Bottom*: radial disc eccentricity distribution at the same time. *Left*: $e_{\rm bin} = 0.08$. *Right*: $e_{\rm bin} = 0.32$.

5.1. Dynamics of the inner cavity

Before discussing in detail the impact of varying $e_{\rm bin}$ and $q_{\rm bin}$, we comment first on the general dynamical behaviour of the inner disc. Figure 8 shows snapshots of the inner disc after 16 000 binary orbits for different binary eccentricities. As seen in several other studies (as mentioned in the introduction) we find that the inner disc becomes eccentric and shows a coherent slow precession. In the figure we overplot ellipses (white dashed lines) that are approximate fits to the central inner cavity, where the semi-major axis ($a_{\rm gap}$) and eccentricity ($e_{\rm gap}$) are indicated. To calculate these parameters we assumed first that the focus of the gap-ellipse is the centre of mass of the binary. We then calculated from our data the coordinates $(R_{\Sigma\rm max}, \varphi_{\Sigma\rm max})$ of the cell with the highest surface density value, which defines the direction to the gap's apocentre. We defined the apastron of the gap $R_{\rm apa}$ as the minimum radius along the line $(R, \varphi_{\Sigma\rm max})$ which fulfils the condition

$$\Sigma(R, \varphi_{\Sigma\rm max}) \geq 0.1 \cdot \Sigma(R_{\Sigma\rm max}, \varphi_{\Sigma\rm max}). \tag{21}$$

The periastron of the gap $R_{\rm peri}$ is defined analogously as the minimum radius along the line $(R, \varphi_{\Sigma\rm max}+\pi)$ in the opposite direction which fulfils

$$\Sigma(R, \varphi_{\Sigma\rm max} + \pi) \geq 0.1 \cdot \Sigma(R_{\Sigma\rm max}, \varphi_{\Sigma\rm max}). \tag{22}$$

Using the apastron and periastron of the gap as defined above, the eccentricity and semi-major axis of the gap are given by

$$a_{\rm gap} = 0.5\left(R_{\rm apa} + R_{\rm peri}\right), \tag{23}$$

$$e_{\rm gap} = R_{\rm apa}/a_{\rm gap} - 1. \tag{24}$$

As shown in Fig. 8 this purely geometrical construction matches the shape of the central cavity very well. Even though the overall disc behaviour shows a rather smooth slow precession, the dynamical action of the central binary is visible as spiral waves near the gap's edges, most clearly seen in the first and last panel. We prepared some online videos to visualise the dynamical behaviour of the inner disc.

An alternative way to characterise the disc gap dynamically is by using the orbital elements $(e_{\rm max}, a_{\rm max})$ of the cell with the maximum surface density. These orbital elements can be calculated with Eq. (15) and the vis-viva equation

$$a = \left(\frac{2}{R} - \frac{\boldsymbol{u}^2}{GM_{\rm bin}}\right)^{-1}. \tag{25}$$

The time evolution of these gap characteristics are plotted in Fig. 9. The gap's size and eccentricity show in phase oscillatory behaviour with a larger amplitude in the eccentricity variations. The period of the oscillation is identical to the precession period of the disc. Clearly, the extension of the gap always lies inside of the location of maximum density $a_{\rm gap} < a_{\rm max}$, but for the

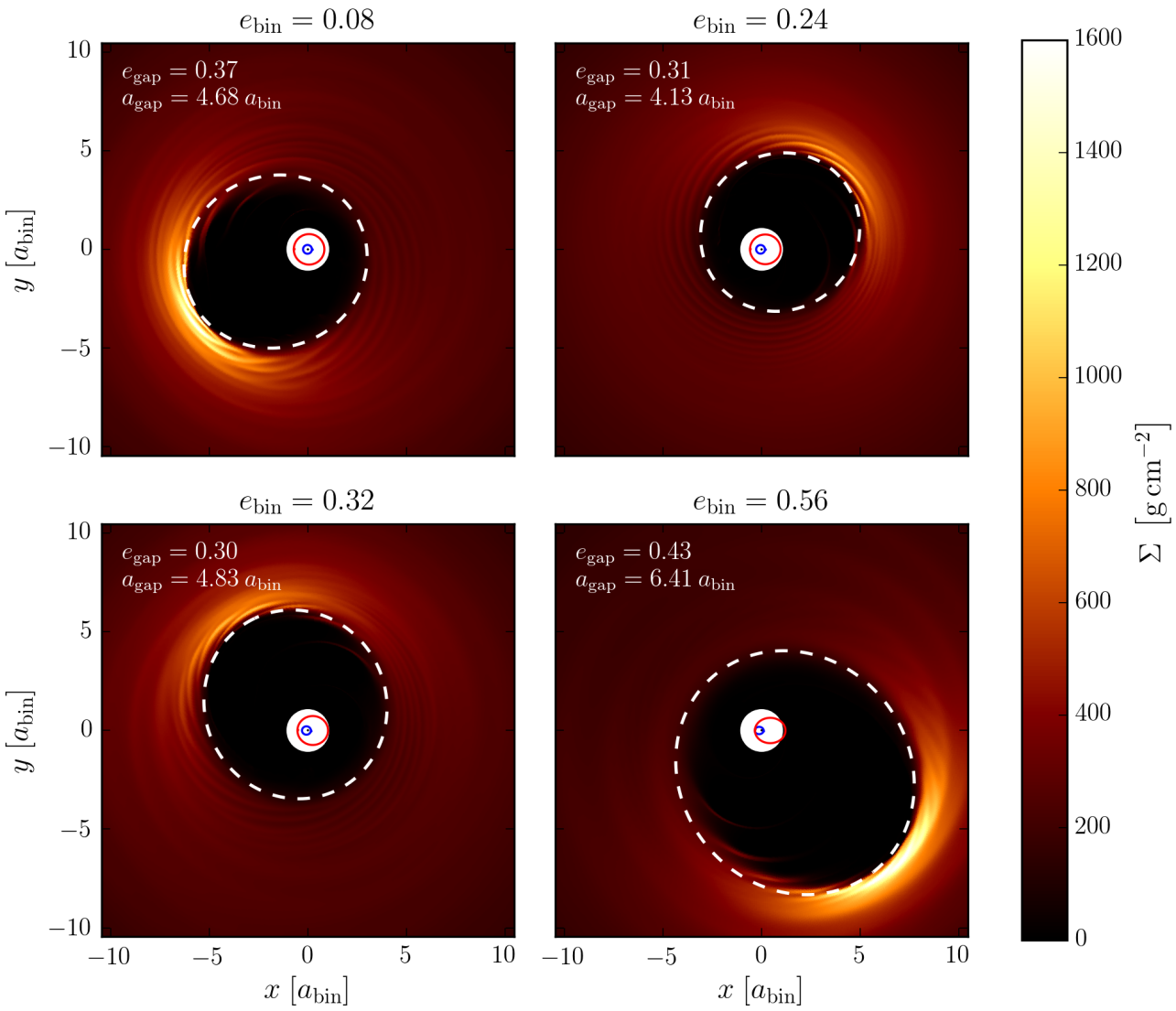

Fig. 8. Structure of the inner disc for different binary eccentricities after 16 000 binary orbits. The surface density is colour-coded in cgs-units. The orbits of the primary and secondary around the centre of mass (central point) are shown in blue and red. The white dashed lines represent approximate ellipses fitted to match the extension of the inner gap (see explanation in text). Videos of these simulations can be found online.

eccentricities the ordering is not so clear. The radial variations of the disc eccentricity as shown in Figs. 4 and 5 indicate that the inner regions of the disc typically have a higher eccentricity. In Fig. 9 $e_{\rm disc}$ is lowest because it is weighted with the density which is very low in the inner disc regions. The eccentricity for the gap $e_{\rm gap}$ stems from a geometric fit to the very inner disc regions and is the highest. Inside the maximum density and even slightly beyond that radius the disc precesses coherently in the sense that the pericentres estimated at different radii are aligned. The data show further that when the disc eccentricity is highest the disc is fully aligned with the orbit of the secondary star, i.e. the pericentre of disc and binary lie in the same direction (see also Appendix A).

5.2. Binary eccentricity

For simulations in this section we fixed $q_{\rm bin} = 0.29$ and varied $e_{\rm bin}$ from 0.0 to 0.64. The binary eccentricity strongly influences the size of the gap as well as the disc precession period of the inner disc.

In Fig. 10 the azimuthally averaged surface density profiles are shown for the various $e_{\rm bin}$ at 16 000 binary orbits. In all cases there is a pronounced density maximum visible which is the strongest for the circular binary with $e_{\rm bin} = 0$ (red curve). The position of the peak varies systematically with binary eccentricity. Increasing $e_{\rm bin}$ from zero to higher values the peak shifts inward. Not only does the gap size decrease, but the maximum surface density also drops with increasing $e_{\rm bin}$ until a minimum at $e_{\rm bin} = 0.18$ is reached. Increasing $e_{\rm bin}$ further causes the density peak to move outward again, whereas the maximum surface density stays roughly constant for higher binary eccentricities.

As mentioned above, the eccentric disc precesses slowly and in Fig. 11 the longitude of the inner disc's pericentre is shown versus time over 16 000 binary orbits. The disc displays a slow prograde precession with inferred period of several thousand binary orbits. For the measurement of the precession period

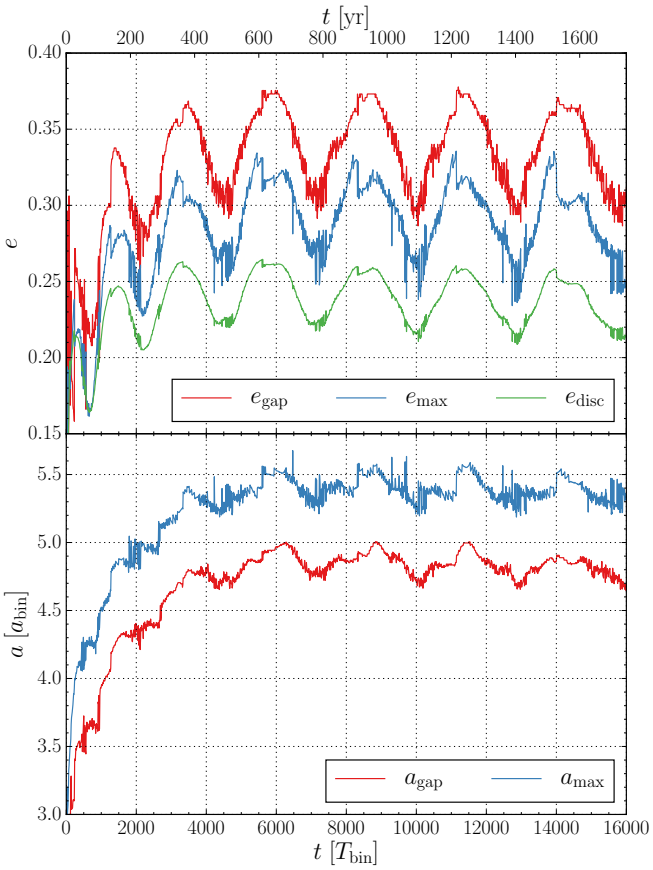

Fig. 9. Evolution of gap eccentricity (*top*) and semi-major axis (*bottom*) for a binary with $e_{\rm bin} = 0.30$. Shown are different measurements for the disc eccentricity. The red lines ($e_{\rm gap}$ and $a_{\rm gap}$) show the eccentricity and semi-major axis of the geometrically fitted ellipses, see Fig. 8. The blue lines ($e_{\rm max}$ and $a_{\rm max}$) show the eccentricity and semi-major axis of the cell with the maximum surface density. The green curve shows the averaged eccentricity of the inner disc. Since the gap size varies with time we use $R_2 = R_{\Sigma{\rm max}}$ in Eq. (18) to calculate the inner disc eccentricity.

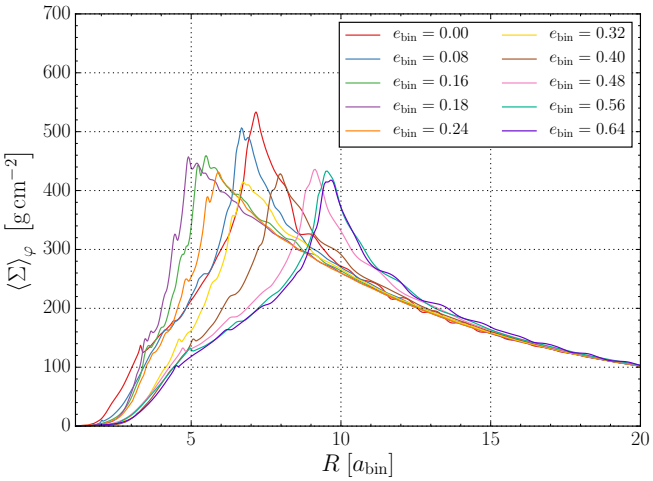

Fig. 10. Azimuthally averaged density profiles for varying binary eccentricities after 16 000 binary orbits. For clarity we only show selected results from the simulated parameter space.

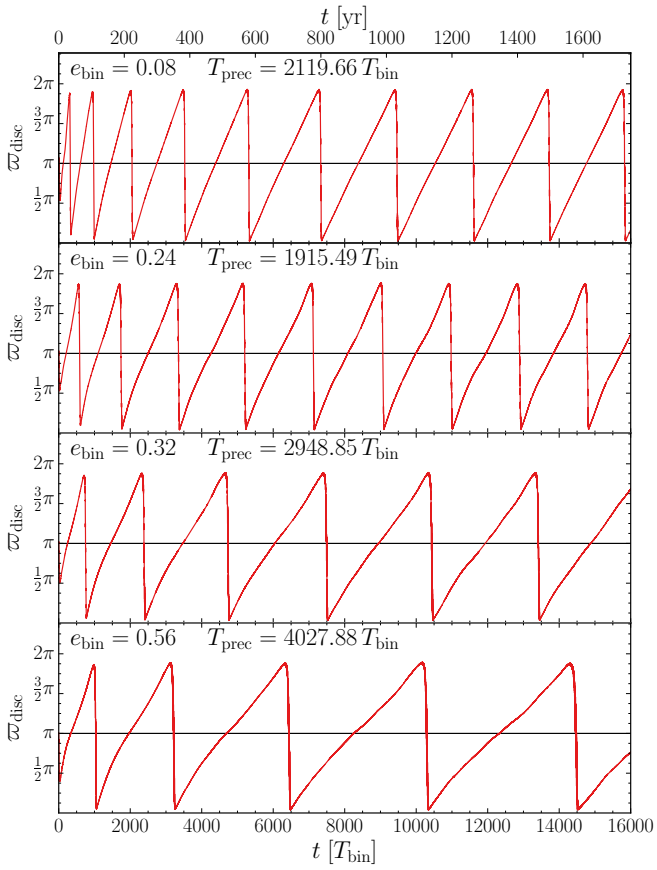

Fig. 11. Disc longitude of periastron for different binary eccentricities for the inner disc $R < 1.0$ au. For all cases a clear prograde precession of the inner disc is visible and the precession period, $T_{\rm prec}$, is indicated in the legend.

we discarded the first 6000 binary orbits since plots of the longitude of periastron show that during this time span the precession period is not constant yet (see Fig. 11). The period is then calculated by averaging over at least two full periods. To be able to average over two periods, models with a very long $T_{\rm prec}$ (e.g. $e_{\rm bin} = 0.64$) were simulated for more than 16 000 binary orbits.

Figure 12 summarises the results from simulations with varying binary eccentricities. The top panel of Fig. 12 shows different measures for the gap size for varying binary eccentricities. In addition to the radial position where the azimuthally averaged surface density reaches its maximum ($R_{\rm peak}$), we plot the positions where the density drops to 50 and 10 percent of its maximum value ($R_{0.5}$ and $R_{0.1}$). The value $R_{0.5}$ was used by Kley & Haghighipour (2014) as a measure for the gap size, whereas Miranda et al. (2017) used $R_{0.1}$ and Mutter et al. (2017) $R_{\rm peak}$. Starting from a non-eccentric binary the curves for $R_{\rm peak}$ and $R_{0.5}$ decrease with increasing binary eccentricity. For $e_{\rm bin} \approx 0.18$ the gap size reaches a minimum and then increases again for higher binary eccentricities. In agreement with Miranda et al. (2017) we see an almost monotonic increase of $R_{0.1}$ for increasing binary eccentricities. The gap size, $a_{\rm gap}$, correlates well with $R_{0.5}$ and is always about 14% smaller.

The middle panel of Fig. 12 shows the eccentricity of the inner cavity, calculated with the method described in Sect. 5.1. The disc eccentricity also changes systematically with $e_{\rm bin}$. For circular binaries it reaches $e_{\rm gap} \approx 0.44$, and then it drops down to about 0.25 for the turning point $e_{\rm bin} = 0.18$, and increases

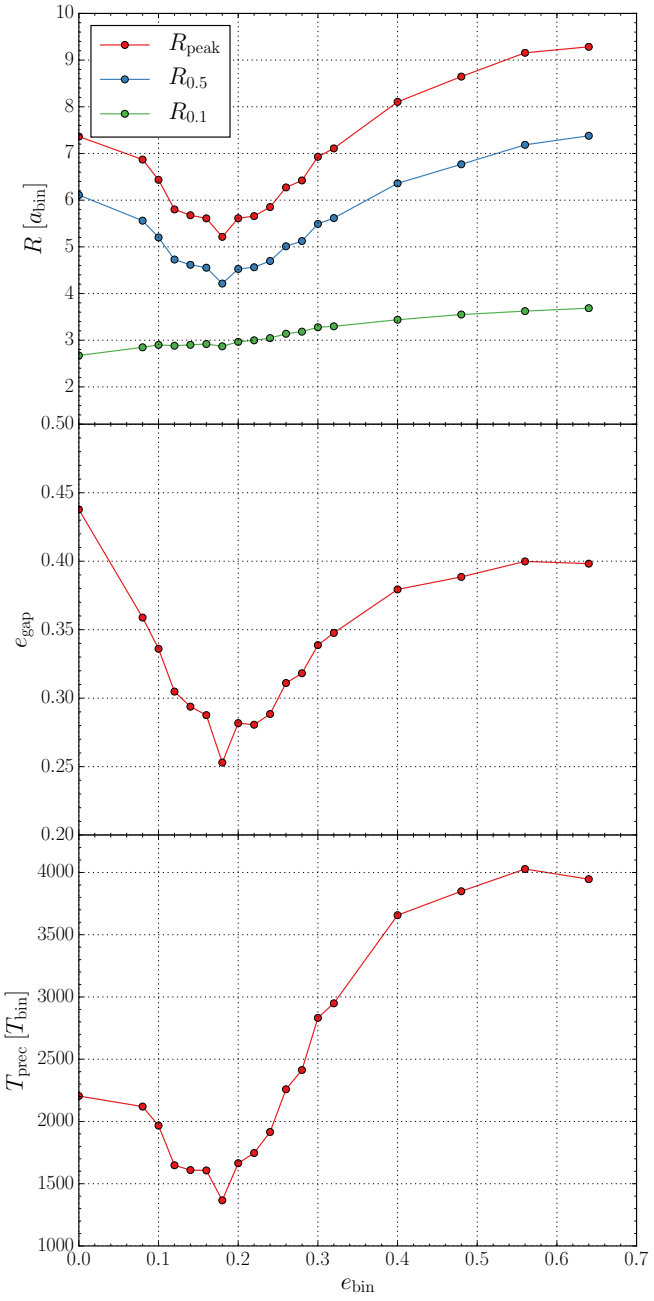

Fig. 12. Influence of different binary eccentricities on gap size, gap eccentricty, and precession rate. *Top*: different measures of the gap size are shown, averaged over several thousand binary orbits. The value $R_{\rm peak}$ refers to the location of maximum of the averaged surface density (see Fig. 10), while $R_{0.5}$ and $R_{0.1}$ refer to density drops of 50 and 10 percent of the maximum value. *Middle*: eccentricity of the gap. *Bottom*: precession period of the disc gap.

again reaching $e_{\rm gap} \approx 0.4$ for the highest $e_{\rm bin} = 0.64$. Hence, for nearly circular binaries $e_{\rm gap}$ can be higher than for more eccentric binaries. A similar variation of the disc's eccentricity and precession rate with binary eccentricity has been noticed by Fleming & Quinn (2017) who attribute this to the possible excitation of higher order resonances for higher disc eccentricities.

The bottom panel of Fig. 12 shows the precession period of the inner disc ($R < 1$ au) for different binary eccentricities. The curve for the precession period shows a similar behaviour to the

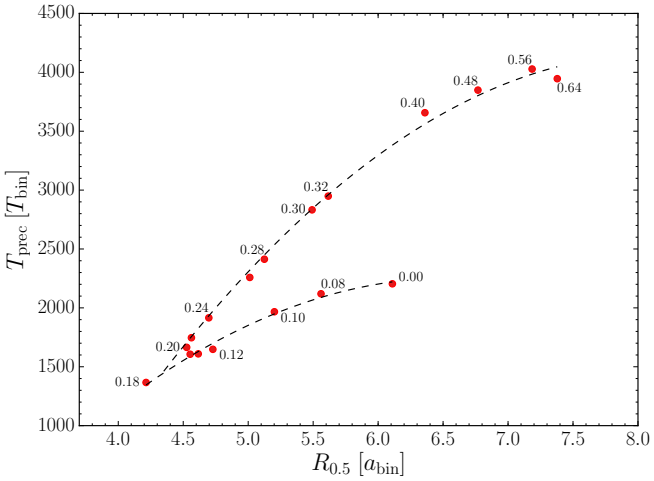

Fig. 13. Precession rate of the gap plotted against the radius where the azimuthally averaged surface density drops to 50 percent of its maximum value ($R_{0.5}$), averaged over several thousand binary orbits. Different dots correspond to different binary eccentricities. The dashed lines are not fit curves but are just drawn to guide the eye.

upper curves for the gap size. To investigate further the correlation of the gap size (here represented by $R_{0.5}$) and the precession period, we show in Fig. 13 the two quantities plotted against each other. Two branches can be seen as indicated by the dashed curves. One starts at $e_{\rm bin} = 0.0$ and goes to $e_{\rm bin} = 0.18$ where the gap size and precession period decrease with increasing binary eccentricities, and the other branch starts at the minimum at $e_{\rm bin} = 0.18$ where both gap properties increase again with increasing binary eccentricities. These two branches may indicate two different physical processes that are responsible for the creation of the eccentric inner gap and show the direct correlation between precession period and gap size.

In our simulations all discs became eccentric and showed a prograde precession, and we did not find any indication for "stand still" discs that are eccentric but without any precession. In contrast, Miranda et al. (2017) find for their disc setup ($h = 0.1, \alpha = 0.1$) that the disc does not precess for binary eccentricities between 0.2 and 0.4. We do not find this behaviour for our disc models, but note that we use a disc with a lower aspect ratio and a lower α-value. To investigate this further we set up a simulation with the same numerical parameters as Miranda et al. (2017) and used a physical setup where they did not observe a precession of the disc ($q_{\rm bin} = 1.0$, $e_{\rm bin} = 0.4$, $h = 0.1$, and $\alpha = 0.1$). We carried out two simulations, one with an inner radius of $R_{\rm min} = (1 + e_{\rm bin})a_{\rm bin}$ and one with an inner radius of $R_{\rm min} = 1.136\,a_{\rm bin}$. The first radius was used by Miranda et al. (2017) and in this case we also observe no precession of the disc. The second radius corresponds to $R_{\rm min} = 0.25$ au, which is the radius we established in Sect. 4.2 as the optimum location of the inner boundary. In the case with the smaller inner radius we observe a clear precession of the inner disc (Fig. 14) with a relatively short precession period $T_{\rm prec}$ as expected for high viscosity and high h (see below). This is another indication of the necessity of choosing $R_{\rm min}$ sufficiently small to capture all effects properly.

5.3. Binary mass ratio

In this section we study the influence of the binary mass ratio. We carried out simulations with a mass ratio from $q_{\rm bin} = 0.1$

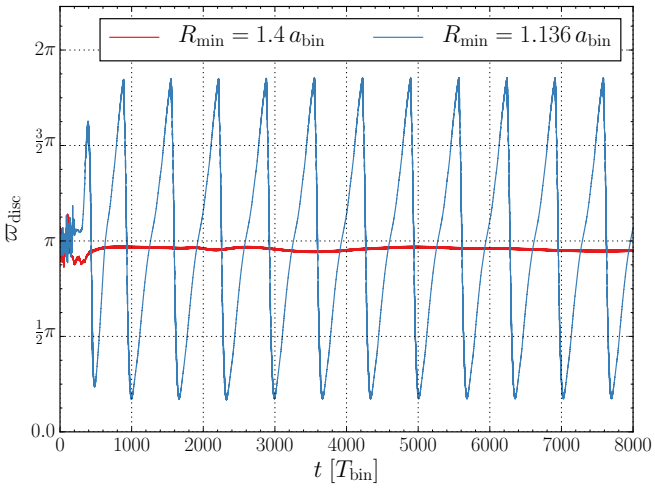

Fig. 14. Disc longitude of periastron for different inner radii of the computational domain. The red line shows results from a simulation with the Miranda et al. (2017) setup where no precession of the disc is observable. The blue line shows results from the same physical setup but with a smaller inner disc radius. In this case a clear precession of the inner disc is visible.

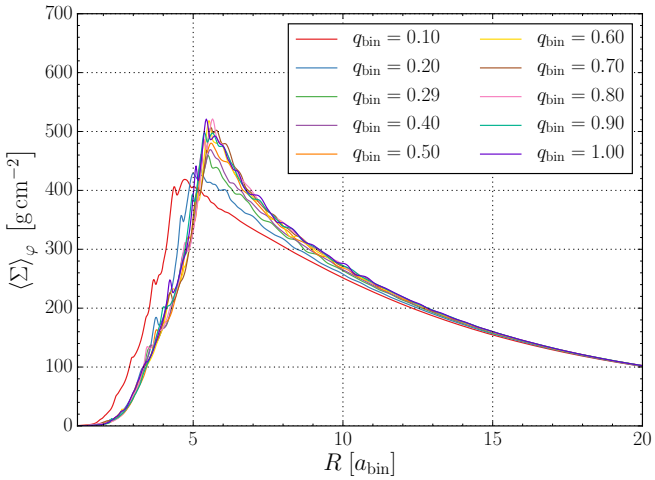

Fig. 15. Azimuthally averaged density profiles for varying binary mass ratio after 16 000 binary orbits.

to $q_{\rm bin} = 1.0$; all other parameters were set according to Table 2. Figure 15 shows the azimuthally averaged density profiles for varying binary mass ratios. The density profiles do not show such a strong variation as in simulations with varying binary eccentricities. Only the density profiles of the two lowest simulated mass ratios $q_{\rm bin} = 0.1$ and $q_{\rm bin} = 0.2$ differ significantly from the other profiles. For these models the position of the peak surface density is closer to the binary and the maximum surface density roughly 20 percent lower. The different gap size measures, introduced in the previous section, are shown in the top panel of Fig. 16. In general, the variations of all three gap-size indicators with mass ratio $q_{\rm bin}$ are relatively weak. All three gap size measurements remain nearly constant for mass ratios greater than 0.3. Since the density profiles do not show a significant variation this is not surprising. At the same time the size and eccentricity of the gap do not vary significantly and lie in the range $a_{\rm gap} \approx 4\,a_{\rm bin}$ and $e_{\rm gap} \approx 0.27$. Overall, compared to simulations with varying binary eccentricity the binary mass ratio

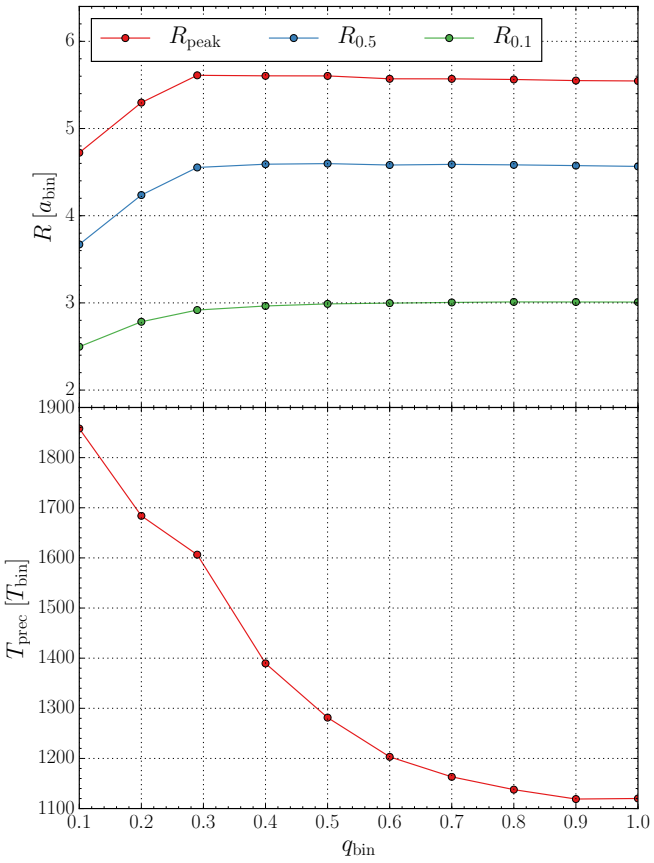

Fig. 16. Influence of different binary mass ratios on gap size and precession rate. *Top*: different measures of the gap size averaged over several thousand binary orbits. *Bottom*: precession period of the disc gap.

does not have such a strong influence on the inner disc structure for $q_{\rm bin} \gtrsim 0.3$.

In contrast, the precession period of the inner disc shows a far stronger dependence on the binary mass ratio than the gap size (bottom panel of Fig. 16). Discs around binaries with a higher mass ratio have a lower precession period than discs around binaries with a low mass ratio. This dependence can be understood in terms of free particle orbits around a binary star that also display a reduction of the precession period with increasing q, as we discuss in more detail in Appendix B.

6. Variation of disc parameters

In this section we explore the influence of discs parameters, namely the aspect ratio and the alpha viscosity, on the inner disc structure. We use the Kepler-16 values for the binary and our standard numerical setup (Table 2).

While performing the simulations for this paper we observed that models with low pressure (low H/R) and high viscosity (high α) seem to be very challenging for the Riemann-Code PLUTO. As a consequence we also present in this section results using the Upwind-Code RH2D. As discussed in Appendix A, the two codes produce results in very good agreement with each other for our standard model. For other parameters they do not necessarily produce results with such good agreement, but the simulation results from both codes always show the same trend. Therefore, we decided to mix simulation results from PLUTO and RH2D to cover a broader parameter range.

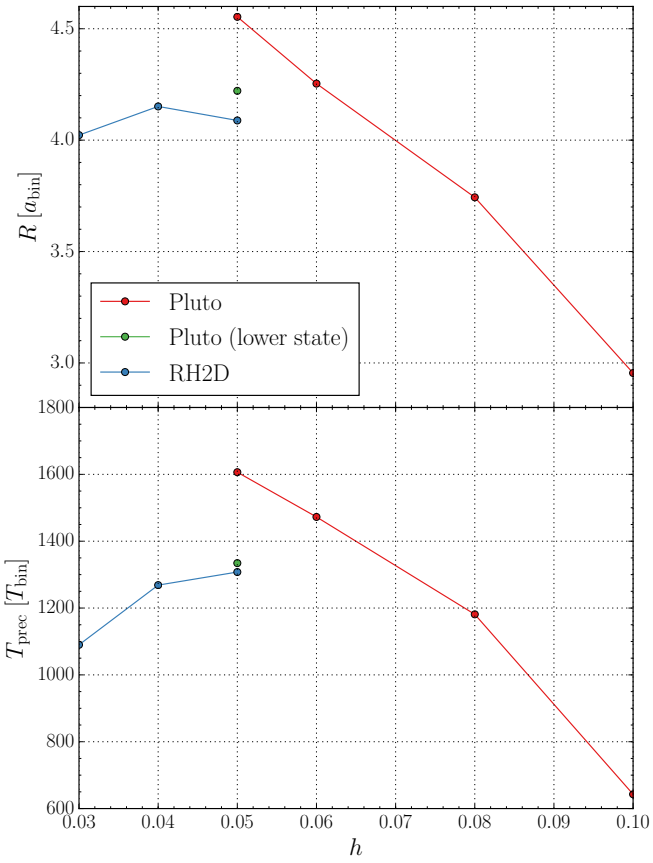

Fig. 17. Influence of different disc aspect ratios on gap size and precession rate. *Top*: radius where the density drops to 50 percent of its maximum value averaged over several thousand binary orbits. Since results from two different codes are shown, we omit the two other measurements for the gap size presented in previous sections. *Bottom*: precession period of the disc gap. For $e_{\rm bin} \approx 0.16$ we observed that PLUTO simulations can switch between two states, an upper state (red) and a lower state (green). For RH2D simulations we only observed the lower state (blue). This is discussed in more detail in Appendix A.

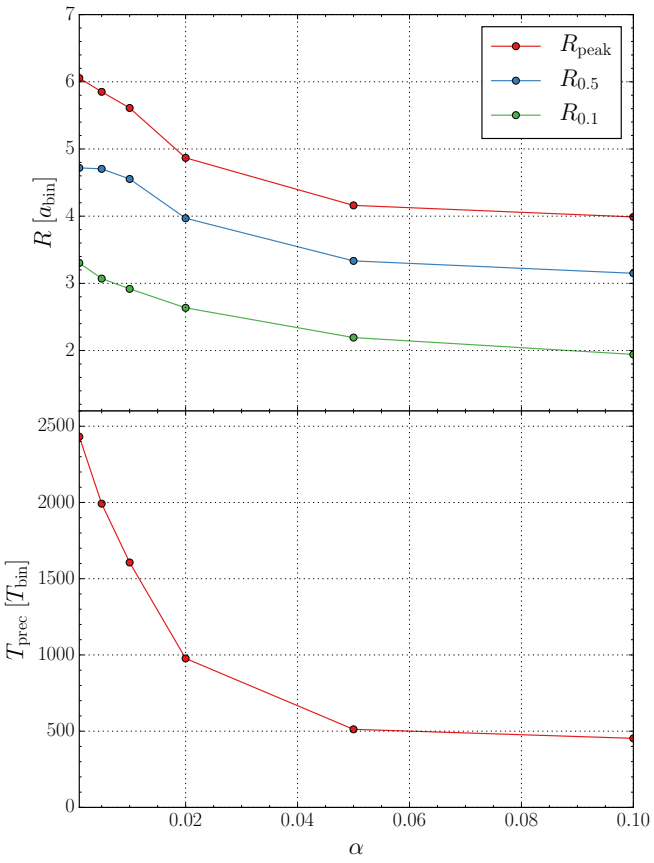

Fig. 18. Influence of different disc viscosities on gap size and precession rate. *Top*: different measures of the gap size averaged over several thousand binary orbits. *Bottom*: precession period of the disc gap.

6.1. Disc aspect ratio

First we varied the disc aspect ratio h from 0.03 to 0.1. Our simulation results show a decreasing gap size for higher aspect ratios (Fig. 17). The gaps precession period is again directly correlated to the gap size, an observation we have already seen for different binary eccentricities. In general, a drop in $T_{\rm prec}$ with higher h is expected because an increase in pressure will tend to reduce the gap size, which will in turn lead to a faster precession. This trend is indeed observed in our simulations for higher h. For simulations with $h < 0.05$ we observed a decrease in gap size and precession period. The drop in $T_{\rm prec}$ with lower values of h may be partly due to the lack of numerical resolution and partly to the lack of pressure support, which may no longer allows for coherent disc precession.

6.2. Alpha viscosity

In this section we discuss the influence of the magnitude of viscosity on the disc structure and therefore set up simulations with different viscosity coefficients ranging from $\alpha = 0.001$ to $\alpha = 0.1$. We then analysed the structure and behaviour of the inner cavity as before. The results are summarised in Fig. 18. A clear trend is visible for the gap size and for the precession period of the gap. For higher viscosities the gap size shrinks and the precession period decreases. Again, we see the direct correlation of gap size and precession rate, as already observed for aspect ratio and binary eccentricity variations. The decrease in the disc's gap size can be explained: for higher α values the viscous spreading of the disc increases. This viscous spreading counteracts the gravitational torques of the binary, which are responsible for the gap creation.

7. Summary and discussion

Using two-dimensional hydrodynamical simulations, we studied the structure of circumbinary discs for different numerical and physical parameters. Since these simulations are, from a numerical point of view, not trivial and often it is not easy to distinguish physical features and numerical artefacts, we checked our results with three different numerical codes. In the following we summarise the most important results from our simulations with different numerical and physical parameters.

Concerning the numerical treatment the most crucial issue with simulations using grid codes in cylindrical coordinates is the treatment of the inner boundary condition. As there has been some discussion in the literature about this issue (Pierens & Nelson 2013; Kley & Haghighipour 2014; Lines et al. 2015; Miranda et al. 2017; Mutter et al. 2017), we decided to perform a careful study of the location of the inner

boundary and the conditions on the hydrodynamical variables at $R_{\rm min}$. Our results can be summarised as follows:

- *Inner boundary condition*. Since there was no agreement on which type of inner boundary condition should be used for circumbinary disc simulations, especially if closed or open boundary conditions should be used, we investigated the influence of the inner boundary condition through dedicated simulations with two different codes. We observed that closed boundaries can lead to numerical instabilities for all codes used in our comparison and no convergence to a unique solution could be found. The use of a viscous outflow condition where the velocity is set to the mean viscous disc speed produced very similar results to the closed boundary because the viscous speed is very low in comparison to the velocities induced by the dynamical action of the binary stars. Open inner boundaries, on the other hand, lead to numerically stable results and are also, from a physical point of view, more logical because material can flow onto the binary and be accreted by one of the stars. Hence, open boundaries with free outflow are the preferred conditions at $R_{\rm min}$.
- *Location of inner boundary*. The location of the inner boundary is also an important numerical parameter. Since an inner hole in the computational domain cannot be avoided in polar coordinates, the inner radius has to be sufficiently small to capture all relevant physical effects. In particular, all important mean motion resonances, which may be responsible for the development of the eccentric inner cavity, should lie inside the computational domain. Through a parameter study we were able to determine that the radius of the inner boundary $R_{\rm min}$ has to be of the order of the binary separation $a_{\rm bin}$ to capture all physical effects in a proper way.

After having determined the best values for the numerical issues we performed, in the second part of the paper a careful study to determine the physical aspects that determine the dynamics of circumbinary discs. Starting from a reference model, where we chose the binary parameter of Kepler-16, we varied individual parameters of the binary and the disc and studied their impact on the disc dynamics. First of all, for all choices of our parameters the models produce an eccentric inner disc that shows a coherent prograde precession. However, the size of the gap, its eccentricity, and its precession rate depend on the physical parameters of binary and disc. Our results can be summarised as follows:

- *Binary parameters*. To study the influence of the binary star on the disc we systematically varied the eccentricity ($e_{\rm bin}$) and the mass ratio ($q_{\rm bin}$) of the binary. The parameter study showed that $e_{\rm bin}$ has a strong influence on the gap size and on the precession period of the gap. We found that two regimes exist where the disc behaves differently to an increasing binary eccentricity (see Fig. 8). The two branches bifurcate at a critical binary eccentricity, $e_{\rm crit} = 0.18$ from each other. From $e_{\rm bin} = 0.0$ to $e_{\rm crit}$ the gap size and precession period decrease, and from $e_{\rm bin} = 0.18$ onward both gap parameters become larger again, as displayed in Fig. 13. The bifurcation of the two branches near $e_{\rm crit} = 0.18$ strongly suggests that different physical mechanisms, responsible for the creation of the eccentric inner cavity, operate in the two regimes. For the lower branch the excitation at the 3:1 outer Lindblad resonance may be responsible, which is supported by a simulation where the inner boundary was outside the 3:1 radius and no disc eccentricity was found. For the upper branch (high $e_{\rm bin}$) non-linear effects may be present, as suggested by Fleming & Quinn (2017) who found similar behaviour.

  As second binary parameter we varied the mass ratio of the secondary to the primary star, $q_{\rm bin}$, between $[0.1, 1.0]$ and studied its impact on the gap size and precession period. Overall the variation of $R_{0.5}$ with $q_{\rm bin}$ is weak. For low $q_{\rm bin}$ the gap size increases until it becomes nearly constant for $q_{\rm bin} \gtrsim 0.3$ with $R_{0.5} \approx 4.6\, a_{\rm bin}$, as shown in Fig. 16. The precession period decreases on average with increasing $T_{\rm prec}$ and for large $q_{\rm bin}$ the behaviour is equivalent to a single particle at a separation of 4.9 au, as we discuss in more detail in Appendix B.
- *Disc parameters*. We also varied different disc parameters, namely the pressure (through the aspect ratio $h = H/R$) and the viscosity (through α). The results are displayed in Figs. 17 and 18. For changes in the aspect ratio no clear trend was visible; both gap size and precession period first increase with increasing h until they reach a maximum at $h = 0.05$; from there both gap properties decrease again with increasing aspect ratio. For high h the behaviour can be understood in term of the gap closing tendency of higher disc pressure. On the other hand, for very low pressure it may be more difficult to sustain a coherent precession of a large inner hole in the disc due to the reduced sound speed. Additionally, the damping action of the viscosity becomes more important for discs with lower sound speed.

  A clear monotonic trend was visible for the viscosity variation, where higher α leads to smaller gaps and shorter gap precession periods. This can be directly attributed to the gap closing tendency of viscosity.

To allow for an alternative view of the impact of different binary and disc parameters on the dynamical structure of the disc we display in Fig. 19 the eccentricity (top) and the precession period (bottom) of the gap plotted against the semi-major axis of the gap for all our simulations where different colours stand for different model series. PLUTO simulations are represented by dots whereas squares stand for RH2D simulations. The reference model is marked with a star. Interestingly the majority of the models lie on a main-sequence branch, which has the trend of increasing eccentricity and precession period with increasing gap width. The smaller branch that bifurcates near the reference model represents the low $e_{\rm bin}$ sequence, which has higher $e_{\rm gap}$ but smaller $T_{\rm prec}$. By coincidence, our reference model with the Kepler-16 parameters lies near the bifurcation point.

How the location of the bifurcation point depends of the disc and binary parameter needs to be explored in subsequent numerical studies. A first simulation series with $q_{\rm bin} = 0.6$ suggest that this critical eccentricity does not depend on the mass ratio of the binary. As outlined in the Appendix, for parameters very near to the critical $e_{\rm bin}$ the models can have the tendency to switch between the two states during a single simulation. The physical cause of the bifurcation needs to be analysed in subsequent simulations.

In addition, there are a more possibilities to further improve our model. First, the use of a non-isothermal equation should be considered to study the effects of viscous heating and radiative cooling. Especially for simulations, which also evolve planets inside the disc, Kley & Haghighipour (2014) showed that radiative effects should been taken into account. Self-gravity effects have been studied by Lines et al. (2015) and Mutter et al. (2017) and are important for galactic discs around a central binary black hole. The backreaction of the disc onto the binary could also be considered in more detail. Angular momentum exchange with the binary occurs through gravitational torques from the disc and direct accretion of angular momentum from the material

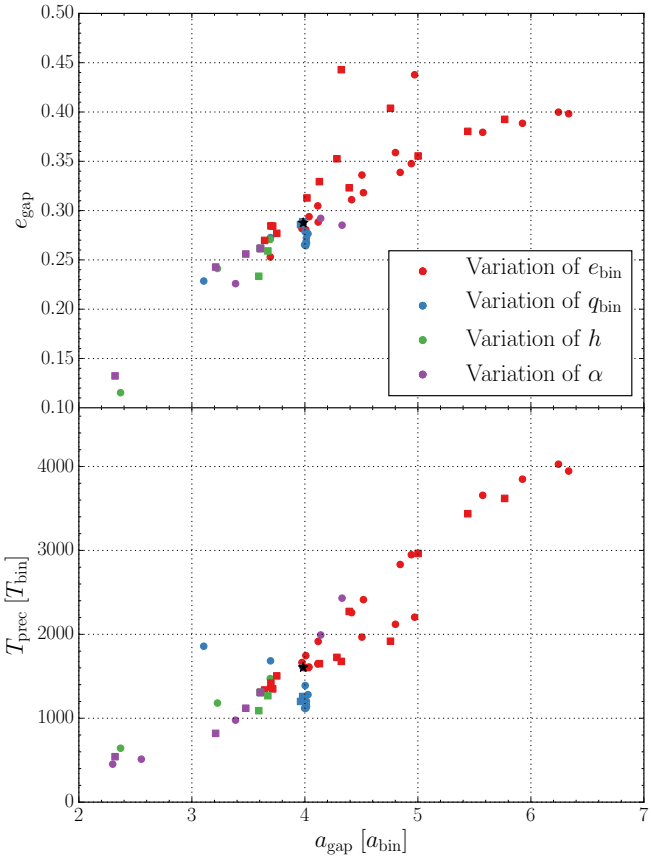

Fig. 19. Eccentricity (*top*) and precession period (*bottom*) of the inner gap plotted against the semi-major axis of the gap. Different simulation series are colour-coded. Both the measured gap eccentricity and gap semi-major axis are averaged over several thousand binary orbits. PLUTO simulations are represented by dots and squares stand for RH2D simulations. The reference model with Kepler-16 parameters is marked with the star.

that enters the central cavity. The first part always leads a decrease in the binary semi-major axis and an increase in eccentricity (Kley & Haghighipour 2015), while Miranda et al. (2017) pointed out that angular momentum advection might even be dominant leading to a binary separation.

Another interesting question is the evolution of planets inside the circumbinary disc and their influence on the disc structure. Since an in situ formation of the observed planets seems very unlikely, the migration and final parking position of planets is an interesting topic that requires further investigations. In view of our extensive parameter studies there is the indication that in several past studies (Pierens & Nelson 2013; Kley & Haghighipour 2014, 2015) an inner radius was considered that was too large and that did not allow for full disc dynamics.

Through fully three-dimensional simulations it will be possible to study the dynamical evolution of inclined discs.

Acknowledgements. Daniel Thun was funded by grant KL 650/26 of the German Research Foundation (DFG), and Giovanni Picogna acknowledges DFG support grant KL 650/21 within the collaborative research program "The first 10 Million Years of the Solar System". Most of the numerical simulations were performed on the bwForCLuster BinAC, supported by the state of Baden-Württemberg through bwHPC, and the German Research Foundation (DFG) through grant INST 39/963-1 FUGG. All plots in this paper were made with the Python library matplotlib (Hunter 2007).

References

Andrews, S. M., Chandler, C. J., Isella, A., et al. 2014, ApJ, 787, 148
Armitage, P. J., & Natarajan, P. 2002, ApJ, 567, L9
Artymowicz, P., Clarke, C. J., Lubow, S. H., & Pringle, J. E. 1991, ApJ, 370, L35
Artymowicz, P., & Lubow, S. H. 1994, ApJ, 421, 651
Artymowicz, P., & Lubow, S. H. 1996, ApJ, 467, L77
Baruteau, C., & Masset, F. 2008, ApJ, 672, 1054
Bate, M. R., Bonnell, I. A., & Bromm, V. 2002, MNRAS, 336, 705
Begelman, M. C., Blandford, R. D., & Rees, M. J. 1980, Nature, 287, 307
Cuadra, J., Armitage, P. J., Alexander, R. D., & Begelman, M. C. 2009, MNRAS, 393, 1423
de Val-Borro, M., Edgar, R. G., Artymowicz, P., et al. 2006, MNRAS, 370, 529
Di Folco, E., Dutrey, A., Le Bouquin, J.-B., et al. 2014, A&A, 565, L2
D'Orazio, D. J., Haiman, Z., Duffell, P., MacFadyen, A., & Farris, B. 2016, MNRAS, 459, 2379
Doyle, L. R., Carter, J. A., Fabrycky, D. C., et al. 2011, Science, 333, 1602
Dunhill, A. C., Cuadra, J., & Dougados, C. 2015, MNRAS, 448, 3545
Dutrey, A., di Folco, E., Guilloteau, S., et al. 2014, Nature, 514, 600
Dutrey, A., Di Folco, E., Beck, T., & Guilloteau, S. 2016, A&ARv, 24, 5
Fleming, D. P., & Quinn, T. R. 2017, MNRAS, 464, 3343
Georgakarakos, N., & Eggl, S. 2015, ApJ, 802, 94
Guilloteau, S., Dutrey, A., & Simon, M. 1999, A&A, 348, 570
Günther, R., & Kley, W. 2002, A&A, 387, 550
Hawley, J. F., Smarr, L. L., & Wilson, J. R. 1984, ApJS, 55, 211
Hunter, J. D. 2007, Comput. Sci. Eng., 9, 90
Kley, W. 1989, A&A, 208, 98
Kley, W. 1999, MNRAS, 303, 696
Kley, W., & Dirksen, G. 2006, A&A, 447, 369
Kley, W., & Haghighipour, N. 2014, A&A, 564, A72
Kley, W., & Haghighipour, N. 2015, A&A, 581, A20
Kley, W., & Nelson, R. P. 2008, A&A, 486, 617
Kostov, V. B., McCullough, P. R., Carter, J. A., et al. 2014, ApJ, 784, 14
Kostov, V. B., Orosz, J. A., Welsh, W. F., et al. 2016, ApJ, 827, 86
Leung, G. C. K., & Lee, M. H. 2013, ApJ, 763, 107
Lines, S., Leinhardt, Z. M., Baruteau, C., Paardekooper, S.-J., & Carter, P. J. 2015, A&A, 582, A5
Liu, B., Muñoz, D. J., & Lai, D. 2015, MNRAS, 447, 747
Lodato, G., Nayakshin, S., King, A. R., & Pringle, J. E. 2009, MNRAS, 398, 1392
Lubow, S. H. 1991, ApJ, 381, 259
MacFadyen, A. I., & Milosavljević, M. 2008, ApJ, 672, 83
Masset, F. 2000, A&AS, 141, 165
Mignone, A., Bodo, G., Massaglia, S., et al. 2007, ApJS, 170, 228
Miranda, R., Muñoz, D. J., & Lai, D. 2017, MNRAS, 466, 1170
Moriwaki, K., & Nakagawa, Y. 2004, ApJ, 609, 1065
Müller, T. W. A., & Kley, W. 2012, A&A, 539, A18
Müller, T. W. A., Kley, W., & Meru, F. 2012, A&A, 541, A123
Mutter, M. M., Pierens, A., & Nelson, R. P. 2017, MNRAS, 465, 4735
Orosz, J. A., Welsh, W. F., Carter, J. A., et al. 2012a, ApJ, 758, 87
Orosz, J. A., Welsh, W. F., Carter, J. A., et al. 2012b, Science, 337, 1511
Papaloizou, J. C. B., Nelson, R. P., & Masset, F. 2001, A&A, 366, 263
Pierens, A., & Nelson, R. P. 2013, A&A, 556, A134
Pringle, J. E. 1991, MNRAS, 248, 754
Rozyczka, M. 1985, A&A, 143, 59
Rozyczka, M., & Laughlin, G. 1997, in IAU Colloq., 163: Accretion Phenomena and Related Outflows, eds. D. T. Wickramasinghe, G. V. Bicknell, & L. Ferrario, ASP Conf. Ser., 121, 792
Schwamb, M. E., Orosz, J. A., Carter, J. A., et al. 2013, ApJ, 768, 127
Shakura, N. I., & Sunyaev, R. A. 1973, A&A, 24, 337
Welsh, W. F., Orosz, J. A., Carter, J. A., et al. 2012, Nature, 481, 475
Welsh, W. F., Orosz, J. A., Carter, J. A., & Fabrycky, D. C. 2014, in IAU Symposium, ed. N. Haghighipour, IAU Symp., 293, 125
Welsh, W. F., Orosz, J. A., Short, D. R., et al. 2015, ApJ, 809, 26
Yang, Y., Hashimoto, J., Hayashi, S. S., et al. 2017, AJ, 153, 7

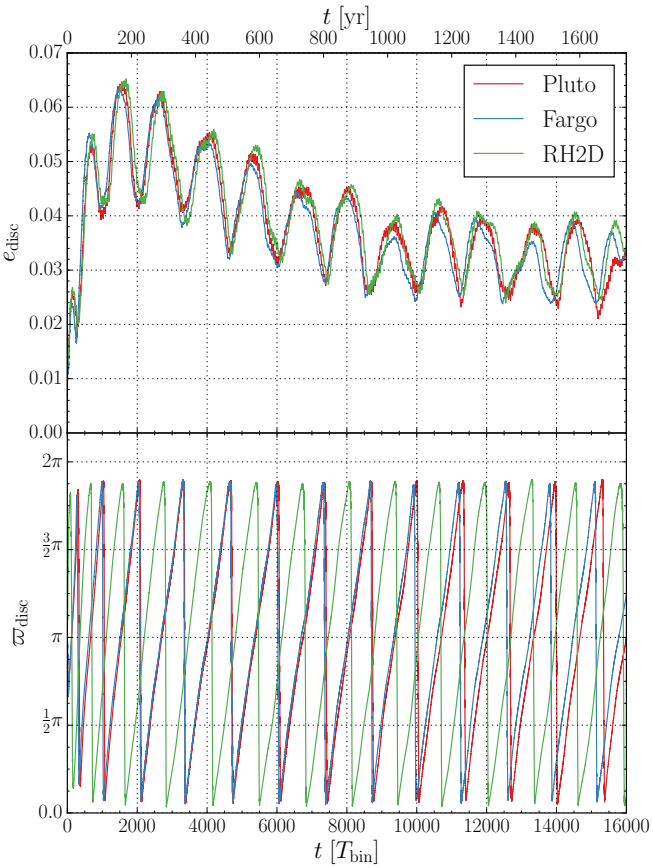

Fig. A.1. Comparison of disc eccentricity (*top*) and disc longitude of pericentre (*bottom*) for the standard model. The disc eccentricity was calculated by summing over the whole disc ($R_2 = R_{\max}$ in Eq. (18)), whereas the disc longitude of pericentre was calculated only for the inner disc ($R_2 = 1.0$ au in Eq. (19)). The π-shift of the green curve in the *bottom panel* is explained in the text. We used a resolution of 512×580 grid cells for PLUTO simulations and for FARGO and RH2D simulations a resolution of 448×512.

Appendix A: Convergence study

The strong gravitational influence of the binary onto the disc, and the complex dynamics of the inner disc presents a big challenge for numerical schemes of grid codes. We therefore study in this appendix the dependence of the disc structure on numerical parameters, such as the numerical scheme or the grid resolution. First, we simulated our reference system, using an open inner boundary and an inner radius of $R_{\min} = 0.25$ au, with the different codes described in Sect. 3.

In Fig. A.1 the long-time evolution of the disc eccentricity (top) and of the longitude of periastron (bottom) are shown. All three codes produce comparable results, although we should note that to get this agreement simulations performed with PLUTO need a slightly higher resolution. PLUTO simulations with a resolution of 448×512 grid cells produce a slightly smaller precession period of the inner disc (red line in Fig. A.3, see also Table A.1). One possible explanation for this could be the size of the numerical stencil. FARGO and RH2D have a very compact stencil because they use a staggered grid. In contrast, PLUTO has a wider stencil because a collocated grid is used, where all variables are defined at the cell centres. In particular the viscosity routine of PLUTO has a very wide stencil to achieve the correct centring of the viscous stress tensor components. This could explain why for PLUTO a slightly higher resolution is needed.

Table A.1. Disc precession rate for different resolutions.

Resolution	$T_{\rm prec}$ [$T_{\rm bin}$]
448×512	1277.49
512×580	1321.48
600×1360	1349.50

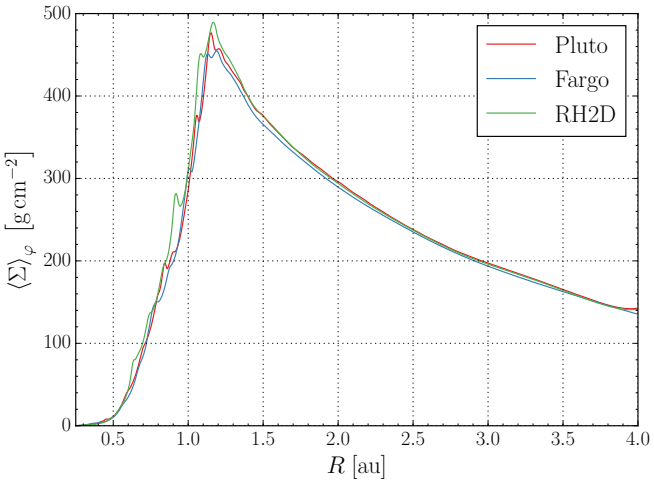

Fig. A.2. Azimuthally averaged density profiles calculated with different codes at $t = 16\,000\,T_{\rm bin}$.

The π-shift of the longitude of periastron calculated with RH2D compared to the values calculated with PLUTO and FARGO (bottom panel of Fig. A.1) can be explained in the following way. Simulations performed with PLUTO and FARGO started the binary at periastron with the pericentre of the secondary at $\varphi = \pi$ (see red ellipses in Fig. 8), whereas RH2D started the binary at apastron with the pericentre of the secondaries orbit at $\varphi = 0$. The data show that when the disc eccentricity is at its maximum the disc is aligned with the orbit of the secondary star. Since the pericentre of the secondary in RH2D simulations is shifted by π we can also see this π-shift in the disc's longitude of periastron.

Figure A.2 shows the azimuthally averaged density profiles at $t = 16\,000\,T_{\rm bin}$. Even after such a long time span all three codes agree very closely. All codes produce roughly the same density maximum and the same density slopes.

To check the influence of the numerical resolution on the disc structure we run PLUTO simulations with different resolutions, summarised in Table A.1. The results of this resolution test are shown in Fig. A.3. The disc eccentricity converges to the same value, whereas it seems that the disc precession rates increases with higher resolution. A closer look at the data shows that after around 6000 orbits the precession rate for the higher resolution converged. Table A.1 summarises the measured precession rate for different resolutions. Since there is no large variation between 512×580 and 600×1360 grid cells, we used a resolution of 512×580 grid cells for our Pluto simulations.

As already discussed in Sect. 4.2 in some cases (for example high binary eccentricities) an outer radius of $R_{\max} = 4.0$ au can lead to wave reflections which interfere with the inner disc. Therefore we increased the outer boundary to

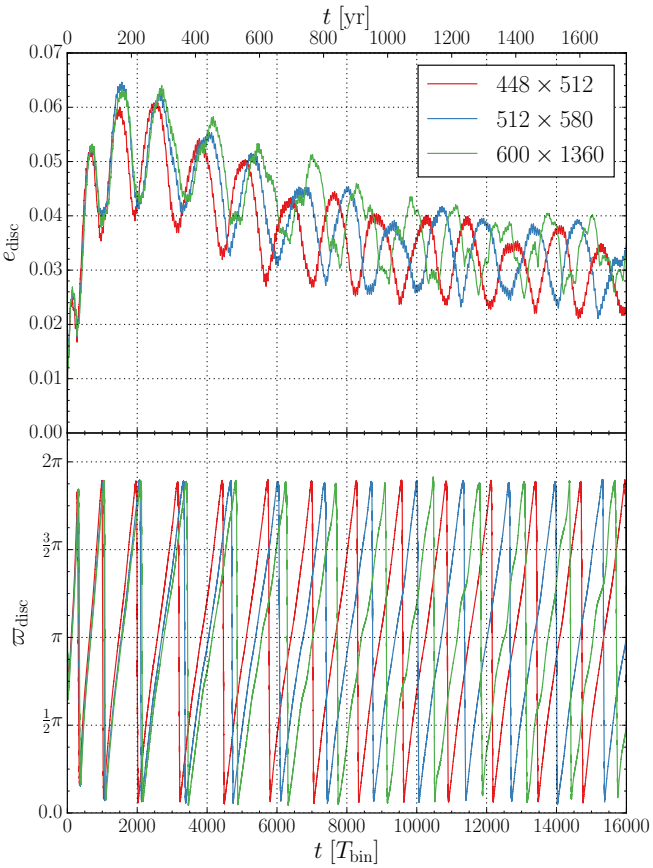

Fig. A.3. Comparison of different resolutions. *Top*: disc eccentricity. *Bottom*: disc longitude of pericentre. All simulations were performed with PLUTO.

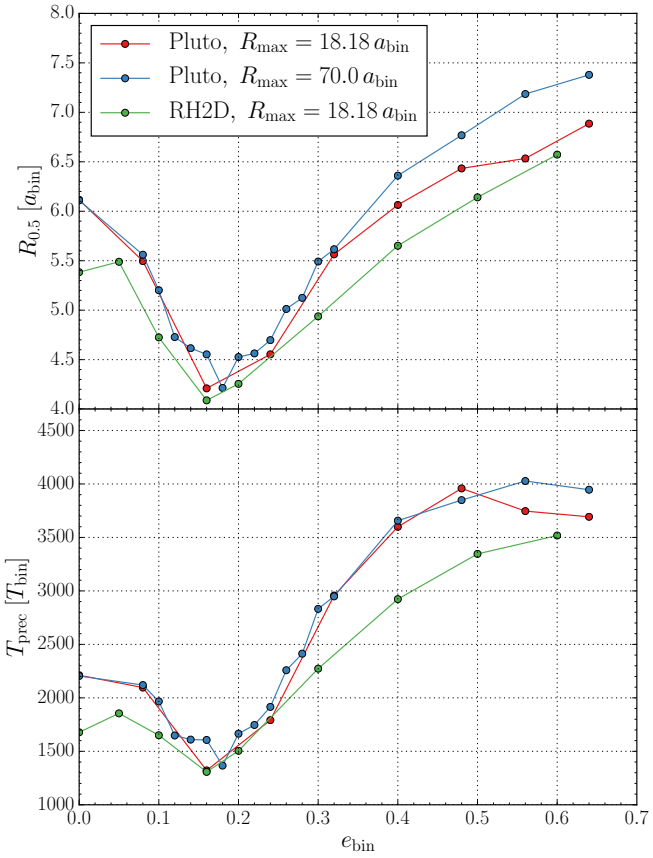

Fig. A.4. Influence of different outer radii on gap size and precession rate while varying the binary eccentricity. *Top*: radius where the azimuthally averaged surface density drops to 50 percent of its maximum value. *Bottom*: precession period of the disc gap.

$R_{\rm max} = 15.4$ au $= 70\,a_{\rm bin}$ (and to ensure the same resolution between 0.25 au and 4.0 au we also increased the number of grid points to 762×582). Figure A.4 compares the effect of different outer radii for the case of varying binary eccentricities. For binary eccentricities greater than 0.32, a larger outer radius makes a difference. Also, around the bifurcation point, at $e_{\rm bin} = 0.18$, a larger outer radius changes the gap size and precession rate of the disc. We also added results from RH2D simulations with an outer radius of $R_{\rm max} = 18.18\,a_{\rm bin}$. These RH2D results follow the same trend as the PLUTO simulations, although for most binary eccentricities we could not reproduce the very good agreement of the $e_{\rm bin} = 0.16$ case. Around $e_{\rm bin} = 0.18$, which is the critical binary eccentricity where the two branches bifurcate, simulations tend to switch between two states. This jump happens after roughly 3000 binary orbits and does not depend on physical parameters. Changes in numerical parameters, like the Courant-Friedrichs-Lewy condition or $R_{\rm max}$, can trigger the jump. This can be seen in Fig. A.4 for $e_{\rm bin} = 0.16$ where simulations with $R_{\rm max} = 18.18\,a_{\rm bin}$ (red curve) and $R_{\rm max} = 70.0\,a_{\rm bin}$ (blue curve) produce different values for the gap size and the precession period. An outer radius of $R_{\rm max} = 18.18\,a_{\rm bin}$ is in the case of $e_{\rm bin} = 0.16$ not too small, since a simulation with $R_{\rm max} = 100\,a_{\rm bin}$ again produced the same values for the gap size and the precession period. For simulations with $e_{\rm bin}$ far away from $e_{\rm crit}$, we did not observe these jumps between states. So far we have only observed these jumps in simulations carried out with PLUTO.

Appendix B: Comparison with massless test particle

In our circumbinary disc evolution we found that the inner disc becomes eccentric with a constant precession rate. In this section we compare this to test particle trajectories around the binary and investigate how a massless particle with orbital elements similar to the disc gap (Fig. 19) would behave under the influence of the binary potential. In particular, we would like to know at what distance from the binary a test particle has to be positioned such that its precession period agrees approximately with that of the disc. Using secular perturbation theory for the coplanar motion of a massless test particle around an eccentric binary star Moriwaki & Nakagawa (2004) derived the following formula for the particle's precession period for low binary eccentricities

$$T_{\rm prec} = \frac{4}{3}\frac{(q_{\rm bin}+1)^2}{q_{\rm bin}}\left(\frac{a_{\rm p}}{a_{\rm bin}}\right)^{7/2}\left(1+\frac{3}{2}e_{\rm bin}^2\right)^{-1} T_{\rm bin}, \tag{B.1}$$

where $a_{\rm p}$ is the semi-major axis of the particle. The same relation was quoted by Miranda et al. (2017) based on results by Liu et al. (2015). A similar relation was given by Leung & Lee (2013) without the $e_{\rm bin}$ term.

In order to verify the applicability of expression (B.1) when varying of binary and planet parameters, we performed series of three-body simulations with very low planet mass ($10^{-6}\,M_\odot$), where we varied individually $q_{\rm bin}$, $e_{\rm bin}$, and $a_{\rm p}$. In addition we varied the planet eccentricity $e_{\rm p}$. For the simulations we used

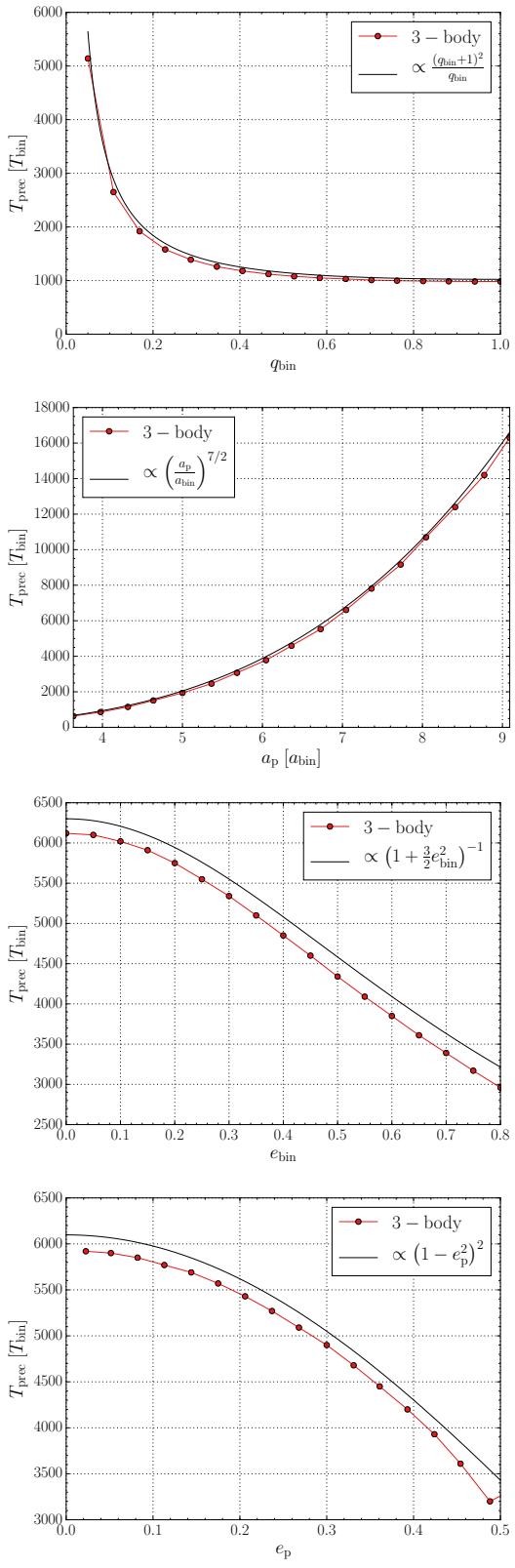

Fig. B.1. Scaling of the precession period of a particle orbiting a binary stars. As base binary parameter we chose the Kepler-16 parameters and for the planet $a_{\rm p} = 1.50$ au and $e_{\rm p} = 0.05$. As an exception we chose for the 1st panel $a_{\rm p} = 1.0$ au. The black curves refer directly to Eq. (B.2) and the corresponding scaling is indicated.

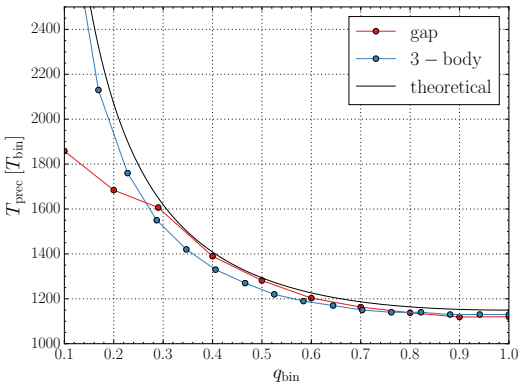

Fig. B.2. Comparison of the precession period of the inner disc with the precession period of free particle. For the particle we used $a_{\rm p} = 4.9\,a_{\rm bin}$, $e_{\rm p} = 0.25$. To obtain the shown agreement the particle's semi-major axis $a_{\rm p}$ has to be roughly 20 percent longer than $a_{\rm gap}$. The theoretical line was calculated with Eq. (B.2).

the parameter of the Kepler-16 systems as a reference (see Table 1) and integrated the system for several 10 000 binary orbits. Our results of these three-body simulations are shown in Fig. B.1. We find that the precession rate scales with $q_{\rm bin}$, $a_{\rm p}$, and $e_{\rm bin}$ exactly as expected from relation (B.1). The fourth panel of Fig. B.1 indicates that the precession period also depends on the particle eccentricity as $T_{\rm prec} \sim (1 - e_{\rm p}^2)^2$, where we plotted the average eccentricity of the orbit which is equivalent to the particle's free eccentricity. The agreement holds up to about $e_{\rm p}^2 \sim 0.5$ for the used $a_{\rm p}$. Clearly, for higher values of $e_{\rm p}$ the particle's orbit will be unstable as this leads to close encounters with the binary. The value of $e_{\rm p}$ where this happens depends on the distance from the binary star. For lower $a_{\rm p}$ the range will be more limited. In summary, we find for the precession period of a particle around a binary star

$$T_{\rm prec} = \frac{4}{3}\frac{(q_{\rm bin}+1)^2}{q_{\rm bin}}\left(\frac{a_{\rm p}}{a_{\rm bin}}\right)^{7/2}\frac{\left(1-e_{\rm p}^2\right)^2}{\left(1+\frac{3}{2}e_{\rm bin}^2\right)}\,T_{\rm bin}. \tag{B.2}$$

This relation is plotted in Fig. B.1 as the solid black line. In addition to the scaling behaviour we find that the numerical results are about 3–5% lower than the theoretical estimate. The agreement of the numerical results with the theoretical prediction becomes better for larger $a_{\rm p}$ because Eq. (B.2) is derived from an approximation for large $a_{\rm p}/a_{\rm bin}$. The full relation (B.2) can be inferred directly from Eq. (11) in Georgakarakos & Eggl (2015).

Now we compare the particle precession rate to our disc simulations. The best option for this comparison is to check the scaling of the precession rate for models where $q_{\rm bin}$ has been varied because for binary mass ratio greater than $q_{\rm bin} = 0.3$ the gap size and eccentricity do not change much (blue points in Fig. 19). This is supported by the small variation of the gap radii in Fig. 16. For higher mass ratios the gap size is approximately $a_{\rm gap} = 4.0\,a_{\rm bin}$ and $e_{\rm gap} = 0.27$. As seen from Eq. (B.2), a test particle with these orbit elements would have a precession period that is far too short. However, if we assume that the test particle has a semi-major axis of $a_p = 4.9\,a_{\rm bin}$ (roughly 20 percent more than $a_{\rm gap}$), the precession period of the gap and the particle match very well for different $q_{\rm bin}$ (Fig. B.2), at least for the higher mass ratios. In general, however, due to the strong sensitivity of the precession period with $a_{\rm p}$, an exact agreement will be difficult to obtain.

A&A 616, A47 (2018)
https://doi.org/10.1051/0004-6361/201832804

Astronomy & Astrophysics

Migration of planets in circumbinary discs

Daniel Thun and Wilhelm Kley

Institut für Astronomie und Astrophysik, Universität Tübingen, Auf der Morgenstelle 10, D-72076 Tübingen, Germany
e-mail: daniel.thun@uni-tuebingen.de; wilhelm.kley@uni-tuebingen.de

Received 10 February 2018 / Accepted 31 May 2018

ABSTRACT

Aims. The discovery of planets in close orbits around binary stars raises questions about their formation. It is believed that these planets formed in the outer regions of the disc and then migrated through planet-disc interaction to their current location. Considering five different systems (Kepler-16, -34, -35, -38, and -413) we model planet migration through the disc, with special focus on the final orbital elements of the planets. We investigate how the final orbital parameters are influenced by the disc and planet masses.
Methods. Using two-dimensional, locally isothermal, and viscous hydrodynamical simulations, we first model the disc dynamics for all five systems, followed by a study of the migration properties of embedded planets with different masses. To strengthen our results, we apply two grid-based hydrodynamical codes using different numerics (PLUTO and FARGO3D).
Results. For all systems, we find that the discs become eccentric and precess slowly. We confirm the bifurcation feature in the precession period – gap-size diagram for different binary mass ratios. The Kepler-16, -35, -38, and -413 systems lie on the lower branch and Kepler-34 on the upper one. For systems with small binary eccentricity, we find a new non-monotonic, loop-like feature.
In all systems, the planets migrate to the inner edge of the disc cavity. Depending on the planet-disc mass ratio, we observe one of two different regimes. Massive planets can significantly alter the disc structure by compressing and circularising the inner cavity and they remain on nearly circular orbits. Lower-mass planets are strongly influenced by the disc, their eccentricity is excited to high values, and their orbits are aligned with the inner disc in a state of apsidal corotation.
In our simulations, the final locations of the planets are typically too large with respect to the observations because of the large inner gaps of the discs. The migrating planets in the most eccentric discs (around Kepler-34 and -413) show the largest final eccentricity in agreement with the observations.

Key words. hydrodynamics – methods: numerical – planets and satellites: formation – protoplanetary disks – binaries: close

1. Introduction

Following the first detection of a circumbinary planet with the *Kepler* space telescope, namely Kepler-16b, eight more binary star systems with a planet on a P-type orbit have been discovered[1]. All these systems show striking similarities. They are all very flat, meaning that the binary and the planet orbit are in the same plane, suggesting that these planets formed in a circumbinary disc aligned with the orbital plane of the central binary. Furthermore, in all systems, the innermost planet (so far only Kepler-47 is known to have more than one planet) is close to the calculated stability limit (Dvorak 1986; Holman & Wiegert 1999). This leads us to question where in the disc these planets formed. Two scenarios are possible: an in situ formation at the observed location, or a formation further outside the disc followed by radial migration of the planet through the disc to the observed location. Strong gravitational interaction between the binary and the disc, which leads to the excitation of spiral waves in the disc, makes an in situ formation unlikely (Pierens & Nelson 2007; Paardekooper et al. 2012; Meschiari 2012; Silsbee & Rafikov 2015), because for orbits close to the binary, destructive collisions between planetesimals are expected. The different alignment of their periapses lead to high relative impact velocities (Scholl et al. 2007; Marzari et al. 2008).

Therefore, it is believed that these circumbinary planets on orbits close to the stability limit were formed in the outer disc where the binary has less influence on the formation process. In order to reach their observed position, the planets then migrated through the disc to their present location either through type-I or type-II migration (Lin & Papaloizou 1986; Ward 1997; Nelson et al. 2000; Tanaka et al. 2002). This leads to the question of how this migration progress can be stopped at the right orbit.

Early work by Artymowicz & Lubow (1994) showed that through tidal interaction between the binary and the disc an eccentric inner gap in the disc forms. The structure of the gap, such as eccentricity and size, depends on disc parameters (viscosity, pressure) as well as on binary parameters (eccentricity, mass ratio). This was confirmed by various studies, which all showed an eccentric inner gap that slowly precesses in a prograde manner around the binary (Pierens & Nelson 2008, 2013; Kley & Haghighipour 2014, 2015; Lines et al. 2015; Miranda et al. 2017; Mutter et al. 2017a; Thun et al. 2017).

In several of these mentioned works, not only was the structure of the circumbinary disc investigated but also the migration of the planets. These simulations showed that the inner cavity of the disc constitutes a barrier for the migrating planet. The sudden drop of density produces a large positive corotation torque balancing the negative Lindblad torques responsible for the inward migration (Masset et al. 2006).

Pierens & Nelson (2013) modelled planets around the systems Kepler-16, Kepler-34, and Kepler-35. In their numerous simulations, they studied the impact of the discs' pressure and

[1] Kepler-16 (Doyle et al. 2011), Kepler-34 and -35 (Welsh et al. 2012), Kepler-38 (Orosz et al. 2012a), Kepler-47 (Orosz et al. 2012b), Kepler-64 (Schwamb et al. 2013), Kepler-413 (Kostov et al. 2014), Kepler-453 (Welsh et al. 2015), and Kepler-1647 (Kostov et al. 2016).

Table 1. Circumbinary systems.

System	M_A [$M_\odot$]	M_B [$M_\odot$]	q_{bin}	a_{bin} [au]	e_{bin}	T_{bin} [d]	m_p [M_{jup}]	a_p [au]	e_p
Kepler-16	0.69	0.20	0.29	0.22	0.16	41.079	0.333	0.7048	0.00685
Kepler-34	1.05	1.02	0.97	0.23	0.52	27.796	0.220	1.0896	0.182
Kepler-35	0.89	0.81	0.91	0.18	0.14	20.734	0.127	0.6035	0.042
Kepler-38	0.95	0.25	0.26	0.15	0.10	18.795	<0.384	0.4644	<0.032
Kepler-413	0.82	0.54	0.66	0.10	0.04	10.116	0.211	0.3553	0.1181

Notes. The mass ratio is defined as $q_{bin} = M_B/M_A$.
References. Kepler-16 (Doyle et al. 2011), Kepler-34 and -35 (Welsh et al. 2012), Kepler-38 (Orosz et al. 2012a), Kepler-413 (Kostov et al. 2014).

viscosity onto the migration process of the planets. They found that the structure (size and eccentricity) of the inner cavity depends strongly on disc parameters, and therefore pressure and viscosity in the disc have a notable influence on the final orbital parameters, since the planets migrate to the edge of the cavity. Additionally, they not only simulated full grown planets but also migrating planetary cores. After the cores reached their final positions, gas accretion and dispersion of the gas disc were initiated. However, the final orbital parameters were comparable, independent of the migration scenario. For all studied systems, they found a set of disc parameters which produced the closest approximation to the observed values. But since they could not precisely reproduce the observed orbital parameters, they suggested more sophisticated disc models.

Kley & Haghighipour (2014) simulated planets around Kepler-38 in isothermal as well as radiative discs. Their radiative disc models include viscous heating, vertical cooling, and radiative diffusion in the midplane of the disc. In both models, the planet migrated as expected to the edge of the inner cavity. In their isothermal models, the inner gap was smaller than the observed orbit of the planet and therefore the planet migrated too close to the binary. However, this small inner cavity was a result of their overly large inner radius of the computational domain with $R_{min} = 1.67\, a_{bin}$. As shown in Thun et al. (2017), this inner radius should be of the order of the binary separation. In the radiative case, the viscous heating produced a disc with an even smaller inner cavity. Only by reducing the disc's mass and its viscosity can a wider inner cavity and a final orbit of the planet close to the observed location be achieved.

In a second paper, Kley & Haghighipour (2015) simulated the evolution of planets in isothermal and radiative discs around the Kepler-34 system. Because of the high eccentricity of the Kepler-34 binary, a disc with a large eccentric inner cavity is created. Therefore, the planets stop at a position far beyond the observed location. Between the isothermal and radiative models, they could not find large differences. Additionally, they observed an alignment of the planets' orbit with the precessing inner gap.

Mutter et al. (2017b) studied planets in self-gravitating circumbinary discs around the systems Kepler-16, -34, and -35. Their main result is that for very massive discs (five to ten times the minimum mass solar nebula, MMSN), the disc's self-gravity can shrink the inner cavity which allows the planet to migrate further inward. This way they could achieve a better agreement between their simulations of the Kepler-16 and Kepler-34 systems and the observed values. In the case of Kepler-35b, the low mass of the planet prevented the planet from migrating close to the observed location.

In this paper, we revisit the evolution of embedded planets in circumbinary discs based on our new, refined disc models presented in Thun et al. (2017). To study the migration of fully formed planets through a circumbinary disc, we carried out two dimensional (2D), isothermal, and viscous hydrodynamical simulations. The binary parameters were chosen according to five selected *Kepler* systems. Table 1 gives an overview of binary and planet parameters of these systems. First, we simulated the circumbinary disc without the presence of a planet to obtain the dynamical properties of the inner cavity that we compare to our first study (Thun et al. 2017). In order to detect purely numerical features and strengthen our results, we used two grid codes, PLUTO and FARGO3D, that use different numerical methods, and compared their results.

For simulations with an embedded planet, we studied the evolution of the planet's orbital elements as well as the planet's impact on the disc. In these simulations, we varied the planet's mass and the mass of the disc, in order to investigate the influence of the planet-to-disc mass ratio on the final orbital parameters of the planet.

The paper is organised in the following way. In Sect. 2, we describe the physical and numerical setup of our simulations. In Sect. 3, we discuss the disc structure prior to inserting the planet and compare it to our earlier study. In Sect. 4, we investigate how planets of different mass migrate through these circumbinary discs. We first discuss the general behaviour of migrating planets of different mass using the example of Kepler-38, and then comment on the other four systems. Our results are discussed and summarised in Sects. 5 and 6.

2. Model setup

2.1. Physical model

To model the migration of planets in circumbinary discs, we use 2D, isothermal, and viscous hydrodynamical simulations. For the disc model, we follow the setup described in Thun et al. (2017, Sect. 2). This means we solve the isothermal, vertically averaged Navier–Stokes equations with an external potential Φ on a polar grid (R, φ)[2], centred at the barycentre of the binary.

We assume a locally isothermal temperature profile of $T \propto R^{-1}$ which corresponds to a disc with constant aspect ratio $h = H/R$, where H is the height of the disc. In all simulations, we use $h = 0.05$. Turbulent viscosity in the disc is modelled through

[2] We use the following notation: $\mathbf{R}$ is the 2D position vector in the $x-y$-plane, $\mathbf{R} = R\hat{\mathbf{e}}_{\mathbf{R}}$.

an α-parameter (Shakura & Sunyaev 1973), with $\alpha = 0.01$. We have chosen these parameters to be consistent with our first paper but have run some exploratory simulations with smaller h and different α, we comment on this in Sects. 3 and 5 below.

The external potential Φ has the following form:

$$\Phi(\mathbf{R}) = -\sum_k \frac{GM_k}{\sqrt{(\mathbf{R}-\mathbf{R}_k)^2 + (\varepsilon H)^2}} + \mathbf{a}_{\rm com}\cdot\mathbf{R}, \tag{1}$$

with k being an index running over both binary components and the planet ($k \in \{\mathrm{A}, \mathrm{B}, \mathrm{p}\}$). The subscripts A and B stand for the primary and the secondary star, and the subscript p for the planet. The smoothing factor εH is used to avoid singularities and to account for the correct treatment of a vertically extended three-dimensional (3D) disc in our 2D thin-disc approximation (Müller et al. 2012). In all our simulations, we use $\varepsilon = 0.6$. The disc height H is evaluated at the location of the cell $H = hR$. Since our coordinate system is located at the centre of mass of the binary, which is accelerated by the planet and the disc, we are not in an inertial reference system. This acceleration of the coordinate system, $\mathbf{a}_{\rm com}$, gives rise to the indirect term $\mathbf{a}_{\rm com}\cdot\mathbf{R}$ in Eq. (1), where $\mathbf{a}_{\rm com}$ is given by

$$\begin{aligned}\mathbf{a}_{\rm com} &= \frac{M_{\rm A}\mathbf{a}_{\rm A} + M_{\rm B}\mathbf{a}_{\rm B}}{M_{\rm bin}} \\ &= \frac{1}{M_{\rm bin}}\sum_{k\in\{\rm A,B\}} \frac{GM_{\rm p}M_k}{|\mathbf{R}_{\rm p}-\mathbf{R}_k|^3}(\mathbf{R}_{\rm p}-\mathbf{R}_k) \\ &\quad + \frac{1}{M_{\rm bin}}\sum_{k\in\{\rm A,B\}} \int_{\rm disc} \frac{GM_k\Sigma(\mathbf{R}')\,\mathrm{d}V'}{\left[(\mathbf{R}'-\mathbf{R}_k)^2 + (\varepsilon H)^2\right]^{3/2}}(\mathbf{R}'-\mathbf{R}_k),\end{aligned} \tag{2}$$

with the mass of the binary $M_{\rm bin} = M_{\rm A} + M_{\rm B}$. The first term in Eq. (2) is the acceleration of the centre of mass due to the planet and the second term is the acceleration due to the disc.

The equation of motion for the binary components and the planet is given by

$$\begin{aligned}\frac{\mathrm{d}^2\mathbf{R}_k}{\mathrm{d}t^2} &= -\sum_{\ell\neq k}\frac{GM_\ell}{|\mathbf{R}_k-\mathbf{R}_\ell|^3}(\mathbf{R}_k-\mathbf{R}_\ell) \\ &\quad + \int_{\rm disc}\frac{G\Sigma(\mathbf{R}')\,\mathrm{d}V'}{\left[(\mathbf{R}'-\mathbf{R}_k)^2+(\varepsilon H)^2\right]^{3/2}}(\mathbf{R}'-\mathbf{R}_k) \\ &\quad - \mathbf{a}_{\rm com}\,.\end{aligned} \tag{3}$$

Again the height of the disc is evaluated at the location of the cell $H = hR'$ (Müller et al. 2012). Equations (2) and (3) show the most general case in which the binary is accelerated by the planets and the disc. For disc-only simulations in Sect. 3, the back-reaction of the disc on the binary is not considered and therefore the disc contributions in Eqs. (2) and (3) are omitted.

2.2. Initial conditions

The initial disc density is given by

$$\Sigma(t=0) = f_{\rm gap}\,\Sigma_{\rm ref}\left(\frac{R}{a_{\rm bin}}\right)^{-1.5}, \tag{4}$$

where $f_{\rm gap}$ models the expected cavity created by the binary (Artymowicz & Lubow 1994; Günther & Kley 2002)

$$f_{\rm gap} = \left[1+\exp\left(-\frac{R-R_{\rm gap}}{\Delta R}\right)\right]^{-1}, \tag{5}$$

with $R_{\rm gap} = 2.5\,a_{\rm bin}$, and $\Delta R = 0.1\,R_{\rm gap}$. For the migration process, the total mass of the disc is an important quantity, since it directly influences the migration speed of the planet. In all our models, we choose an initial disc mass of $M_{\rm disc} = 0.01\,M_{\rm bin}$. With this choice, the reference surface density in Eq. (4) can then be calculated:

$$M_{\rm disc} = \int_0^{2\pi}\int_{R_{\rm min}}^{R_{\rm max}} \Sigma(t=0) R\,\mathrm{d}R\,\mathrm{d}\varphi \tag{6}$$

$$= 2\pi\Sigma_{\rm ref}\int_{R_{\rm min}}^{R_{\rm max}}\left[1+\exp\left\{-\frac{\frac{R}{a_{\rm bin}}-2.5}{0.25}\right\}\right]^{-1}\left(\frac{R}{a_{\rm bin}}\right)^{-1.5} R\,\mathrm{d}R\,. \tag{7}$$

Introducing the dimensionless variable $u = R/a_{\rm bin}$ (with $u_{\rm min/max} = R_{\rm min/max}/a_{\rm bin}$) gives

$$M_{\rm disc} = 2\pi\Sigma_{\rm ref}a_{\rm bin}^2 \underbrace{\int_{u_{\rm min}}^{u_{\rm max}}\left[1+\exp\left\{-\frac{u-2.5}{0.25}\right\}\right]^{-1} u^{-0.5}\,\mathrm{d}u}_{=I(u_{\rm min},u_{\rm max})}\,. \tag{8}$$

Finally, the reference density is given in our case in code units[3] with $u_{\rm min} = 1$ and $u_{\rm max} = 40$ by

$$\frac{\Sigma_{\rm ref}}{\Sigma_0} = \frac{0.01}{2\pi I(1,40)} = 1.67535\times10^{-4}\,; \tag{9}$$

the integral $I(1,40)$ was evaluated numerically.

The initial radial velocity is set to zero $u_R(t=0) = 0$ and the initial azimuthal velocity is set to the local Keplerian velocity $u_\varphi(t=0) = \sqrt{GM_{\rm bin}/R}$.

2.3. Numerics

The grid spans from $R_{\rm min} = 1\,a_{\rm bin}$ to $R_{\rm max} = 40\,a_{\rm bin}$ in the radial direction with a logarithmic spacing and from 0 to 2π in the azimuthal direction with a uniform spacing. In all simulations, we use a resolution of 684×584 grid cells. At the inner edge, we use a zero-gradient boundary condition ($\partial/\partial R = 0$) for density, radial velocity, and angular velocity $\Omega_\varphi = u_\varphi/R$. We further allow only outflow and no inflow into the computational domain. At the outer boundary, we set the azimuthal velocity to the local Keplerian velocity. For the density and radial velocity, we use a damping boundary condition in the range from $(1-f)R_{\rm max}$ to $R_{\rm max}$ (with $f = 0.1$) as described in de Val-Borro et al. (2006). This means we damp a quantity x (here surface density Σ or radial velocity u_R) to its initial value x^0 according to

$$x^{n+1} = x^n - (x^n - x^0)\frac{\Delta t}{\tau}\mathcal{P}(R), \tag{10}$$

where Δt is the current time-step, τ is the damping time scale and equal to one tenth of the orbital period at the outer boundary $\tau = 0.1\times2\pi\sqrt{R_{\rm max}^3/(GM_{\rm bin})}$. The damping function $\mathcal{P}(R)$ is a quadratic polynomial which fulfils the following conditions $\mathcal{P}([1-f]R_{\rm max}) = 0.0$, $\mathcal{P}(R_{\rm max}) = 1.0$ and $\mathcal{P}'([1-f]R_{\rm max}) = 0.0$. Therefore,

$$\mathcal{P}(R) = \frac{1}{f^2}\left(\frac{R}{R_{\rm max}}\right)^2 + \frac{2(f-1)}{f^2}\frac{R}{R_{\rm max}} + \frac{(1-f)^2}{f^2}\,. \tag{11}$$

[3] In all simulations, we use the following code units: $R_0 = a_{\rm bin}$, $M_0 = M_{\rm bin}$, $t_0 = \sqrt{R_0^3/(GM_0)}$ and $\Sigma_0 = M_0/R_0^2$, with the gravitational constant G.

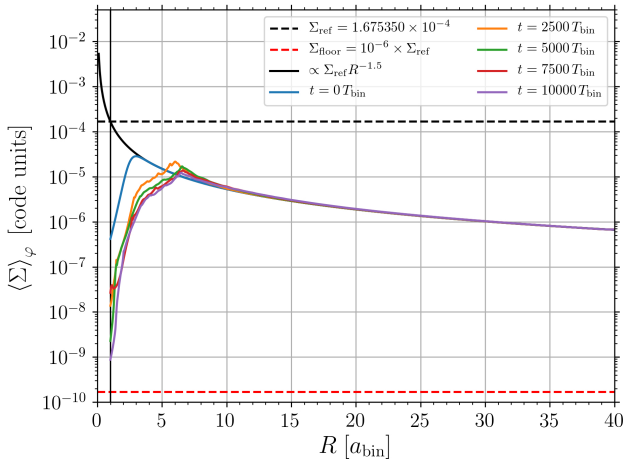

Fig. 1. Azimuthally averaged surface density at various times for the Kepler-38 system calculated with PLUTO. The blue curve shows the initial density distribution. The black vertical line marks the 1 $a_{\rm bin}$ location where the density would reach the reference density if we had not imposed an initial gap (blue curve). The dashed horizontal lines mark the reference density (in black) and the density floor (in red).

In the azimuthal direction, we use periodic boundary conditions.

For stability reasons, especially in the inner cavity where the density drops to very low values, we use a global density floor,

$$\Sigma_{\rm floor} = 10^{-6}\,\Sigma_{\rm ref}, \tag{12}$$

in all our simulations. Without a density floor, some hydrodynamical codes, especially PLUTO, tend to produce negative densities and abort the calculation. Test simulations with lower floors did not show any differences in disc dynamics, but negative densities and code abortions occurred more frequently. Simulations with density floors higher than $10^{-6}\,\Sigma_{\rm ref}$ did not agree with the lower floor results, hence our choice for $\Sigma_{\rm floor}$.

In this paper, we use two hydrodynamical codes, namely PLUTO (Mignone et al. 2007)[4] and FARGO3D (Benítez-Llambay & Masset 2016). For a quick overview of the numerical options used in our simulations see Thun et al. (2017, Sect. 3.1). Some details about the N-body solver implemented in PLUTO are shown in Appendix A.

FARGO3D uses an artificial von Neumann–Richtmyer viscosity to smooth out shocks. The artificial viscosity follows the ZEUS implementation (Stone & Norman 1992). The number of cells over which the shock is spread can be adjusted through a constant $C_{\rm av}$ (in the ZEUS paper, this constant is referred to as C_2). FARGO3D sets this constant by default to $C_{\rm av} = 1.41$. As discussed in Appendix B, to obtain a good agreement with PLUTO a lower artificial viscosity is needed. Therefore, we have chosen $C_{\rm av} = 0.5$ for all FARGO3D simulations shown in this paper.

Figure 1 summarises our setup using the Kepler-38 system as an example. Displayed are various snapshots of the azimuthally averaged surface density in order to show that the density floor does not directly interfere with the disc evolution. The density snapshot is from a PLUTO simulation of Kepler-38 without a planet. The planets are then embedded at $t = 10\,000$ binary orbits into the disc. In Table 2, all numerical and physical parameters which were not varied in our simulations are summarised.

[4] We use a modified version of PLUTO 4.2 which runs on GPUs and is also capable of solving a N-body system.

Table 2. Fixed numerical and physical parameters of our simulations.

Physical parameters	
h	0.05
α	0.01
$M_{\rm disc}$	0.01 $M_{\rm bin}$
Numerical parameters	
Resolution	684×584
$R_{\rm min}$	1 $a_{\rm bin}$
$R_{\rm max}$	40 $a_{\rm bin}$
$\Sigma_{\rm floor}$	$10^{-6}\,\Sigma_{\rm ref}$
ε	0.6

3. Circumbinary disc structure

Before studying the evolution of embedded planets, we present our results on the dynamical behaviour of the circumbinary disc around the five systems under investigation. In Fig. 2, we display the time evolution over 40 000 orbits of the binary of the disc's precession period as well as the semi-major axis and the eccentricity of the disc's gap. In the left column, results from PLUTO simulations are shown and in the right column FARGO3D results are presented.

The semi-major axis and eccentricity of the gap are calculated with the help of a fitted ellipse. The detailed fitting procedure is described in Thun et al. (2017, Sect. 5.1). The displayed data show some noise since we calculated the semi-major axis and eccentricity of the disc only every 100 binary orbits. The final estimates are time averages, starting at 6000 binary orbits (roughly the time when all discs reached a quasi steady state). The precession period is calculated in two ways: we searched for positive ($\pi - \delta \to \pi + \delta, \delta \ll 1$) and negative ($\pi + \delta \to \pi - \delta$) transitions in the $\varpi_{\rm disc}$-t-diagram (e.g., of a $\varpi_{\rm disc}$-t-diagram see Fig. 12 below). The time between two subsequent positive ($\times$ in Fig. 2) or negative (+ in Fig. 2) transitions gives the precession period of the gap, which is shown in the first row of Fig. 2 ordered by their number of occurrence. To obtain a better estimate, we averaged over all periods after the discs reached a quasi-steady state, which happens after about 6000 binary orbits. The overall agreement between the results obtained with PLUTO and FARGO3D is very good; we discuss some notable differences below.

Considering the different binary eccentricities in our systems, as noted in Table 1, we can place them in a $T_{\rm prec}$ versus $a_{\rm gap}$ diagram; see Fig. 3. In a previous study, we discovered a bifurcation with two separate branches depending on the binary eccentricity (Thun et al. 2017, Sect. 5.2). In that study we found that on the lower branch, starting with circular binaries, the precession period and gap size decrease for increasing binary eccentricities. The minimum gap size and precession period are reached at a critical binary eccentricity of $e_{\rm crit} \approx 0.18$. From there, the upper branch starts on which both quantities increase for increasing binary eccentricities. The vertical axis in Fig. 3 has been rescaled using the factor

$$\frac{q_{\rm bin}}{(q_{\rm bin}+1)^2} \times \left(1 + \frac{3}{2} e_{\rm bin}^2\right), \tag{13}$$

to account for the different binary mass ratios and eccentricities. As shown in Thun et al. (2017, Appendix B) the precession

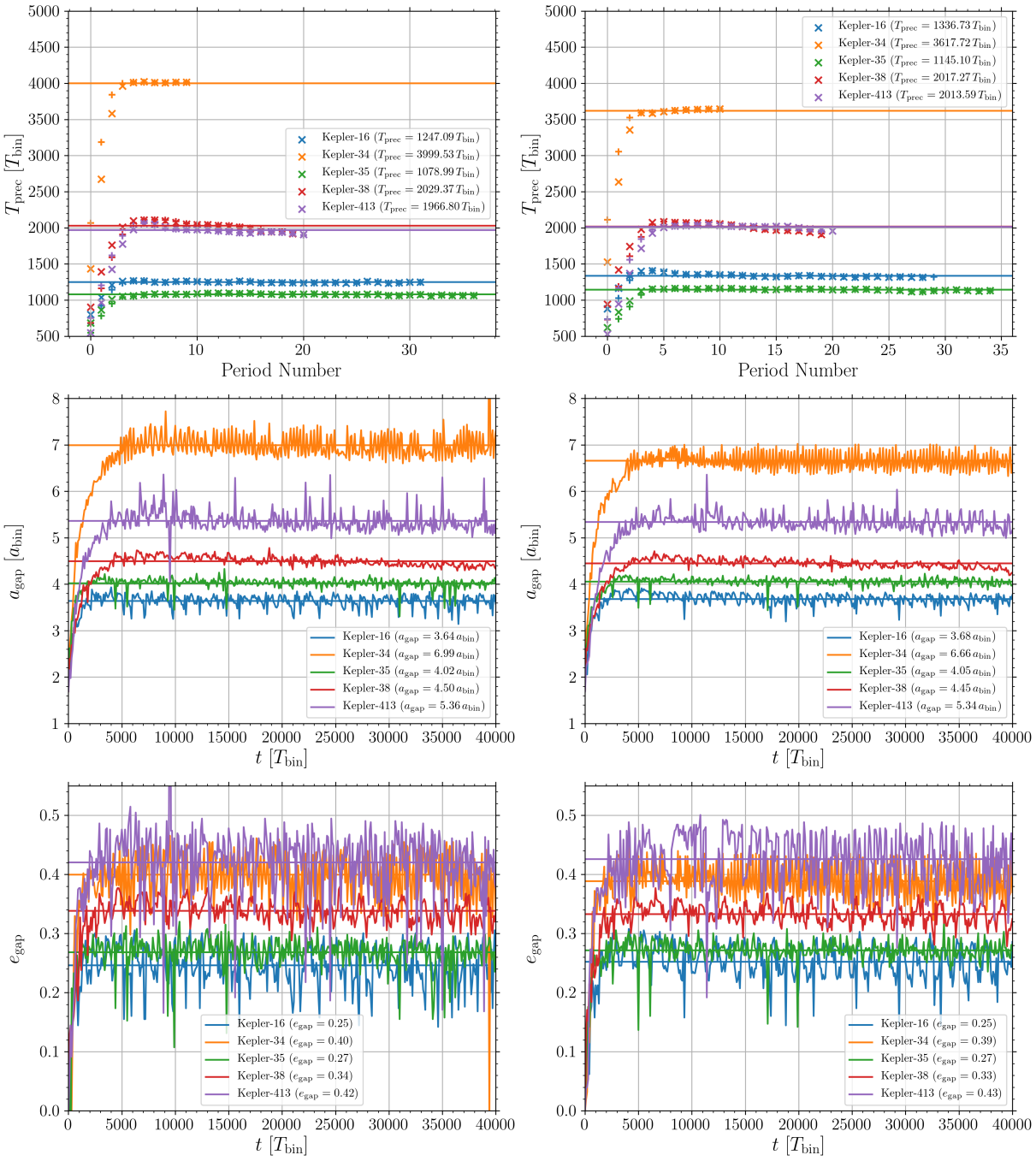

Fig. 2. The precession period, semi-major axis, and eccentricity of the disc gap vs. time, for our five different systems. Disc models on the *left* are calculated with PLUTO and disc models on the *right* are calculated with FARGO3D. The precession period, $T_{\rm prec}$, in the *first row* is given in terms of the corresponding period number. The horizontal lines indicate the time average starting from 6000 binary orbits, roughly the time when the discs reached a quasi-steady state. See the text for an explanation of the meaning of the + and × signs in the first row.

period of the disc gap is comparable to the precession period of a single particle around a binary,

$$T_{\rm prec} = \frac{4}{3}\frac{(q_{\rm bin}+1)^2}{q_{\rm bin}}\left(\frac{a_{\rm p}}{a_{\rm bin}}\right)^{7/2}\frac{\left(1-e_{\rm p}^2\right)^2}{\left(1+\frac{3}{2}e_{\rm bin}^2\right)}T_{\rm bin}\,. \tag{14}$$

Our scaling factor does not include the gap eccentricity term $\left(1-e_{\rm gap}^2\right)^2$, in order to allow for a clear relation between binary and individual disc properties, here $T_{\rm prec}$ versus $a_{\rm gap}$. From Fig. 4, it is, in principle, possible to construct a relation between $e_{\rm gap}$ and $a_{\rm gap}$ and add this to the scaling in Fig. 3. Using $e_{\rm gap}$ in the scaling for Fig. 3 does not change it qualitatively, only the exponents are different then.

Using this scaling, the numerically obtained disc parameters can be placed into the diagram for all systems, which lie indeed very close to the discovered bifurcation curve of Thun et al. (2017). While Kepler-16 and Kepler-35 are located

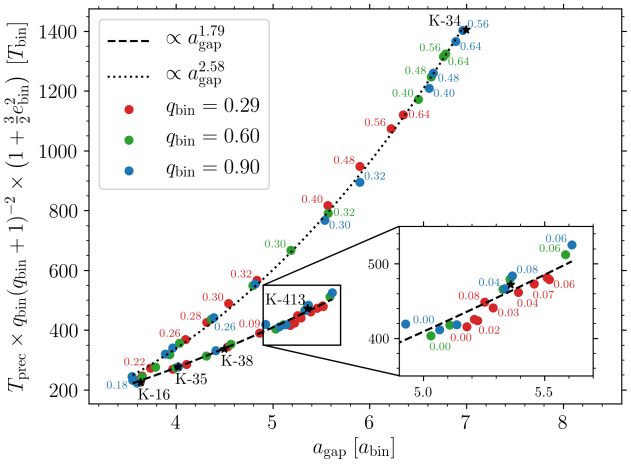

Fig. 3. Precession period of the inner gap, scaled by the factor $q_{\rm bin}/(q_{\rm bin}+1)^2 \times \left(1+\frac{3}{2}e_{\rm bin}^2\right)$ to account for the different mass ratios and eccentricities of the binary stars, plotted against the semi-major axis of the gap. Different bullets correspond to numerical results for different binary eccentricities whereas different colours stand for different binary mass ratios. The black dashed and dotted lines are fits to all data points on the lower (dashed) and upper (dotted) branch. The five different *Kepler* systems considered in this paper are marked by the black stars.

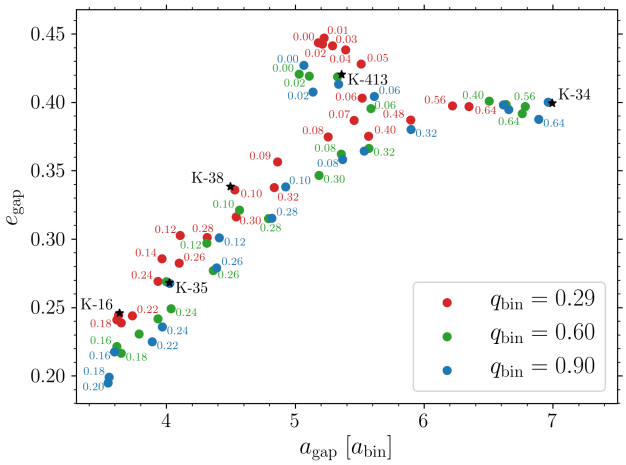

Fig. 4. Gap eccentricity plotted against the semi-major axis of the gap. Different bullets correspond to numerical results for different binary eccentricities whereas different colours stand for different binary mass ratios. The five different *Kepler* systems considered in this paper are marked by the black stars.

close to the branching point, the systems Kepler-38 and Kepler-413 lie on the lower branch. The Kepler-34 system, which has a very large gap with a slow precession, is located at the end of the upper branch in Fig. 3.

Fits to the upper and lower branch data points show that the scaled precession period is proportional to $\propto a_{\rm gap}^{1.79}$ on the lower branch and $\propto a_{\rm gap}^{2.58}$ on the upper branch. These exponents are lower than the exponent 7/2 expected from the test particle precession period relation, Eq. (14). This deviation represents the fact that gap's dynamical behaviour is determined by hydrodynamical effects and does not fully behave like a free particle around a binary.

To generate Fig. 3, we did not use the data from Thun et al. (2017) but generated all points for the different binary mass ratios and eccentricities using our new improved numerical setup as described above, in particular a smaller $R_{\rm min}$. The red points in the figure are all calculated for the Kepler-16 binary mass ratio of $q_{\rm bin} = 0.29$, and the green and blue bullets correspond to mass ratios of $q_{\rm bin} = 0.60$ and $q_{\rm bin} = 0.90$. We also set up simulations series for these high mass ratios since Kepler-34 also has a high mass ratio of $q_{\rm bin} = 0.97$. For binary eccentricities, $e_{\rm bin} \geq 0.06$, we observe the same behaviour as in our earlier study: upon increasing $e_{\rm bin}$, the points move along the lower branch towards smaller $a_{\rm gap}$ and $T_{\rm prec}$ until the critical value $e_{\rm crit} \approx 0.18$ is reached, from which both $T_{\rm prec}$ and $a_{\rm gap}$ increase with increasing $e_{\rm bin}$. However, for binary eccentricities smaller than $e_{\rm bin} = 0.06$, we observe a new phenomenon. Starting from circular binaries, the gap size as well as the precession period first increase until a maximum is reached for $e_{\rm bin} = 0.06$; see inlay in Fig. 3. Increasing the binary eccentricity past $e_{\rm bin} = 0.06$ leads to smaller gaps and lower precession periods again, following the known trend. From $e_{\rm bin} = 0.0$ to $e_{\rm bin} = 0.08$, a loop-like structure is created. In Thun et al. (2017), we did not notice this loop-type behaviour for small $e_{\rm bin}$ because we only simulated $e_{\rm bin} = 0.0$ and $e_{\rm bin} = 0.08$ and no values in between. Using a smaller $R_{\rm min} = a_{\rm bin}$ and a better coverage of small $e_{\rm bin}$ values allowed us to discover this new, complex behaviour. Although this constitutes a very exciting new finding, we defer further investigation to a subsequent study. We only note here that, as shown in the inlay of Fig. 3, this loop-like structure is also present for higher mass ratios of $q_{\rm bin}$ =0.60 and $q_{\rm bin} = 0.90$ confirming the generality of our results.

Figure 4 shows the correlation of gap eccentricity and gap size for different binary eccentricities as well as different binary mass ratios. Discs around binaries with eccentricities close to zero create the most eccentric gaps, while binaries with eccentricities close to the branching point have the smallest and least eccentric gaps. High eccentric binaries create the largest gaps which are also highly eccentric.

Figures 3 and 4 have been generated from models using our standard aspect ratio and viscosity. Exploratory simulations with different h (0.03, 0.04) and α (0.001, 0.05) show the same trend as described in Thun et al. (2017). Increasing the viscosity leads to smaller, more circular gaps with shorter precession periods, and the same trend holds for smaller aspect ratios. Due to the neglect of the disc backreaction on the binary for these simulations without embedded planet, the results displayed in Figs. 3 and 4 refer to the zero disc mass limit. In our case of small disc mass ($M_{\rm disc} = 0.01\, M_{\rm bin}$) this is a very good approximation. For a test simulation for our standard model (Kepler-38), which included disc backreaction, the change in $e_{\rm bin}$ over the first 50 000 binary orbits was less than 2%.

Table 3 summarises the gap properties of the five systems as calculated using the PLUTO code. Although the systems studied in this paper have mass ratios different from $q_{\rm bin} = 0.29$, which is the value of Kepler-16 investigated in Thun et al. (2017), the general behaviour is in good agreement with our earlier study. The most circular system (Kepler-413) produces the most eccentric gap, with an eccentricity of $e_{\rm gap} = 0.43$, while the largest gap is formed by the most eccentric binary (Kepler-34), which also has the longest precession period of $T_{\rm prec} = 4000\, T_{\rm bin}$. Systems close to the branching point (Kepler-16 and Kepler-35) have the smallest gaps with the shortest precession periods. Kepler-35 has the shortest precession period of $T_{\rm prec} = 1079\, T_{\rm bin}$, since the mass ratio of Kepler-35 is, with $q_{\rm bin} = 0.91$, almost equal to one, and higher mass ratios lead to shorter precession periods (Thun et al. 2017). Since the mass ratio does not change the gap size significantly, Kepler-16, which has an

Table 3. Disc properties of the five systems obtained with PLUTO simulations.

System	$T_{\rm gap}$ [$T_{\rm bin}$]	$a_{\rm gap}$ [$a_{\rm bin}$]	$e_{\rm gap}$
Kepler-16	1247.09	3.64	0.25
Kepler-34	3999.53	6.99	0.40
Kepler-35	1078.99	4.02	0.27
Kepler-38	2029.37	4.50	0.34
Kepler-413	1966.80	5.36	0.42

eccentricity closer to the critical eccentricity than Kepler-35, has the smallest gap of all systems considered in this paper. As already seen in our earlier study we find that the size of the gap is directly correlated with the precession period of the gap, for all systems under investigation. This behaviour is expected from single particle trajectories and supported by the used scaling for $T_{\rm prec}$ in Fig. 3. Comparing with Table 1, one can see that the two systems with the highest gap eccentricity (Kepler-34 and -413) also possess the planets with the highest eccentricity.

Concerning the outcome of the different numerical methods, the best agreement between PLUTO and FARGO3D is obtained for Kepler-38 and -413; both systems are on the lower branch and far away from the branching point. For our two systems close to the branching point (Kepler-16 and -35), FARGO3D produces slightly higher precession periods than PLUTO, however the gap size and eccentricity match very well. The largest deviations between the two codes can be seen for the Kepler-34 system, which produces the largest gap. Here, the precession period deviates by roughly ten percent and the gap size by five percent between the two codes.

Overall, the static disc parameters (gap size and eccentricity) are in good agreement between the two codes for all systems. However, for the dynamical parameter (precession period of the gap) the codes can deviate slightly, depending on the observed system. This could be a consequence of the very low precession rate, especially for Kepler-34, where the gap is nearly stationary with respect to the inertial frame.

4. Planets in circumbinary discs

In this section, we describe the evolution of planets in the circumbinary discs around our five systems under investigation. In the first part, we give an account of the general behaviour using the sample system Kepler-38, and then describe the specifics of the other systems below. Before inserting the planets into the discs, we evolved the circumbinary discs for all systems without a planet for 10 000 binary orbits such that a quasi steady state was reached; see Fig. 2. We then inserted the planet into the disc and kept it on a fixed circular orbit for another 2000 binary orbits, so that the disc could adjust to the presence of the planet. After that we switched on the back-reaction of the disc onto the planet, meaning the planet was allowed to migrate freely through the disc. We also switch on the back-reaction of the disc onto the binary which leads to a very slow increase of the binary eccentricity and a slow decrease of the binary separation, accompanied with a small reduction of the binary orbital period, $T_{\rm bin}$. When we refer to $T_{\rm bin}$, we always mean the initial, unperturbed binary period $T_{\rm bin} = 2\pi\sqrt{a_{\rm bin}^3/(GM_{\rm bin})}$, calculated using the observed values summarised in Table 1. The back-reaction from the planet and the disc causes also a precession of the binary, which is much slower compared to the precession of the inner gap and the planet's orbit. The azimuthally averaged density profiles of the disc for all five systems after 10 000 $T_{\rm bin}$ is displayed in Fig. 5 together with the initial positions of the embedded planets.

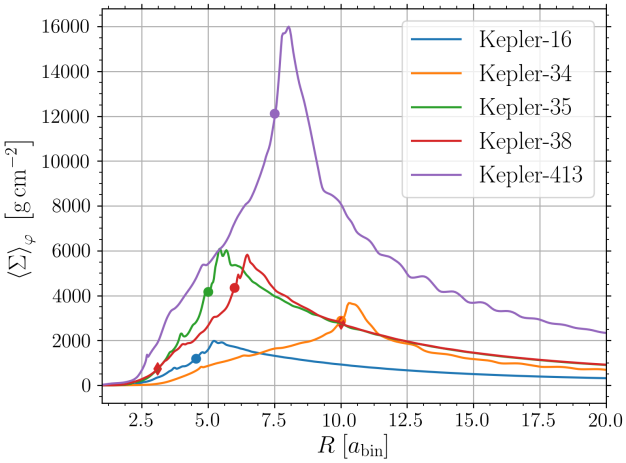

Fig. 5. Azimuthally averaged density profiles after 10 000 binary orbits for the five different *Kepler* systems. The dots mark the initial planet position.

When simulating planets with the observed mass for our five systems, we found two regimes with different dynamical behaviour of the planet. To trigger these two regimes in all systems, we have chosen planet-to-binary mass ratios q from $q \approx 10^{-4}$, approximately the observed planet-to-binary mass ratio in the Kepler-34 system (light case), up to $q \approx 3.6 \times 10^{-4}$, approximately the observed planet-to-binary mass ratio in the Kepler-16 system (massive case). This range of mass ratios leads in the case of Kepler-34, -35, and -413 to planets which are way more massive than the observed planet. Nonetheless, we simulated these high-mass planets to explore if the two regimes (here the massive case) can also be triggered in those systems as well.

In this section, all presented results were obtained by PLUTO simulations. In Appendix B, we compare PLUTO and FARGO3D simulations of a circumbinary disc with an embedded planet.

4.1. Kepler-38

In this section, we use the Kepler-38 system as our reference system to illustrate the general behaviour of a planet embedded in a circumbinary disc. We have chosen Kepler-38 because for this system the best agreement between PLUTO and FARGO3D is obtained. Furthermore, we can compare our results directly with Kley & Haghighipour (2014) who also looked at Kepler-38 applying a different numerical setup. They used an initial density slope proportional to $R^{-0.5}$ whereas we use $\Sigma \propto R^{-1.5}$ in this study. However, test calculations have shown that the initial density profile has no influence on the final quasi-steady state. A more crucial difference is the position of the inner boundary. Kley & Haghighipour (2014) used an inner radius of $R_{\rm min} = 1.67\, a_{\rm bin}$. However, as we have shown in Thun et al. (2017) this radius is too large because it does not allow the full disc dynamics to develop and results in very small and circular gap edges. For this reason, we have chosen here $R_{\rm min} = a_{\rm bin}$ for all systems.

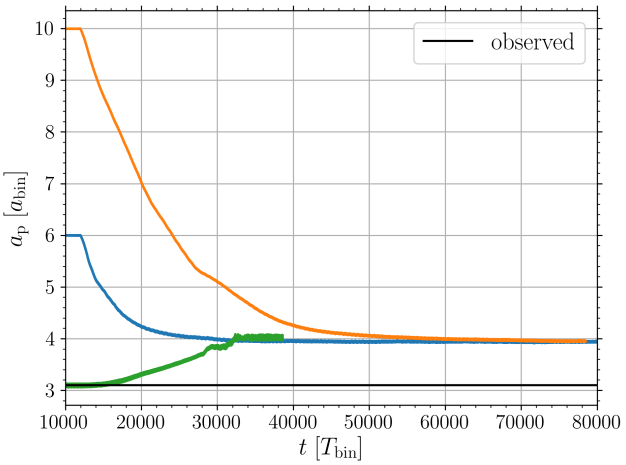

Fig. 6. Time evolution of the semi-major axis of a $m_p = 0.384\,M_{jup}$ planet with different initial positions in a circumbinary disc around the Kepler-38 system. The black line shows the observed position of the planet.

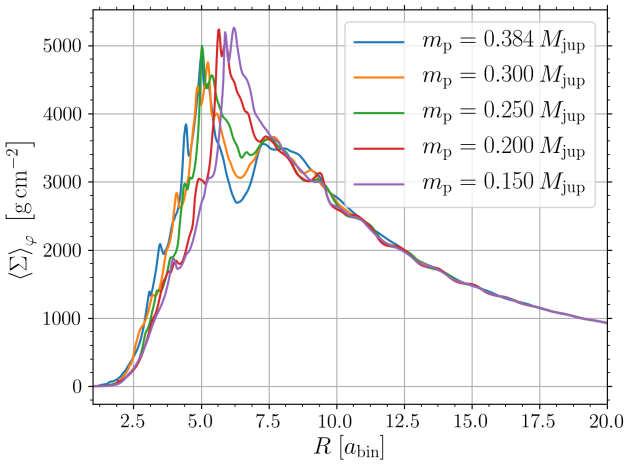

Fig. 7. Azimuthally averaged density profiles for the Kepler-38 disc with embedded planets after 12 000 binary orbits. The planets were held on a fixed orbit ($a_p = 6.0\,a_{bin}$) for 2000 binary orbits.

4.1.1. Initial planet position

In a first series of simulations, we investigate how the final stopping position of the planet depends on its initial starting position. We simulated a Saturn-like planet with a mass of $m_p = 0.384\,M_{jup}$, which is the upper mass limit for Kepler-38b. Initially, we placed the planet at three different locations inside the disc. The red curve in Fig. 5 shows the density profile for Kepler-38, and the red symbols mark the three initial locations of the planet. The outermost starting point is at $R_p(t = 0) = 10\,a_{bin}$, beyond the density maximum, which is produced by the binary-disc interaction. The second starting point was placed just inside of the density maximum at $6.0\,a_{bin}$, and finally the last starting point was placed at the observed location $3.096\,a_{bin}$.

Figure 6 shows the time evolution of the semi-major axis of the planet for the three initial starting points. Independently of its initial position, the planet migrates through the disc until it stops at a distance of approximately $3.98\,a_{bin} = 0.597$ au. The observed semi-major axis of Kepler-38b is $a_{obs} = 0.4644$ au. For the two outer starting points, the planet migrates inward until it reaches the edge of the inner cavity, which is created by the gravitational interaction of the binary on the disc. This behaviour is expected since at this point the negative Lindblad torques, responsible for inward migration, are balanced by the positive corotation torques and the planet migration comes to rest (Masset et al. 2006). If we initially place the planet at the observed location, which lies inside of the cavity, then the planet starts to migrate outward to the edge of the disc where the torques are again in balance (green curve in Fig. 6). Such an outward migration of a planet when starting inside of the cavity has been found for the Kepler-34 system by Kley & Haghighipour (2015). It is caused by the transfer of positive angular momentum to the planet when interacting with the eccentric inner disc.

The independence of the final planet position from its initial conditions suggest that the planet is subject to type I migration, since the disc is hardly perturbed. To investigate this further, we calculated the gap open criterion by Crida et al. (2006)

$$P = \frac{h}{q^{1/3}} + \frac{50\alpha h^2}{q} \leq 1\,. \tag{15}$$

For our range of planet-to-binary mass ratios and our fixed disc parameters ($h = 0.05$, $\alpha = 0.01$) the gap open criterion is not met, confirming the type I migration regime. Even very high-mass planets cannot open a full gap ($P \approx 4$); they only produce a small dip in the density profile of the disc. This can be seen in Fig. 7 for the case of Kepler-38.

Our findings are in good agreement with Kley & Haghighipour (2014) who also did not find a dependence of the final planet position on the initial position. However, in their simulations, the planet migrated further in and stopped at $a_p = 0.436$ au, which is very close to the observed location. However, this extended inward motion was an artefact of the incorrect location of the inner boundary of the grid for which an overly large inner radius was chosen.

Since the initial location of the planet does not impact its final stopping position, we always place the planet for Kepler-38 and the other systems slightly inside the peak density to save some computational time. The azimuthally averaged density profiles of all systems after 10 000 binary orbits together with the initial planet positions can be seen in Fig. 5.

4.1.2. Variation of planet mass

In this section, we investigate the influence of the planet mass on the migration process. In Fig. 8, we display the time evolution of the semi-major axis (top panel) and the eccentricity (bottom panel) of planets with different masses which range here from $m_p = 0.150\,M_{jup}$ to $m_p = 0.384\,M_{jup}$, the upper limit of the observed planet. One can see that, depending on the mass of the planet, two eccentricity states exist and that the migration path of the planet through the disc differs for those two states. The heaviest planet (with $m_p = 0.384\,M_{jup}$) migrates smoothly to its final position and its eccentricity remains very low. The lighter planets start migrating inwards until they reach a turning point (the lighter the planet is, the earlier this point is reached). From there on, the planet undergoes a fast and short period of outward migration, during which the eccentricity of the planet is increased to ≈0.20−0.22. This increase in eccentricity does not depend strongly on the planet mass. After the eccentricity is increased, the planets migrate towards the binary very slowly, compared to the first inward migration phase.

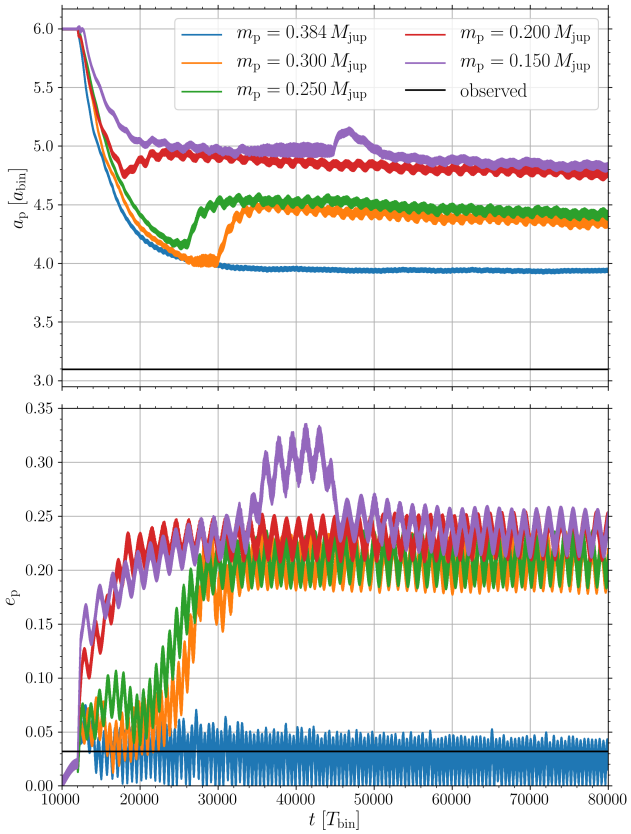

Fig. 8. Orbital elements of migrating planets in a circumbinary disc around the Kepler-38 system with different masses. *Top panel*: semi-major axis of the planet. *Bottom panel*: eccentricity of the planet. The black lines show the observed values, for the eccentricity only an upper limit is known. The upper mass limit for Kepler-38b is $m_p = 0.384\,M_{jup}$.

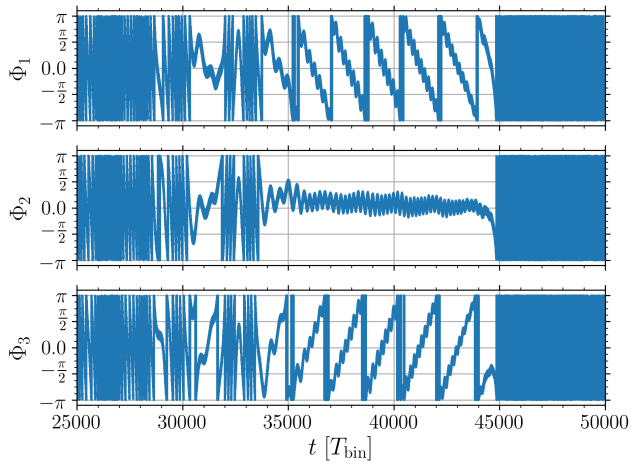

Fig. 9. Three out of eleven resonant angles for the $m_p = 0.150\,M_{jup}$ case. While the resonant angles Φ_1 and Φ_3 cover the full range from 0 to 2π the resonant angle Φ_2 librates around zero during the resonant phase of the planet (from $t = 34\,000\,T_{bin}$ to $t = 45\,000\,T_{bin}$). The resonant angles Φ_3 to Φ_{11} also cover the full range from 0 to 2π but are not shown for clarity.

Before discussing the origin of these different migration scenarios, we focus briefly on a special behaviour of the lightest planet with mass $m_p = 0.150\,M_{jup}$. At around $t \approx 34\,000\,T_{bin}$ into the evolution, one notices an additional increase in eccentricity of the planet while the migration seems to stall at around $a_p = 4.93\,a_{bin}$; see purple curves in Fig. 8. This phase of constant semi-major axis and increase of eccentricity lasts until 45 000 binary orbits. During this phase, we find for the quotient of the planet's period to the binary period, $T_p/T_{bin} \approx 11.2$, suggesting a possible capture into the 11:1 resonance between the planet and the binary as the reason for this behaviour of the planet. The position of this 11:1 resonance lies at $a_{11:1} = 4.93\,a_{bin}$. To check for this idea, we calculated the k resonance angles, which are for a general p:q resonance with $p > q$ given by

$$\Phi_k = p\lambda_p - q\lambda_{bin} - p\varpi_p + q\varpi_{bin} + k(\varpi_p - \varpi_{bin}), \tag{16}$$

with $q \le k \le p$. Here, λ_p and λ_{bin} are the mean longitudes of the planet and the binary and ϖ_p and ϖ_{bin} the longitudes of periapse. The planet and the binary are in a p:q resonance when at least one resonant angle Φ_k does not cover the full range from 0 to 2π (Nelson & Papaloizou 2002; Kley & Haghighipour 2014). In our case, Φ_2 librates around zero and all other angles cover the full range. Figure 9 shows the first three resonant angles as a selection to illustrate the behaviour of the librating angle and angles which cover the full range. This confirms that the planet is indeed captured in a 11:1 resonance with the binary. After 45 000 binary orbits, the planet is kicked out of this resonance, its semi-major axis increases shortly and its eccentricity decreases to the value before the resonant capture occurred. After this short resonant capture, the planet resumes its slow inward migration, similarly to the other planets. As seen in Fig. 9, previous to this extended phase of being engaged in the 11:1 resonance, there was a brief capture into the same resonance at $t \approx 31\,000\,T_{bin}$.

Coming back to the interaction of the planets with the disc, the impact of an embedded planet has on the ambient disc with constant aspect ratio and constant turbulent viscosity depends on its mass. For the most massive planet, we found that the inner disc became more circular with a reduced size of the inner gap. This allowed the planet to migrate further inward towards the binary. Lighter planets cannot alter the disc structure in such a strong way due to the reduced gravitational impact. The change of the inner disc structure in the presence of a planet is illustrated in Fig. 10. This figure shows the 2D surface density for three different planet masses as well as the disc structure prior to inserting the planet (top left panel). The white dashed lines show the fitted ellipses to the inner cavity. One can immediately see how the size and eccentricity of the gap decrease with increasing planet mass. Another observation is that the final position of the planet is always close to the edge of the gap. The dashed blue lines show the orbit of the planet, which lies in all cases just outside the fitted ellipse. Going from the upper left panel to the lower right panel, we see the clear trend that eccentricity and semi-major axis of the gap is decreasing as the planet mass is increased.

A more quantitative image of this behaviour can be seen in Fig. 11, which shows the time evolution of the inner disc eccentricity. The disc eccentricity and the disc pericentre (in Fig. 12) are calculated according to Thun et al. (2017, Sect. 2.5) within a limited radial interval $[R_1, R_2]$, where $R_1 = R_{min}$ and R_2 is chosen differently for each system such that it lies at a point slightly outside the density maximum. For the five systems considered in this paper, we have chosen $R_2 = \{7.0, 12.0, 7.0, 7.0, 9.0\}\,a_{bin}$ (compare to Fig. 5). For the first 10 000 binary orbits, no planet is present in the simulations and the disc eccentricity rises to about $e_{disc} \approx 0.25$. After 10 000 binary orbits, the planet is introduced

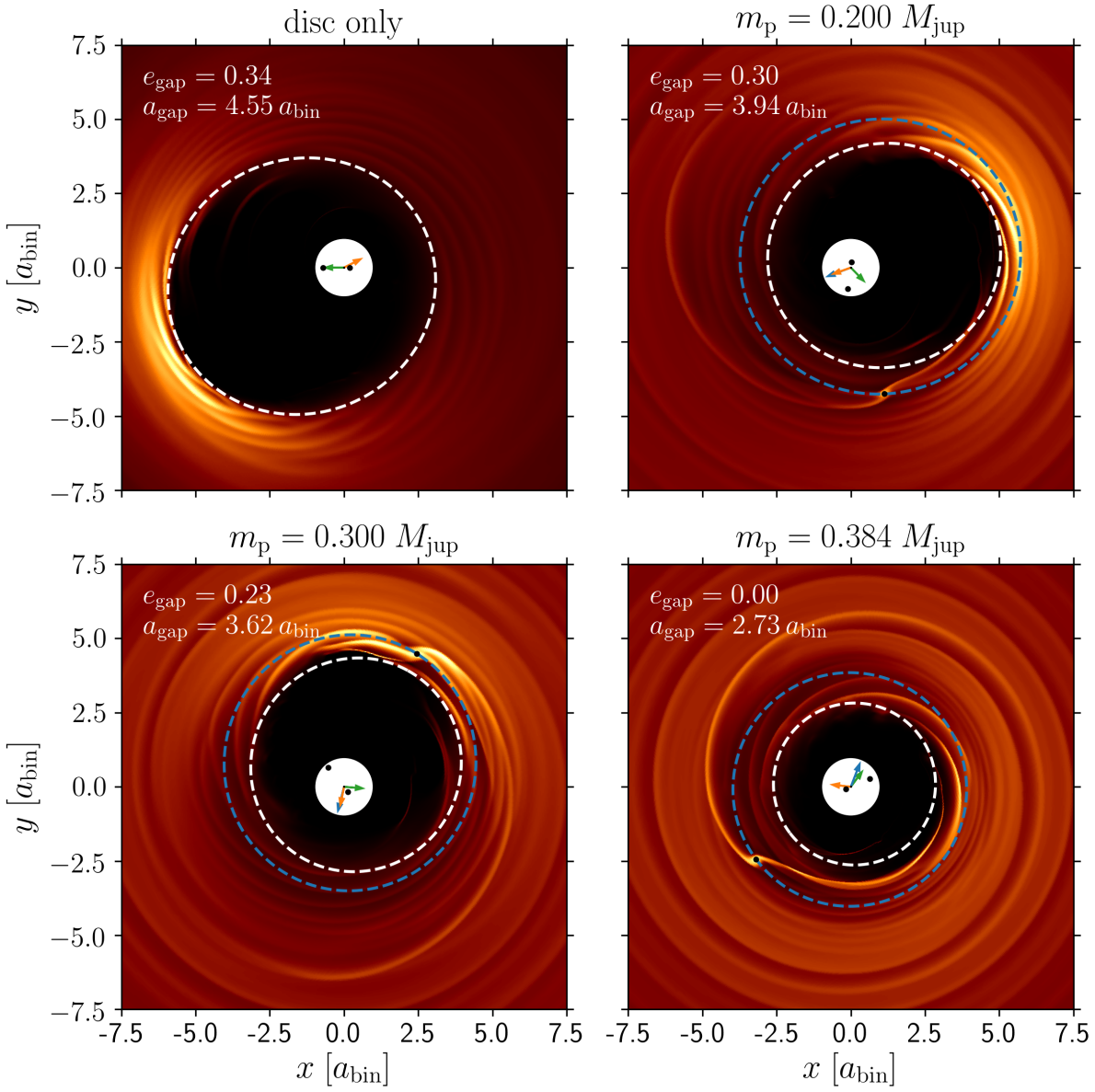

Fig. 10. Structure of the inner disc for the Kepler-38 system. The surface density is colour-coded, since the absolute density values are not important for the disc structure we omit the density scale for clarity (brighter colours mean higher surface densities). The *top-left panel* shows the circumbinary disc after 10 000 binary orbits before the planet is inserted. The remaining three panels show the disc structure with an embedded planet of varying mass after 76 500 binary orbits. The binary components and the planets are marked with black dots. The direction of pericentre of the secondary (green), the planet (blue), and the disc (orange) are marked by the arrows. Additional fitted ellipses to the central cavity are plotted in dashed white lines and the actual orbit of the planet is shown as dashed blue line. Using the fitted ellipses, the size and eccentricity of the disc gap, shown in the upper left edge of each panel, are calculated at the same time. As we saw in Fig. 2 these quantities show small variations in time around some average value.

into the simulation, and after 12 000 binary orbits, the planet is allowed to migrate through the disc. At the moment the planet is embedded, the disc's eccentricity decreases; the heavier the planet is, the more abrupt the decrease. For the light planets, except the planet with mass $m_p = 0.150\ M_{jup}$, the disc "pushes" back, increasing its eccentricity again. From this point, the inner disc eccentricity stays more or less constant. This push-back phase coincides with the outward migration phase of the planet (see Fig. 8). Interestingly, this increase of the disc eccentricity only increases the planet's semi-major axis but not the eccentricity of the planet. In the case of the massive planet, the disc is not able to "push back", as it is not massive enough, and the disc eccentricity continues to decrease smoothly to a final value of $e_{disc} = 0.043$.

As indicated by the arrows in Fig. 10, which mark the pericentre of the secondary (green), the planet (blue), and the disc (orange), the pericentre of the disc and the planet are aligned in the case of the light planets. For the massive planet, no such alignment is observed; the similar directions of disc and planet pericentre at this snapshot are coincidental. Also, the definition of a unique pericentre becomes difficult in the case of massive planets, because the planet orbit and the disc gap have

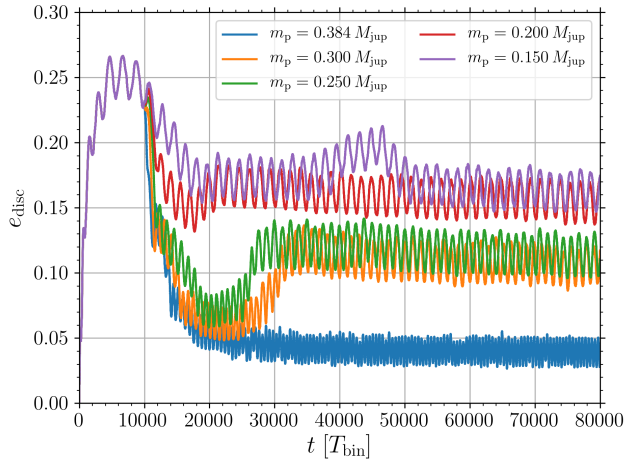

Fig. 11. Time evolution of the inner disc eccentricity for Kepler-38. Planets of different mass were introduced into the simulations at 10 000 binary orbits on circular orbits and allowed to migrate through the disc after 12 000 binary orbits.

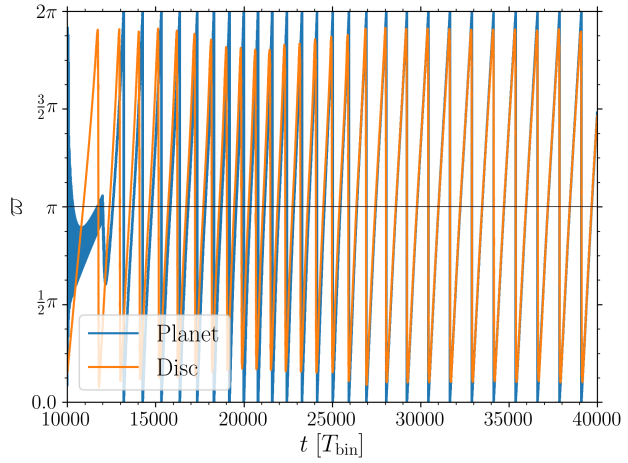

Fig. 12. Time evolution of the pericentres of a planet with mass $m_p = 0.250\,M_{jup}$ (blue) and the disc (orange) for Kepler-38. Until $t = 12\,000\,T_{bin}$ the planet is on a fixed circular orbit and therefore the pericentre is not well defined. After switching on the back-reaction onto the planet, its orbit soon becomes aligned with the inner precessing cavity of the disc.

an eccentricity close to zero. The time evolution of the directions of pericentre for disc and planet is shown in Fig. 12 for the $m_p = 0.250\,M_{jup}$ case. The orbital alignment between disc and planet is achieved during the first 10 000 binary orbits after releasing the planet.

Kley & Haghighipour (2015) and Mutter et al. (2017b) also found this alignment of planet orbit and inner disc cavity for the Kepler-34 system.

4.1.3. Variation of disc mass

As we have seen in the previous section, the planet can, depending on its mass, modify the disc structure. To investigate now the influence of the disc mass on this behaviour, we set up simulations with a different disc mass before introducing the planet into the disc. In all our models, we started with an initial disc mass of $M_{disc} = 0.01\,M_{bin}$. Since material can leave the computational domain through the inner open boundary, the disc will lose mass over time. After 10 000 binary orbits, before adding the planet to the simulation, the disc in the standard model has a mass of $M_{10000} \equiv M_{disc}(t = 10\,000\,T_{bin}) = 0.008967\,M_{bin}$. For two different planet masses, we increased or decreased the disc mass and followed the evolution of the embedded planets. Due to the local isothermal assumption, the neglect of the disc self-gravity and the independence of the potential of the surface density (the back-reaction of the disc onto the binary is not yet switched on, this means the disc terms in Eqs. (2) and (3) are neglected), the mass of the disc can be rescaled without changing its dynamics. The set of models using this disc mass rescaling is summarised in Table 4.

Table 4. Planet mass m_p, disc mass M_{disc} and the ratio $q = m_p/M_{disc}$ for models using different disc masses.

$m_p\ [M_{jup}]$	$M_{disc}\ [M_{bin}]$	q
0.384	M_{10000}	0.03388
0.200	M_{10000}	0.01765
0.384	$3M_{10000}$	0.01142
0.200	$\frac{1}{2}M_{10000}$	0.03568

Notes. The quantity $M_{10\,000} = 0.008967\,M_{bin}$ refers to the disc mass after 10 000 orbits of the standard model for Kepler-38 without an embedded planet.

The top part of Table 4 gives an overview of the planet-disc mass ratio of two models, using the standard disc mass. As seen in the previous section, the planet with mass $m_p = 0.384\,M_{jup}$, which was the most massive planet, could alter the disc structure, whereas a planet with mass $m_p = 0.200\,M_{jup}$ could not. The bottom part of Table 4 shows the planet-disc mass ratio for models with increased or decreased disc mass. For the $m_p = 0.384\,M_{jup}$ model, we increased the disc mass by a factor of three so that the planet-disc mass ratio is now comparable to the $m_p = 0.200\,M_{jup}$ case with standard disc mass. Therefore, we expect that now the massive planet cannot alter the disc structure and will end up in a state with high eccentricity. In the case where $m_p = 0.200\,M_{jup}$, we decreased the disc mass by a factor of one half to increase the disc-planet mass ration to the regime where the planet can alter the disc. In this case, the planet should migrate smoothly inwards and end up in a state with very low eccentricity.

The results of these simulations are summarised in Fig. 13. The colours for the simulations with the standard disc mass are identical to Fig. 8. The migration speed of the $m_p = 0.384\,M_{jup}$ planet in the disc with triple mass is very rapid compared to the standard disc. Since the migration speed is directly proportional to the disc mass, this behaviour is expected. This fast inward migration period lasts for approximately 552 binary orbits, during which the eccentricity of the planet is increased to $e_p = 0.184$. Following that phase, the planet migrates again outward for a very short period of time, as already seen for low-mass planets in the standard disc. After that short period of outward migration, the planet resumes its inward migration but with a very low speed compared to the initial inward migration period. This is probably due to the high eccentricity of the planet. At around 80 000 binary orbits, the planet is captured in a 9:1 resonance with the binary, which increases its eccentricity further to a final value of $e_p = 0.273$. The capture in resonance is confirmed by analysing the resonant angles; see Eq. (16). Again, Φ_2 librates around zero, while all the other angles circulate and

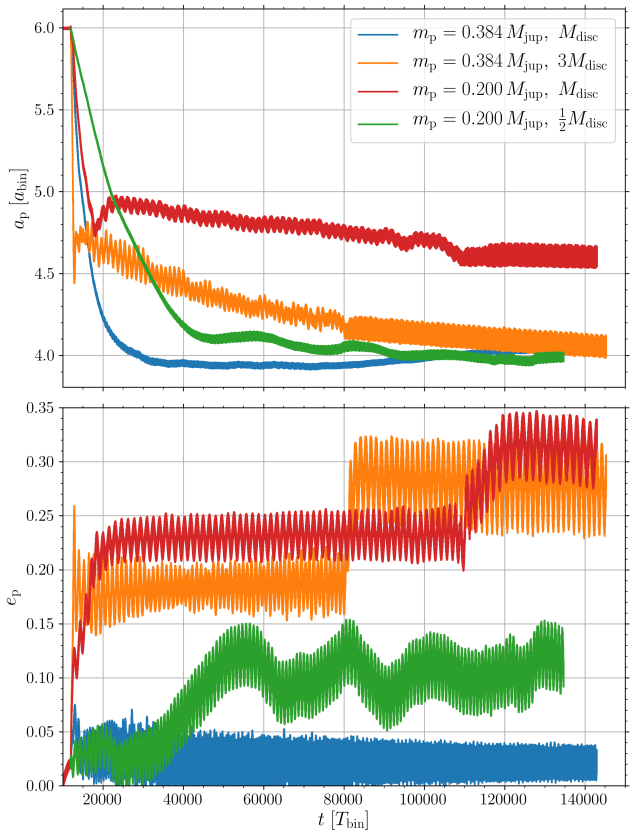

Fig. 13. Time evolution of semi-major axis (*top*) and eccentricity (*bottom*) of planets with different mass in discs of different mass, for the Kepler-38 system.

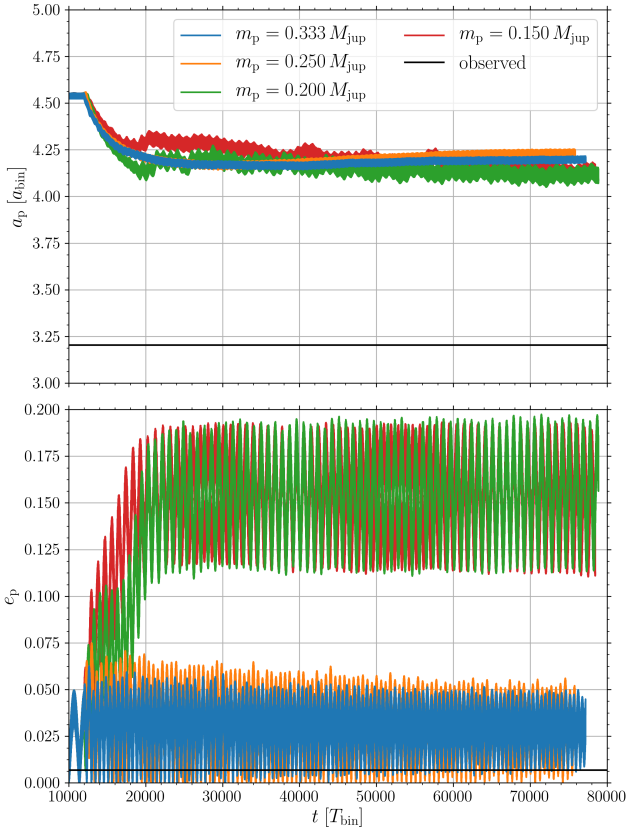

Fig. 14. Orbital elements of migrating planets in a circumbinary disc around the Kepler-16 system with different masses. *Top panel*: semi-major axis of the planet. *Bottom panel*: eccentricity of the planet. The black lines show the observed values. The observed mass of Kepler-16b is $m_p = 0.333\,M_{jup}$.

cover the full range. Although the planet is in resonance with the binary its semi-major axis still decreases slowly. This is due to the fact that the binary separation decreases faster than in the standard case due to the three times increased disc mass. This time, the planet's orbit is aligned with the precessing inner gap of the disc.

The $m_p = 0.2\,M_{jup}$ planet in the standard-disc-mass case is captured in a 8:1 resonance with the binary after $t = 110\,000\,T_{bin}$. For the reduced-disc-mass case (last row in Table 4), the $m_p = 0.2\,M_{jup}$ planet migrates slowly through the disc with no turning point. At the beginning, the eccentricity of the planet is close to zero, as expected, because due to the reduced disc mass the planet is now able to circularise the disc. Additionally, the orbit of the planet is not aligned with the inner gap. At around 30 000 binary orbits, the eccentricity increases and starts to fluctuate around $e_p = 0.10$ on a long timescale.

After having described the main features of planet migration in circumplanetary discs for the Kepler-38 system, we turn now to the other four systems. As before, we run the disc with initially $10^{-2}\ M_{bin}$ without a planet for $10\,000\,T_{bin}$ and then embed planets of different masses. For the first $2000\,T_{bin}$ the planet is fixed at its orbit, then released and evolved for about $70\,000\,T_{bin}$. The final orbital parameters for the planets with the observed mass can be found in Table 5, together with the observed values.

4.2. Kepler-16

To study the evolution of planets in the Kepler-16 system, we performed simulations with different planet masses starting from the observed mass of $m_p = 0.333\,M_{jup}$ down to a mass of $m_p = 0.150\,M_{jup}$. Figure 14 shows the time evolution of the semi-major axis (top) and eccentricity (bottom) of the different planets. As seen in the eccentricity evolution, there are two distinct states, similar to the Kepler-38 case. The eccentricity of the more massive planets is not excited and remains close to zero, oscillating around $e_p = 0.029$, whereas the eccentricity of the lighter planets is increased during the first 8000 binary orbits, after releasing the planets, to a mean value of $e_p = 0.15$. These two states also differ in their alignment of the orbits with the inner gap of the disc. The lighter planets with high eccentricity end up in a state with aligned orbits, whereas no such alignment can be observed for the heavier planets. In the semi-major axis evolution, these two states are not as clearly visible as in the Kepler-38 system. Nonetheless, a difference between the massive and light planets can be observed. Heavy planets migrate smoothly through the disc, whereas the semi-major axis evolution of the lighter planets shows more noise. The massive planets start to migrate inwards smoothly, as expected from the Kepler-38 case. This phase smoothly transitions to a slow outward migrating phase, as seen also in long time simulations of Kepler-38 (see blue curve in Fig. 13). The lighter planets have also a period of outward migration, but this period is very short and followed by a second period of inward migration, as in the Kepler-38 case. The migration speed during this second inward period is far lower than during the first phase. The light planets show the same general behaviour as in the Kepler-38 case and they even migrate further

Table 5. Final orbital parameters of the embedded planets using the observed m_p for the five systems investigated, calculated using the PLUTO simulations.

System	a_p [a_{bin}]	a_{obs} [a_{bin}]	e_p	e_{obs}
Kepler-16	4.18	3.20	0.03	0.00685
Kepler-34	7.77	4.74	0.31	0.182
Kepler-35	4.47	3.35	0.12	0.042
Kepler-38	3.98	3.10	0.02	0.032
Kepler-413	5.53	3.55	0.30	0.1181

Notes. The observed data are displayed also, for comparison. The semi-major axis (a_p) and eccentricity (e_p) of the planets are obtained through time averages over several thousand binary orbits at the end of the simulations.

in than their heavier counterparts. One reason for this could be that Kepler-16 has the smallest gap with the lowest eccentricity and therefore the circularising effect of heavier planets is not as important as in the other systems. This also implies that the increase of eccentricity is connected to the alignment of the planets orbit with the disc gap.

4.3. Kepler-34

For the Kepler-34 system, we simulated planets with masses from the observed mass of $m_p = 0.220\,M_{jup}$ up to $m_p = 0.800\,M_{jup}$. Figure 15 gives an overview of the orbital elements (semi-major axis and eccentricity) of the simulated planets. In all cases, we observe nearly the same migration behaviour, first a fast inward migration followed by a short period of outward migration. After that, the planets are relatively soon (after around 40 000 T_{bin}) parked in their final position. In all cases, the final orbits of the planets are relatively eccentric, with e_p well above 0.2, and they are fully aligned with the eccentric gap of the disc and precess at the same rate. Although the massive planets can circularise the inner cavity slightly, this effect is not strong enough, because of the large and highly eccentric initial gap ($a_{gap} = 6.99\,a_{bin}$, $e_{gap} = 0.4$). For the planet with the observed mass of $m_p = 0.220\,M_{jup}$ we find a final semi-major axis of $a_p = 7.77\,a_{bin}$ and an eccentricity of $e_p = 0.31$ (see also Table 5).

In their study of the planet in Kepler-34, Kley & Haghighipour (2015) observed the same migration behaviour as we find here: a fast inward migration to the edge of the inner cavity. They find in their simulations a smaller semi-major axis of $a_p = 6.1\,a_{bin}$ and a comparable eccentricity of $e_p = 0.3$. One reason for the difference in the planets semi-major axis could be again the position of the inner computational boundary. Kley & Haghighipour (2015) used a value of $R_{min} = 1.47\,a_{bin}$, which is too large (Thun et al. 2017). Furthermore, they use a uniformly spaced grid in the R-direction with only 256 cells. Therefore, their resolution in the inner part of the computational domain is very low, which could be another reason for the observed differences, but they also found an alignment of the planet's orbit with the inner eccentric cavity.

For Kepler-34, Mutter et al. (2017b) found for their one- and two-MMSN disc models (our disc mass lies in between these two) a final semi-major axis of $a_p \approx 8.7\,a_{bin}$ and an eccentricity of $e_p = 0.25-0.3$, in relatively good agreement with our results.

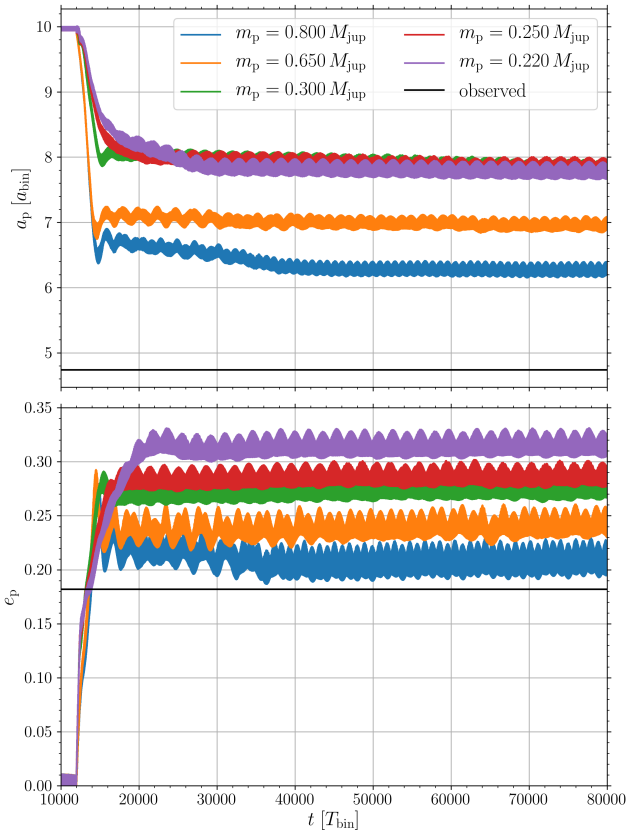

Fig. 15. Orbital elements of migrating planets in a circumbinary disc around the Kepler-34 system with different masses. *Top panel*: semi-major axis of the planet. *Bottom panel*: eccentricity of the planet. The black lines show the observed values. The observed mass of Kepler-34b is $m_p = 0.220\,M_{jup}$.

Furthermore, they also find an alignment of the planet's orbit with the disc cavity. They mention this alignment only in the case of a planetary core with very low mass, but since they see no big difference between the full mass planet and the planetary core, we assume that this alignment also happens in the case of the fully grown planet.

4.4. Kepler-35

For Kepler-35, we studied the migration of planets starting from the observed mass $m_p = 0.127\,M_{jup}$ up to $m_p = 0.550\,M_{jup}$. Figure 16 shows results of simulations with the different planet masses. The two most massive planets with $m_p = 0.550\,M_{jup}$ and $m_p = 0.500\,M_{jup}$ show the typical behaviour of massive planets, as already discussed for the other systems. Their eccentricity remains low and they do not align their orbit with the precessing inner gap of the disc.

The eccentricity of planets with masses from $m_p = 0.300\,M_{jup}$ to $m_p = 0.450\,M_{jup}$ become excited to a mean value of about 0.15. The planet with mass $m_p = 0.300\,M_{jup}$ ends up in a 9:1 resonance with the binary after 55 000 binary orbits, and therefore its eccentricity is increased further. This planet also shows the general migration behaviour of lighter planets, as seen for the other systems. This behaviour is not as clearly visible for the planets with masses $m_p = 0.400\,M_{jup}$ and $m_p = 0.450\,M_{jup}$, since they are both captured in a 8:1 resonance with the binary after $t \approx 23\,000\,T_{bin}$.

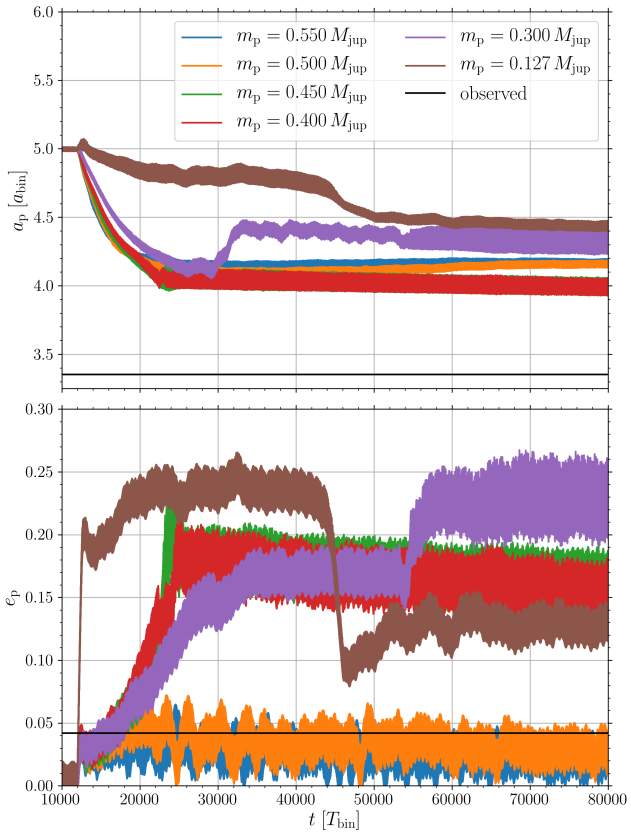

Fig. 16. Orbital elements of migrating planets in a circumbinary disc around the Kepler-35 system with different masses. *Top panel*: semi-major axis of the planet. *Bottom panel*: eccentricity of the planet. The black lines show the observed values. The observed mass of Kepler-35b is $m_p = 0.127\ M_{jup}$.

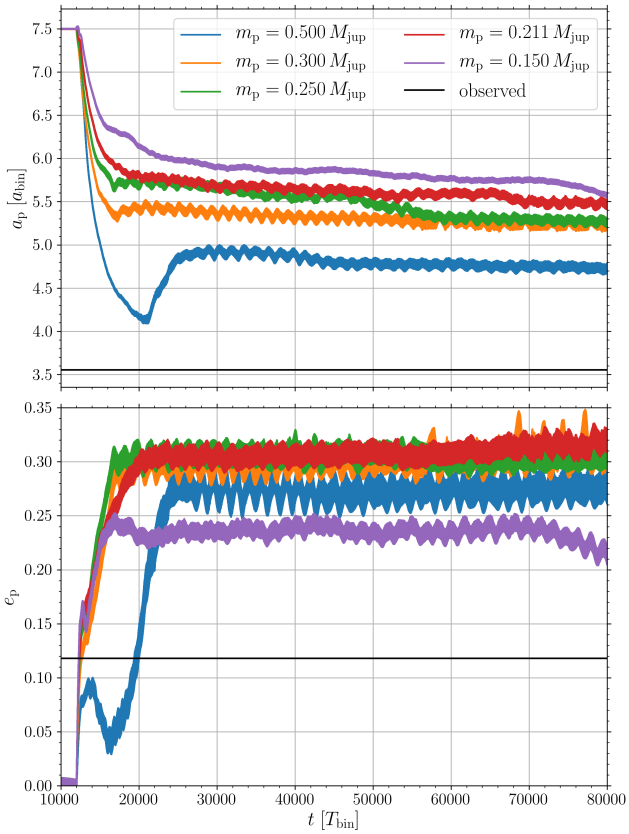

Fig. 17. Orbital elements of migrating planets in a circumbinary disc around the Kepler-413 system with different masses. *Top panel*: semi-major axis of the planet. *Bottom panel* eccentricity of the planet. The black lines show the observed values. The observed mass of Kepler-413b is $m_p = 0.211\ M_{jup}$.

The planet with the observed mass of $m_p = 0.127\ M_{jup}$ shows a behaviour not yet observed for the other systems. Its eccentricity is increased fast to a value slightly below 0.25. After roughly 44 000 binary orbits, its eccentricity drops rapidly to a value below 0.15. This drop is also visible in the semi-major axis of the planet. A FARGO3D comparison simulation with a planet of this mass shows the same behaviour, but at a later time. The fast drop in eccentricity happens there at roughly 59 000 binary orbits. Besides this time shift, the PLUTO and FARGO3D curves for the semi-major axis and the eccentricity have a very similar evolution. For both codes, the drop in eccentricity (for $m_p = 0.127\ M_{jup}$) happens when the planet crosses $a_p \approx 4.75\ a_{bin}$. Since in the case of FARGO3D, the planet migrates slower, it needs more time to reach this point. A reason for this behaviour could be the very low mass of the planet compared to the disc in this case. Therefore, the influence of the disc on the planet is very high, and the disc eccentricity drops simultaneously. The final orbital parameters of the migrated planet are summarised in Table 5.

4.5. Kepler-413

For Kepler-413, we model embedded planets with masses ranging from m_p =0.150 M_{jup} up to $m_p = 0.500\ M_{jup}$; the observed mass is $m_p = 0.211\ M_{jup}$. Concerning the disc dynamics, Kepler-413 is very similar to Kepler-34; they both show a gap with high eccentricity. As a consequence no low-eccentricity state seems to exist for the planet as shown in Fig. 17. Again, all planets show more or less the same migration behaviour: a fast inward migration, followed by a short period of outward migration (only visible for massive planets), and then a fast arrival at their final position. In addition, all planet orbits are aligned with the inner gap, as in Kepler-34. The time of alignment depends on the planet mass and is earlier for the lightest planets. The final orbital parameters of the simulated planet with the observed mass can be found in Table 5.

5. Discussion

Through 2D hydrodynamical simulations, we first studied the structure of the circumbinary disc around five observed systems (Kepler-16, -34, -35, -38, and -413). After determining the structure of the inner disc (gap size and eccentricity as well as precession period of the gap), we inserted planets of various masses into our simulations and examined how they migrated through the disc and how the presence of the planet changed the disc structure. In the following, we summarise the most important results of our simulations with and without planets.

5.1. Disc dynamics

Firstly, we looked at the structure of the inner gap created by the gravitational interaction between the binary and the disc. For simplicity, we restricted ourselves here to locally isothermal discs with a fixed aspect ratio ($h = 0.05$) and viscosity ($\alpha = 0.01$)

and studied different binary parameters. In agreement with previous studies (Miranda et al. 2017; Thun et al. 2017), we found that for all systems, the circumbinary discs became eccentric and showed a coherent slow prograde precession. Plotting the obtained precession period $T_{\rm prec}$ versus the obtained gap size $a_{\rm gap}$, we confirmed the existence of two different branches for varying binary eccentricities, as shown in Fig. 3. As seen in the figure, the four systems, Kepler-16, 35, -38, and -413, fall exactly on the lower branch of the relation found in our first study (Thun et al. 2017). While Kepler-34 lays on the extreme end of the upper branch, due to the very large binary mass ratio and eccentricity of the system. To account for the different binary parameters, the y-axis has been rescaled according to the scaling of free particle orbits around binaries, Eq. (14).

In addition to these two known branches, we discovered a new behaviour for small binary eccentricities between $e_{\rm bin} = 0.0$ and $e_{\rm bin} = 0.05$. Starting from circular binaries, the precession period of the gap as well as the gap size increases up to $e_{\rm bin} = 0.05$. From there on, both quantities decrease again, as expected on the lower branch. At a critical $e_{\rm bin} \approx 0.18$, the trend reverses again. A more detailed investigation of this additional new loop in the $T_{\rm prec}$-$a_{\rm gap}$ diagram lies beyond the scope of this paper and is deferred to a future study.

In general, the five simulated systems behaved as expected and also the results from the two different codes used in this study, namely PLUTO and FARGO3D, produced matching results.

5.2. Evolution of embedded planets

After we had investigated the disc structure without the presence of a planet, we introduced planets to the simulations and studied how they migrated through the discs. The migration of planets and especially the final orbital parameters of the planets are important since it is assumed that planets in a P-type orbit around a binary form in the outer part of the disc, where the gravitational influence of the forming process due to the binary is negligible, and migrate inward to their final observed position.

Firstly, the disc without a planet was simulated until a quasi-steady state was reached, then we added the planet on a circular orbit for 2000 binary orbits so that the disc could adjust to the planet. After that initialisation period, the planet was allowed to freely move through the disc according to the disc torques acting on it. In the following, we summarise the main results using the example of Kepler-38.

- Initial planet position: in a first simulation series, where we varied the initial planet position, we found that the final parking position of the planet does not depend on this initial planet location. In all cases, the planet migrates until it reaches the edge of the disc. At this point a strong positive corotation torque balances the negative Lindblad torque, responsible for inward migration, and the planet stops (Masset et al. 2006).
- Variation of planet mass: when we varied the planet mass, we observed two different final configurations. In one state, the eccentricity of the planet is not excited and the planets remain on a nearly circular orbit around the binary. This low-eccentricity state applies for "massive" planets. These massive planets migrate smoothly through the disc until they reach their final position. During this migration process, they are able to alter the disc structure by shrinking and circularising the inner cavity of the disc. In contrast, the eccentricity of "lighter" planets becomes excited during their inward migration through the disc. Their migration path is not as smooth as in the massive planet case. An initial period of rapid inward migration is typically followed by a short and fast period of outward migration, that is again followed by a period of inward migration but with a much slower speed than in the first phase. During this migration through the disc, the orbit of the planets becomes fully aligned with the precessing inner gap of the disc and they end up in a state of apsidal corotation.

  We were not able to find a sharp boundary between the massive and the light planets. The two different codes PLUTO and FARGO3D agreed well on the general migration behaviour of the planets (two eccentricity states) but showed small differences concerning the boundary between the two states of massive and light planets.
- Variation of disc mass: a planet's behaviour is not only determined by its mass but also the planet-to-disc mass ratio. In a simulation with a massive planet and a disc with reduced mass, we could observe that the massive planet behaves now like the light planets before, showing eccentricity excitation and orbital alignment. In other cases, we were able to switch the behaviour of a light planet to that of a massive one by decreasing the disc's mass. Therefore, whether a planet in its final starting position shows an orbital alignment with the disc and an eccentric orbit or a more circular non-aligned orbit depends on the mass ratio between disc and planet.
- Resonances: during our simulations, we quite often observed that planets were captured into a high-order resonance (11:1, 9:1, 8:1) with the binary. Planets which are trapped in a resonance do not migrate further to their observed location and their eccentricity is excited. We observed the capture into a resonance only for the "light" planet case during the second, slower inward migration phase.

The existence of two different eccentricity states was observed for the three systems Kepler-16, -35, and -38. For the systems Kepler-34 and -413, we could only observe the high eccentricity state for the light planet case with full orbital alignment between disc and planet. Even for planets with a mass around half a Jupiter mass or more, we were not able to trigger the massive planet case for these two systems. The reason for this behaviour could be the initial large and eccentric disc gaps in Kepler-34 and -413. Although the heavier planets were able to partly circularise the inner gap, they could never decrease the discs eccentricity below a value of 0.1. The two eccentricity states depend on the planet-to-disc mass ratio as well as on the binary parameters, since the latter determines the size and eccentricity of the disc's gap for otherwise identical disc parameter like pressure and viscosity.

In this paper, we did not study the influence of the disc's pressure and viscosity. In all simulations, we chose an aspect ratio of $h = 0.05$ and a viscosity of $\alpha = 0.01$ to be consistent with our first paper, although an aspect ratio of $h = 0.05$ leads to rather high gas temperatures at the location of the planet. A comparison with a test simulation that also considered viscous heating and radiative cooling (for the same disc mass) suggests that an aspect ratio of $h = 0.04$ represents a more realistic gas temperature.

Test simulations of circumbinary discs around Kepler-38 with $\alpha = 0.001$ and $\alpha = 0.05$ show that in the case of low viscosity the observed planet with mass $m_{\rm p} = 0.384\, M_{\rm jup}$ behaves accordingly to the light case, whereas in the case of high viscosity all three simulated planets with masses $m_{\rm p} = \{0.384,\ 0.300,\ 0.250\}\, M_{\rm jup}$ are able to dominate the disc. Since higher viscosity leads to a higher mass flow through the disc, the disc with $\alpha = 0.05$ is less massive than in our standard

case; therefore all simulated planets are able to shrink and circularise the gap. In the case of $\alpha = 0.001$, the disc is more massive, meaning that even the planet with mass $m_p = 0.384\,M_{jup}$ behaves like a light planet.

In general, we see both migration regimes if we vary the viscosity or the aspect ratio of the disc; only the final orbital parameters can change. This influence of the disc's pressure and viscosity on the final orbital parameters of the planet needs to be examined in future studies together with a more realistic equation of state rather than the isothermal one used in this study.

6. Summary

In all our simulations, the planet migration stopped at the inner boundary of the disc. However, the general observation in all five *Kepler* systems considered was that the planets stop their migration outside of the observed location; see Table 5. Two of the modelled systems (Kepler-16 and -38) ended up in the non-eccentric state where the final stopping point was about 30% larger than the observed locations, while the eccentricities were more or less comparable to the observed values. Kepler-35b reached an intermediate case where the final eccentricity was $e_p = 0.12$ and a semi-major axis which was 30% larger than the observed one. Two systems (Kepler-34 and -413) ended up in the high eccentric, aligned state with a calculated final position about 1.5 times larger than the observed location and calculated eccentricities about 2–2.5 times larger than the observed ones. Although the final orbital elements did not match the observed ones very well, our simulations nevertheless did reproduce the fact that the systems with the highest gap eccentricity (Kepler-34 and -413) have the planets with the highest observed eccentricity among all systems considered in this study. We therefore suggest that the large observed planet eccentricities for these systems are caused by an eccentric circumbinary disc.

Nevertheless, because the calculated final position of the planets is too large in all cases, a mechanism is needed that is able to reduce the inner gap size of the disc to allow the planets to migrate further into the observed locations. One such mechanism could be disc self-gravity as described in Mutter et al. (2017b), although, according to the authors, only for very massive discs with masses ten times the minimum mass solar nebula or more, will the inner gap shrink further. Another way to reduce the disc's gap size could be to change the disc parameters, such as pressure and viscosity. Increasing the temperature and/or the viscosity will produce smaller gaps. But as calculations in our first study (Thun et al. 2017) have shown, possibly unusually high pressures or viscosities may be needed to reduce the gap size substantially.

Furthermore, the impact that radiative effects have on the inner gap of the disc should be investigated. A good starting point will be simulations that include viscous heating and radiative cooling from the disc surface. Even more sophisticated simulations could also consider the radiative transport in the disc's midplane and irradiation from the central binary. Finally, whether full 3D simulations will show different results remains to be seen. Considering the long timescales to be simulated, this is still numerically very challenging.

Acknowledgements. Daniel Thun was funded by grant KL 650/26 of the German Research Foundation (DFG). Most of the numerical simulations were performed on the bwForCluster BinAC. The authors acknowledge support by the High Performance and Cloud Computing Group at the Zentrum für Datenverarbeitung of the University of Tübingen, the state of Baden–Württemberg through bwHPC and the German Research Foundation (DFG) through grant no INST 37/935-1 FUGG. All plots in this paper were made with the Python library matplotlib (Hunter 2007).

References

Artymowicz, P., & Lubow, S. H. 1994, ApJ, 421, 651
Benítez-Llambay, P., & Masset, F. S. 2016, ApJS, 223, 11
Crida, A., Morbidelli, A., & Masset, F. 2006, Icarus, 181, 587
de Val-Borro, M., Edgar, R. G., Artymowicz, P., et al. 2006, MNRAS, 370, 529
Doyle, L. R., Carter, J. A., Fabrycky, D. C., et al. 2011, Science, 333, 1602
Dvorak, R. 1986, A&A, 167, 379
Günther, R., & Kley, W. 2002, A&A, 387, 550
Holman, M. J., & Wiegert, P. A. 1999, AJ, 117, 621
Hunter, J. D. 2007, Comput. Sci. Eng., 9, 90
Kley, W., & Haghighipour, N. 2014, A&A, 564, A72
Kley, W., & Haghighipour, N. 2015, A&A, 581, A20
Kostov, V. B., McCullough, P. R., Carter, J. A., et al. 2014, ApJ, 784, 14
Kostov, V. B., Orosz, J. A., Welsh, W. F., et al. 2016, ApJ, 827, 86
Lin, D. N. C., & Papaloizou, J. 1986, ApJ, 309, 846
Lines, S., Leinhardt, Z. M., Baruteau, C., Paardekooper, S.-J., & Carter, P. J. 2015, A&A, 582, A5
Marzari, F., Thébault, P., & Scholl, H. 2008, ApJ, 681, 1599
Masset, F. S., Morbidelli, A., Crida, A., & Ferreira, J. 2006, ApJ, 642, 478
Meschiari, S. 2012, ApJ, 761, L7
Mignone, A., Bodo, G., Massaglia, S., et al. 2007, ApJS, 170, 228
Miranda, R., Mu} noz, D. J., & Lai, D. 2017, MNRAS, 466, 1170
Müller, T. W. A., Kley, W., & Meru, F. 2012, A&A, 541, A123
Mutter, M. M., Pierens, A., & Nelson, R. P. 2017a, MNRAS, 465, 4735
Mutter, M. M., Pierens, A., & Nelson, R. P. 2017b, MNRAS, 469, 4504
Nelson, R. P., & Papaloizou, J. C. B. 2002, MNRAS, 333, L26
Nelson, R. P., Papaloizou, J. C. B., Masset, F., & Kley, W. 2000, MNRAS, 318, 18
Orosz, J. A., Welsh, W. F., Carter, J. A., et al. 2012a, ApJ, 758, 87
Orosz, J. A., Welsh, W. F., Carter, J. A., et al. 2012b, Science, 337, 1511
Paardekooper, S.-J., Leinhardt, Z. M., Thébault, P., & Baruteau, C. 2012, ApJ, 754, L16
Pierens, A., & Nelson, R. P. 2007, A&A, 472, 993
Pierens, A., & Nelson, R. P. 2008, A&A, 483, 633
Pierens, A., & Nelson, R. P. 2013, A&A, 556, A134
Scholl, H., Marzari, F., & Thébault, P. 2007, MNRAS, 380, 1119
Schwamb, M. E., Orosz, J. A., Carter, J. A., et al. 2013, ApJ, 768, 127
Shakura, N. I., & Sunyaev, R. A. 1973, A&A, 24, 337
Silsbee, K., & Rafikov, R. R. 2015, ApJ, 808, 58
Stone, J. M., & Norman, M. L. 1992, ApJS, 80, 753
Tanaka, H., Takeuchi, T., & Ward, W. R. 2002, ApJ, 565, 1257
Thun, D., Kley, W., & Picogna, G. 2017, A&A, 604, A102
Ward, W. R. 1997, Icarus, 126, 261
Welsh, W. F., Orosz, J. A., Carter, J. A., et al. 2012, Nature, 481, 475
Welsh, W. F., Orosz, J. A., Short, D. R., et al. 2015, ApJ, 809, 26

Appendix A: N-body solver for PLUTO

The N-body solver for PLUTO was developed by ourselves in the framework of this project and we briefly discuss some implementation details. In the discussion, we restrict ourselves to the 2D polar case. The PLUTO-code solves the hydrodynamic equations with the help of a finite-volume method which evolves volume averages in time. For the time evolution, we use the second-order Runge–Kutta method (RK2) provided by PLUTO. Given the hydrodynamical variables $\mathbf{V}^n = (\varrho^n, u_R^n, u_\varphi^n)$ at time t^n, the positions $\mathbf{x}_\ell^n$ and velocities $\mathbf{v}_\ell^n$ of the N bodies ($\ell = 1, ...N$) also at time t^n, the whole system (hydrodynamical variables and N bodies) are advanced from time t^n to $t^{n+1} = t^n + \Delta t$ using the following RK2 method:

$$\mathbf{U}^* = \mathbf{U}^n + \Delta t \mathcal{L}^n \tag{A.1}$$

$$\mathbf{U}^{n+1} = \frac{1}{2}\left(\mathbf{U}^n + \mathbf{U}^* + \Delta t \mathcal{L}^*\right) . \tag{A.2}$$

For a definition of the "right-hand-side" operator $\mathcal{L}$ see Mignone et al. (2007). Here, $\mathbf{U} = (\varrho, \varrho u_R, \varrho u_\varphi)$ denotes the vector of conserved variables. The intermediate predictor state, $\mathbf{U}^*$, is given at time t^{n+1} which is important for the correct stepping of the N bodies. During the first RK2-substep (called A) we perform the following substeps:

A1 Set boundaries.

A2 Calculate disc feedback on each body ℓ (second term in Eq. (3))

$$\mathbf{a}_{\mathrm{disc},\ell}^n(\mathbf{U}^n) = \sum_{ij} \frac{G\Sigma_{ij}^n \, \mathrm{d}V_{ij}}{\left[(x_{c,ij} - x_\ell^n)^2 + (y_{c,ij} - y_\ell^n)^2 + (\varepsilon h R_i)^2\right]^{3/2}} \times \begin{pmatrix} x_{c,ij} - x_\ell^n \\ y_{c,ij} - y_\ell^n \end{pmatrix}, \tag{A.3}$$

where $x_{c,ij} = R_i \cos(\varphi_j)$ and $y_{c,ij} = R_i \sin(\varphi_j)$ denote the x- and y-coordinate of grid cell (i, j). The volume element $\mathrm{d}V_{ij}$ of this cell is given in polar coordinates by

$$\mathrm{d}V_{ij} = \frac{1}{2}\left(R_{i+\frac{1}{2}}^2 - R_{i-\frac{1}{2}}^2\right) \times \left(\varphi_{j+\frac{1}{2}} - \varphi_{j-\frac{1}{2}}\right). \tag{A.4}$$

A3 Calculate the acceleration (disc force and mutual gravitational attraction) on each of the N bodies (Eq. (3), first two terms)

$$\begin{aligned}\mathbf{a}_\ell^n =& \mathbf{a}_{\mathrm{grav},\ell}^n\left(\mathbf{x}_1^n, \ldots, \mathbf{x}_N^n\right) + \mathbf{a}_{\mathrm{disc},\ell}^n(\mathbf{U}^n) \\ =& -\sum_{k\neq\ell}^{N} \frac{GM_k}{\left[(x_\ell^n - x_k^n)^2 + (y_\ell^n - y_k^n)^2\right]^{3/2}} \begin{pmatrix} x_\ell^n - x_k^n \\ y_\ell^n - y_k^n \end{pmatrix} \\ &+ \mathbf{a}_{\mathrm{disc},\ell}^n(\mathbf{U}^n).\end{aligned} \tag{A.5}$$

A3 Calculate the indirect term, due to the acceleration of the centre of mass of the binary (Eq. (3), here 1 is the index of the primary and 2 is the index of the secondary).

$$\mathbf{a}_{\mathrm{com}}^n = \frac{M_1 \mathbf{a}_1^n + M_2 \mathbf{a}_2^n}{M_1 + M_2}. \tag{A.6}$$

A4 Hydro update $\mathbf{U}^* = \mathbf{U}^n + \Delta t \mathcal{L}(\mathbf{U}^n)$. During this step we need to calculate the potential (Eq. (1)) at each cell location (i, j)

$$\Phi_{ij}^n = -\sum_{\ell=0}^{N} \frac{GM_\ell}{\sqrt{(x_{c,ij} - x_\ell^n)^2 + (y_{c,ij} - y_\ell^n)^2 + (\varepsilon h R_i)^2}}, \tag{A.7}$$

$$+ \mathbf{a}_{\mathrm{com}}^n \cdot \begin{pmatrix} x_{c,ij} \\ y_{c,ij} \end{pmatrix}. \tag{A.8}$$

During the second RK2-substep (B) the following steps are necessary:

B1 Set boundaries.

B2 Advance bodies from $\mathbf{x}^n$ to $\mathbf{x}^{n+1}$ using a fourth order Runge–Kutta integrator (RK4) using the acceleration from Eq. (A.5). In every substep of the RK4 integrator the mutual gravitational accelerations of the bodies are recalculated using the new substep positions (first term in Eq. (3)). For the disc feedback we use $\mathbf{a}_{\mathrm{disc},\ell}^n$ in every substep. After the N-body update we transform all quantities back to the centre of mass (let $\mathbf{X}^{n+1}$ and $\mathbf{V}^{n+1}$ denote the position and velocity of the centre of mass of the binary):

$$\mathbf{x}_\ell^{n+1} = \mathbf{x}_\ell^{n+1} - \mathbf{X}^{n+1}, \tag{A.9}$$

$$\mathbf{v}_\ell^{n+1} = \mathbf{v}_\ell^{n+1} - \mathbf{V}^{n+1}. \tag{A.10}$$

This simple shift accounts for the indirect term $\mathbf{a}_{\mathrm{com}}$ in Eq. (3).

B2 Calculate acceleration of each body (Eq. (3)) using the updated body positions $\mathbf{x}^{n+1}$ and the updated hydro variables U^*.

B3 Calculate the indirect term, due to the acceleration of the centre of mass of the binary (Eq. (3)) using the accelerations of the binary from step B2.

B4 Hydro update $\mathbf{U}^{n+1} = \frac{1}{2}(\mathbf{U}^n + \mathbf{U}^* + \Delta t \mathcal{L}(U^*))$. During this step we need to calculate the potential (Eq. (1)) at each cell location.

Now all quantities (hydro and N-body positions) are at time t^{n+1} and a new RK2 cycle starts.

Appendix B: Comparison with FARGO3D

To test the implementation of our N-body solver for PLUTO we compared circumbinary disc simulations with an embedded planet for the Kepler-38 system with FARGO3D simulations (used in a 2D setup).

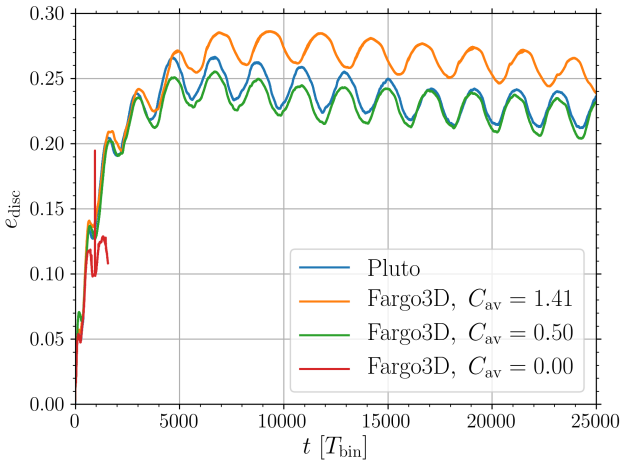

Fig. B.1. Time evolution of the disc eccentricity for the Kepler-38 system. The blue curve shows a PLUTO simulation, while all other curves show results from FARGO3D simulations, where the strength of the artificial viscosity was varied.

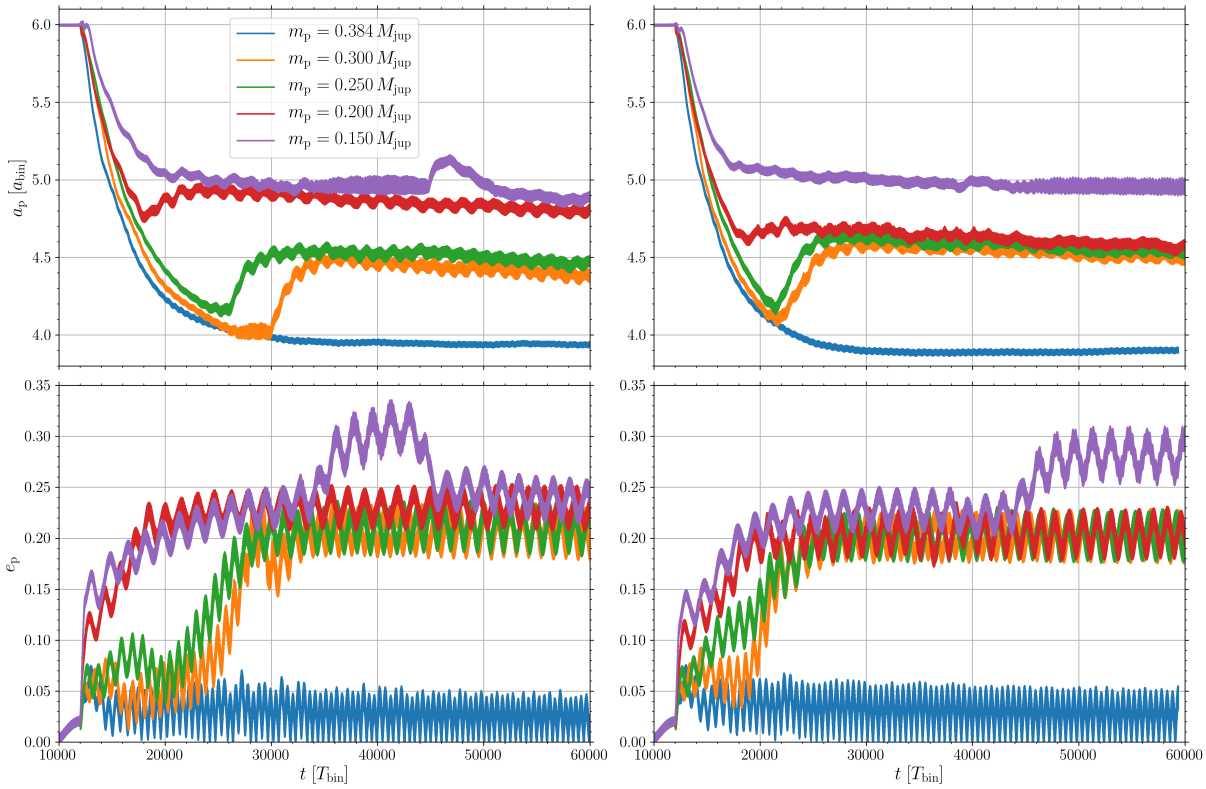

Fig. B.2. Orbital elements of planets with different mass. *Top panel*: semi-major axis of the planets. *Bottom panel*: eccentricity. *Left column*: PLUTO simulations. *Right column*: FARGO3D simulations.

As briefly discussed in Sect. 2.3, FARGO3D uses an artificial viscosity (AV) to smooth out shocks over various cells. The strength of the artificial viscosity is controlled by the constant C_{av}. This constant is basically the number of cells over which the shock is smoothed. To study the impact of AV on the disc dynamics, we varied the constant C_{av} leaving the physical setup unchanged Fig. B.1 shows that the strength of the AV can change the simulation outcome significantly. Shown is the time evolution of the inner disc eccentricity for the Kepler-38 system. The eccentricity obtained with the standard artificial viscosity constant of FARGO3D ($C_{av} = 1.41$, orange curve) does not reproduce the PLUTO result (blue curve). To obtain a better agreement between the codes, we had to reduce the artificial viscosity used in FARGO3D to $C_{av} = 0.5$. Using these adjustments, the new FARGO3D results (green curve in Fig. B.1) and the PLUTO agree very well indeed. Simulations with no artificial viscosity are not stable at all (red curve in Fig. B.1).

For the rest of this section, we compare PLUTO and FARGO3D simulations of a circumbinary disc around Kepler-38 with an embedded planet. Figure B.2 shows the semi-major axis (top row) and the eccentricity time evolution (bottom row) of five planets with different masses from $m_p = 0.150\,M_{jup}$ to $m_p = 0.384\,M_{jup}$. The left column shows PLUTO results whereas the right column shows FARGO3D results. The codes agree very well for the $m_p = 0.384\,M_{jup}$ case (blue curve in Fig B.2). In both simulations the planet smoothly migrates inward until it reaches a final position slightly below $4\,a_{bin}$. In the FARGO3D simulations the planet migrates faster and a little bit more inward. Additionally, in both simulations the eccentricity of the massive planet stays below 0.05.

The codes produce also in the $m_p = 0.150\,M_{jup}$ case the same results. This lighter planet does not migrate as far inward as the massive planet discussed earlier. It reaches its final parking position at roughly $5\,a_{bin}$, but its eccentricity is increased to a value between 0.2 and 0.25. In both simulations the planet is captured in a 11:1 resonance with the binary. The only difference here is that in the PLUTO simulation the planet is kicked out of this resonance while in the FARGO3D simulations the planet remains in resonance with the binary. A more detailed analysis of the resonance can be found in Sect. 4.1.2.

For the planets with masses $m_p = 0.250\,M_{jup}$ and $m_p = 0.300\,M_{jup}$, the two codes produce the same overall behaviour but deviate in the details. As discussed in Sect. 4.1.2, these planets migrate first inward, then they reverse their migration direction and undergo a period of fast outward migration. After that they start to migrate inward again but on a much longer timescale than during the first inward migration period. This behaviour is observed with both codes. In the FARGO3D simulations the planets start their outward migration period in both cases a bit earlier than in the PLUTO simulations. A reason why in the PLUTO simulations the planets' outward migration period starts at different times could be the fact that the $m_p = 0.300\,M_{jup}$ planet is briefly captured in a 8:1 resonance with the binary between $t = 27\,000\,T_{bin}$ and $t = 30\,000\,T_{bin}$. But besides these differences the codes produce the results in good agreement for the final orbital parameters of the planets. A final position around $4.5\,a_{bin}$ and an increased eccentricity of around 0.20.

For the case $m_p = 0.200\,M_{jup}$, the codes differ in the final orbital elements of the planet. In the PLUTO simulations, this planet ends up with orbital parameters like the light planet with mass $m_p = 0.150\,M_{jup}$, whereas in the FARGO3D simulations

the planet's final orbital parameter are similar to the intermediate planets with $m_p = 0.250\,M_{jup}$ and $m_p = 0.200\,M_{jup}$. As discussed in the main part of this paper, we observe a different migration behaviour and different final orbital elements for light and massive planets. For very massive and very light planets the codes produce consistent and matching results. However, the exact point (in mass) at which the transition between massive and lighter planets occurs depends somewhat on the code used. Whether intermediate mass planets land on the massive or light branch depends on the code, but the absolute difference in mass is not very large. This was not only observed for the Kepler-38 system but also for Kepler-16 and -35.

For example, a FARGO3D simulation of Kepler-35 with a planet of mass $m_p = 0.550\,M_{jup}$ shows the same results as the PLUTO simulation. But results of a FARGO3D simulation with planet mass $m_p = 0.500\,M_{jup}$ shows the behaviour of a light planet (eccentricity excitation, orbital alignment), whereas in PLUTO simulations the $m_p = 0.500\,M_{jup}$ planet is on the massive branch (see Sect. 4.4).

For the Kepler-34 and -413 systems, we only observed one state with both codes. In both codes, the large and highly eccentric inner gap always dominated the planet.

Finally, we comment on the code performance on this problem. In Table B.1, we compare the average CPU-time per time step in seconds for PLUTO and FARGO3D for simulations of a disc around Kepler-38 with and without an embedded planet. The simulations that used a numerical resolution of 684×584 grid cells were carried out on one or two Nvidia Titan X GPUs. As seen, the two codes show a relatively similar performance in spite of the different numerical methods used. For both codes, the runs on two GPUs are about 1.6 times faster that on a single GPU.

Table B.1. Average CPU-time per time step in seconds for PLUTO and FARGO3D test simulations (using 684×584 grid cells) with and without planet.

Disc only	1 GPU	2 GPUs
PLUTO	1.00×10^{-2}	6.11×10^{-3}
FARGO3D	9.52×10^{-3}	5.92×10^{-3}
Disc with embedded migrating planet	**1 GPU**	**2 GPUs**
PLUTO	1.21×10^{-2}	7.47×10^{-3}
FARGO3D	1.39×10^{-2}	8.30×10^{-3}

Notes. The Fargo algorithm was not used in these simulations.

4 Results and outlook

The following chapter will summarise the main results of the publications presented in Chapter 3. Starting with the numerical conditions at the inner boundary, followed by a recap of the binary-disc interaction and the migration behaviour of embedded planets. Finally improvements of the disc model to get a better agreement of simulated and observed orbital parameters are discussed.

4.1 Numerics

To simulate circumbinary discs with a grid code, it is essential to use a polar grid, to achieve conservation of angular momentum. The drawback of a polar grid is the inner hole in the computational domain due to the coordinate singularity at the origin. The radius R_{min} of this inner hole and the boundary condition at this location has been debated extensively in the literature (Pierens and Nelson, 2013; Kley and Haghighipour, 2014; Lines et al., 2015; Miranda et al., 2017; Mutter et al., 2017a). Mainly three types of boundaries are used at the inner radius. Open boundaries, where gas can freely leave the computational domain, but not reenter it, viscous outflow boundaries, where the radial velocity is set to the mean viscous flow speed in the disc and closed boundaries, where basically a wall is built around the binary.

In Thun et al. (2017) these two issues are addressed and the results are as follows. To capture all relevant effects, especially the mean motion resonances, responsible for the development of the eccentric inner gap, the inner radius should be of the order of the binary semi-major axis $R_{\mathrm{min}} \approx a_{\mathrm{bin}}$. Concerning the boundary condition at the inner boundary simulations with different grid codes have shown that closed boundaries lead to unstable results, whereas open boundary conditions produce stable results independent of numerical parameters. Viscous outflow boundaries are comparable to the closed boundaries since the viscous speed is very low compared to the speeds induced by the binary. Therefore open boundary conditions are the favourable type of boundary at the inner radius from a numerical point of view. Further simulations which do not suffer from an inner hole in the computational domain, like particle based simulations (Artymowicz and Lubow, 1994) or simulations using a dual grid technique to overlay the central hole with a Cartesian grid (Günther and Kley, 2002; Günther et al., 2004), show clearly that gas streams can enter the inner cavity and the formation of circumstellar discs around both binary components. This means that also from a physical point of view outflow boundaries are the preferred type of boundary condition.

4.2 Disc-binary interaction: Binary parameters

As discussed in Thun et al. (2017) and Thun and Kley (2018) the binary eccentricity has the largest influence onto the disc structure and the properties of the inner gap. For varying binary eccentricities two branches of different behaviour exist. Starting from zero binary eccentricity until a critical eccentricity of $e_{\mathrm{crit}} \approx 0.18$, the gap size as well as the precession period decrease for increasing binary eccentricities. Increasing the binary eccentricity from the

critical eccentricity further leads then again to larger gap sizes and longer precession periods. In the upper panel of Fig. 4.1 this behaviour is plotted for three different binary mass ratios and various binary eccentricities. Since the binary mass ratio does not change the gap size and decreases the precession period slightly for increasing mass ratios, the bifurcation and the critical eccentricity are independent of the binary mass ratio. The upper panel shows two inconsistencies: First starting form zero eccentricity until $e_{\mathrm{bin}} = 0.06$ gap size and precession period increase with increasing binary eccentricity, before at $e_{\mathrm{bin}} = 0.06$ the typical lower branch behaviour starts. Second for high binary eccentricities $e_{\mathrm{bin}} > 0.4$ the values do not lie on the upper branch any more.

Motivated by the fact that the binary mass ratio does not change the gap size and that low mass planets align their orbit with the precessing inner gap (this will be summarised in detail in Sec. 4.4 below), the lower panel of Fig. 4.1 scales the precession period by the factor

$$\frac{q_{\mathrm{bin}}}{(q_{\mathrm{bin}}+1)^2} \cdot \left(1 + \frac{3}{2} e_{\mathrm{bin}}^2\right) . \tag{4.1}$$

This factor is motivated by the following formula for the precession period of the orbit of a test particle around a binary (Georgakarakos and Eggl, 2015)

$$T_{\mathrm{prec}} = \frac{4}{3} \frac{(q_{\mathrm{bin}}+1)^2}{q_{\mathrm{bin}}} \left(\frac{a_{\mathrm{p}}}{a_{\mathrm{bin}}}\right)^{7/2} \frac{\left(1-e_{\mathrm{p}}^2\right)^2}{1+\frac{3}{2}e_{\mathrm{bin}}^2} T_{\mathrm{bin}} . \tag{4.2}$$

The scaling in the lower panel of Fig. 4.1 does not include the term $\left(1-e_{\mathrm{gap}}^2\right)^2$ (please note that in case of a precessing gap instead of a precessing test particle $\left(1-e_{\mathrm{p}}^2\right)^2$ becomes $\left(1-e_{\mathrm{gap}}^2\right)^2$) to show a clear relation between binary parameters and individual disc properties. Adding the gap eccentricity term does not change the lower panel of Fig. 4.1 qualitatively. Including the scaling term (4.1) shows now clearly the two branches for a wide range of binary mass ratios. The scaling resolves the problem that for high binary eccentricities the points do not lie on the upper branch. Curves fitted to the lower and upper branch data points have lower exponents than 7/2 expected from equation (4.2), showing that the inner gap does not totally behave like a free particle and that hydrodynamical effects, like pressure and viscosity, still play a role.

The two branches suggest that two physical processes cause the eccentric inner cavity. For the lower branch, a possible explanation seems to be the 3:1 outer Lindblad resonance (Papaloizou et al., 2001). This is supported by the fact that simulations where the 3:1 outer Lindblad resonance is excluded from the computational domain do not develop a significant eccentric inner disc. For the upper branch higher order resonances could become more and more important (Fleming and Quinn, 2017).

For eccentricities ranging from $e_{\mathrm{bin}} = 0.0$ until $e_{\mathrm{bin}} = 0.08$ a loop like structure can be seen (see inlet of the lower panel of Fig. 4.1). In this binary eccentricity range also the gaps with the highest eccentricity are created.

4.3 Disc-binary interaction: Disc parameters

Besides the binary parameters, the disc parameters (pressure and viscosity) also have an influence on the disc structure and behaviour. Both parameters counteract the tidal effects of the binary which are responsible for the creation of the inner gap.

A clear trend is observable for the viscosity of the disc varied through the parameter α: Discs with higher viscosities have smaller gaps and shorter precession periods. This is consistent with the gap closing property of viscosity in the disc.

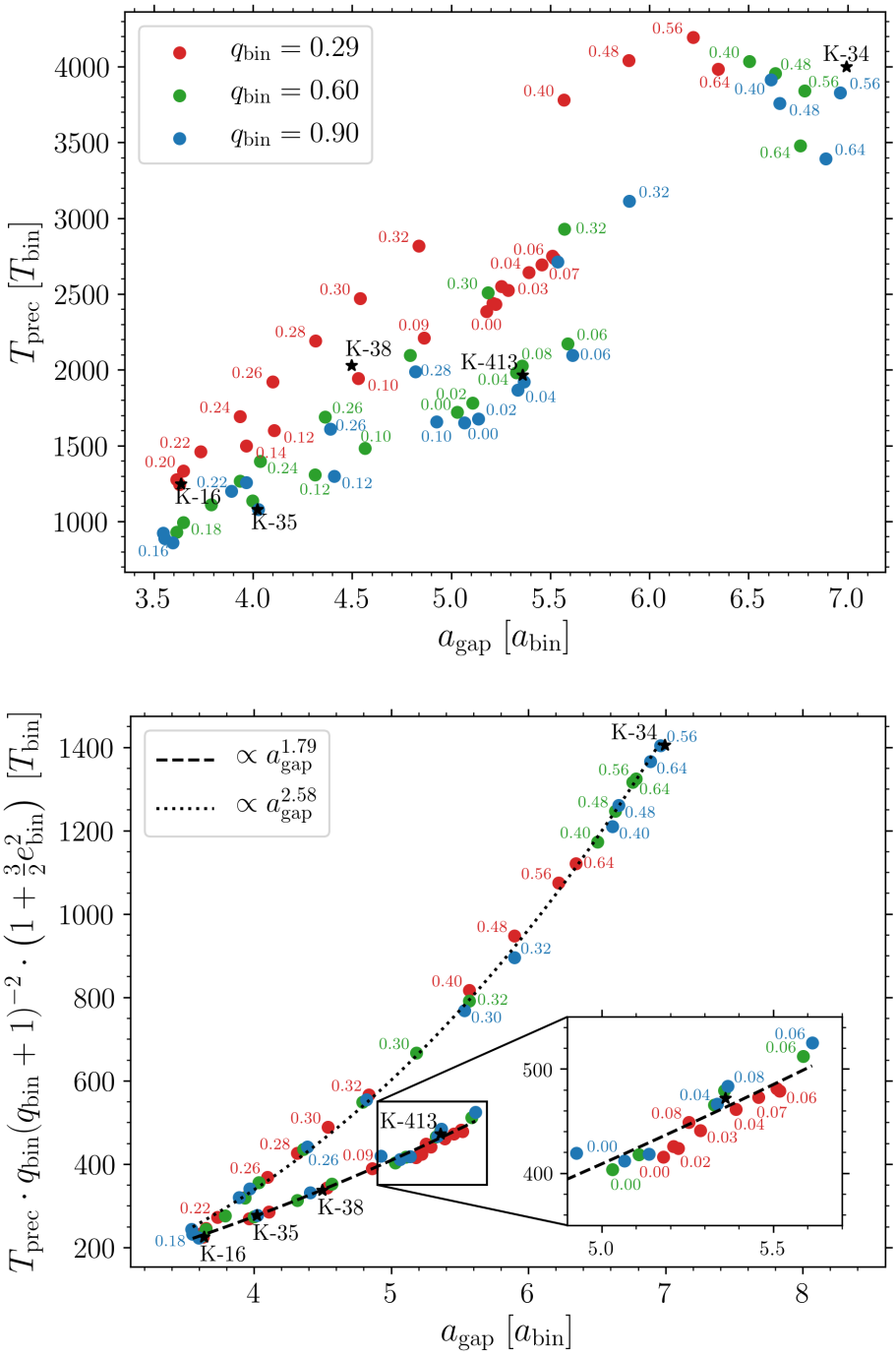

Figure 4.1: *Upper panel*: Precession period of the inner gap plotted against the semi-major axis of the gap, for different binary mass ratios (different colours) and binary eccentricities. Five Kepler circumbinary systems are also shown. *Lower panel*: Same as the upper panel but the precession period is scaled by the factor $q_{\rm bin}/\left(q_{\rm bin}+1\right)^2 \cdot \left(1+\frac{3}{2}e_{\rm bin}^2\right)$. Lower panel taken from Thun and Kley (2018).

Increasing the pressure in the disc (in isothermal simulations this can be achieved through the parameter $h = H/R$, the aspect ratio of the disc) from $h = 0.05$, leads to smaller gaps and shorter precession periods, as one would expect from the gap closing behaviour of higher disc pressures. For smaller pressures no clear trend could be observed, which could be due to the difficulty to sustain a coherent precession for low disc pressures.

4.4 Disc-planet interaction

Thun and Kley (2018) examines the evolution of embedded planets in circumbinary discs based on simulations of five Kepler systems (Kepler-16, -34, -35, -38 and -413).

A simulation series with varying initial planet positions showed that the final orbital parameters of the planet are independent of its initial location. In all cases the planets migrated until the edge of the inner gap.

Depending on the mass of the planet there are two states for the final semi-major axis and eccentricity. Massive planets migrate smoothly through the disc and can shrink and circularise the inner gap, while light planets are more dominated by the circumbinary disc. Light planets initially migrate rapidly inwards, followed by a short and fast outward migration period. After this phase a slow inward migration period starts. During the outward migration period the eccentricity of the planets is excited and they align their orbit with the precessing inner gap of the disc. On the contrary the eccentricity of a massive planet is not excited and its orbit is not aligned with the inner gap. Fig 4.2 shows the time evolution of the semi-major axis (upper panel) and eccentricity (lower panel) of planets with different masses around the Kepler-38 system. The two states are clearly visible. In case of the observed planet mass, $m_\mathrm{p} = 0.384\,\mathrm{M_{jup}}$, (blue curve in Fig. 4.2), the eccentricity is in good agreement with the observation but the semi-major axis is too large by a factor of 1.28.

The effect of a migrating planet onto the inner disc structure can be seen in Fig. 4.3. The upper left panel shows the surface density after 10 000 binary orbits, before the planet is introduced into the simulation. The remaining panels of Fig 4.3 show the disc surface density after 76 500 binary orbits, perturbed by a planet of increasing mass, ranging from $m_\mathrm{p} = 0.200\,\mathrm{M_{jup}}$ to $m_\mathrm{p} = 0.384\,\mathrm{M_{jup}}$. A fit to the eccentric inner gap is shown as white dashed line and the momentarily orbit of the planet is shown as blue dashed line. Additionally the pericentres of the disc (orange arrow), the secondary (green arrow) and the planet (blue arrow) are marked. It is clearly visible how planets of increasing mass shrink and circularise the inner cavity. Further for the case of $m_\mathrm{p} = 0.200\,\mathrm{M_{jup}}$ and $m_\mathrm{p} = 0.300\,\mathrm{M_{jup}}$ the pericentres of the disc and the planets are aligned (the orange and blue arrows point in the same direction). This alignment is not present in the massive case.

The above described behaviour was found in all examined systems. In the case of the Kepler-34 and Kepler-413 systems which create very eccentric inner gaps, no "massive" case was observed. In these systems the disc was always able to dominate the planet, even very high mass planets.

The final orbital parameters are summarised in Table 4.1. Compared to the observations the final semi-major axis is in all cases too large. The two systems which create large eccentric gaps, Kepler-34 and Kepler-413, produce planet orbits with a high eccentricity, which is also observed, although the simulated eccentricity is still to high.

In case of the "light" planet case, it was often observed that planets are captured in high mean motion resonances with the binary, especially during the second slow inward migration phase. This can be seen in Fig. 4.2. The planet with mass $m_\mathrm{p} = 0.150\,\mathrm{M_{jup}}$ is briefly captured

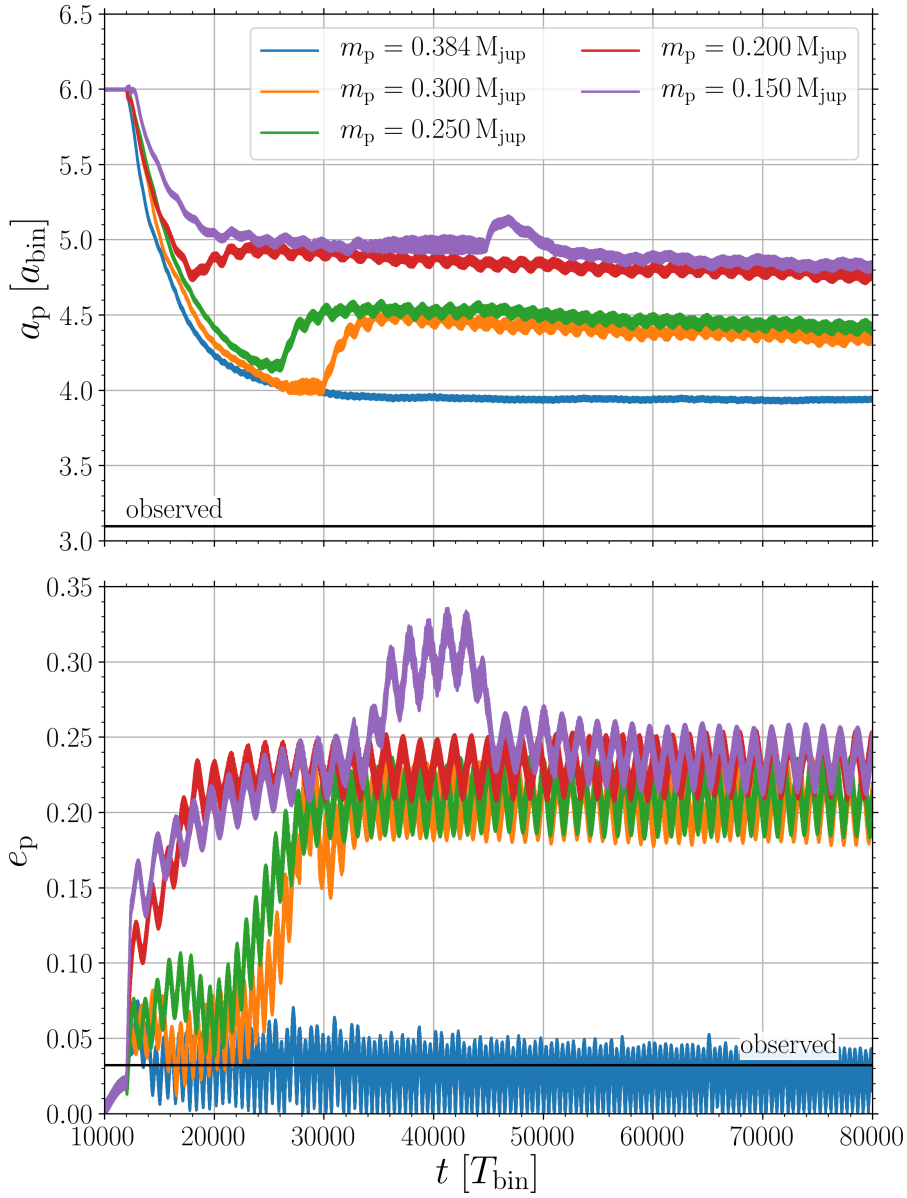

Figure 4.2: Time evolution of the orbital elements of migrating planets with different masses in an isothermal circumbinary disc around the Kepler-38 system. In each case the planet was introduced into the disc after 10 000 binary orbits and kept on a fixed circular orbit for another 2000 binary orbits. *Upper panel*: Evolution of the semi-major axis. *Lower panel*: Evolution of the eccentricity. Taken from Thun and Kley (2018).

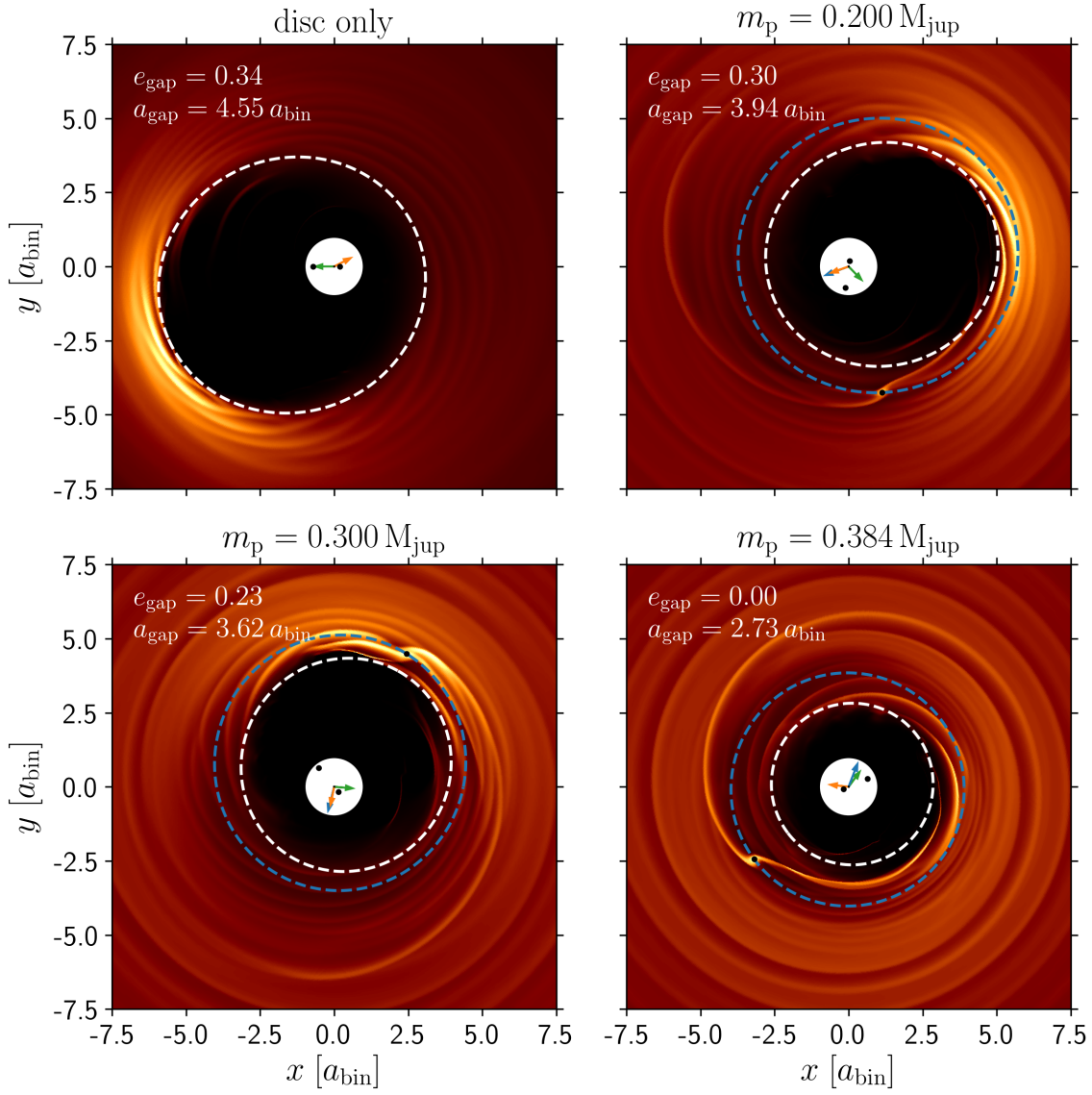

Figure 4.3: Structure of the inner disc around the Kepler-38 system. Colour-coded is the surface density. The *top left panel* shows the surface density after 10 000 binary orbits before the planet is inserted. The remaining panels show the surface density after 76 500 binary orbits, perturbed by a planet of increasing mass. In addition a fit to the inner gap (dashed white line) and the instantaneous orbit of the planet (dashed blue line) are shown. The arrows mark the pericentres of the disc (orange), the secondary (green) and the planet (blue). Taken from Thun and Kley (2018).

System	a_p [a_bin]	a_obs [a_bin]	e_p	e_obs
Kepler-16	4.18	3.20	0.03	0.007
Kepler-34	7.77	4.74	0.31	0.182
Kepler-35	4.47	3.35	0.12	0.042
Kepler-38	3.98	3.10	0.02	0.032
Kepler-413	5.53	3.55	0.30	0.118

Table 4.1: Final orbital parameters of simulated planets with the observed mass. For comparison the actual observed orbital elements are also shown. The semi-major axis (a_p) and eccentricity (e_p) of the planets are calculated by averaging over several thousand binary orbits at the end of the simulations. Taken from Thun and Kley (2018).

(from $t = 34\,000\,\mathrm{T_{bin}}$ until $t = 45\,000\,\mathrm{T_{bin}}$) in a 11:1 resonance with the binary.

The two migration scenarios do not depend solely on the planet mass, instead the disc-to-planet mass ratio determines if a planet behaves like a massive or light planet. It is possible by increasing or decreasing the disc mass to switch from the massive to the light case or vice versa. Since typically the observed circumbinary planets are very close to the binary it is reasonable to assume that they followed the migration path of a "massive" planet. This could mean that they formed late in the evolution of the circumbinary disc, where much of the gas was already dispersed and they could easily dominate the disc.

4.5 Outlook

As seen, typically the final semi-major axis of the simulated circumbinary planets is too large compared to the observations (Table 4.1). In all simulations of a circumbinary discs with an embedded planet, the migration stopped at the inner cavity of the disc. This is expected since the strong density gradient creates a large corotational torque, which can balance the Lindblad torques, responsible for the inward migration (Masset et al., 2006). One way to achieve a smaller semi-major axis of the planets orbit, is to decrease the inner gap size by varying the discs parameters, since the binary parameters are fixed by the observations[1]. As shown in Thun et al. (2017) small inner cavities can be achieved through a high viscosity and/or a high pressure in the disc. Unfortunately to reach gap sizes comparable to the observed final positions of the planets unnatural high viscosities and pressures are needed.

Although, smaller viscosities create in general larger gaps one needs also to consider the effect the planet has onto the disc. In low viscosity discs the planet is able to create a deep gap, see Fig. 4.4. Displayed is the azimuthally averaged surface density of two discs with different viscosities and an embedded planet of mass $m_\mathrm{p} = 0.384\,\mathrm{M_{jup}}$ after 12 000 binary orbits. The planet separates the disc in the low viscosity case (orange curve) into an inner and an outer

[1]The change of the binary parameters, due to the back reaction of the disc and the planet is very slow compared to all other timescales in the system.

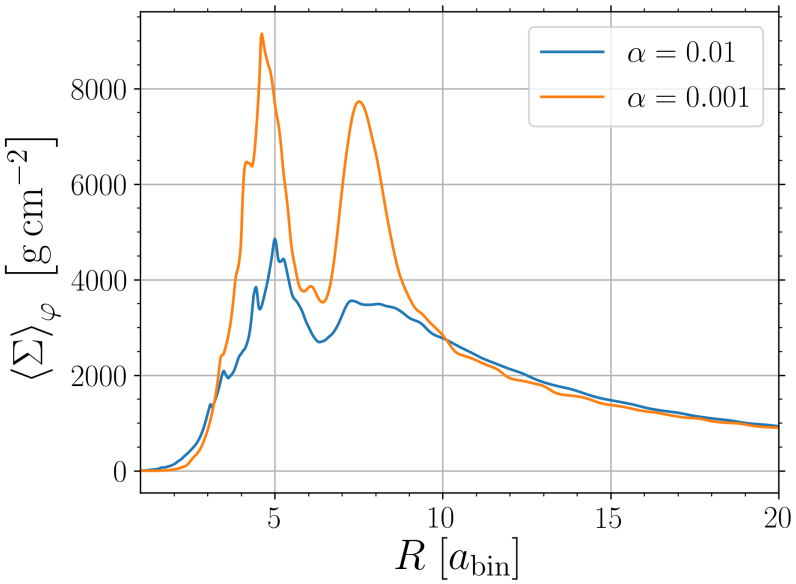

Figure 4.4: Azimuthally averaged density profiles for two different viscosities after 12 000 binary orbits, before the planet, with the observed mass, was allowed to migrate freely through the disc. The planet can create a much deeper gap in the low viscosity disc (orange curve) than in the high viscosity disc (blue curve).

part. Evolving the system further reveals that the inner disc is lost through the open boundary (basically accreted onto the binary) and the outer disc is not much affected by the binary any more. This allows the planet to migrate further in, see Fig. 4.5.

Another way to better reproduce the observed orbital parameters is to refine the physical model of the disc. Recently, Mutter et al. (2017b) simulated circumbinary planets in discs considering also self-gravity. They showed that in heavy discs, approximately five to ten times the minimum mass solar nebula, self-gravity can significantly shrink the inner cavity, allowing the planets to migrate closer to the binary. Typically, such high disc masses are very uncommon.

Another improvement of the disc model is to replace the locally isothermal equation of state by a more realistic equation of state. This can be achieved by including the equation of conservation of energy in the system of hydrodynamical equations together with the ideal gas equation of state. Since the energy equation contains a term which models heat generated by viscous friction a mechanism to cool the disc is needed. The implementation of this cooling term is described in detail in Müller and Kley (2012). Even more realistic models can also include radiative diffusion in the midplane of the disc. Such radiative models have been simulated for the Kepler-38 system by Kley and Haghighipour (2014) and for the Kepler-34 system by Kley and Haghighipour (2015). In both systems they could not recreate the observed orbital parameters. One reason for this discrepancy could be their numerical setup. In both cases the position of the inner boundary is too large.

In the rest of this section first results from simulations including viscous heating and radiative cooling from the disc surfaces will be presented. Fig. 4.6 compares the locally isothermal model to the radiative model. The radiative temperature profile is calculated at $t = 100\,000\,T_{\mathrm{bin}}$, the time the disc reached a quasi-steady state. The initial temperature profile for the radiative

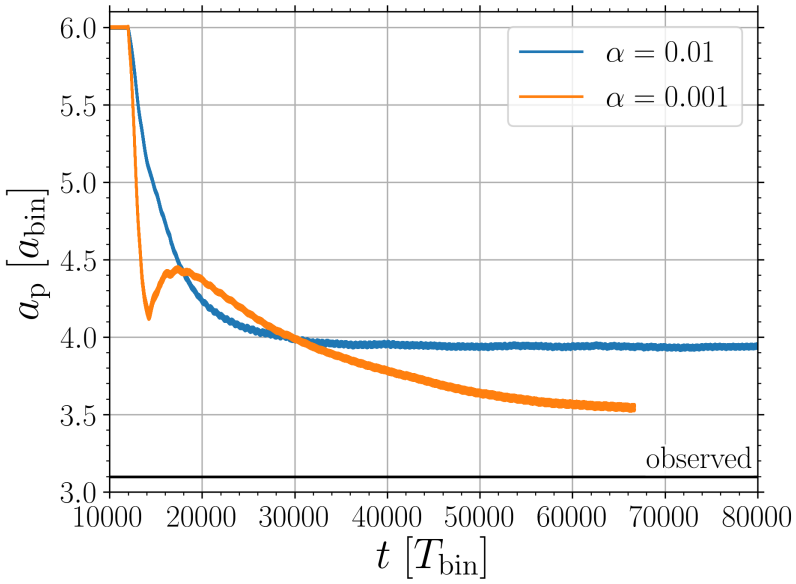

Figure 4.5: Time evolution of the semi-major axis of a planet with mass $m_\mathrm{p} = 0.384\,\mathrm{M_{jup}}$ for two different viscosities.

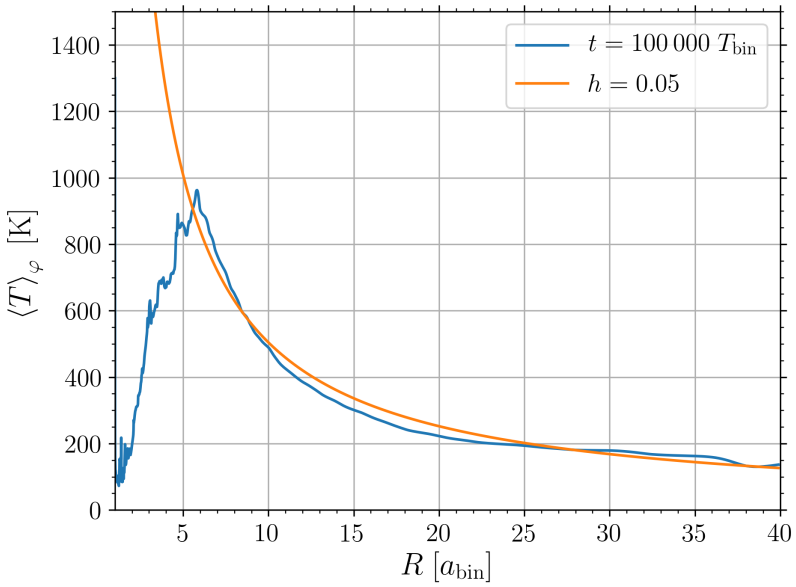

Figure 4.6: Comparison of the locally isothermal model and the radiative model including viscous heating and cooling form the disc surfaces. Shown is the azimuthally averaged temperature profile. The isothermal model is shown in orange and the radiative model in blue. The temperature profile of the radiative model was calculated after 100 000 binary orbits, the time after which the disc reached a quasi-steady state.

model was the isothermal one (orange curve). Both discs are around the Kepler-38 system and have a total disc mass of $M_{\rm disc} = 0.01\,M_{\rm bin}$ and a viscosity of $\alpha = 0.01$. In the outer part of the disc the assumption of an locally isothermal disc is justified, since both models agree reasonably well. But in the interesting inner part of the disc, where the cavity is created and the migration process of the planet is stopped, the isothermal model strongly deviates from the radiative model.

In the radiative model the pressure inside the disc is calculated self consistently and the only free disc parameters are the mass of the disc and the viscosity. Fig. 4.7 shows the evolution of the semi-major axis (upper panel) and eccentricity (lower panel) of the inner gap for different viscosities and disc masses. The binary in these simulations was modelled with the parameters of the Kepler-38 system. The first observation is that, large eccentric gaps are created at the beginning. During this phase the precession period is also very long. Interestingly, discs with higher viscosity produce a larger initial gap compared to discs with lower viscosity. This larger gaps are created because in discs with higher viscosity the pressure, in the inner part of the disc, is reduced by a factor of two, compared to the low viscosity case. After roughly 100 000 binary orbits all disc models reached a quasi-steady state. Compared to the isothermal case (red curve in Figure 2 of Thun and Kley (2018)) a smaller inner gap is created when a more realistic equation of state is used (blue curve in Fig. 4.7). The final properties of the disc seem almost independent of the viscosity and the disc mass.

After the discs reached a quasi-steady state, in this case after 88 000 binary orbits, a planet of the observed mass, $m_{\rm p} = 0.384\,{\rm M_{jup}}$, was inserted into the simulations. The planet was kept on a fixed circular orbit for another 2000 binary orbits before it was allowed to migrate freely through the disc. The initial planet position was chosen slightly outside of the gap like in the isothermal case. Fig. 4.8 shows the evolution of the semi-major axis (upper panel) and the eccentricity (lower panel) of the planet.

Two migration scenarios can occur like in the isothermal case. For the high viscosity models ($\alpha = 0.01$) the planet behaves like a "light" planet, independent of the disc mass. This is surprising since the high viscosity models lose almost half of their initial disc mass during their evolution, therefore one would expect that in these cases the planet can dominate the disc. The low viscosity models behave like the "massive" case, also independent of the initial disc mass. In these cases the planet migrates smoothly to its final parking position. Again, like in the isothermal case, planets in discs with $\alpha = 10^{-3}$ migrate further in than planets in discs with higher viscosity. The reason for this behaviour is the same as in the isothermal case: Planets in discs with low viscosity can create a gap, which separates the disc in an inner and outer part. The semi-major axis of the $\alpha = 10^{-3}$ and $M_{\rm disc} = 0.01\ M_{\rm bin}$ case is $a_{\rm p} = 3.359\,a_{\rm bin}$, which is quite close to the observed value of $a_{\rm obs} = 3.096\,a_{\rm bin}$. How the radiative model improves the final orbital parameters of the other systems, especially the systems with large eccentric discs, remains to be seen. Nevertheless, these first results with a radiative model are very promising.

The challenge of the radiative models are the long timescales. To reach a quasi-steady disc around 100 000 binary orbits are needed. An at least another 100 000 binary orbits are needed to follow the evolution of an embedded planet. Together this translate to over one billion time steps. This makes detailed parameter studies, comparable to the isothermal ones presented in this thesis, very challenging.

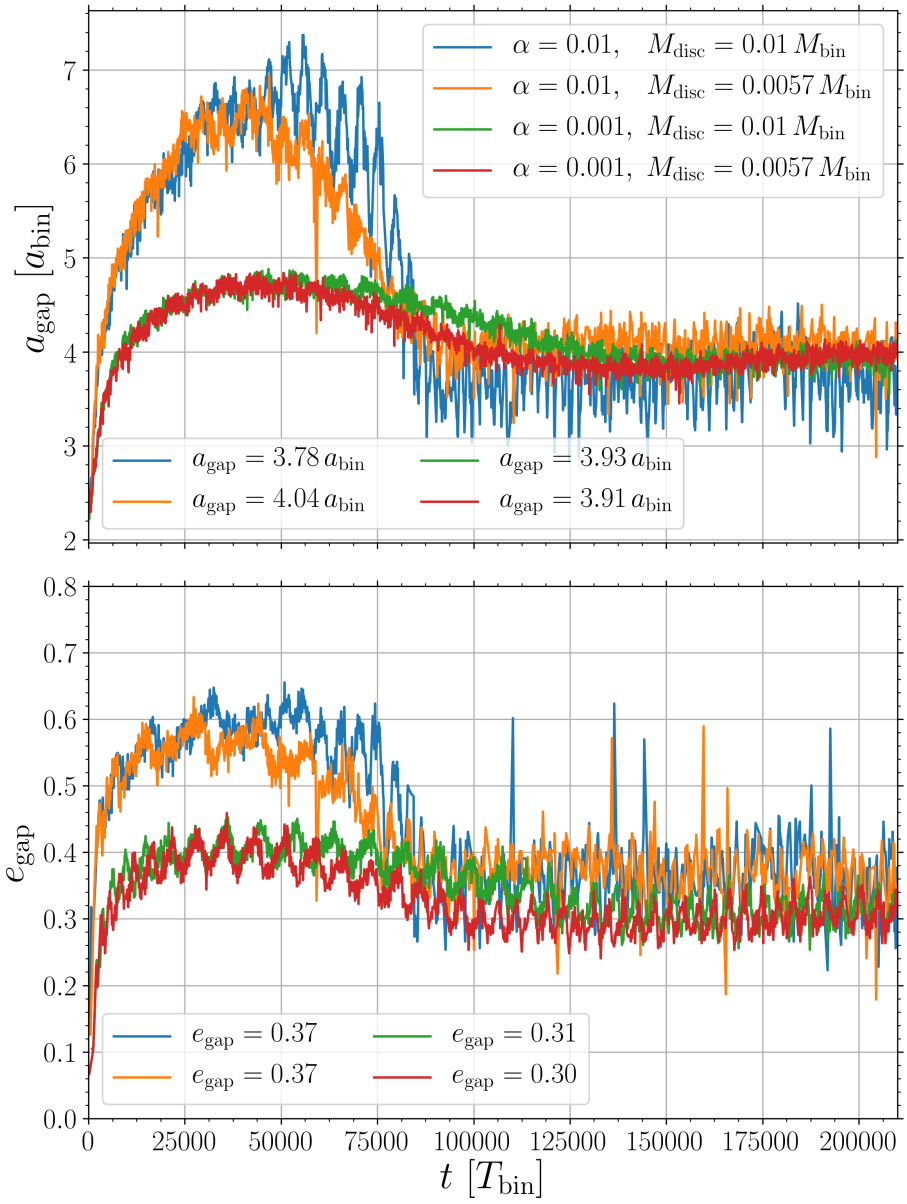

Figure 4.7: Time evolution of the semi-major axis and eccentricity of the gap for different disc models with varying viscosity and mass. The values for $a_{\rm gap}$ and $e_{\rm gap}$ are averaged in time starting from $t = 120\,000\,\mathrm{T_{bin}}$.

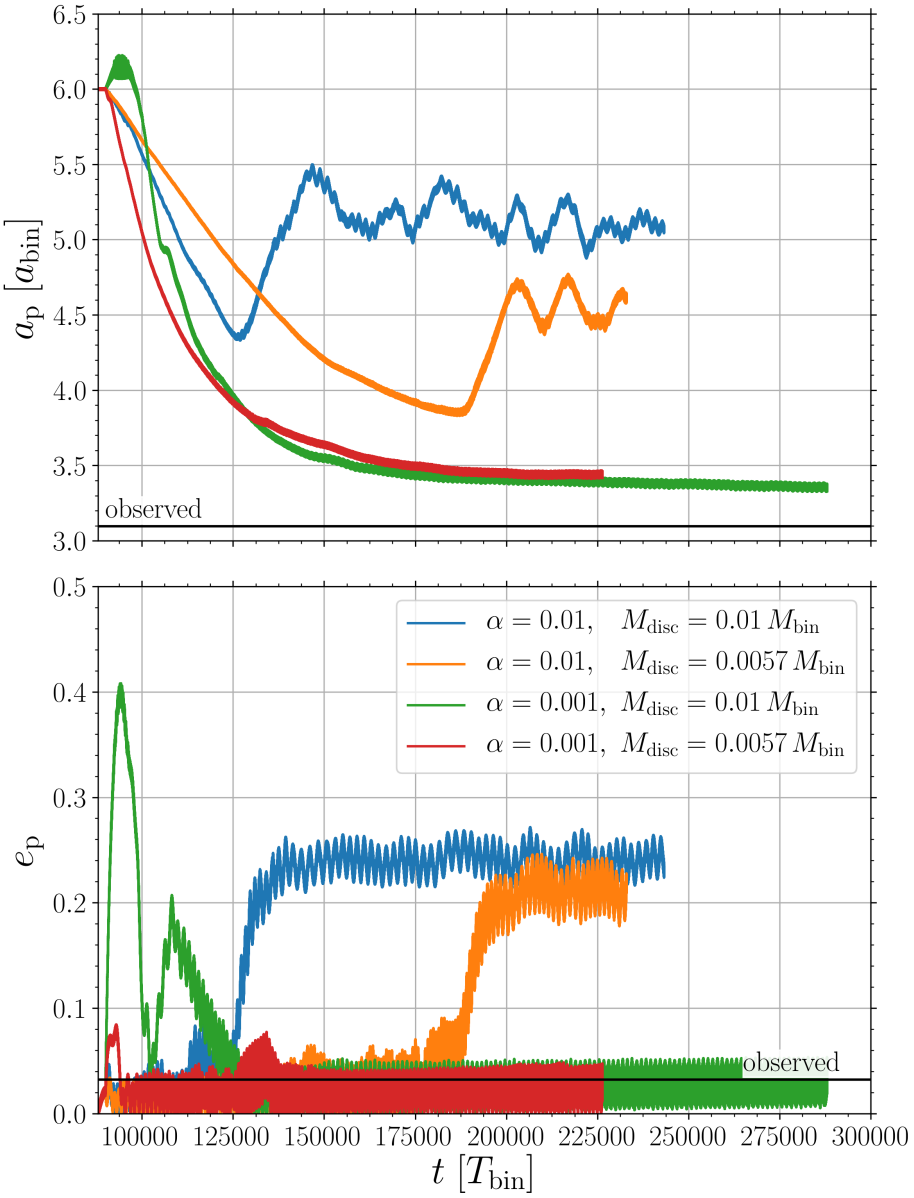

Figure 4.8: Time evolution of the orbital elements of a migrating planet in non-isothermal circumbinary discs with varying viscosity and mass around the Kepler-38 system. The planet was introduced into the discs after 88 000 binary orbits and kept on a fixed circular orbit for another 2000 binary orbits. *Upper panel*: Evolution of the semi-major axis. *Lower panel*: Evolution of the eccentricity

Acknowledgements

First of all, I would like to thank my supervisor Prof Dr Wilhelm Kley for the opportunity to write this thesis in his working group and the excellent supervision. He always had time to discuss any problems concerning numerical or astrophysical issues. He also gave me the necessary freedom to write the GPU version of Pluto and I am very grateful for that.

Second, I want to thank PD Dr Roland Speith, who passed away after a long struggle with cancer before this thesis was finished. Roland was the second supervisor of this thesis, and always a great help. I also want to thank Prof Dr Klaus Werner who stepped in for Roland on short notice.

I am very grateful for the financial support from the German Research Foundation through grant KL 650/26. Most of the simulations in this work were performed on the BinaAC cluster in Tübingen. I thank the High Performance and Cloud Computing Group at the Zentrum für Datenverarbeitung of the University of Tübingen for providing the necessary computational power.

A special thanks goes to my long term office colleague Dr Christoph Schäfer, with whom discussing serious problems as well as complete nonsense was always possible. I will greatly miss our coffee breaks.

Further, I want to thank also the rest of the Computational Physics Group, especially Dr Marius Hertfelder, Dr Giovanni Picogna, and Oliver Wandel for the great time and countless discussions. Not to forget Heike Fricke who was always a great help in all bureaucratic matters.

Last but not least I want to thank my family for their continuously support and encouragement and not asking too often when this thesis will finally be finished.

Bibliography

Y. Alibert, C. Mordasini, W. Benz, and C. Winisdoerffer. Models of giant planet formation with migration and disc evolution. *Astronomy and Astrophysics*, 434:343–353, April 2005. doi: 10.1051/0004-6361:20042032.

Sean M. Andrews and Jonathan P. Williams. High-Resolution Submillimeter Constraints on Circumstellar Disk Structure. *The Astrophysical Journal*, 659:705–728, April 2007. doi: 10.1086/511741.

P.J. Armitage. *Astrophysics of Planet Formation*. Cambridge University Press, 2010. ISBN 9780521887458.

P. Artymowicz and S. H. Lubow. Dynamics of binary-disk interaction. 1: Resonances and disk gap sizes. *The Astrophysical Journal*, 421:651–667, February 1994. doi: 10.1086/173679.

Steven A. Balbus and John F. Hawley. A Powerful Local Shear Instability in Weakly Magnetized Disks. I. Linear Analysis. *The Astrophysical Journal*, 376:214, July 1991. doi: 10.1086/170270.

C. Baruteau and F. Masset. On the Corotation Torque in a Radiatively Inefficient Disk. *The Astrophysical Journal*, 672:1054–1067, January 2008. doi: 10.1086/523667.

Konstantin Batygin and Michael E. Brown. Evidence for a Distant Giant Planet in the Solar System. *The Astronomical Journal*, 151:22, February 2016. doi: 10.3847/0004-6256/151/2/22.

P. Benítez-Llambay and F. S. Masset. FARGO3D: A New GPU-oriented MHD Code. *Astrophysical Journal Supplement Series*, 223:11, March 2016. doi: 10.3847/0067-0049/223/1/11.

Alan P. Boss. Rapid Formation of Outer Giant Planets by Disk Instability. *The Astrophysical Journal*, 599:577–581, December 2003. doi: 10.1086/379163.

M. E. Brown, C. A. Trujillo, and D. L. Rabinowitz. Discovery of a Planetary-sized Object in the Scattered Kuiper Belt. *The Astrophysical Journal*, 635:L97–L100, December 2005. doi: 10.1086/499336.

Daniel Carrera, Anders Johansen, and Melvyn B. Davies. How to form planetesimals from mm-sized chondrules and chondrule aggregates. *Astronomy and Astrophysics*, 579:A43, July 2015. doi: 10.1051/0004-6361/201425120.

A. Cassan, D. Kubas, J.-P. Beaulieu, M. Dominik, K. Horne, J. Greenhill, J. Wambsganss, J. Menzies, A. Williams, U. G. Jørgensen, A. Udalski, D. P. Bennett, M. D. Albrow, V. Batista, S. Brillant, J. A. R. Caldwell, A. Cole, C. Coutures, K. H. Cook, S. Dieters, D. Dominis Prester, J. Donatowicz, P. Fouqué, K. Hill, N. Kains, S. Kane, J.-B. Marquette, R. Martin, K. R. Pollard, K. C. Sahu, C. Vinter, D. Warren, B. Watson, M. Zub, T. Sumi, M. K. Szymański, M. Kubiak, R. Poleski, I. Soszynski, K. Ulaczyk, G. Pietrzyński, and

Ł. Wyrzykowski. One or more bound planets per Milky Way star from microlensing observations. *Nature*, 481:167–169, January 2012. doi: 10.1038/nature10684.

J. E. Chambers and G. W. Wetherill. Making the Terrestrial Planets: N-Body Integrations of Planetary Embryos in Three Dimensions. *Icarus*, 136:304–327, December 1998. doi: 10.1006/icar.1998.6007.

A. Crida, A. Morbidelli, and F. Masset. On the width and shape of gaps in protoplanetary disks. *Icarus*, 181:587–604, April 2006. doi: 10.1016/j.icarus.2005.10.007.

Gennaro D'Angelo and Stephen H. Lubow. Three-dimensional Disk-Planet Torques in a Locally Isothermal Disk. *The Astrophysical Journal*, 724:730–747, November 2010. doi: 10.1088/0004-637X/724/1/730.

L. R. Doyle, J. A. Carter, D. C. Fabrycky, R. W. Slawson, S. B. Howell, J. N. Winn, J. A. Orosz, A. Prša, W. F. Welsh, S. N. Quinn, D. Latham, G. Torres, L. A. Buchhave, G. W. Marcy, J. J. Fortney, A. Shporer, E. B. Ford, J. J. Lissauer, D. Ragozzine, M. Rucker, N. Batalha, J. M. Jenkins, W. J. Borucki, D. Koch, C. K. Middour, J. R. Hall, S. McCauliff, M. N. Fanelli, E. V. Quintana, M. J. Holman, D. A. Caldwell, M. Still, R. P. Stefanik, W. R. Brown, G. A. Esquerdo, S. Tang, G. Furesz, J. C. Geary, P. Berlind, M. L. Calkins, D. R. Short, J. H. Steffen, D. Sasselov, E. W. Dunham, W. D. Cochran, A. Boss, M. R. Haas, D. Buzasi, and D. Fischer. Kepler-16: A Transiting Circumbinary Planet. *Science*, 333:1602, September 2011. doi: 10.1126/science.1210923.

C. Dürmann and W. Kley. Migration of massive planets in accreting disks. *Astronomy and Astrophysics*, 574:A52, February 2015. doi: 10.1051/0004-6361/201424837.

A. Dutrey, S. Guilloteau, and M. Simon. Images of the GG Tauri rotating ring. *Astronomy and Astrophysics*, 286:149–159, June 1994.

B. Einfeldt, P. L. Roe, C. D. Munz, and B. Sjogreen. On Godunov-Type Methods near Low Densities. *Journal of Computational Physics*, 92:273–295, February 1991. doi: 10.1016/0021-9991(91)90211-3.

David P. Fleming and Thomas R. Quinn. Coevolution of binaries and circumbinary gaseous discs. *Royal Astronomical Society, Monthly Notices*, 464:3343–3356, January 2017. doi: 10.1093/mnras/stw2624.

N. Georgakarakos and S. Eggl. Analytic Orbit Propagation for Transiting Circumbinary Planets. *The Astrophysical Journal*, 802:94, April 2015. doi: 10.1088/0004-637X/802/2/94.

M. Gillon, A. H. M. J. Triaud, B.-O. Demory, E. Jehin, E. Agol, K. M. Deck, S. M. Lederer, J. de Wit, A. Burdanov, J. G. Ingalls, E. Bolmont, J. Leconte, S. N. Raymond, F. Selsis, M. Turbet, K. Barkaoui, A. Burgasser, M. R. Burleigh, S. J. Carey, A. Chaushev, C. M. Copperwheat, L. Delrez, C. S. Fernandes, D. L. Holdsworth, E. J. Kotze, V. Van Grootel, Y. Almleaky, Z. Benkhaldoun, P. Magain, and D. Queloz. Seven temperate terrestrial planets around the nearby ultracool dwarf star TRAPPIST-1. *Nature*, 542:456–460, February 2017. doi: 10.1038/nature21360.

P. Goldreich and S. Tremaine. The excitation of density waves at the Lindblad and corotation resonances by an external potential. *The Astrophysical Journal*, 233:857–871, November 1979. doi: 10.1086/157448.

Richard Greenberg, John F. Wacker, William K. Hartmann, and Clark R. Chapman. Planetesimals to planets: Numerical simulation of collisional evolution. *Icarus*, 35:1–26, July 1978. doi: 10.1016/0019-1035(78)90057-X.

Giovanni F. Gronchi. Classical and modern orbit determination for asteroids. *Proceedings of the International Astronomical Union*, 2004(IAUC196):293–303, 2004. doi: 10.1017/S174392130500147X.

R. Günther and W. Kley. Circumbinary disk evolution. *Astronomy and Astrophysics*, 387: 550–559, May 2002. doi: 10.1051/0004-6361:20020407.

R. Günther, C. Schäfer, and W. Kley. Evolution of irradiated circumbinary disks. *Astronomy and Astrophysics*, 423:559–566, August 2004. doi: 10.1051/0004-6361:20040223.

Jr. Haisch, Karl E., Elizabeth A. Lada, and Charles J. Lada. Disk Frequencies and Lifetimes in Young Clusters. *The Astrophysical Journal*, 553:L153–L156, June 2001. doi: 10.1086/320685.

M. J. Holman and P. A. Wiegert. Long-Term Stability of Planets in Binary Systems. *The Astronomical Journal*, 117:621–628, January 1999. doi: 10.1086/300695.

Eric L. N. Jensen and Robert D. Mathieu. Evidence for Cleared Regions in the Disks Around Pre-Main-Sequence Spectroscopic Binaries. *The Astronomical Journal*, 114:301–316, July 1997. doi: 10.1086/118475.

I. Kant. *Allgemeine Naturgeschichte und Theorie des Himmels*. Works. Fischer, 1755.

Sascha Kempf, Susanne Pfalzner, and Thomas K. Henning. N-Particle-Simulations of Dust Growth. I. Growth Driven by Brownian Motion. *Icarus*, 141:388–398, October 1999. doi: 10.1006/icar.1999.6171.

W. Kley. Radiation hydrodynamics of the boundary layer in accretion disks. I - Numerical methods. *Astronomy and Astrophysics*, 208:98–110, January 1989.

W. Kley. Mass flow and accretion through gaps in accretion discs. *Royal Astronomical Society, Monthly Notices*, 303:696–710, March 1999. doi: 10.1046/j.1365-8711.1999.02198.x.

W. Kley and N. Haghighipour. Modeling circumbinary planets: The case of Kepler-38. *Astronomy and Astrophysics*, 564:A72, April 2014. doi: 10.1051/0004-6361/201323235.

Wilhelm Kley and Nader Haghighipour. Evolution of circumbinary planets around eccentric binaries: The case of Kepler-34. *Astronomy and Astrophysics*, 581:A20, September 2015. doi: 10.1051/0004-6361/201526648.

Eiichiro Kokubo and Shigeru Ida. On Runaway Growth of Planetesimals. *Icarus*, 123:180–191, September 1996. doi: 10.1006/icar.1996.0148.

Eiichiro Kokubo and Shigeru Ida. Oligarchic Growth of Protoplanets. *Icarus*, 131:171–178, January 1998. doi: 10.1006/icar.1997.5840.

V. B. Kostov, P. R. McCullough, J. A. Carter, M. Deleuil, R. F. Díaz, D. C. Fabrycky, G. Hébrard, T. C. Hinse, T. Mazeh, J. A. Orosz, Z. I. Tsvetanov, and W. F. Welsh. Kepler-413b: A Slightly Misaligned, Neptune-size Transiting Circumbinary Planet. *The Astrophysical Journal*, 784:14, March 2014. doi: 10.1088/0004-637X/784/1/14.

Veselin B. Kostov, Jerome A. Orosz, William F. Welsh, Laurance R. Doyle, Daniel C. Fabrycky, Nader Haghighipour, Billy Quarles, Donald R. Short, William D. Cochran, Michael Endl, Eric B. Ford, Joao Gregorio, Tobias C. Hinse, Howard Isaacson, Jon M. Jenkins, Eric L. N. Jensen, Stephen Kane, Ilya Kull, David W. Latham, Jack J. Lissauer, Geoffrey W. Marcy, Tsevi Mazeh, Tobias W. A. Müller, Joshua Pepper, Samuel N. Quinn, Darin Ragozzine, Avi Shporer, Jason H. Steffen, Guillermo Torres, Gur Windmiller, and William J. Borucki. Kepler-1647b: The Largest and Longest-period Kepler Transiting Circumbinary Planet. *The Astrophysical Journal*, 827:86, August 2016. doi: 10.3847/0004-637X/827/1/86.

L.D. Landau and E.M. Lifshitz. *Course of Theoretical Physics, Vol. 6, Fluid Mechanics*. Pergamon Press, 1959.

P.S. Laplace. *Exposition du système du monde*. Mme. Ve. Courcier, 1796.

D. N. C. Lin and J. Papaloizou. On the tidal interaction between protoplanets and the protoplanetary disk. III - Orbital migration of protoplanets. *The Astrophysical Journal*, 309: 846–857, October 1986. doi: 10.1086/164653.

S. Lines, Z. M. Leinhardt, C. Baruteau, S.-J. Paardekooper, and P. J. Carter. Modelling circumbinary protoplanetary disks. I. Fluid simulations of the Kepler-16 and 34 systems. *Astronomy and Astrophysics*, 582:A5, October 2015. doi: 10.1051/0004-6361/201526295.

F. Marzari, P. Thébault, and H. Scholl. Planetesimal Evolution in Circumbinary Gaseous Disks: A Hybrid Model. *The Astrophysical Journal*, 681:1599-1608, July 2008. doi: 10.1086/588423.

F. Masset. FARGO: A fast eulerian transport algorithm for differentially rotating disks. *Astronomy and Astrophysics Supplement*, 141:165–173, January 2000. doi: 10.1051/aas: 2000116.

F. S. Masset and J. C. B. Papaloizou. Runaway Migration and the Formation of Hot Jupiters. *The Astrophysical Journal*, 588:494–508, May 2003. doi: 10.1086/373892.

F. S. Masset, A. Morbidelli, A. Crida, and J. Ferreira. Disk Surface Density Transitions as Protoplanet Traps. *The Astrophysical Journal*, 642:478–487, May 2006. doi: 10.1086/500967.

J. S. Mathis, W. Rumpl, and K. H. Nordsieck. The size distribution of interstellar grains. *The Astrophysical Journal*, 217:425–433, October 1977. doi: 10.1086/155591.

Michel Mayor and Didier Queloz. A Jupiter-mass companion to a solar-type star. *Nature*, 378: 355–359, November 1995. doi: 10.1038/378355a0.

N. Meyer-Vernet and B. Sicardy. On the physics of resonant disk-satellite interaction. *Icarus*, 69:157–175, January 1987. doi: 10.1016/0019-1035(87)90011-X.

A. Mignone, G. Bodo, S. Massaglia, T. Matsakos, O. Tesileanu, C. Zanni, and A. Ferrari. PLUTO: A Numerical Code for Computational Astrophysics. *Astrophysical Journal Supplement Series*, 170:228–242, May 2007. doi: 10.1086/513316.

R. Miranda, D. J. Muñoz, and D. Lai. Viscous hydrodynamics simulations of circumbinary accretion discs: variability, quasi-steady state and angular momentum transfer. *Royal Astronomical Society, Monthly Notices*, 466:1170–1191, April 2017. doi: 10.1093/mnras/stw3189.

H. Mizuno. Formation of the Giant Planets. *Progress of Theoretical Physics*, 64:544–557, August 1980. doi: 10.1143/PTP.64.544.

T. W. A. Müller and W. Kley. Circumstellar disks in binary star systems. Models for γ Cephei and α Centauri. *Astronomy and Astrophysics*, 539:A18, March 2012. doi: 10.1051/0004-6361/201118202.

T. W. A. Müller, W. Kley, and F. Meru. Treating gravity in thin-disk simulations. *Astronomy and Astrophysics*, 541:A123, May 2012. doi: 10.1051/0004-6361/201118737.

M. M. Mutter, A. Pierens, and R. P. Nelson. The role of disc self-gravity in circumbinary planet systems - I. Disc structure and evolution. *Royal Astronomical Society, Monthly Notices*, 465:4735–4752, March 2017a. doi: 10.1093/mnras/stw2768.

Matthew M. Mutter, Arnaud Pierens, and Richard P. Nelson. The role of disc self-gravity in circumbinary planet systems - II. Planet evolution. *Royal Astronomical Society, Monthly Notices*, 469:4504–4522, August 2017b. doi: 10.1093/mnras/stx1113.

Richard P. Nelson, Oliver Gressel, and Orkan M. Umurhan. Linear and non-linear evolution of the vertical shear instability in accretion discs. *Royal Astronomical Society, Monthly Notices*, 435:2610–2632, November 2013. doi: 10.1093/mnras/stt1475.

G. I. Ogilvie and S. H. Lubow. On the wake generated by a planet in a disc. *Royal Astronomical Society, Monthly Notices*, 330:950–954, March 2002. doi: 10.1046/j.1365-8711.2002.05148.x.

J. A. Orosz, W. F. Welsh, J. A. Carter, E. Brugamyer, L. A. Buchhave, W. D. Cochran, M. Endl, E. B. Ford, P. MacQueen, D. R. Short, G. Torres, G. Windmiller, E. Agol, T. Barclay, D. A. Caldwell, B. D. Clarke, L. R. Doyle, D. C. Fabrycky, J. C. Geary, N. Haghighipour, M. J. Holman, K. A. Ibrahim, J. M. Jenkins, K. Kinemuchi, J. Li, J. J. Lissauer, A. Prša, D. Ragozzine, A. Shporer, M. Still, and R. A. Wade. The Neptune-sized Circumbinary Planet Kepler-38b. *The Astrophysical Journal*, 758:87, October 2012a. doi: 10.1088/0004-637X/758/2/87.

J. A. Orosz, W. F. Welsh, J. A. Carter, D. C. Fabrycky, W. D. Cochran, M. Endl, E. B. Ford, N. Haghighipour, P. J. MacQueen, T. Mazeh, R. Sanchis-Ojeda, D. R. Short, G. Torres, E. Agol, L. A. Buchhave, L. R. Doyle, H. Isaacson, J. J. Lissauer, G. W. Marcy, A. Shporer, G. Windmiller, T. Barclay, A. P. Boss, B. D. Clarke, J. Fortney, J. C. Geary, M. J. Holman, D. Huber, J. M. Jenkins, K. Kinemuchi, E. Kruse, D. Ragozzine, D. Sasselov, M. Still, P. Tenenbaum, K. Uddin, J. N. Winn, D. G. Koch, and W. J. Borucki. Kepler-47: A Transiting Circumbinary Multiplanet System. *Science*, 337:1511, September 2012b. doi: 10.1126/science.1228380.

S. J. Paardekooper and G. Mellema. Halting type I planet migration in non-isothermal disks. *Astronomy and Astrophysics*, 459:L17–L20, November 2006. doi: 10.1051/0004-6361:20066304.

S. J. Paardekooper and J. C. B. Papaloizou. On disc protoplanet interactions in a non-barotropic disc with thermal diffusion. *Astronomy and Astrophysics*, 485:877–895, July 2008. doi: 10.1051/0004-6361:20078702.

S. J. Paardekooper, C. Baruteau, A. Crida, and W. Kley. A torque formula for non-isothermal type I planetary migration - I. Unsaturated horseshoe drag. *Royal Astronomical Society, Monthly Notices*, 401:1950–1964, January 2010. doi: 10.1111/j.1365-2966.2009.15782.x.

J. C. B. Papaloizou, R. P. Nelson, and F. Masset. Orbital eccentricity growth through disc-companion tidal interaction. *Astronomy and Astrophysics*, 366:263–275, January 2001. doi: 10.1051/0004-6361:20000011.

A. Pierens and R. P. Nelson. On the formation and migration of giant planets in circumbinary discs. *Astronomy and Astrophysics*, 483:633–642, May 2008. doi: 10.1051/0004-6361:200809453.

A. Pierens and R. P. Nelson. Migration and gas accretion scenarios for the Kepler 16, 34, and 35 circumbinary planets. *Astronomy and Astrophysics*, 556:A134, August 2013. doi: 10.1051/0004-6361/201321777.

James B. Pollack, Olenka Hubickyj, Peter Bodenheimer, Jack J. Lissauer, Morris Podolak, and Yuval Greenzweig. Formation of the Giant Planets by Concurrent Accretion of Solids and Gas. *Icarus*, 124:62–85, November 1996. doi: 10.1006/icar.1996.0190.

M. M. Romanova, P. S. Lii, A. V. Koldoba, G. V. Ustyugova, A. A. Blinova, R. V. E. Lovelace, and L. Kaltenegger. 3D Simulations of Planet Trapping at Disc-Cavity Boundaries. *ArXiv e-prints*, art. arXiv:1809.04013, September 2018.

A. Sachs. Babylonian Observational Astronomy. *Philosophical Transactions of the Royal Society of London Series A*, 276:43–50, May 1974. doi: 10.1098/rsta.1974.0008.

H. Scholl, F. Marzari, and P. Thébault. Relative velocities among accreting planetesimals in binary systems: the circumbinary case. *Royal Astronomical Society, Monthly Notices*, 380: 1119–1126, September 2007. doi: 10.1111/j.1365-2966.2007.12145.x.

M. E. Schwamb, J. A. Orosz, J. A. Carter, W. F. Welsh, D. A. Fischer, G. Torres, A. W. Howard, J. R. Crepp, W. C. Keel, C. J. Lintott, N. A. Kaib, D. Terrell, R. Gagliano, K. J. Jek, M. Parrish, A. M. Smith, S. Lynn, R. J. Simpson, M. J. Giguere, and K. Schawinski. Planet Hunters: A Transiting Circumbinary Planet in a Quadruple Star System. *The Astrophysical Journal*, 768:127, May 2013. doi: 10.1088/0004-637X/768/2/127.

N. I. Shakura and R. A. Sunyaev. Black holes in binary systems. Observational appearance. *Astronomy and Astrophysics*, 24:337–355, 1973.

G. A. Sod. Review. A Survey of Several Finite Difference Methods for Systems of Nonlinear Hyperbolic Conservation Laws. *Journal of Computational Physics*, 27:1–31, April 1978. doi: 10.1016/0021-9991(78)90023-2.

R. Speith and W. Kley. Stability of the viscously spreading ring. *Astronomy and Astrophysics*, 399:395–407, February 2003. doi: 10.1051/0004-6361:20021783.

R. Speith and H. Riffert. The viscous gas ring as an astrophysical test problem for a viscous SPH- code. *Journal of Computational and Applied Mathematics*, 109:231–242, September 1999.

Volker Springel. E pur si muove: Galilean-invariant cosmological hydrodynamical simulations on a moving mesh. *Royal Astronomical Society, Monthly Notices*, 401:791–851, January 2010. doi: 10.1111/j.1365-2966.2009.15715.x.

M. H. R. Stoll and W. Kley. Vertical shear instability in accretion disc models with radiation transport. *Astronomy and Astrophysics*, 572:A77, December 2014. doi: 10.1051/0004-6361/201424114.

H. Tanaka, T. Takeuchi, and W. R. Ward. Three-Dimensional Interaction between a Planet and an Isothermal Gaseous Disk. I. Corotation and Lindblad Torques and Planet Migration. *The Astrophysical Journal*, 565:1257–1274, February 2002. doi: 10.1086/324713.

Daniel Thun and Wilhelm Kley. Migration of planets in circumbinary discs. *Astronomy and Astrophysics*, 616:A47, August 2018. doi: 10.1051/0004-6361/201832804.

Daniel Thun, Rolf Kuiper, Franziska Schmidt, and Wilhelm Kley. Dynamical friction for supersonic motion in a homogeneous gaseous medium. *Astronomy and Astrophysics*, 589: A10, May 2016. doi: 10.1051/0004-6361/201527629.

Daniel Thun, Wilhelm Kley, and Giovanni Picogna. Circumbinary discs: Numerical and physical behaviour. *Astronomy and Astrophysics*, 604:A102, August 2017. doi: 10.1051/0004-6361/201730666.

A. Toomre. On the gravitational stability of a disk of stars. *The Astrophysical Journal*, 139: 1217–1238, May 1964. doi: 10.1086/147861.

E.F. Toro. *Riemann Solvers and Numerical Methods for Fluid Dynamics: A Practical Introduction*. Springer Berlin Heidelberg, 2009. ISBN 9783540498346.

W. R. Ward. Horsehoe Orbit Drag. In *Lunar and Planetary Science Conference*, volume 22, page 1463, March 1991.

S. J. Weidenschilling. Aerodynamics of solid bodies in the solar nebula. *Royal Astronomical Society, Monthly Notices*, 180:57–70, July 1977. doi: 10.1093/mnras/180.1.57.

W. F. Welsh, J. A. Orosz, J. A. Carter, D. C. Fabrycky, E. B. Ford, J. J. Lissauer, A. Prša, S. N. Quinn, D. Ragozzine, D. R. Short, G. Torres, J. N. Winn, L. R. Doyle, T. Barclay, N. Batalha, S. Bloemen, E. Brugamyer, L. A. Buchhave, C. Caldwell, D. A. Caldwell, J. L. Christiansen, D. R. Ciardi, W. D. Cochran, M. Endl, J. J. Fortney, T. N. Gautier, III, R. L. Gilliland, M. R. Haas, J. R. Hall, M. J. Holman, A. W. Howard, S. B. Howell, H. Isaacson, J. M. Jenkins, T. C. Klaus, D. W. Latham, J. Li, G. W. Marcy, T. Mazeh, E. V. Quintana, P. Robertson, A. Shporer, J. H. Steffen, G. Windmiller, D. G. Koch, and W. J. Borucki. Transiting circumbinary planets Kepler-34 b and Kepler-35 b. *Nature*, 481:475–479, January 2012. doi: 10.1038/nature10768.

W. F. Welsh, J. A. Orosz, J. A. Carter, and D. C. Fabrycky. Recent Kepler Results On Circumbinary Planets. In N. Haghighipour, editor, *Formation, Detection, and Characterization of Extrasolar Habitable Planets*, volume 293 of *IAU Symposium*, pages 125–132, April 2014. doi: 10.1017/S1743921313012684.

W. F. Welsh, J. A. Orosz, D. R. Short, W. D. Cochran, M. Endl, E. Brugamyer, N. Haghighipour, L. A. Buchhave, L. R. Doyle, D. C. Fabrycky, T. C. Hinse, S. R. Kane, V. Kostov, T. Mazeh, S. M. Mills, T. W. A. Müller, B. Quarles, S. N. Quinn, D. Ragozzine, A. Shporer, J. H. Steffen, L. Tal-Or, G. Torres, G. Windmiller, and W. J. Borucki. Kepler 453 b – The 10th Kepler Transiting Circumbinary Planet. *The Astrophysical Journal*, 809:26, August 2015. doi: 10.1088/0004-637X/809/1/26.

G. W. Wetherill and G. R. Stewart. Accumulation of a swarm of small planetesimals. *Icarus*, 77:330–357, February 1989. doi: 10.1016/0019-1035(89)90093-6.

P. Woodward and P. Colella. The Numerical Stimulation of Two-Dimensional Fluid Flow with Strong Shocks. *Journal of Computational Physics*, 54:115–173, April 1984. doi: 10.1016/0021-9991(84)90142-6.

Andrew N. Youdin and Jeremy Goodman. Streaming Instabilities in Protoplanetary Disks. *The Astrophysical Journal*, 620:459–469, February 2005. doi: 10.1086/426895.